Doctoral theses at NTNU, 2014:86

Erin Elizabeth Bachynski

Design and Dynamic Analysis of Tension Leg Platform Wind Turbines

ISBN 978-82-326-0097-7 (printed version)
ISBN 978-82-326-0096-0 (electronic version)
ISSN 1503-8181

NTNU
Norwegian University of Science and Technology
Thesis for the degree of Philosophiae Doctor
Faculty of Engineering Science and Technology
Department of Marine Technology

NTNU – Trondheim
Norwegian University of
Science and Technology

Doctoral Thesis

Erin Elizabeth Bachynski

Doctoral theses at NTNU, 2014:86

NTNU – Trondheim
Norwegian University of
Science and Technology

Erin Elizabeth Bachynski

Design and Dynamic Analysis of Tension Leg Platform Wind Turbines

Thesis for the degree of philosophiae doctor

Trondheim, March 2014

Norwegian University of Science and Technology
Faculty of Engineering Science and Technology
Department of Marine Technology

NTNU – Trondheim
Norwegian University of
Science and Technology

NTNU
Norwegian University of Science and Technology

Thesis for the degree of philosophiae doctor

Faculty of Engineering Science and Technology
Department of Marine Technology

ISBN 978-82-326-0097-7 (printed version)
ISBN 978-82-326-0096-0 (electronic version)
ISSN 1503-8181

Doctoral Theses at NTNU, 2014:86

Printed by Skipnes Kommunikasjon as

Abstract

There is an increasing interest in using wind turbines offshore, and in deeper water. The tension leg platform wind turbine (TLPWT) concept is promising for intermediate (45 - 150 m) or deep (> 150 m) water. The limited platform motions are expected to reduce the structural loading on the tower and blades compared to other floating concepts, without requiring the large draft of a spar or the spread mooring system and complex construction of a semi-submersible. Although numerous TLPWT designs exist on paper, there is very little consensus regarding size, tendon design, and analysis requirements. In order to determine whether or not such concepts could be feasible and to lead the way for future optimization work, a better understanding of how design choices affect the global system performance, an investigation of potential design-driving load cases, and an evaluation of the simulation sensitivity are required.

TLPWT systems are complex and dynamic: time-varying environmental loads from the sea, soil, and air act on a flexible integrated structure with a wide range of natural frequencies. Furthermore, the wind turbine may enter and exit various operational, start-up, shut-down, and failure modes. Dynamic simulation of TLPWTs requires multidisciplinary consideration of aerodynamics, hydrodynamics, control systems, and structural mechanics. Frequency-domain methods from offshore structures are not well-suited to the flexible structure and wind forces, while the computationally intense simulations common to the wind turbine industry are impractical with respect to the long time series required to capture wave- and low-frequency dynamics.

A new computational tool (SIMO-RIFLEX-AeroDyn) was developed and used to examine both the design and analysis of TLPWTs. The combination of three well-known codes under a single structural solver gave a stable, state-of-the-art numerical tool for analysis of floating wind turbines. Additionally, the wind turbine control system was implemented in Java, including options for applying a control system fault at an arbitrary point in time. This framework enabled detailed studies of parametric design effects, comparisons of different hydrodynamic models using a single structural model - including the implementation of a different ringing force model - and simulation of off-design conditions.

This thesis presents several baseline designs based on a parametric approach. Preliminary coupled simulations using first order wave forces suggested that a reasonable single column design with displacement between 3500 and 6500 m^3, three pontoons (for easier installation), and pontoon

radius between 28 and 35 m, may be able to support a 5 MW wind turbine and withstand harsh environmental conditions. Having established these designs as test cases, various analysis methods were compared. Neither linear frequency-domain analysis nor Morison-type forces gave acceptable results. Second-order sum-frequency wave forces were found to be important for fatigue and extreme response calculations for certain TLPWTs, particularly those with relatively soft tendons. Third order ringing forces were found to be critical for TLPWTs with large diameters (14-18 m), especially when the turbine was idling or parked. Finally, the analysis tool was extended to several different severe operational conditions. Control system faults were found to cause large tower top loads and yaw motions for TLWPTs, while wind-wave misalignment resulted in generally smaller responses than aligned conditions. Second-order forces, however, had a greater impact in misaligned wind and waves than in aligned conditions.

The original contributions of this thesis - including participation in developing the novel analysis tool (and the implementation of ringing loads), the development of a simplified design method, and the presented simulation results - provide the background for further studies of TLPWTs and other floating wind turbine concepts.

Acknowledgments

This Ph.D. work has been carried out at the Centre for Ships and Ocean Structures (CeSOS), which is supported by the Research Council of Norway. Support has been provided by Statoil through an MIT-NTNU Gemini cooperative research project. Additional support was provided by the MARINA Platform project, Grant Agreement no. 241402, funded by the European Union Seventh Framework Programme theme FP7-ENERGY.

Prof. Torgeir Moan was the supervisor for this work, and I am grateful for all of his guidance and support. His incredible wealth of experience and unflagging commitment to research never cease to amaze me.

I very much appreciate the time and effort of committee members Dr. John Niedzwecki, Dr. Amy Robertson, and Dr. Zhen Gao, who have reviewed the thesis and provided interesting discussions.

Dr. Harald Ormberg and Dr. Elizabeth Passano of MARINTEK provided many hours of support and cooperation in the development and testing of the coupled computer code Simo-Riflex-AeroDyn. Early conversations about TLPWT design with Dr. Steven Leverette (SBM) and Dagfinn Sveen (Olav Olsen) were very influential in the development of the studied concepts, and the work on ringing loads would have been impossible without many hours of discussion and guidance from Dr. Jørgen Krokstad of Statkraft.

I am very grateful for the help, guidance, and encouragement of colleagues, friends, and family during my Ph.D. studies. I have had the best office mates in the world – Dr. Ida Aglen and Lin Li – who have been constant sources of insight and inspiration. I have also benefited greatly from friendship and cooperation with Marit Kvittem, Chenyu Luan, Dr. Mahmoud Etemaddar, Zhiyu Jiang, Kai Wang, Jabus de Vaal, Dr. Madjid Karimirad, Eirik Bøckmann, Dr. Maxime Thys, Dražen Polić, and many other PhD candidates and post-doctoral fellows at NTNU. Outside of the university, my experience in Trondheim was made all the richer by interactions with flatmates, quartet musicians, orchestra members, church members, and the triathlon club.

A special thank-you goes to my family: my parents, sister, brother, and extended family have provided love, support, and hours of proofreading.

Nomenclature

Abbreviations

DLC	Design load case
DOF	Degree of freedom
EC	Environmental condition
ETM	Extreme turbulence model
PRVS	Pitch-regulated variable speed
FE	Finite element
FLS	Fatigue limit state
FMEA	Failure mode and effect analysis
FNV	Faltinsen, Newman, Vinje (ringing force)
FWT	Floating wind turbine
IBPC	Individual blade pitch control
LRFD	Load and resistance factor design
NTM	Normal turbulence model
O&G	Oil and gas
OWT	Offshore wind turbine
PDF	Probability density function
PI	Proportional-integral (control)
QTF	Quadratic transfer function

TF	Transfer function
TLBWT	Tension leg buoy wind turbine
TLP	Tension leg platform
TLPWT	Tension leg platform wind turbine
ULS	Ultimate limit state

Parametric TLPWT Design Variables

A_t	Tendon cross-sectional area
BF	Ballast fraction: ballast mass divided by displaced water mass of the center columns
b_t	Freeboard to the tower base
D_1 & D_2	Diameter of upper (1) and lower (2) main column
d_t	Tendon outer diameter
E_t	Tendon Young's modulus
F_t	Pretension per line
h_1 & h_2	Length of upper (1) and lower (2) main column
h_p/w_p or d_p	Height/width or diameter of pontoons
l_0	Tendon unstretched length
l_p	Length of pontoons
n_p	Number of pontoons
n_t	Number of tendons
r_p	Pontoon radius (measured from TLPWT hull centerline)
T	TLPWT draft
z_s	Vertical location of pontoons
Δ	TLPWT hull displacement
ρ_t	Tendon dry mass per unit length

Mathematical Model and Response Variables

$\boldsymbol{A}$	Added mass matrix
a	Waterline radius
A_{wp}	Waterplane area
$A_{ij}(\omega)$	Frequency-dependent added mass matrix entry
A_j	Wave component amplitude
a_t	Transverse added mass per unit length
$\boldsymbol{B}$	Linear damping matrix
b_1	Linear damping (Eq. 3.19)
b_2	Quadratic damping (Eq. 3.19)
B_{aero}	Aerodynamic damping
$B_{ij}(\omega)$	Frequency-dependent radiation damping matrix entry
$\boldsymbol{B_{Rayleigh}}$	Structural damping matrix
$\boldsymbol{C}$	Hydrostatic stiffness matrix
C_a	Added mass coefficient (Morison's equation)
C_D	Quadratic drag coefficient (Morison's equation)
C_{jk}	Hydrostatic stiffness matrix entry
C_m	Inertia coefficient (Morison's equation)
D_{RFC}	Fatigue damage
E	Expected value
E_{xx}	Green strain (longitudinal)
f_{1p}	Rotor rotation frequency (1p)
$F_3^{(1)}$	Third-order force component due to the first-order potential
$F_3^{(2)}$	Third-order force component due to the nonlinear potential
f_{3p}	Blade passing frequency (3p)

F_T	Wind turbine thrust force
$F_x^{FNV(3)}$	Third-order ringing force
G	Shear modulus
g	Acceleration due to gravity
H	Water depth
h	Cylinder draft (FNV)
h_{hub}	Hub height above still water line
H_s	Significant wave height
I	Turbulence intensity
I_{wp}	Waterplane area moment of inertia
$\boldsymbol{K}$	Mooring system stiffness matrix
k	Wavenumber ($k = 2\pi/\lambda$)
K, K_1, K_2	Material property for S-N curves
$\boldsymbol{K_g}$	Finite element stiffness matrix
K_{jk}	Mooring system stiffness matrix entry
$L(V)$	Loss of energy per cycle (Eq. 3.21-3.25)
$\boldsymbol{M}$	Mass matrix
m, m_1, m_2	Slope of S-N curve
M_{edge}	Blade root edgewise bending moment (local system)
M_{FA}	Fore-aft tower bending moment at the base
M_{flap}	Blade root flapwise bending moment (local system)
$\boldsymbol{M_g}$	Finite element mass matrix
M_{Ip}	Blade root in-plane bending moment
M_{jk}	Mass matrix entry
M_{Oop}	Blade root out-of-plane bending moment

M_{SS}	Side-to-side tower bending moment at the base
M_θ	Twist moment
P	Electrical power
p	Pressure
PR	Blade pitch rate during emergency shutdown
P_y	Tendon yield load
R	Response amplitude operator (RAO)
$\vec{R}^{ext}$	External loads
$\vec{R}^{int}$	Internal reaction forces
R_{xx}	Autocorrelation function
s_0	Characteristic wave steepness
S_{resp}	Spectral response
S_w	Wave spectrum
S_{xx}	Spectral density function
SF	Safety factor
t	Time
t_d	Time to control system fault detection
t_f	Time of control system fault
T_i	Tension in line i
T_{nj}	Natural period in motion j
T_p	Peak wave period
t_{ref}	Reference thickness for S-N curves
$\bar{U}$	Mean wind speed
U	Wind speed
U_{10}	Mean wind speed at 10 m

$\bar{U}_{ref}$	Mean wind speed at reference height
V	Energy per unit mass
$v^{+}(\xi)$	Upcrossing rate
$\tilde{X}_j(\omega)$	Frequency-dependent first-order wave excitation force
$\ddot{x}_{nac}$	Nacelle fore-aft acceleration
z_{ref}	Reference height for wind speed
β	Newmark-Beta integration parameter
β_{wave}	Wave direction
γ	Newmark-Beta integration parameter
ζ	Wave elevation
$\widetilde{\zeta_j}$	Platform rigid body motion in mode j
ζ_j	Platform rigid body motion amplitude in mode j
η	General degree of freedom (Eq. 3.19)
θ	Cross-sectional location for fatigue calculation
λ	Wavelength
μ	Mean value
ρ	Water density
ρ_{air}	Air density
σ	Standard deviation
σ_x	Axial stress
σ_y	Yield stress
τ_θ	Shear stress
$\Phi^{(1)}$	First-order velocity potential
$\Phi^{(2)}$	Second-order velocity potential
$\varphi,\ \ \varphi_j$	Azimuth angle, blade j azimuth angle

ω	Wave frequency
ω_0	Undamped natural frequency
ω_{axial}	Tendon natural frequency (axial)
ω_{trans_n}	Tendon natural frequency (n-th transverse)
∇	Displaced volume

Commonly used expressions

cut-in wind speed: the wind speed at which the turbine first delivers power [1, Ch. 1,p. 7]

cut-out wind speed: the maximum wind speed at which the turbine delivers power [1, Ch. 1,p. 7]

pitch/bending mode: a natural mode of the TLPWT system which combines hull pitch motion and tower bending

rated wind speed: the wind speed at which the rated (maximum) power output is reached [1, Ch. 1,p. 7]

soft-stiff: the fundamental eigenfrequency is in between f_{1p} and f_{3p}

Contents

List of Tables **xix**

List of Figures **xxi**

1 Introduction **1**
1.1 Motivation 1
1.1.1 Design Challenges for TLPWTs 2
1.1.2 Analysis Challenges for TLPWTs 4
1.1.3 Severe Operational Conditions 6
1.2 Aim and Scope 7

2 Related Work **9**
2.1 Floating Foundations for Intermediate Water Depth 9
2.2 TLPWT Designs 11
2.2.1 Early Designs (MIT) 11
2.2.2 Recent Single-Column 5 MW Designs 13
2.2.3 Multi-Column TLPWT Designs 16
2.3 Floating Wind Turbine Analysis 17
2.3.1 Numerical Tools 18
2.3.2 Experiments 19
2.3.3 Sea Trials 20
2.4 Floating Wind Turbine Load Conditions 20
2.5 Offshore Oil and Gas Tension Leg Platforms 21
2.5.1 Tension Leg Platform Dynamics 23
2.5.2 Tension Leg Platform Hydrodynamics 24

3 Theoretical Background **29**
3.1 Structural Mechanics of Steel Structures 29
3.1.1 Rigid Body Mechanics for Floating Bodies 30
3.1.2 Modal Analysis 31

3.1.3 Nonlinear Beam Element Theory 32
3.1.4 Time Domain FE formulation 34
3.1.4.1 Mass Matrix Formulation 34
3.1.4.2 Rayleigh Structural Damping 35
3.1.4.3 Direct Time Integration: Newmark-Beta with Newton-Raphson Iteration 36
3.1.4.4 Decay Test Analysis 38
3.1.4.5 Fatigue Damage 39
3.1.5 Natural Frequencies of Tensioned Beams 42
3.2 Hydrodynamics of TLPWTs 42
3.2.1 Hydrostatic Analysis 43
3.2.2 First-Order Potential Flow Theory 44
3.2.3 Second-Order Potential Flow Theory 45
3.2.4 3rd Order Long-Wave Forces (Ringing) 46
3.2.4.1 Direct Computation of Irregular Wave FNV 46
3.2.4.2 Bandwidth-limited, Sum-frequency Implementation of Irregular Wave FNV 47
3.2.5 Morison's Equation 49
3.3 Wind Turbine Aerodynamics 51
3.3.1 Blade Element Momentum 51
3.3.2 Generalized Dynamic Wake 52
3.3.3 Dynamic Stall and Skewed Inflow 53
3.3.4 Upwind Tower Influence 53
3.3.5 Tower Drag 55
3.4 Wind Turbine Control Systems 55
3.4.1 Pitch-Regulated Variable Speed Control 56
3.4.2 Control Challenges for Floating Wind Turbines 57
3.4.3 Control and Electrical System Faults 58
3.4.3.1 Blade Pitch Control System Faults 58
3.4.3.2 Grid Faults 59
3.5 Stochastic Methods for Offshore Structures 59
3.5.1 Definition of a Stochastic Process 59
3.5.2 Random Environmental Processes 61
3.5.2.1 Ocean Waves 61
3.5.2.2 Wind 63
3.5.2.3 Joint North Sea Wind-Wave Distributions . 65
3.5.2.4 Selected Environmental Conditions 66
3.5.3 Response Statistics 69
3.5.3.1 Calculation of Mean and Standard Deviation 70
3.5.3.2 Response Spectra 71

3.5.3.3 Extreme Value Statistics 72
3.6 SIMO-RIFLEX-AeroDyn + Java Control 73
3.6.1 RIFLEX Model Components 74
3.6.2 Modifications to AeroDyn 74
3.6.3 Control System 76
3.6.4 Floating Wind Turbine Model 76

4 TLPWT Design **79**
4.1 Spreadsheet-based Parametric TLPWT Design 80
4.1.1 Parametric TLPWT Definition 80
4.1.2 Spreadsheet Design Calculations 81
4.1.2.1 Added Mass Estimation 82
4.1.2.2 Mooring System Stiffness Estimation 83
4.1.3 Design Criteria 84
4.1.4 Resulting TLPWT Designs 86
4.1.4.1 Hydrodynamic Coefficients 89
4.1.4.2 Natural Periods 91
4.1.4.3 Linear and Quadratic Damping Ratios . . . 98
4.1.4.4 Tendon Yield Loads 99
4.1.4.5 Cost Estimates 99
4.1.5 Conclusions 100
4.2 Effects of Parameter Variation on TLPWT Behavior 102
4.2.1 Performance Comparison Parameters 102
4.2.2 Comparison of Baseline TLPWT Designs 102
4.2.3 Comparison of Baseline Designs with the Land-based Turbine 107
4.2.4 Parameter Variations 109
4.2.4.1 Diameter 109
4.2.4.2 Water Depth 111
4.2.4.3 Pontoon Radius 112
4.2.4.4 Ballast Fraction 113
4.2.5 Design Trends 114
4.2.6 Conclusions 116

5 TLPWT Analysis **119**
5.1 Linear vs. Nonlinear Analysis of TLPWTs 120
5.1.1 Wave-only Frequency-Domain Analysis 120
5.1.2 Wind-Wave Frequency-Domain Analysis 121
5.1.3 Linear and Nonlinear Responses 123
5.1.4 Conclusions 127
5.2 Effects of Hydrodynamic Modeling Approaches 130

5.2.1 Morison Model vs. First-Order Potential Model 132
5.2.1.1 Conclusions 135
5.2.2 Effects of Sum-Frequency Second-Order Forces 137
5.2.2.1 Conclusions 140
5.2.3 Effects of Ringing Forces 141
5.2.3.1 Baseline TLPWT Designs 142
5.2.3.2 Soft TLPWT Designs 145
5.2.3.3 Operational vs. Parked Turbines 147
5.2.3.4 Viscous Damping Effects 148
5.2.3.5 Conclusions 148

6 Severe Operational Conditions 151
6.1 Effects of Wind Turbine Controller Faults on TLPWTs . . . 152
6.1.1 Fault Conditions 152
6.1.2 Constant Wind 154
6.1.2.1 Azimuth Angle Dependence 154
6.1.2.2 Pitch Rate Dependence 157
6.1.3 Turbulent Wind and Irregular Waves 159
6.1.3.1 Response Maxima 161
6.1.3.2 Platform Motions and Mooring System Loads 163
6.1.3.3 Tower Base Bending Moments 165
6.1.3.4 Tower Top Bending Moments 165
6.1.3.5 Blade Root Bending Moments 167
6.1.4 Conclusions 168
6.2 Effects of Wind-Wave Misalignment on TLPWTs 169
6.2.1 Cross-Sectional Fatigue Damage Calculation 170
6.2.2 Fatigue Damage from First-Order Wave Loads 171
6.2.3 Second-Order Sum-Frequency Wave Load Effects . . . 172
6.2.4 Blade Root Bending Moments 177
6.2.5 Maximum Stress 178
6.2.6 Conclusions 179

7 Conclusions and Recommendations for Future Work 181
7.1 TLPWT Design 181
7.2 TLPWT Analysis 183
7.3 Severe Operational Conditions 184
7.4 Original Contributions 185
7.5 Limitations 187
7.6 Recommendations for future work 187

References 191

A Tower and Tendon Modes Shapes **209**
A.1 TLPWT 1 Tower and Tendon Mode Shapes 210
A.2 TLPWT 2 Tower and Tendon Mode Shapes 211
A.3 TLPWT 4 Tower and Tendon Mode Shapes 212
A.4 TLPWT 5 Tower and Tendon Mode Shapes 214
A.5 Soft TLPWT 1 Tower and Tendon Mode Shapes 215
A.6 Soft TLPWT 2 Tower and Tendon Mode Shapes 217
A.7 Soft TLPWT 3 Tower and Tendon Mode Shapes 218
A.8 Soft TLPWT 4 Tower and Tendon Mode Shapes 220

B Parameter Variations **223**

C Second-Order Potential Flow Calculations **233**
C.1 Free Surface Meshing 234
C.2 TLPWT 1 235
C.2.1 Free Surface Meshes 235
C.2.2 Sum-Frequency Forces on Stationary TLPWT 1 . . . 236
C.2.3 Difference-Frequency Forces on Stationary TLPWT 1 237
C.2.4 Sum-Frequency Forces on Moving TLPWT 1 239
C.2.5 Difference-Frequency Forces on Moving TLPWT 1 . . 241
C.3 TLPWT 2 242
C.3.1 Free Surface Meshes 243
C.3.2 Sum-Frequency Forces on Stationary TLPWT 2 . . . 243
C.3.3 Difference-Frequency Forces on Stationary TLPWT 2 244
C.3.4 Sum-Frequency Forces on Moving TLPWT 2 245
C.3.5 Difference-Frequency Forces, Moving TLPWT 2 . . . 248
C.4 TLPWT 3 249
C.4.1 Sum-Frequency Forces on Stationary TLPWT 3 . . . 249
C.4.2 Difference-Frequency Forces on Stationary TLPWT 3 250
C.4.3 Sum-Frequency Forces on Moving TLPWT 3 251
C.4.4 Difference-Frequency Forces on Moving TLPWT 3 . . 252
C.5 Discussion 254

List of Tables

2.1 Selected 5MW single column, vertical tendon TLPWT designs 14

3.1 Structural damping for the NREL 5 MW wind turbine. . . . 36
3.2 Newmark-Beta integration parameters 38
3.3 S-N curves for fatigue analysis 41
3.4 Implemented aerodynamic theories. 52
3.5 Control system parameters 57
3.6 Baseline environmental conditions 67
3.7 Extended baseline environmental conditions 67
3.8 Ringing environmental conditions 68
3.9 Fault environmental conditions 70
3.10 Wind-wave misalignment environmental conditions 70

4.1 Weight approximations for structural steel 81
4.2 Baseline designs (water depth 150 m) 87
4.3 Natural periods according to uncoupled and coupled models . 92
4.4 Soft TLPWT natural periods 93
4.5 Tendon natural periods (analytical) 94
4.6 Tendon natural periods (FEM) 96
4.7 Rotor eigenperiods based on land-based WT 97
4.8 Damping coefficients based on decay tests 98
4.9 Tendon yield loads 99
4.10 Cost estimation model 99
4.11 Fixed turbine with 77.6 m tower: loads and power generation 107
4.12 Effects of parameter variations on performance measures . . . 110

5.1 Summary of hydrodynamic models 131
5.2 Range of ringing conditions for each TLPWT 142

6.1 Load cases resulting in absolute/expected maxima 162

B.1 Natural periods of parametric variations 225

C.1 TLPWT 1 free surface meshes 236
C.2 TLPWT 2 free surface meshes 244

List of Figures

1.1 Tension leg platform wind turbines 2
1.2 SIMO-RIFLEX-AeroDyn overview 6

2.1 Semi-submersible, catenary moored spar, and TLP wind turbine designs 10
2.2 Illustrations of TLPWT designs 12

3.1 Nonlinear beam theory displacement relations 33
3.2 Stiffness-proportional damping for the NREL 5 MW wind turbine. 36
3.3 Coordinate system for sectional loads 40
3.4 Ringing loads for variable bandwidth $d\omega$. 50
3.5 Tower influence coordinate system 54
3.6 Tower influence models. 55
3.7 Blade pitch and generator torque control overview 58
3.8 Turbulent wind box schematic 64
3.9 Wind-wave misalignment at the Cabo Silleiro buoy. 66
3.10 50-year contours of H_s and T_p for different wind speeds . . . 68
3.11 RIFLEX wind turbine components 74
3.12 SIMO-RIFLEX-AeroDyn FWT model 77

4.1 Parametric design definitions 80
4.2 Baseline designs (water depth 150 m) 88
4.3 Added mass and damping coefficients 89
4.4 Wave force excitation in surge, heave, and pitch 90
4.5 TLPWT 3 pitch decay 93
4.6 Tower bending modes, TLPWT 3 95
4.7 Tendon bending modes, TLPWT 3 96
4.8 Tower and tendon bending modes, TLPWT 3 97
4.9 Hull and tendon simplified cost estimates 100

4.10 Baseline TLPWT comparisons . . . 103
4.11 Spectrum of M_{FA} for EC 2 . . . 105
4.12 Spectrum of T_1 for EC 2 . . . 106
4.13 Comparison of baseline TLPWTs and land-based WT . . . 108
4.14 Total pretension vs. displacement for various TLPWTs . . . 110
4.15 Effect of surge natural period on surge motions . . . 115
4.16 Effect of yaw natural period on yaw motions . . . 116
4.17 Effect of total pretension on standard deviation of tendon tension . . . 117

5.1 Aerodynamic damping calculation . . . 122
5.2 Thrust force spectra for linear analysis . . . 123
5.3 Linear and nonlinear surge response predictions. . . . 124
5.4 Linear and nonlinear nacelle acceleration predictions. . . . 124
5.5 Linear and nonlinear dynamic tension predictions. . . . 125
5.6 Linear and nonlinear surge and nacelle acceleration spectra . 126
5.7 Linear and nonlinear tendon 1 tension spectra . . . 128
5.8 Potential and Morison excitation forces, TLPWT 1 . . . 133
5.9 Differences in μ, M vs. P1+V, baseline designs . . . 133
5.10 Differences in σ, M vs. P1+V, baseline designs . . . 134
5.11 Differences in σ, M vs. P1+V, soft designs . . . 134
5.12 Tendon tension spectra, TLPWT 3, M and P1+V . . . 136
5.13 Sum-frequency pitch force QTFs, TLPWTs 1 and 3 . . . 138
5.14 Differences in σ, P2+V vs. P1+V, baseline designs . . . 139
5.15 Fatigue damage P1+V, baseline designs . . . 140
5.16 Differences in D_{RFC}, P2+V vs. P1+V, baseline designs . . . 141
5.17 Baseline designs: 1-hour expected maximum T_1 and M_{FA} . . 143
5.18 TLPWTs 2 and 3: ringing responses (wave, M_{FA}, T_1) . . . 144
5.19 Baseline designs: 1-hour expected tendon D_{RFC} . . . 145
5.20 Soft designs: 1-hour expected maximum T_1 and M_{FA} . . . 146
5.21 Soft designs: 1-hour expected tendon D_{RFC} . . . 147
5.22 Ringing: maximum and fatigue loads, operational and idling turbine . . . 148
5.23 Ringing: 1-hour expected maximum T_1 and M_{FA} vs. C_D . . 149

6.1 Fixed wind turbine behavior during blade seize . . . 153
6.2 Blade azimuth angle definition . . . 154
6.3 Azimuthal dependence of the tower base fore-aft load, fault D 155
6.4 Azimuthal dependence of the blade root loads, fault D . . . 156
6.5 Azimuthal dependence of the tower base fore-aft load, fault C 157

6.6 Azimuthal dependence of the blade root loads, fault C, faulted blade . . . 158
6.7 Azimuthal dependence of the blade root loads, fault C, non-faulted blade . . . 158
6.8 Fixed wind turbine behavior during blade seize, pitch rate variation . . . 159
6.9 Pitch rate dependence of M_{FA} and ζ_6, fault C, TLPWT 3 . . 160
6.10 Pitch rate dependence of blade bending loads, fault D, TLPWT 3 . . . 160
6.11 Range of response maxima for different seeds . . . 164
6.12 Expected maximum tower top fore-aft bending moment . . . 166
6.13 Expected maximum tower top side-side bending moment . . . 167
6.14 Spar and TLP blade pitch fault response . . . 167
6.15 Wind-wave misalignment . . . 169
6.16 Tower base and top damage distribution, EC M3 . . . 170
6.17 One-hour fatigue damage, P1+V . . . 172
6.18 One-hour fatigue damage, P2+V . . . 174
6.19 Relative change in one-hour D_{RFC}, P2+V vs P1+V . . . 175
6.20 Spectra of axial stress at the tower base, ECs M1 and M4 . . 176
6.21 Blade root bending moments . . . 177
6.22 Cross-sectional location of maximum stresss . . . 178
6.23 Expected maximum stress and minimum tension . . . 180

A.1 Tendon bending modes, TLPWT 1 . . . 210
A.2 Tower and tendon bending modes, TLPWT 1 . . . 211
A.3 Tendon bending modes, TLPWT 2 . . . 212
A.4 Tower and tendon bending modes, TLPWT 2 . . . 212
A.5 Tendon bending modes, TLPWT 4 . . . 213
A.6 Tower and tendon bending modes, TLPWT 4 . . . 214
A.7 Tendon bending modes, TLPWT 5 . . . 215
A.8 Tower and tendon bending modes, TLPWT 5 . . . 215
A.9 Tendon bending modes, soft TLPWT 1 . . . 216
A.10 Tower and tendon bending modes, soft TLPWT 1 . . . 217
A.11 Tendon bending modes, soft TLPWT 2 . . . 218
A.12 Tower and tendon bending modes, soft TLPWT 2 . . . 218
A.13 Tendon bending modes, soft TLPWT 3 . . . 219
A.14 Tower and tendon bending modes, soft TLPWT 3 . . . 220
A.15 Tendon bending modes, soft TLPWT 4 . . . 221
A.16 Tower and tendon bending modes, soft TLPWT 4 . . . 221

B.1 Baseline TLPWT comparison (coefficient of variation) . . . 226

B.2 Change in $\sigma(\zeta_1)$ due to parametric variations 227
B.3 Change in $\sigma(\zeta_5)$ due to parametric variations 228
B.4 Change in $\sigma(\zeta_6)$ due to parametric variations 229
B.5 Change in $\sigma(M_{FA})$ due to parametric variations 230
B.6 Change in $\sigma(T_1)$ due to parametric variations 231

C.1 Free surface meshing 234
C.2 TLPWT 1 free surface meshes 237
C.3 First-order and double-frequency surge, heave, and pitch excitation TF components, stationary TLPWT 1 238
C.4 Sum-frequency heave and pitch QTFs, stationary TLPWT 1 239
C.5 Difference-frequency surge force, stationary TLPWT 1 239
C.6 TLPWT 1: first-order motion RAOs 240
C.7 First-order and double-frequency surge, heave, and pitch excitation TF components, stationary and moving TLPWT 1 . 241
C.8 Sum-frequency heave and pitch excitation QTFs, TLPWT 1 . 242
C.9 Sum-frequency pitch moment at first natural frequency, stationary vs. moving TLPWT 1 242
C.10 Difference-frequency surge force, moving TLPWT 1 243
C.11 First-order and double-frequency surge, heave, and pitch excitation TF components, stationary TLPWT 2 245
C.12 Sum-frequency heave and pitch excitation QTFs, TLPWT 2 . 246
C.13 Difference-frequency surge force, stationary TLPWT 2 246
C.14 TLPWT 2: first-order motion RAOs 247
C.15 Double-frequency surge, heave, and pitch TF excitation components, stationary and moving TLPWT 2 247
C.16 Sum-frequency heave and pitch excitation QTFs, TLPWT 2 . 248
C.17 Sum-frequency pitch moment at first natural frequency, stationary vs. moving TLPWT 2 248
C.18 Difference-frequency surge force, moving TLPWT 2 249
C.19 First-order and double-frequency surge, heave, and pitch excitation TF components, stationary TLPWT 3 250
C.20 Sum-frequency heave and pitch QTFs, stationary TLPWT 3 251
C.21 Difference-frequency surge force QTF, stationary TLPWT 3 . 252
C.22 TLPWT 3: first-order motion RAOs 252
C.23 Double-frequency surge, heave, and pitch excitation TF components, stationary and moving TLPWT 3 253
C.24 Sum-frequency heave and pitch excitation QTF, TLPWT 3 . 253
C.25 Sum-frequency pitch motion at first natural frequency, stationary vs. moving TLPWT 3 254

C.26 Difference-frequency surge force, moving TLPWT 3 254

Chapter 1

Introduction

1.1 Motivation

The use of wind turbines for electricity generation is increasingly common. In particular, offshore wind turbines (OWTs) are an attractive solution for energy conversion due to the higher wind speeds, more consistent wind patterns, and decreased noise and visual effects for human population centers compared to land-based turbines [2, 3]. Several wind turbine installations in shallow water ($\leq$ 45 m) using fixed foundations – such as monopile, gravity, or jacket structures – are already connected to the electrical grid (e.g. Horns Rev, Beatrice) [2].

In order to access a larger wind resource and move the noise and visual effects farther offshore, wind turbine support platforms for intermediate water depth (45 - 150 m) and deep water ($>$ 150 m) are also being considered. At these depths, gravity and monopile foundations are not economically feasible, although fixed jacket structures may be appropriate for some intermediate depths (45 - 80 m) [4]. A wide variety of floating wind turbine concepts have also been proposed, such as spar, semi-submersible, and tension leg platforms.

Floating wind turbine (FWT) concepts are presently limited by their cost and by the fact that they are a relatively new and unproven technology. Design innovations and improved load predictions can help to reduce the construction, installation, and maintenance costs. Tension leg platform wind turbines (TLPWTs, illustrated in Fig. 1.1) have been suggested as a possible solution for intermediate water depths, since the tendon system may be better suited for shallow water than a catenary mooring system. Furthermore, the limited platform motions may reduce turbine and power cable ultimate and fatigue loads. The present thesis addresses the design

and analysis of TLPWTs in order to provide a better understanding of the system behavior, design parameter effects, and requirements for dynamic analysis.

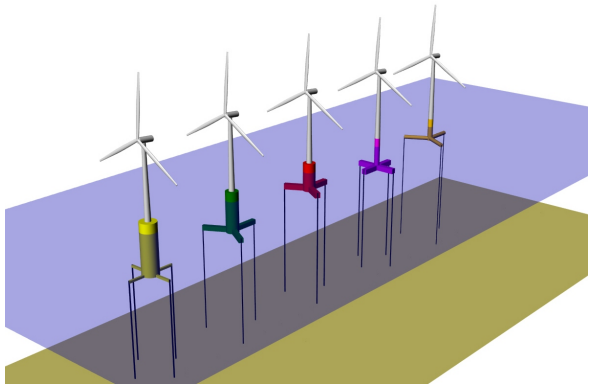

Figure 1.1: Tension leg platform wind turbines

When examining a relatively novel concept, such as a TLPWT, design and analysis are necessarily intertwined. In order to evaluate a potential design, analysis tools must be developed to model the relevant physics; in order to develop an analysis tool, there must be some general idea of the physical system to which it will be applied. Furthermore, the design-driving environmental or operational conditions are not known a priori, and may depend on both the platform and the component under consideration. For example, a blade pitch actuator fault condition may result in extreme tower top loads in fairly benign weather conditions, while the tower base loads could be large in both near-rated wind speeds and extreme weather conditions. The methods and fidelity required to simulate different situations may vary, which means that the load conditions are also related to the analysis methods.

TLPWTs present unique challenges in terms of both design and analysis. A multidisciplinary approach has to be employed in studying such concepts, and prior knowledge from both the offshore oil and gas (O&G) industry and the wind turbine industry can be useful - but not necessarily sufficient - in addressing these challenges.

1.1.1 Design Challenges for TLPWTs

In designing a TLPWT, the main objective is to create a platform which can safely generate electricity at the lowest possible cost. A complete consideration of the costs includes material and construction costs, installation

costs, operation and maintenance costs, and decommissioning and removal costs. Given the payload of a single platform - assumed here to be a single 5 MW wind turbine, weighing approximately 700 tonnes and producing a maximum steady-state thrust of approximately 800 kN at 90 m above sea level - one should create an economical design which can reliably produce electricity as a part of a larger wind farm.

Construction costs, which constitute a large portion of the overall initial investment, depend on the structural design. The structural design, in turn, depends on the ultimate (ULS) and fatigue (FLS) loads encountered over the structure's lifetime. TLPWTs are subjected to a wide range of load conditions dictated by the environment (wind, waves, current, ice), by their operation (tow-out and installation, start-up, shutdown, normal operation, idling, parked, and possibly faulted), and - possibly - by accident (ship collision, ballast system failure, loss of mooring line, fire). Design standards for wind turbines require the consideration of extensive design load cases (DLCs) [5, 6, 7, 8]. New design standards for FWTs introduce additional considerations specifically related to the mooring system and to the interaction between the floating platform and the wind turbine [9, 10]. The question of which DLCs are design-driving in terms of both fatigue and ultimate strength for different types of FWTs is, however, still open.

A better understanding of the sensitivity of different designs to particular load situations is needed in order to compare the wide range of TLPWT designs available in the literature. For example, a governing choice in the design process is the displacement (Δ) of the TLPWT. Δ governs the pretension, which then governs the natural periods and tendon strength requirements. The geometry, which must provide the desired Δ, also directly affects the wave loads and the potential for a self-stable installation. A self-stable platform has a sufficient restoring moment (in ballasted condition) without the tendons, and can thus be towed to location without using extra equipment for buoyancy.

Although numerous researchers have suggested possible designs, there is very little consensus, with published 5 MW designs ranging from 846 tonnes [11] to 12,187 tonnes [12]. Even the idea of self-stable installation is open to discussion, as one may argue that the construction cost savings for a whole farm of floating wind turbines may offset the cost of building a specialized installation device to provide stability during the marine operations [13]. Self-stable designs are generally larger and do not necessarily perform better after installation. Furthermore, although some attempts at TLPWT optimization for selected conditions have been published, their analysis tools have been found to be faulty, casting doubt on the results of

the optimization process.

This thesis aims to provide a new starting point for optimization by suggesting some simple criteria, describing a method for initial screening, and presenting the results of an examination of parametric variations on the operational performance of TLPWTs. The simple initial design criteria are given as:

1. The surge and sway natural periods should be longer than 25 s in order to avoid first order wave excitation.

2. The heave, roll/bending, and pitch/bending natural periods should be shorter than 3.5 s in order to avoid first order wave excitation.

3. In order to limit the angle at the tendon connectors, the mean offset should not exceed 5% of the water depth [14, Ch. 7.6.3].

4. The tendon area must be sufficient to prevent yield (σ_y), within a given safety factor (SF), for tensions up to twice the initial tension (F_t).

In addition to the parametric design study based on simply-generated designs, this work examines certain atypical conditions (such as pitch controller faults and misaligned wind and waves). Thus, this work provides a first step towards informing designers about the relative importance of different load cases. By identifying critical load cases, a more efficient optimization process may be possible.

1.1.2 Analysis Challenges for TLPWTs

Beyond the inherent analysis challenges of a novel multidisciplinary design problem, TLPWTs present particular challenges with regards to the range of time scales involved in the problem, the coupled structural modes, and the complex hydrodynamic loads.

Important time scales for global analysis of TLPWTs range from approximately 0.2 s (for the second platform pitch/tower bending mode) up to approximately 60 s (for the platform surge motion), with even longer periods present in the wind and in the difference-frequency wave forcing. In between those limits, there are contributions from rotor frequencies, controller frequencies, high- and low-frequency structural resonances, and wave excitation. An analysis tool has to be able to capture the important high-frequency effects while being sufficiently computationally efficient to allow for the simulation of numerous cycles of slower events.

Unlike most other floating wind turbine concepts, the flexibility of the tower and blades play an important role in the natural frequencies of the platform itself in the case of TLPWTs. That is, it is not possible to identify rigid body modes in pitch and roll: tower bending and pitch motion are combined. This, in addition to the nonlinearities inherent in the wind turbine control system, makes a traditional frequency-domain analysis more complex.

Hydrodynamic loads on TLPWTs are a particularly interesting challenge: these structures may fall on the border between "slender" and "large-volume" structures, such that the use of Morison's equation may not be appropriate. Due to the system natural frequencies, first order potential flow may not be sufficient to capture all of the important effects. In the difference-frequency loading, the surge natural period may be too short for Newman's approximation to work. A more detailed hydrodynamic analysis including the computation of the second-order sum- and difference-frequency loads may then be required. In steep waves, the structure may also be subjected to third-order "ringing" loads, which can greatly increase both the extreme loads for ULS and the fatigue damage in a given environmental condition.

Numerical studies, laboratory-scale experiments, and sea trials of larger prototypes may be used to analyze this type of problem. The present work considers numerical analysis, which must be further validated through comparisons with physical tests when such results are made available.

Researchers have developed numerous time-domain numerical analysis tools to capture the coupled aero-hydro-servo-elastic response of FWTs. Cordle and Jonkman provided an overview of many of these codes [15]. For example, two of the leading codes are FAST [16] (from NREL) and HAWC2 [17] (DTU Wind Energy). Both were developed for land-based turbines and later adapted to offshore turbines. At the time of this work, the FAST code was somewhat limited in its structural, hydrodynamic, and mooring system capabilities (ie, linear structural response, no twist degree of freedom in the blades, no horizontal Morison elements, and only quasi-static catenary mooring line solutions). Some of these limitations are being addressed in more recent versions of FAST. HAWC2 provides better structural fidelity, but limited hydrodynamic force models and long computation time.

In this work, a novel state-of-the-art analysis tool for TLPWTs is presented (SIMO-RIFLEX-AeroDyn). This coupled code, as outlined in Fig. 1.2, takes advantage of the nonlinear beam element solver in RIFLEX, hydrodynamics models in SIMO, and the aerodynamic force models in AeroDyn. As a part of the present work, the interface between RIFLEX and Aero-

Dyn was written and tested, and the control system was implemented in Java. Using the results from this analysis tool, the accuracy of a simplified frequency-domain method (including wind forcing) is examined. Studies of the importance of second-order and third-order forces, whose effects have not been previously studied for a similar range of TLPWT designs, are also presented.

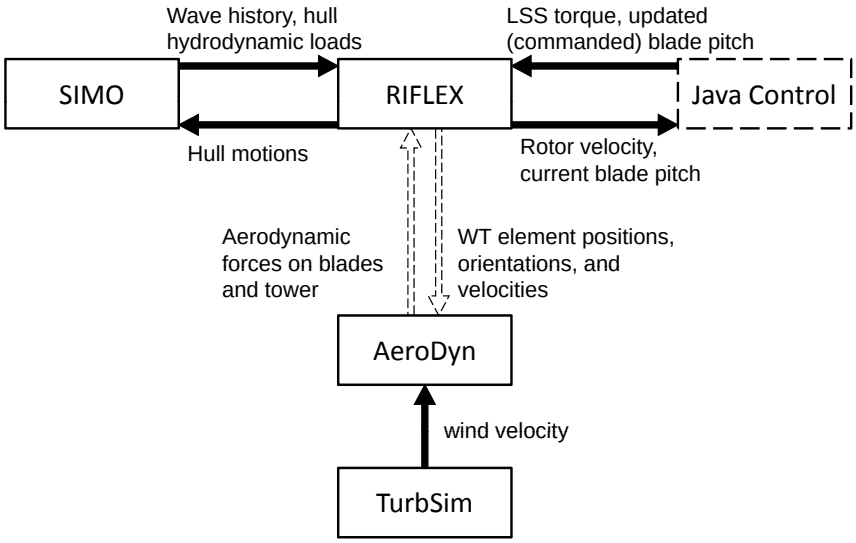

Figure 1.2: SIMO-RIFLEX-AeroDyn overview. Dashed lines indicate contributions by the author.

1.1.3 Severe Operational Conditions

Having established a reasonable design and an analysis tool that can model the system, it is interesting to extend this analysis to certain conditions which may cause severe dynamic responses. Although one may imagine a wide range of conditions - control system faults, tether slack, wind-wave misalignment, yaw misalignment, ice or impact loads - there are inherent limitations in the time available to consider every condition. In the present thesis, control system faults and wind-wave misalignment during the operational portion of the system's lifetime were considered.

Within the extensive range of control system faults, blade pitch actuator and grid faults were chosen for study. For pitch-regulated wind turbines, the blade pitch control system of a wind turbine is known to contribute significantly to the failure rate [18]. Blade pitch actuator errors, which

introduce imbalance in the rotor, and emergency shutdown events (following grid loss and with blade pitch errors) were studied using the SIMO-RIFLEX-AeroDyn model of a single TLPWT. These conditions, which include both deterministic and stochastic components, can lead to large transient loads on certain components.

Wind-wave misalignment was identified as another potentially interesting condition with respect to both ultimate and fatigue loads. It is not uncommon for the wind and waves to come from different directions, particularly in stable atmospheric conditions [19, 20]. Barj et al. noted increased extreme side-side tower base loads in simulations of a spar wind turbine due to wind-wave misalignment [21]. These side-side loads were, nevertheless, smaller than the fore-aft loads. Furthermore, wind-wave misalignment causes increased tower fatigue loading for monopiles [20], since the aerodynamic damping does not mitigate wave-induced loading. The effects of misalignment on the tower stresses and fatigue loading of TLPWTs, and the effect of second-order sum-frequency wave loads in such conditions, were not previously examined.

1.2 Aim and Scope

Based on the challenges described above, and in view of the related work in this field, this thesis examines the design and global analysis of single-column 5 MW TLPWT designs with multiple tendons. The aim of the work is to inform designers and regulatory bodies about the global dynamic response of such concepts. The present results are intended to pave the way for future optimization work, provide a better understanding of how design choices affect the global system performance, examine potential design-driving load cases, and evaluate the analysis procedure with respect to hydrodynamic modeling.

The design space is limited to platforms with a central column, 3-4 pontoons, and one tendon per pontoon. Furthermore, the focus of the thesis is on global analysis of the system in the installed condition: important couplings between elements are included and investigated, but local loads and structural details are not considered. For example, the hull is considered as a rigid body, since it is relatively stiff compared to the wind turbine and tendons. The installation process is not studied.

Despite these restrictions, computational analyses remain expensive, and restrictions must also be placed on the number of models, environmental conditions, and operational conditions that can be investigated. Representative loading conditions were chosen in order to demonstrate general trends

in behavior, to highlight differences between analysis methods, and to suggest nominal loads, but these conditions are not sufficient for the calculation of long-term fatigue or the extrapolation of lifetime extreme events.

The thesis is divided into seven chapters. A survey of relevant literature is provided in Chap. 2, which gives a more thorough background for the aim and scope of the thesis. A more detailed exposition of the theory underlying the nonlinear simulations follows in Chap. 3.

Chap. 4 considers the design of TLPWTs. A simplified parametric single column TLPWT model is introduced, including simplified weight, natural frequency, and cost estimates. The effects of variations in the diameter, pontoon radius, water depth, and ballast weight are examined through simulations of parametric variations on five representative baseline designs. These simulations are carried out using a SIMO-RIFLEX-AeroDyn, considering first order potential flow and viscous damping for the hydrodynamic loading. Although an optimal design is not identified, trends are identified and some suggestions for further improvements are provided.

In order to better understand the results of the design study, it is also important to examine the sensitivity of the results to the analysis methods. Chap. 5 focuses on different analysis methods. First, a simplified frequency-domain analysis, which can quickly evaluate many potential designs, is developed and applied in Sec. 5.1. Next, in Sec. 5.2, several different hydrodynamic models are examined for a range of representative TLPWT designs. Morison's equation, first order potential theory, second-order sum-frequency forces, and ringing loads are considered.

Finally, the performance of one representative TLPWT in selected abnormal operational conditions is examined in Chap. 6, which addresses the global performance during control system faults and wind-wave misalignment. Such conditions may have important consequences for the extreme and fatigue loads of certain components.

The results are summarized in Chap. 7, which also provides some suggestions for future work in this field.

Chapter 2

Related Work

2.1 Floating Foundations for Intermediate Water Depth

Foundation options for wind turbines in intermediate (45 - 200 m) water depth include both fixed and floating structures. Jacket structures, which are already in use for water depths up to 45 m, may be more economical than floating structures for depths up to 80 m, while floating solutions are likely to prevail in deeper water [4].

Three primary types of floating wind turbines (FWTs) are under consideration for intermediate water depth: semi-submersible designs, with multiple widely spaced columns; catenary moored spar designs, which require heavy ballast and a deep keel for stability; and TLP designs, which depend on the mooring system for stability. Examples of these three design types in 200 m water depth are shown in Figure 2.1. This visualization highlights the deep draft required for the spar platform and the extensive mooring system of the semi-submersible platform. All three types of platforms have been inspired by activities in the offshore oil and gas (O&G) industry.

For any type of foundation for OWTs, the placement of the natural frequencies is paramount [24]. One should avoid both ocean wave frequencies and the wind turbine's rotational frequencies (in particular, the f_{1p} rotor frequency and the f_{3p} blade passing frequency). While many fixed foundations may be described as soft-stiff (ie, the fundamental eigenfrequency is in between f_{1p} and f_{3p}), floating structures introduce an additional level of complexity. Spar and semi-submersible designs typically can be described as soft in all six degrees of freedom (DOFs): the surge, sway, heave, roll, pitch, and yaw frequencies are lower than typical wave frequencies. The tower bending frequency is then typically soft-stiff with regards to f_{1p} and

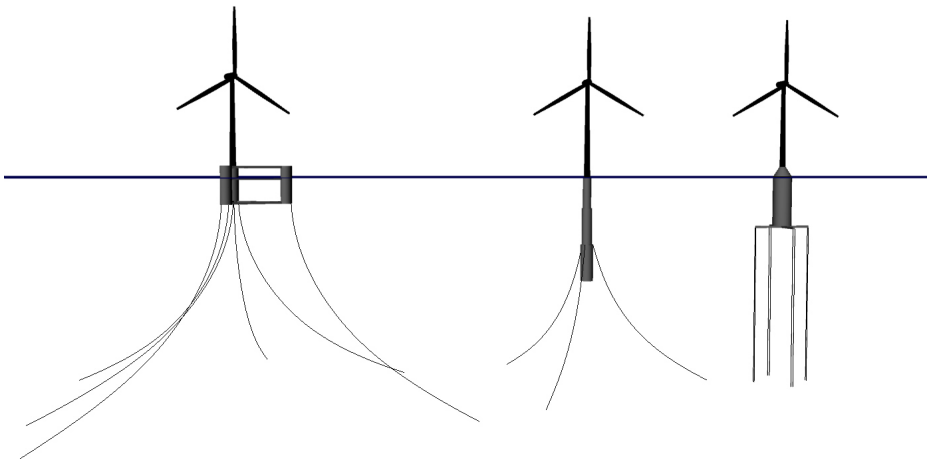

Figure 2.1: Semi-submersible (left, based on [22]), catenary moored spar (middle, based on [23]), and TLP (right, based on [12]) wind turbine designs. Horizontal line indicates still water line.

f_{3p}.

Spar wind turbine designs are primarily intended for deep water, but may have lower cost and simpler installation than TLPWTs. The spar's natural stability is an attractive feature [3]. The Hywind concept from Statoil is the most well-known catenary spar concept. Skaare et al. presented comparisons with experimental results, including variations in the wind turbine control system [23]. The Hywind concept is in full-scale testing near Norway's southwestern coast [25]. An academic 5 MW version of the Hywind concept - the OC3 Hywind - has been used for international comparison of numerical tools [26, 27].

Semi-submersible wind turbine designs are currently in consideration for both intermediate and deep water. Semi-submersibles may have advantages over TLPWTs in terms of mooring system cost, installation cost and installation simplicity [3]. A semi-submersible platform with heave plates (WindFloat) design has been developed by Roddier et al. and presented in 3 conference papers [22, 28, 29]. The system includes a 3-column platform, with a 5 MW wind turbine positioned on one of the stabilizing columns [22]. A 2 MW prototype was deployed off the coast of Portugal in 2011 [30]. A larger semi-submersible design with a 5 MW wind turbine positioned on a central column is under study as an international test case through Phase II of the OC4 project [31].

TLPWTs are fundamentally different from semi-submersible and spar

WTs: the natural frequencies of vertical platform motions (heave, pitch, roll) of TLPWTs are placed above the wave frequencies, rather than below. With respect to f_{1p} and f_{3p}, the combined platform pitch and tower bending mode of large TLPWTs may be either soft-stiff or stiff-stiff, depending on the tendon stiffness and tower design. The TLPWT concept is promising for intermediate water depths, particularly for water depths where catenary mooring system design is challenging. The limited platform motions are expected to reduce the structural loading on the tower and blades compared to other floating concepts [3, 32].

2.2 TLPWT Designs

The design of TLPWT platforms remains an active field of study. The present work focuses on single-column designs with vertical tendons, although many alternative designs exist. The following subsections discuss the early design development, newer 5 MW single column designs for direct comparison with the present work, and some relevant tension leg buoy wind turbine (TLBWT) and multi-column designs. Fig. 2.2 illustrates some of the concepts described in the following sections.

2.2.1 Early Designs (MIT)

Significant early work on TLPWT concepts was performed at MIT, including several master's and PhD theses.

Withee's PhD dissertation (MIT, 2004) presented a coupled dynamic analysis of a 1.5 MW TLPWT in 200 m water depth [40]. In contrast to some TLPWT designs from MIT, stable float-out was not a requirement. As a result, the design has no ballast and provides almost 200% reserve buoyancy. Computational free decay tests in each mode of motion showed that the wind turbine dominates the pitch and yaw damping, while viscous drag is more important in translational modes. The operational simulations indicated that, compared to land-based turbines, the power output decreases by approximately 1% and the fatigue life decreases significantly for the tower. Withee also concluded that the operational loads on turbine components (due to the operation of the power takeoff system) would be higher than the structural loads due to the extreme wind or wave events on the parked turbine.

Lee's master's thesis (MIT, 2005) presented two 1.5 MW TLPWT concept designs: a three-legged floater with vertical tendons, and a spar-type buoy with 8 taut tendons at 35-42° [41]. Linear seakeeping analyses were

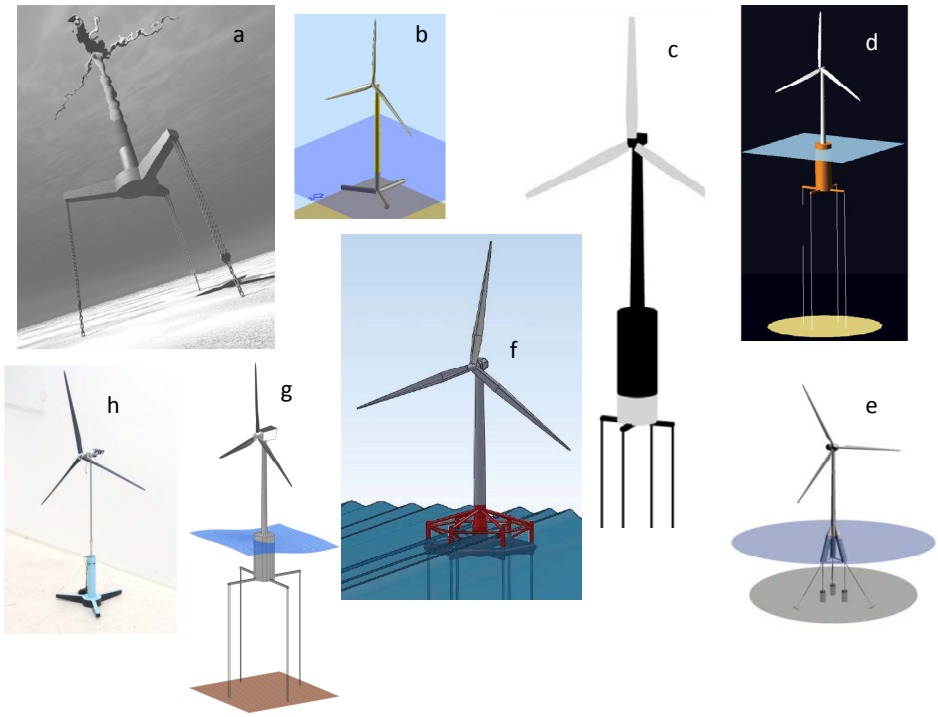

Figure 2.2: Illustrations of selected TLPWT designs: a) Glosten [33], b) GLGH [34], c) Tracy 10 m #1 [35], d) MIT/NREL [12], e) IDEAS [36], f) EsaFloater [37], g) Crozier 10 MW [38], h) UMaine (model scale) [39]

performed for irregular seas with constant wind. The structure was considered as a rigid body and the aerodynamic damping was added to the linear damping matrix. A brief investigation of higher harmonic events suggested that nonlinear wave excitation may be important.

Wayman et al. presented the first iteration of the MIT-NREL TLP for a 5 MW wind turbine in 2006 [42]. Rigid body motions were considered, assuming the tethers to have infinite stiffness. The design provides for stable ballasted tow-out with the wind turbine installed, and includes almost 50% reserve buoyancy in the operational condition.

Tracy's master's thesis built further on Lee's and Wayman's work by examining parametric design of single column wind turbine support structures with catenary, taut catenary, and tension leg moorings [43]. In order to find the Pareto-optimal front for 200 m and 60 m water depth, three cost indicators were evaluated: nacelle RMS acceleration, static and 3σ mooring line

tension (both windward and leeward lines), and the structure displacement. The responses were computed using rigid-body frequency-domain analysis in two relatively severe sea states (identified by 6 m and 10 m significant wave height).

Tracy found two Pareto optimal TLPWT designs in each sea state: a relatively large, deep-draft design and a smaller, shallow-draft design. The larger structure out-performed the smaller structure in terms of limited nacelle accelerations and decreased tension variation. Furthermore, the analysis indicated that TLPWTs performed well compared to the alternative Pareto-optimal designs in both sea states.

An extension of Tracy's work was also presented by Sclavounos et al. in 2007 [35]. In addition to the limitations of the linear model employed in the dynamic analysis, Matha later identified important computational flaws in the mass matrix computation used in Tracy's master's thesis and in the later extension of the work [12]. These limitations suggest that the identified designs may not be optimal.

2.2.2 Recent Single-Column 5 MW Designs

In addition to Wayman's and Tracy's designs, recent 5 MW single column designs are compared in Table 2.1 and discussed below. In Table 2.1, H is the water depth, D is the center column diameter, T is the draft, r_p is the pontoon radius, n_t is the number of tendons, Δ is the displacement, and F_t is the pretension (per tendon). Values from Tracy's master's thesis have been corrected, as the displacement was given in incorrect units in the original document [43]. The steel mass was estimated from the displacement, turbine mass, concrete ballast mass, and pretension. The designs support 5 MW turbines with hub heights ranging from 80-95.5 m above the still water line, and rotor diameters 120-126 m.

Matha, in his master's thesis (UC-Boulder, 2009), evaluated a TLP in 200 m water depth, with additional comparisons to alternative designs [12]. This design, which was slightly modified from Tracy's TLP#1 for the 10 m sea state, is considered the current MIT/NREL design. The National Renewable Energy Laboratory (NREL) FAST software was used for the analysis, which included load cases following the IEC 61400-3 design standard. Matha modeled the mooring system as quasi-static using HydroDyn and noted that this is an area which requires additional modeling effort. The fatigue load analysis used only the associated wave height and median peak spectral period for each wind speed, rather than considering all of the joint probabilities. In agreement with Withee's results, Matha's TLPWT had a shorter lifetime than a land-based system (based on fatigue of wind tur-

Table 2.1: Selected 5MW single column, vertical tendon TLPWT designs. Values given in () indicate that the value was not specified in the original source, but has been calculated based on the given information.

	Water depth (H), m	Waterline diameter (D), m	Draft (T), m	Pontoon radius (r_p), m	Number of tendons (n_t)	Displacement (Δ), tonnes	Steel mass, tonnes	Pretension per line (F_t), kN
Wayman [42]	100/200	22.0	20.0		4	7797		6250
Tracy 6 m #1 [43]	200	21.0	30.2	-	8	10 711	(279)	2 492
Tracy 6 m #2 [43]	200	33.0	6.1	-	8	5 381	(276)	4 018
Tracy 10 m #1 [43, 35]	200	18.0	47.9	-	8	12 491	(372)	3 931
Tracy 10 m #2 [43, 35]	200	34.0	10.8	-	8	10 045	(371)	6 242
Tracy 10 m #3 [43, 35]	60	29.0	21.7	-	8	14 712	(410)	4 561
MIT/NREL [12]	200	18.0	47.9	27.0	8	12 491	(384) [44]	3 931
Glosten [33]	55	7.2	-	-	9	-	-	-
GLGH [34]	50	5.0	20.0	32.5	3	1870	700	(1738)
UMaine [32, 39]	200	6.5/15.0	24.0	30.0	3	2836	(1000)	(4 778)
Nihei Model 350 [11]	500	-	21.5	-	6	846	-	900
Nihei Model 550 [11]	500	-	38	-	6	3 500	-	2260
Crozier [38]	200	13.4	44.0	32.0	8	6 360	420	2179

bine components) but performed well compared to other floating platforms (barge and OC3-Hywind). Additionally, Matha identified system instabilities in yaw, surge (related to blade pitch control), and in a mode including the turbine yaw, tower side-to-side motion, and platform motions. These instabilities are difficult to analyze, but additional results suggest that the platform yaw instability is coupled with blade aerodynamics [45].

Sclavounos et al. (MIT/ENEL) recently presented designs for a TLPWT and a tension leg buoy wind turbine (TLBWT) which relax the stable tow-out requirement [13]. The designs are intended to support 3 to 5 MW turbines in water depths from 30 to 150 m. According to Sclavounos et al., the TLBWT, which uses inclined pre-tensioned lines, is a better solution for water depths less than 50 m; the TLPWT is proposed for deeper water [13]. Both designs require a stabilizing floater for installation, which leads to smaller concepts compared to self-stable units. Design specifics were not published; however, results for tendon tensions and nacelle accelerations according to frequency-domain analysis are promising. In their analysis, mooring system restoring coefficients were computed at the static offset using the program LINES.

Moon and Nordstrom, of Glosten Associates, described the design of a 5 MW TLPWT sited in conditions similar to the United Kingdom Round 3 Development Area [33]. The three-spoked design with 3 chain tendons per spoke was specified for 55 m water depth and 50 year extreme events. A proprietary driven plate anchor system was incorporated in the design in order to reduce installation costs. The design is claimed to be cost-competitive with fixed structures for water depths above 50 m [33]. The design has been further refined as the PelaStar design, which has 2 tendons per spoke [46]. Due to the commercial nature of the project, few details about the PelaStar dimensions have been published.

Another extension of the Glosten design has resulted in the University of Maine (referred to here as UMaine) TLPWT [32, 39]. A 1:50 scaled model of the three-legged design for 200m water depth has been tested at MARIN, giving a unique opportunity for examining the numerical simulation tool (FAST) [39]. Note that the UMaine design, although inspired by [33], uses neutrally buoyant steel pipe tendons.

GL Garrad Hassan presented a TLPWT design (referred to here as GLGH) for German waters with 50 m water depth [34]. The design supports a 5 MW turbine with 85 m hub-height. No ballast is included in the design, which has a very open profile and a small waterline diameter. Henderson et al. also examined different tendon solutions for the GLGH design, such as wire rope and synthetic fiber lines [34].

Two additional designs were presented by a Japanese collaboration (Nihei et al.) [11]. The reported values of pretension were quite low and were therefore assumed to be in units of kN rather than the presented unit (kg). These three-legged designs were tested at 1:100 model scale. In the experiments, the smaller design (Model 350) experienced both slack and capsize, which were attributed to large yaw motions.

In addition to these designs, Crozier's master's thesis [38], which is focused on a 10 MW design, also includes an optimized, self-stable TLPWT design for the NREL 5 MW wind turbine with a displacement of 6,360 tonnes. Interestingly, the self-stable 5 MW and 10 MW designs were very similar despite the increased turbine capacity, and the draft was quite similar to the deep-draft solution identified by Tracy [38]. Crozier's optimal design has approximately half of the displacement of the MIT-NREL design due to the smaller diameter.

In addition to the numerous designs with vertical tendons, there is also significant design activity around TLBWT concepts which are stabilized by spread taut moorings. The previously mentioned MIT/ENEL TLBWT [13] uses tendons at approximately 45 ° inclination in order to further limit horizontal plane motions (surge, sway, yaw) as well as vertical plane motions (heave, roll, pitch). Myhr et al. have investigated several alternative TLBWT designs, both numerically and experimentally [47, 48]. These designs have a center column and 6 taut mooring lines, attached at two different vertical positions. According to Myhr et al., the added taut lines may reduce the steel mass of the floater and virtually eliminate nacelle motions, but the large anchor loads become a significant design challenge [48]. The GICON concept, which has been studied experimentally and numerically, employs 8 mooring lines: four vertical and four inclined [49]. GICON plans to deploy a full-scale prototype in the German Baltic Sea [49]. TLBWT concepts may require large displacement to ensure pretension in the spread taut moorings.

2.2.3 Multi-Column TLPWT Designs

Several researchers have also suggested multi-column TLPWT designs, which may provide easier installation due to the increased hydrostatic stiffness provided by the columns. The main drawback to such designs is the increased complexity of fabrication relative to single column designs.

Fulton et al. presented a self-installing tension leg design in 2007 [50]. The tri-floater type platform is to be towed out with a gravity anchor attached, which is then released while the tendons are reeled out. Simulations (using Orcaflex and Bladed) were carried out for 62 m water depth and

a fairly detailed cost analysis was performed. The analysis indicated that the mooring system loads are within an acceptable range, peak and fatigue loads on the nacelle in the tower increase compared to onshore turbines, and the cost of electrical connections is a major factor in the final cost of energy.

A TLPWT design for Japanese waters was developed by Suzuki et al. [51]. The three-spoked design with two tendons per spoke was proposed for 100 m water depth. This 4100 tonne TLPWT for a 2.4 MW turbine has a center column and three additional surface-piercing columns for buoyancy, stability, and easy access to the tendon attachment points. The analysis included a consideration of the dynamic response in waves, a vibration analysis for the first 10 modes, and an earthquake analysis. The tendon tensions and platform motions were found to be within design criteria for wind, current, wave, and seismic loading.

The EsaFloater (Δ = 3113 tonnes) described by Casale et al. uses a hexagonal TLPWT hull to support a 6 MW turbine [52, 37]. The resulting platform has an overall diameter of approximately 50 m, 12 locked-coil rope mooring lines, and numerous bracings. The platform can be ballasted to provide for stable tow-out with the wind turbine installed. For the foundation at the seabed, Casale et al. considered piles, suction buckets and gravity anchors, and concluded in favor of piles [52].

The IDEAS design [36] for a 5 MW wind turbine introduces both additional inclined columns which pierce the surface (to limit vortex-induced motions) and lateral taut moorings (to limit the mean offset and platform set-down). The resulting system has a displacement of 1800 tonnes and natural frequencies that are similar to TLPWTs - that is, the system is still relatively soft in surge and sway.

Zhao et al.'s 5 MW TLPWT design (Δ = 4275 tonnes) is a relatively clean structure with a center column and three corner columns [53]. The publication describes the preliminary design, including the hull structural layout, and presents analysis results using the FAST software and NASTRAN. The flexibility of the hull itself affects the heave and pitch natural frequencies. Despite the extra columns, this design requires temporary buoyancy during installation.

2.3 Floating Wind Turbine Analysis

The development of commercial FWTs requires extensive analysis of the proposed designs, typically through numerical studies, laboratory-scale experiments, and sea trials of larger prototypes. The present work is focused

on numerical analysis, which must be further validated through comparisons with physical tests.

2.3.1 Numerical Tools

Several time-domain numerical analysis tools have been used to capture the coupled aero-hydro-servo-elastic response of FWTs. Cordle and Jonkman provided an overview of many of these codes [15]. More direct comparisons of numerous analysis codes have been carried out through the IEA's Offshore Code Comparison Collaboration (OC3) and Offshore Code Comparison Collaboration Continuation (OC4) [54, 55, 56]. These numerical tools are useful for identifying system natural frequencies through eigenvalue analysis, computing static deformations, and evaluating global dynamic responses.

Two of the leading codes developed in the wind industry are FAST [16] (from NREL) and HAWC2 [17] (DTU Wind Energy). Both were developed for land-based turbines and later adapted to offshore turbines. The FAST code is based on modal theory, which gives linear structural response, and is somewhat limited in its structural, hydrodynamic, and mooring system capabilities. At the time of this study, no twist degree of freedom was included in the blades, no horizontal Morison elements were allowed, and only quasi-static catenary mooring line solutions were included. Subsequent releases of the code have improved the hydrodynamic modeling, and new capabilities are planned. HAWC2 is based on a multi-body formulation for the non-linear structural response. The applicability of HAWC2 to floating platforms is currently limited to cases where Morison's equation can be used to model the hydrodynamic forces.

In order to address the need for large volume hydrodynamics and second-order forces in FWT analysis, simulation codes built upon existing marine simulation tools have also been developed. MARINTEK's SIMO-RIFLEX combination has been updated to include wind turbine analysis capabilities. A rigid-body model was first developed [57], followed by the development of an elastic model [58, 59]. As a part of the present work, an academic version of SIMO-RIFLEX was developed: SIMO-RIFLEX-AeroDyn, which allows for the inclusion of turbulent wind and the use of either a Blade Element Momentum (BEM) or Generalized Dynamic Wake (GDW) theory. Comparisons between the AeroDyn BEM and GDW implementations and RIFLEX's internal BEM implementation for land-based and floating wind turbines were carried out to verify the implementation and examine the effects of different theories [60]. The SIMO-RIFLEX-AeroDyn code is described in greater detail in Section 3.6.

A particularly sophisticated simulation tool is required for studying the

transient effect of fault on floating wind turbines. Hansen et al. used HAWC2 and DIgSILENT together to evaluate mechanical loads on a land-based turbine due to grid faults, showing that tower loads may be affected by grid faults and that an open loop simulation is not sufficient to capture the generator speed during such events [61]. A closed loop simulation with DIgSILENT provided some insight into the shaft, tower, and blade loads during grid fault and emergency shutdown of an active stall wind turbine [62]. Although the grid behavior cannot be simulated, the coupled simulation tool SIMO-RIFLEX-AeroDyn is well-suited to account for the hydrodynamic modeling of a range of different platforms, the structural modeling of the wind turbine and mooring systems, the control system for the generator torque and blade pitch, including actuator and measurement errors, and the aerodynamic forces on the blades and tower.

2.3.2 Experiments

A relatively limited number of experiments have been performed on floating wind turbines, and very few results are publicly available. Molin presented two sets of TLPWT tests in 2004: wind and wave tests at two different laboratories with variable turbulence qualities [63]. Despite the tests' limitations (the blade rotation was only measured at one laboratory, the tendons were much stiffer than intended, no blade control was used), the tests demonstrated the influence of the tower flexibility on the platform modes, and the importance of motions perpendicular to the wind and wave direction.

More recently, wind and wave tests were performed for three wind turbine platforms (TLP, spar, semi-submersible) [64, 65]. Certain modeling difficulties remained, such as the large weight of the measurement equipment and scaling challenges related to the rotor design. The aerodynamic forces on a geometrically scaled rotor do not give the correct thrust force for a Froude-scaled model, such that higher wind speeds were required in order to match the desired thrust forces. Nonetheless, these tests provide new insights into the behavior of floating wind turbines over a range of environmental conditions, including turbulent wind and the effects of the operational turbine.

More detailed analysis of the semi-submersible test results was presented by Coulling et al. [66], while Stewart et al. discussed the TLPWT results [39]. Comparisons between the FAST model and the experimental results for the TLPWT indicated good general agreement in the wave-frequency range, while viscous damping, high-frequency responses, and f_{1p} excitation were not very well captured by the numerical simulation [39]. The f_{1p} excitation may be related to rotor imbalance, which was not considered

in the FAST model.

The tests were repeated for the semi-submersible concept using a different Froude-scaled turbine, which was not geometrically scaled, but had different airfoils in order to better match the turbine performance [67]. Results from these tests are expected to be made publicly available over the next few years.

Independent tests of a tension leg platform concept were performed at the University of Aalborg [68]. Wave-only tests in severe sea states suggested that the wave generation method (with or without harmonic components) had a significant effect on the results. The number of slack line events, for example, increased when the higher harmonics were included. The wave nonlinearity and tower flexibility had significant effects on the nacelle acceleration.

Myhr et al. have also examined 1:100 scale wave tests of two tension leg buoys performed at the NTNU/MARINTEK MCLab [47]. Generally good agreement was seen between computational and experimental models in regular waves, although the experiments showed yaw motions which were not present in the numerical simulations (using an in-house code from the Norwegian University of Life Science called 3Dfloat).

2.3.3 Sea Trials

A very limited number of concepts have been tested at full or pilot scale in the natural environment. According to a report by Main(e) International Consulting, Statoil's Hywind and Principal Power's WindFloat concepts are the front runners in terms of full scale testing [69]. Among TLPWT concepts, the Blue H two-bladed concept was tested at a small scale in 2008 off the coast of Southern Italy [69]. Although very little information from these full-scale tests has been released, they are a promising sign for the future development of such projects.

2.4 Floating Wind Turbine Load Conditions

Over its lifetime, a FWT may be subjected to a wide range of load conditions dictated by the environment, (wind, waves, current, ice), by its operation (tow-out and installation, start-up, shutdown, normal operation, idling, parked, and possibly faulted), and - possibly - by accident (ship collision, ballast system failure, loss of mooring line, fire). In order to identify potential design-driving loads, it is necessary to consider extensive design load cases (DLCs) [5, 6, 10].

The question of which DLCs are design-driving in terms of both fatigue and ultimate strength for different types of FWTs is still open. Current (drag and vortex-induced vibration), ice, tow-out, installation, turbine start-up, and accidental loads are not considered in the present work, and very little published information is available regarding these conditions. Some preliminary work on ice loading for OWTs was presented in 2013 [70, 71].

In general, there is correlation between the environmental conditions and the turbine operational condition. For very low wind speeds, the turbine idles until the cut-in operational speed is reached. Operational conditions, where the turbine produces power, are associated with a range of wind speeds from cut-in to cut-out (3 m/s to 25 m/s at hub height for the NREL 5 MW turbine [72]). For higher wind speeds, the blades are feathered and the turbine is either parked or allowed to idle. Many studies have investigated the performance of FWTs in operational and idling conditions, including most of the previously referenced design studies and some comparisons [44]. The majority of these studies focus on aligned wind and wave conditions.

In addition to operational and idling conditions, the occurrence, consequences, detection, and mitigation of wind turbine faults are important research areas, particularly for OWTs, where maintenance and repair may be complicated by limited access windows [73, Chap. 1]. The blade pitch system was found to be the least reliable sub-assembly in a 1400 turbine-year survey of onshore turbines [73, Chap. 3]. Analyses of both land-based and spar-type wind turbines under pitch system fault conditions have been performed previously. The work of Jiang et al. indicates that certain fault loads may be less significant for spar wind turbines compared to land-based wind turbines, but the effects on the mooring system remain unclear [74]. Different faults may show similar signals, making detection and mitigation more challenging [75]. During the course of the present thesis, the work of Jiang et al. was extended to a comparison of blade pitch controller fault effects on different platforms [76].

2.5 Offshore Oil and Gas Tension Leg Platforms

Tension leg platforms (TLPs) for the offshore oil and gas (O&G) industry have been a topic of interest since the 1960's, with particular attention being paid after the construction of the Hutton platform [77]. Although TLPWTs are generally smaller than TLPs designed for the offshore O&G industry, and the requirements for carrying the rotor thrust and torque are different

than those for a drilling rig, considerations based on the O&G experience are clearly valuable in designing and analyzing TLPWTs. For example, many of the design considerations Halkyard introduces apply equally well to TLPWTs: transport and installation, pretension and set-down calculations, rough estimates of the maximum allowable horizontal offset, springing and ringing forces, and the effects of platform dynamics on the tension legs [14, Chp. 7.6]. On the other hand, station-keeping requirements (based on drilling operations and power cable motions for TLPs and TLPWTs, respectively), installation considerations (single unit TLP vs. a farm of TLPWTs), and safety factors (manned TLPs vs. unmanned TLPWTs) may differ.

Several design guidelines for O&G TLPs may be useful. In particular, the American Petroleum Institute's recommended practice for TLP planning, design, and construction (API RP 2T) provides detailed guidance regarding load and response calculation during different phases of the system's lifetime [78]. Guidelines for treatment of the tendon system are of particular interest, since the tendon system differentiates TLPWTs from other floating platforms. In API RP 2T, the maximum tension load is found as a combination of quasi-static tension, wave-induced tension, and individual tendon effects, including consideration of the statistics of the joint driving functions. Some general recommendations regarding tendon system design include:

- The tendon system should be designed for the possibility of one tendon being removed.
- The flex element(s) (at the fairlead and anchor) should accommodate the maximum tendon angles due to horizontal platform motions.
- Single event fatigue should be considered.
- The consequence of minimum tension (i.e. buckling or damage to flex elements) should be considered.
- Installation loads should be considered.
- Local stresses due to diameter or thickness transition should be considered.
- The hydrostatic collapse capacity should be checked.

DNV's guideline for structural design of TLPs (DNV-OS-C105) is based on the load and resistance factor design (LRFD) method [79]. For ultimate

limit state (ULS) calculations, two combinations of load factors for permanent and variable functional loads, environmental loads, and deformation loads are required. The ULS and fatigue limit state (FLS) load considerations for the tendons are largely based on the API RP 2T. Bureau Veritas has also published rules for TLP classification which reference the API RP 2T [80].

In addition to the DNV-OS-C105 guideline, DNV provides an example of offshore reliability analysis of a TLP [81]. Low-frequency offset and wave-frequency effects were combined in the ULS analysis of the tendons. External water pressure, axial force, and bending moment were considered. Given a close correlation between axial force and bending moment, a simplified approach without outcrossing analysis was shown to be possible. In the tendon FLS analysis, the springing effects on the tendon were emphasized.

Analysis procedures for TLP dynamics and hydrodynamics are also very relevant for TLPWT analysis, as presented in the following subsections.

2.5.1 Tension Leg Platform Dynamics

In the horizontal plane, TLP dynamics resemble the dynamics of other floating systems: surge, sway, and yaw motions are fairly well-defined and tend to occur at the wave frequency and at the low-frequency natural period. The definition of the vertical platform dynamics is, however, a challenge that applies to both TLPWTs and O&G TLPs. Assuming that the hull can be considered as a rigid body, the relationship between the surge and heave motions (set-down) can introduce an awkward non-symmetric linearized stiffness matrix for a symmetric platform [82]. Although finite element models for the tethers have become more common, a simple analytical model has advantages in terms of computational cost. One solution for maintaining some non-linear effects within an analytical solution is to consider the set-down and pure heave motion separately [83].

Furthermore, marine structures with natural frequencies in the range of 1-5 seconds (such as gravity-based structures, TLPs, and long ships) may experience two types of resonant response: steady-state “springing” responses due to sum-frequency wave effects, and transient “ringing” responses in severe seas [84]. Springing, which may have significant effects on fatigue estimation, is observed in mild, moderate, and extreme seas, while ringing, which is more related to extreme loads, generally follows large, steep waves. Relevant studies on the hydrodynamic loads associated with such responses are described in Section 2.5.2.

An additional dynamic effect - which is particular to TLPs and TLPWTs - is the response to tension loss. Low tension can lead to buckling or ac-

cidental tether disconnection [85], which can in turn lead to capsize, as in the TLP Typhoon in the Gulf of Mexico during Hurricane Rita in 2005. On the other hand, short-duration tension loss may not cause severe platform motions, large bending stresses, or significant stresses during re-tensioning (snatch) [86]. The present numerical model does not consider tendon disconnect.

2.5.2 Tension Leg Platform Hydrodynamics

There exists a significant body of research regarding the hydrodynamic loads on large volume floating structures, which will not be reviewed in detail here, as this can be considered textbook material [87, 88, 89]. Some of the extensions of this research that have been driven by TLP development - such as second-order sum-frequency effects and third-order ringing loads - merit a brief summary due to their relevance to the present work.

Lighthill presented early work on sum-frequency forces in the late 1970's [90]. Molin pursued a similar approach, with extension to finite water depth, that same year [91]. Various approaches to managing the free surface integral were attempted, including asymptotic relations based on assumptions about the far field behavior [92, 93], and disregarding the component of the force which comes from the second-order potential flow solution (keeping only components arising from the first-order potential solution) [94]. Herfjord and Nielsen suggested that the sum-frequency forcing due to the first-order potential in the range of 3 - 5 seconds may be of the same order of magnitude as the first-order force for large structures in irregular waves [94].

The assumption that the first-order potential provides the main contribution to sum-frequency forcing was, however, soon refuted by Kim and Yue [95]. A significant component of the second-order force is associated with the particular solution of the inhomogeneous boundary condition on the free surface [93, 95]. Kim and Yue's panel method analysis of a (stationary) four-column TLP design showed that the RMS of the tendon tension could be several times larger than that predicted using only first-order wave excitation [95]. Kim further demonstrated the effects of second-order wave interaction between TLP columns in 1991 [96].

The effects of first-order motions on the second-order forces were subsequently investigated by Liu et al. in 1995 using a higher order boundary element momentum method [97]. For a compliant TLP, the effects of first-order motions depended on frequency, but were not found to be very significant for the studied platform [97]. While improvements to the numerical procedures for the free surface integral have since been implemented in numerous codes, the main developments in the second-order force computation

were largely introduced in the mid 1990's [98, 99].

In addition to second-order forcing, third-order forcing also sparked significant interest in the mid 1990's. The second-order forcing was found to be insufficient to explain the ringing response observed on several O&G TLPs [100]. Ringing responses occur for platforms with natural periods shorter than the wave period. In intermediate or deep water, where TLPWTs may be employed, ringing is known to occur in steep wave conditions [100]. Some hydrodynamic criteria for ringing loads have been described in previous studies [100, 101], including:

1. Presence of surface-piercing columns.

2. Low Keulegan-Carpenter number ($KC = 2\pi U/\omega D$, where U is the fluid particle velocity amplitude, ω is the wave period, and D is the diameter) (fluid loading dominated by inertial loads): $KC < 5$.

3. Low diameter-wavelength (D/λ) ratio (linear diffraction is not significant): $D/\lambda < 0.2$. (Alternatively: $ka < 0.63$, where $k = 2\pi/\lambda$ and $a = D/2$)

4. Wave height comparable to cross-sectional structure dimensions.

TLPWT platforms, particularly single column designs with relatively large diameters, may meet the given criteria for certain wave conditions. In order to model these forces, a model for the nonlinear third-order force on cylindrical columns is required.

Faltinsen, Newman, and Vinje (FNV) pursued a regular wave long-wave formulation for the forces on a vertical cylinder due to the third-order potential using perturbation expansion for $ka << 1$, $kA << 1$, and $A/a = O(1)$, where A is the wave elevation [100]. The FNV formulation was extended to irregular waves by Newman in 1996 [102]. During the same time period, Rainey suggested an alternative method of computing third-order wave loads on slender structures, using nonlinear wave kinematics and Morison's equation [103]. Gurley and Kareem, also considering nonlinear wave elevation, argued that viscous loads could lead to ringing-type responses for slender systems [84]. The nonlinear wave elevation models have not been pursued in the present work, although there may be some cases where they give better comparisons to model tests [101].

The FNV formulation includes both second and third-order components. While the second-order component of the long-wave excitation force has been shown to compare well to full second-order diffraction only up to approximately $ka = 0.1$, the third-order FNV formulation is known to compare

well to full third-order diffraction theory up to $ka = 0.4$ [104]. Krokstad et al. [104] therefore developed the following approach: the full second-order sum-frequency quadratic transfer function (QTF) forces are included, and the third-order sum-frequency horizontal forces according to the FNV formulation are added. Krokstad et al. also included the explicit expression for the moment proposed by Marthinsen [105]. This expression for the ringing moment is not fully consistent, and, for a TLPWT, the ringing moment is expected to be less important than the moment about the center of gravity induced by the horizontal force applied at the still water level.

Direct implementations of the FNV formulation have been compared to experiments on several occasions. Even using the second-order QTF rather than the second-order FNV component, Krokstad et al. found that the FNV formulation slightly overpredicted the high-frequency loads on a stationary cylinder [104]. The overprediction was somewhat steepness-dependent, with steeper waves leading to larger overprediction. Stansberg presented experimental results for the first, second, and third-order loads on fixed cylinders of different diameters [106]. Although similar overprediction of the forces was observed, the FNV model was shown to correctly predict the trends in the third-order force with regards to wave number.

An alternative implementation of the FNV formulation for irregular waves was presented by Johannessen in 2012 [107]. This implementation addresses two of the challenges associated with a direct implementation of FNV: the spectrum cut-off dependency and the presence of low-frequency components. FNV includes terms which do not decay at high frequency, which implies that nonphysical wave components can be amplified, and the resulting force can be altered based on the input wave spectrum. Furthermore, a direct implementation of the irregular FNV formula includes undesired difference-frequency components [108]. By rewriting the FNV formulation as a sum of Fourier components including only sum-frequency terms, and restricting the bandwidth of frequencies which are allowed to interact, Johannessen is able to avoid these difficulties [107]. Results compare well to model tests of a gravity based structure [107]. This approach is further described in Sec. 3.2.4.2, and applied to TLPWTs in Sec. 5.2.

On the other hand, none of the aforementioned approaches succeeds in capturing the secondary hydrodynamic loading cycle which was experimentally observed as early as 1993 [109]. This loading cycle, which was documented for moderately steep waves and relatively large radii ($kA > 0.3$, $0.1 < ka < 0.33$, $3.8 < KC < 7$ and $Fr > 0.4$, where $Fr = \omega A/\sqrt{gD}$), takes place approximately one quarter wave period after the main force peak [110]. This phenomenon may also affect TLPWTs, but cannot be modeled

by current numerical methods.

Chapter 3

Theoretical Background

TLPWTs are complex systems, which must be analyzed in a multidisciplinary context, including at a minimum structural mechanics, hydrodynamics, aerodynamics, and control. Additional consideration of soil-tendon foundation interaction, drivetrain mechanics, and electrical engineering is possible, but outside the scope of the present work. Relevant theoretical background for analysis with different levels of fidelity is discussed in Sections 3.1 (structural mechanics), 3.2 (hydrostatics and hydrodynamics), 3.3 (wind turbine aerodynamics), and 3.4 (wind turbine control). In order to consider the system behavior over its lifetime, some knowledge of environmental conditions, stochastic processes, and extreme value estimation is required, as introduced in Section 3.5. Finally, additional information about the primary computational codes used in this work (SIMO-RIFLEX-AeroDyn with external control) is given in Section 3.6.

3.1 Structural Mechanics of Steel Structures

Global structural dynamic analysis of a floating flexible structure can be performed with varying degrees of fidelity, such as a linear rigid body approach, modal methods, nonlinear beam models, and more detailed finite element (FE) models considering 2-D or 3-D shell elements. The present work is focused on very simple methods (frequency-domain linear rigid body models) and more refined methods that can still be solved on a reasonable time scale (nonlinear beam element models). Rigid body mechanics are introduced in Sec. 3.1.1. Modal methods, which are used in some FWT analysis tools, are briefly introduced in Sec. 3.1.2, while the nonlinear beam theory applied in the finite element model in the present work is discussed in Sec. 3.1.3.

The finite element model is solved in the time domain, as described in Sec. 3.1.4, which includes a description of the time-domain formulation as well as information about decay analyses and fatigue damage calculation based on the time-domain results. Finally, Sec. 3.1.5 addresses natural frequency estimation for the tendon system.

3.1.1 Rigid Body Mechanics for Floating Bodies

The simplest dynamic structural model of a platform is a single rigid body. One can define up to six traditional global motions about a given inertial reference point: surge (ζ_1), sway (ζ_2), heave (ζ_3), roll (ζ_4), pitch (ζ_5), and yaw (ζ_6). These global motions can be represented mathematically by the motion vector, $\vec{\zeta}(t)$, where

$$\vec{\zeta}(t) = [\zeta_1(t), \zeta_2(t), ...\zeta_6(t)]^T, \tag{3.1}$$

and t represents time. Newton's second law is then applied in an inertial reference frame as

$$\boldsymbol{M}\ddot{\vec{\zeta}} = \vec{F} \tag{3.2}$$

where $\boldsymbol{M}$ is a 6x6 matrix containing the entries M_{ij} representing the dry mass of the structure, with the inertia computed about the body reference point; $\vec{F}$ is a time-dependent vector of all of the forces acting on the body; and the double dot represents two differentiations with respect to time.

For a moored floating body subjected to waves, a linear analysis of the global motions can be carried out by separating the force vector into several components: an added mass component which opposes the body acceleration, a linear damping component which is proportional to the body velocity, a linear stiffness due to hydrostatics which is proportional to the body motion, a linear stiffness due to the mooring system, and external wave excitation loads. By collecting the added mass, damping, and stiffness terms on the left hand side, the equation of motion becomes:

$$[\boldsymbol{M} + \boldsymbol{A}]\ddot{\vec{\zeta}} + \boldsymbol{B}\dot{\vec{\zeta}} + [\boldsymbol{C} + \boldsymbol{K}]\vec{\zeta} = \vec{X}, \tag{3.3}$$

where $\boldsymbol{A}$ represents added mass coefficients, $\boldsymbol{B}$ represents damping coefficients, and $\boldsymbol{C}$ and $\boldsymbol{K}$ represent linear stiffness coefficients due to hydrostatics and the mooring system, respectively. $\boldsymbol{A}$, $\boldsymbol{B}$, $\boldsymbol{C}$, and $\boldsymbol{K}$ are 6x6 matrices, including coupling terms, and $\boldsymbol{A}$ and $\boldsymbol{B}$ are frequency-dependent. The 6x1 vector $\vec{X}$ contains the external wave excitation force for each mode of motion.

For a linear wave-only analysis of a floating body, it is then convenient to consider the problem in the frequency domain [88]. Neglecting nonlinear

wave excitation terms (such as quadratic damping, or amplitude-dependent higher order terms), the wave excitation at one frequency - and therefore the body response - can be assumed harmonic. For a given frequency ω, the regular wave excitation takes the form

$$\vec{X}(\omega) = \mathrm{Re}\left(\vec{\tilde{X}} e^{-i\omega t}\right), \tag{3.4}$$

where the tilde represents a complex value.

Eq. 3.3 can then be re-written for a single wave frequency:

$$\left(-\omega^2[\boldsymbol{M} + \boldsymbol{A}(\omega)] + i\omega \boldsymbol{B}(\omega) + [\boldsymbol{C} + \boldsymbol{K}]\right) \vec{\tilde{\zeta}} = \vec{\tilde{X}}(\omega). \tag{3.5}$$

Given the frequency-dependent coefficients A_{jk} and B_{jk}, the system of equations can be solved very quickly. The response in irregular seas can then be estimated by assuming linear superposition of many such wave components [88]. For some applications, the frequency-domain response works quite well for capturing the most important responses. For a floating wind turbine, modification may be necessary in order to include the wind-induced loading and damping. This approach is discussed in greater detail in Sec. 5.1.

In order to include nonlinear load effects in a rigid body model, the equations of motion should, however, be solved in the time domain. In that case, the frequency-dependence can be included through a convolution integral or by a state-space representation of the time-dependent coefficients [111]. In the current formulation in SIMO, the convolution integral approach is used [112].

3.1.2 Modal Analysis

Rather than limiting the analysis to six rigid body motions, the equations of motion can alternatively be solved for a set of mode shapes including structural deflections. That is, certain structural deformation patterns are defined, and the time-varying structural deformations are found from the sum of a combination of these patterns (or mode shapes).

If the mode shapes are determined accurately, modal analysis is reasonably accurate and computationally efficient for wind turbine analysis. The well-known FAST software from NREL is based on a combination of modal and multibody dynamics formulations [16]. Nonlinearity on the load side of the equation can be accounted for, though material nonlinearity (elasto-plastic behavior) and geometrical stiffening due to large deformations cannot be considered [113, Ch. 11.7, p. 398]. An important disadvantage of modal analysis is that it requires accurate pre-processing of the system modes.

For a TLPWT, there may be some question about which mode shapes should be included. In FAST, two modes are employed for the tower fore-aft (and two for the tower side-side) motions, in addition to the six rigid body platform motions. Currently, there are no mode shapes included for tendon behavior in FAST.

3.1.3 Nonlinear Beam Element Theory

Additional dynamic effects can be captured by modeling the structure using beam, shell, or solid elements and solving the equations of motion in a stepwise analysis. Beam elements can capture overall deflections of long, slender structures. Shell elements, which remove a level of abstraction from the beam element model, can capture flexural stresses which are not considered in a beam model [113, Ch. 10.2, p. 337]. A solid element model removes another level of abstraction, but requires even greater computational effort. In the present work, a nonlinear beam element formulation was applied to investigate the global behavior of TLPWTs.

While this formulation is less computationally efficient than a modal method, a nonlinear beam element formulation captures higher structural modes without pre-processing. This formulation is also more flexible when considering multiple bodies or a combination of wind and wave energy devices. Results presented in this thesis employ the RIFLEX nonlinear beam element software.

The beam element theory present in RIFLEX is based on a co-rotated ghost element formulation, which allows for large rotational deformations without requiring tensor transformation of the stress and strain [114]. The slender beam theory applied here assumes that:

1. A plane section normal to the longitudinal axis remains plane and normal to the longitudinal axis.

2. There are no shear deformations due to lateral loading.

3. There is negligible lateral contraction due to axial elongation.

4. The strains are small.

Since the cross sections are assumed to remain plane, the resistance to torsion is provided by shear stresses in the cross-sectional plane (St. Venant torsion) and warping resistance to torsion is neglected [114]. This is a reasonable assumption for a beam with a closed cross section.

Fig. 3.1 illustrates the initial rotated coordinate system C_{0n} and the displaced position of point P with local coordinates (x, y, z). The updated

rotated coordinate system is called C_n. Here, the displacements in (x, y, z) are called (u, v, w), and the torsional deflection about the (longitudinal) x-axis is denoted θ.

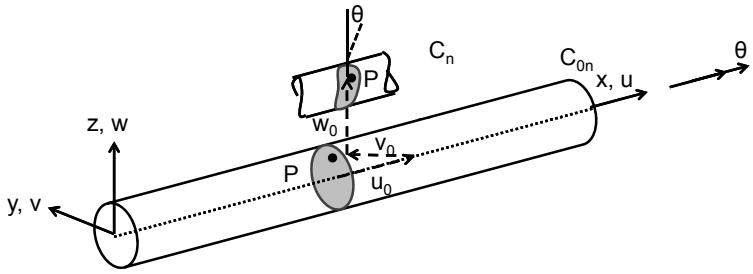

Figure 3.1: Nonlinear beam theory displacement relations

The displacement of point P for small strains is given by:

$$\vec{u}(x, y, z) = \vec{u_0}(x) - y\frac{d\vec{v_0}}{dx} - z\frac{d\vec{w_0}}{dx} \tag{3.6}$$

$$\vec{v}(x, y, z) = \vec{v_0}(x) - z\theta \tag{3.7}$$

$$\vec{w}(x, y, z) = \vec{w_0}(x) + y\theta. \tag{3.8}$$

Then, the strain is calculated from:

$$E_{xx} = \frac{d\vec{u_0}}{dx} - y\frac{d^2\vec{v_0}}{d^2x} - z\frac{d^2\vec{w_0}}{d^2x}, \tag{3.9}$$

where the quadratic strain terms that are zero on the longitudinal (x) axis are neglected, and the quadratic axial strain term is neglected. Further, the torsional behavior is modeled simply as

$$M_\theta = GI_t\theta_x, \tag{3.10}$$

where M_θ is the twist moment and GI_t is the (St. Venant) torsional stiffness.

The displacements on the reference axis are given by a standard FE formulation using linear interpolation for $\vec{u_0}$ and $\vec{\theta_0}$ and cubic interpolation for $\vec{v_0}$ and $\vec{w_0}$ [114, 113]. In the present thesis, this basic theory is applied to the tendons, tower, and blades in the FE simulations of TLPWTs. These simulations are carried out in the time domain, as described in the following section.

3.1.4 Time Domain FE formulation

The governing equation for structural dynamics can be formulated by requiring that the virtual work done by externally applied loads be equal to the sum of the virtual work absorbed by inertial, dissipative, and internal forces [113]. The global form of the governing equation can be written as in Eq. 3.11 assuming that the element mass ($\boldsymbol{M_g}$) and damping ($\boldsymbol{B_g}$) matrices follow from the discretization and use the same shape function as the stiffness matrix.

$$\boldsymbol{M_g}\ddot{\vec{D}} + \boldsymbol{B_g}\dot{\vec{D}} + \vec{R}^{int} = \vec{R}^{ext} \tag{3.11}$$

In Eq. 3.11, $\vec{D}$ is the system displacement vector, $\vec{R}^{int}$ are the internal reaction forces and $\vec{R}^{ext}$ are the external loads. For a linear elastic material, the internal forces can be written:

$$\vec{R}^{int} = \boldsymbol{K_g}\vec{D}, \tag{3.12}$$

where $\boldsymbol{K_g}$ is the global stiffness matrix.

The system of equations in Eq. 3.11 are coupled second-order differential equations that are continuous in time (and discretized in space). The mass and damping matrices are described in greater detail in Secs. 3.1.4.1 and 3.1.4.2, while the numerical solution method and the updated stiffness matrix are explained in Sec. 3.1.4.3.

3.1.4.1 Mass Matrix Formulation

There are several ways to formulate the mass matrix for a global FE model: lumped mass, consistent, combined, HRZ lumping, or optimal lumping [113]. A lumped mass model yields a diagonal mass matrix, which is convenient for explicit time domain integration (see Sec. 3.1.4.3). A consistent mass matrix uses the same shape function as the stiffness matrix. For implicit time domain integration, employed here, it is less important to obtain a diagonal mass matrix, as non-diagonal terms in the stiffness matrix are also present on the left hand side of the equation.

A consistent mass matrix is employed in the SIMO-RIFLEX-AeroDyn analyses in order to give better accuracy. The consistent formulation is also applied to the added mass of beam elements in the model and to the external hydrodynamic loads. (Aerodynamic loads are applied in a lumped formulation). The use of the consistent mass matrix implies that computed natural frequencies are an upper bound on the exact natural frequencies of the model [113].

3.1.4.2 Rayleigh Structural Damping

Rayleigh damping is a convenient formulation for the structural damping in finite element analysis. The structural damping $\boldsymbol{B_{Rayleigh}}$ can be specified as a linear combination of the mass $\boldsymbol{M_g}$ and stiffness $\boldsymbol{K_g}$ matrices, as in Eq. 3.13. (More precisely, the tangential damping matrix is a function of the tangential mass and stiffness matrices). In Eq. 3.13, a_1 is the mass-proportional coefficient, and a_2 is the stiffness proportional coefficient. In practice, different coefficients can be specified for the tension, torsion, and bending degrees of freedom.

$$\boldsymbol{B_{Rayleigh}} = a_1 \boldsymbol{M_g} + a_2 \boldsymbol{K_g} \tag{3.13}$$

If global coefficients a_1 and a_2 are used, the Rayleigh damping formulation gives an orthogonal structural damping matrix. The resulting frequency-dependent modal damping λ_i for a linear dynamic system with global coefficients a_1 and a_2 is then:

$$\lambda_i = \frac{1}{2}\left[\frac{a_1}{\omega_i} + a_2 \omega_i\right], \tag{3.14}$$

where ω_i is the frequency of interest. This equation does not apply directly when different coefficients are used for different degrees of freedom, but it can still be used to specify independent damping in tension, torsion, and bending with reasonable accuracy [114]. Furthermore, although Eq. 3.14 refers to global coefficients, damping coefficients were specified on an element-by-element basis in the present work. Different structural damping characteristics could then be applied to each flexible component (tendons, tower, and blades).

From Eq. 3.14, one can see that mass-proportional damping is effective for low frequencies, while stiffness-proportional damping is effective for high frequencies. For a floating system, which may have important rigid-body motions, it is typical to set $a_1 = 0$. The damping ratio then becomes a linear function of frequency.

Modal damping ratios for the tower and blades are specified for the NREL 5 MW wind turbine [72]. It is not possible to obtain exactly the same damping for all modes using Rayleigh stiffness-proportional damping, so some compromise must be made. In this case, a coefficient of $a_2 = 0.007$ was specified for the tower and $a_2 = 0.002$ for the blades. The resulting damping is compared to the specified modal damping for the land-based turbine in Fig. 3.2 and Table 3.1.

Although Fig. 3.2 and Table 3.1 refer to the land-based turbine, similar remarks can be made for the TLPWTs. In this case, the tower modes are

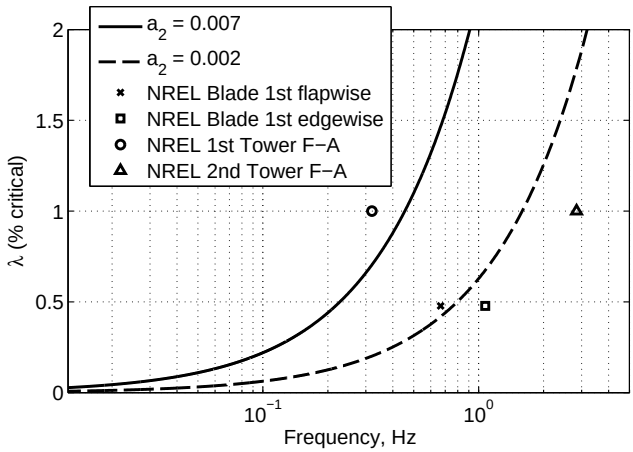

Figure 3.2: Stiffness-proportional damping for the land-based NREL 5 MW wind turbine. The curves show the obtained damping using Rayleigh structural damping, symbols show the specified coefficients [72].

Table 3.1: Structural damping for the land-based NREL 5 MW wind turbine.

	Frequency (Hz)	Specified λ (% critical) [72]	Modeled λ (% critical)
1st tower F-A	0.32	1.00	0.70
2nd tower F-A	2.84	1.00	6.25
1st blade flapwise	0.67	0.477465	0.42
1st blade edgewise	1.07	0.477465	0.67

coupled to platform pitch, yielding a small change in the natural frequency. Still, the first tower mode is expected to be damped slightly less than the desired 1% damping. The second tower mode is damped significantly more than the desired value.

3.1.4.3 Direct Time Integration: Newmark-Beta with Newton-Raphson Iteration

The governing FE equations (Eq. 3.11) are solved step-by-step in time: the response is computed at discrete time instants ($t = \Delta t, 2\Delta t, ..., n\Delta t$). In general, explicit or implicit methods can be used for time integration. An explicit method relies only on historical data to compute the response

$\vec{D}_{n+1}$, while an implicit method contains the terms $\dot{\vec{D}}_{n+1}$ and $\ddot{\vec{D}}_{n+1}$ on the right hand side of the equation. Explicit algorithms require a smaller time increment Δt for stability, but the computation for each time step is more efficient. Implicit algorithms require more computational time per step, but fewer total steps [113]. Furthermore, implicit algorithms are better suited to structural dynamics problems, such as the analysis of FWTs.

A commonly used family of implicit algorithms is the Newmark-Beta family. The Newmark relations are:

$$\dot{\vec{D}}_{n+1} = \dot{\vec{D}}_n + \Delta t \left[\gamma \ddot{\vec{D}}_{n+1} + (1-\gamma)\ddot{\vec{D}}_n\right] \tag{3.15}$$

$$\vec{D}_{n+1} = \vec{D}_n + \Delta t \dot{\vec{D}}_n + \frac{1}{2}\Delta t^2 \left[2\beta \ddot{\vec{D}}_{n+1} + (1-2\beta)\ddot{\vec{D}}_n\right] \tag{3.16}$$

where γ and β are numerical factors which control the accuracy, numerical stability, and the amount of numerical damping [113]. By applying the Newmark relations to Eq. 3.11 and eliminating terms including $\ddot{\vec{D}}_{n+1}$ and $\dot{\vec{D}}_{n+1}$, one obtains:

$$\begin{aligned} \boldsymbol{K^{eff}}\vec{D}_{n+1} = &\vec{R}^{ext}_{n+1} + \boldsymbol{M_g}\left\{\frac{1}{\beta\Delta t^2}\vec{D}_n + \frac{1}{\beta\Delta t}\dot{\vec{D}}_n + \left(\frac{1}{2\beta}-1\right)\ddot{\vec{D}}_n\right\} \\ &+ \boldsymbol{B_g}\left\{\frac{\gamma}{\beta\Delta t}\vec{D}_n + \left(\frac{\gamma}{\beta}-1\right)\dot{\vec{D}}_n + \Delta t\left(\frac{\gamma}{2\beta}-1\right)\ddot{\vec{D}}_n\right\}, \end{aligned} \tag{3.17}$$

where

$$\boldsymbol{K^{eff}} = \frac{1}{\beta\Delta t^2}\boldsymbol{M_g} + \frac{\gamma}{\beta\Delta t}\boldsymbol{B_g} + \boldsymbol{K_g}, \tag{3.18}$$

assuming a linear stiffness matrix $\boldsymbol{K_g}$.

The Newmark-Beta algorithm of Eq. 3.17 is unconditionally stable for $2\beta \geq \gamma \geq 0.5$. Algorithmic damping is introduced for $\gamma > 0.5$, but the accuracy reduces from $O(\Delta t^2)$ to (Δt). All simulations in SIMO-RIFLEX-AeroDyn were performed with integration parameters presented in Table 3.2. These parameters maintain unconditional stability while introducing a small amount of algorithmic damping. A slight reduction in accuracy occurs.

In practice, however, the stiffness matrix is not necessarily linear: $\boldsymbol{K_g}$ is, in general, a function of $\vec{D}$. In order to account for such nonlinearities, $\boldsymbol{K_g}$ is replaced by the tangential stiffness matrix and a Newton-Raphson iteration procedure is implemented [113, 114]. At each time step, the displacements are computed iteratively, and the tangent stiffness matrix is updated for each iteration. Pure Newton-Raphson iteration was applied

Table 3.2: Newmark-Beta integration parameters used in SIMO-RIFLEX-AeroDyn simulations

Δt	0.005 s
γ	0.505
β	0.2564

for all SIMO-RIFLEX-AeroDyn simulations, but the prescribed maximum number of iterations (50) for the desired accuracy (10×10^{-5}) was never reached due to the small time step.

The results of the structural analyses include displacements and internal loads on flexible elements. The displacement time histories can be used to determine natural frequencies (Sec. 3.1.4.4), while the load time histories may be post-processed to obtain stresses and fatigue cycles (Sec. 3.1.4.5). Additional statistical analysis of FE results for stochastic simulations is described in Sec. 3.5.

3.1.4.4 Decay Test Analysis

In order to determine the natural frequencies of a floating structure through time domain simulation with a complete FE model, a numerical decay test may be performed. The structure is displaced to a given offset and then released. The ensuing response shows both the damped natural period in water and the decay. In general, such tests are used for rigid body motions. In the case of the TLPWT, the pitch decay response includes significant contributions from tower bending.

For a TLPWT, the restoring forces are dominated by the mooring system, and can be reasonably approximated as linear. The damping forces, however, include important viscous contributions. In order to determine the linear and quadratic decay contributions, one can follow Hoff's work [115], simplified for linear restoring forces. Assuming uncoupled motions, the decay for any degree of freedom η can then be described by the following equation of motion:

$$\ddot{\eta} + b_1\dot{\eta} + b_2|\dot{\eta}|\dot{\eta} + \omega_0^2\eta = 0 \tag{3.19}$$

where ω_0 is the undamped natural frequency and b_1 and b_2 are damping coefficients. The energy per mass (V) at any given time is then:

$$V(t) = \frac{1}{2}\dot{\eta}^2 + \frac{1}{2}\omega_0^2\eta^2. \tag{3.20}$$

Since the TLPWT damping is small, the solution is approximately harmonic with constant period $2\pi/\omega_0$ and slowly decaying amplitude (ie, V is constant over one cycle). The loss of energy $L(V)$ over each cycle can then be found by Eq. 3.21-3.25.

$$L(V) = -\frac{d}{dt}V \tag{3.21}$$

$$= \frac{\omega_0}{2\pi}\int_0^{2\pi/\omega_0} dt\dot{\eta}\left[b_1\dot{\eta} + b_2|\dot{\eta}|\dot{\eta}\right] \tag{3.22}$$

$$= \frac{\omega_0}{2\pi}\int_0^{2\pi/\omega_0} dt\left[b_1\dot{\eta}^2 + b_2|\dot{\eta}|\dot{\eta}^2\right] \tag{3.23}$$

$$= \frac{\omega_0}{2\pi}\int_0^{2\pi/\omega_0} dt\left[b_1 2V\sin^2\omega_0 t + b_2|2\sqrt{2}V^{3/2}\sin^3\omega_0 t|\right] \tag{3.24}$$

$$= b_1 V + b_2\frac{8}{3}2\sqrt{2}V^{3/2} \tag{3.25}$$

At the peaks and troughs at time t_n, $\dot{\eta} = 0$ (there is no kinetic energy), so V can be calculated from the amplitude η_n:

$$V(t_n) = \frac{1}{2}\omega_0^2\eta_n^2. \tag{3.26}$$

A least-squares fit is used to determine b_1 and b_2 to best match the decay dV/dt. Since ω_0 is not known a priori, one can approximate $\omega_0 \approx \omega_n$, where ω_n is the damped natural frequency. This approximation is quite reasonable for lightly damped systems.

3.1.4.5 Fatigue Damage

High-cycle fatigue failure is caused by stresses that are lower than a structure's yield stress. Material imperfections lead to the formation of minute cracks. Cyclic loading leads to crack propagation, which is eventually responsible for fatigue failure in metallic materials [116]. For metallic materials, physical testing leads to the establishment of stress-cycle or S-N diagrams, which relate the number of cycles to failure (N) to different stress range levels (S). These curves are typically presented with a logarithmic x-axis (N axis), and the resulting plot is most often linear or bi-linear.

In order to estimate the fatigue lifetime of the structure, one first needs to determine the stress time history at different points on the structure, particularly near welds and bolts. Hot spot stress can then be estimated by

appropriate concentration factors [117], but that step in the analysis is not considered here.

The dynamic FE results give the time history of loads at a cross section. Here, the loads are denoted N_x (axial force), V_y and V_z (shear forces), M_x (torsional moment), and M_y and M_z (bending moments). Based on the coordinate system in Fig. 3.3, the axial stress (σ_x) and shear stress (τ_θ) at a given point (r, θ) on the hollow circular beam cross section are given by Eqs. 3.27 and 3.28.

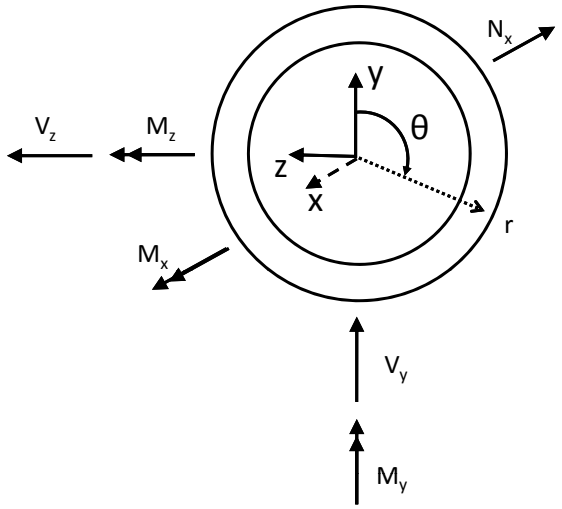

Figure 3.3: Coordinate system for sectional loads

$$\sigma_x = \frac{N_x}{A} + \frac{M_y}{I_y} r \sin(\theta) + \frac{M_z}{I_z} r \cos(\theta) \tag{3.27}$$

$$\tau_\theta = \frac{M_x r}{J} + \frac{2V_y}{A} \sin(\theta) + \frac{2V_z}{A} \cos(\theta) \tag{3.28}$$

In Eqs. 3.27 and 3.28, A is the cross-sectional area, J is the polar moment of area, and I_y and I_z are the second moment of area for the cross section computed about the y and z axes, respectively. Note that τ_θ is defined to be positive in the same direction as θ and that these coordinates differ from the local coordinate system in RIFLEX.

Based on the time history of the stress, the number of load cycles at different stress levels must be computed. The rainflow counting technique was proposed by Matsuishi and Endo in 1968 [118] and is generally considered to be the best method for fatigue damage estimation, at least for

metal structures [119]. Effective stress ranges are counted based on the time history of peaks and valleys. In the present work, the implementation of rainflow cycle counting and fatigue damage summation in WAFO (Wave Analysis for Fatigue and Oceanography [120]) was employed with a small modification to allow for bilinear S-N curves.

Finally, given the stress cycle count for different stress levels S_i, the fatigue damage D_{RFC} for the simulation time period is found by Palmgren-Miner's rule (Eq. 3.29), where n_s is the total number of stress levels in the simulation time history and n_i is the number of cycles at stress level S_i. In Eq. 3.29, a simple SN curve with slope m is assumed, but it is a trivial modification to select the appropriate slope m and material property K for each stress range.

$$D_{RFC} = \sum_{i=1}^{n_s} K^{-1} n_i S_i^m \tag{3.29}$$

Representative bilinear S-N curves (with slopes m_1 and m_2 and material properties K_1 and K_2) were selected for different components based on DNV recommendations [117], as shown in Table 3.3. Characteristic curves from DNV-RP-C203 Table 2-1 are for steel in air, and DNV-RP-C203 Table 2-2 is for seawater with cathodic protection [117]. In all cases, the reference thickness is taken as $t_{ref} = 25$ mm. When the section thickness is less than t_{ref}, the K values are obtained directly from the presented values of $\bar{a}$ [117].

Table 3.3: Characteristic bilinear S-N curves for fatigue analysis for design of structural components. N^* indicates the maximum value of N for m_1 and k_1.

component	m_1	$\log(K_1)$	N^*	m_2	$\log(K_2)$	S-N Curve [117]
tower (σ_x)	3.0	-12.164	1×10^7	5.0	-15.606	2-1, D
tower (τ_θ)	3.0	-12.449	1×10^7	5.0	-16.081	2-1, C1
tendons (σ_x)	3.0	-11.455	1×10^6	5.0	-15.091	2-2, F
tendons (τ_θ)	3.0	-11.901	1×10^6	5.0	-15.835	2-2, C2

Since fatigue damage is expected to occur first in welds rather than in the base material, SN curves for girth welds were used. In order to obtain a first measure for comparison, the base metal cross sections of the members were used in stress calculation with a stress concentration factor of 1. Furthermore, axial and shear stresses were considered separately. More detailed

studies may consider different stress concentration factors for different load types, more detailed geometry of the joints between structural members, and address the combined stress state.

3.1.5 Natural Frequencies of Tensioned Beams

For a TLPWT, special consideration should be given to the tendon characteristics. The tendon natural frequencies can be important when considering the coupled motions of the platform and the possibility of resonant excitation. The natural frequencies for transverse modes of a beam with pretension can be estimated following, for example, Shaker's 1975 summary [121]. For a TLPWT tendon with pretension F_t, diameter d_t, thickness t_t, and pinned-pinned end conditions, the n lowest natural frequencies for transverse deflections are found from

$$\omega_{trans_n} = \frac{n^2\pi^2}{l_0^2}\sqrt{1+\frac{F_t l_0^2}{E_t I_t n^2\pi^2}}\sqrt{\frac{E_t I_t}{\rho_t + a_t}}, \tag{3.30}$$

where l_0 is the tendon length, E_t is the Young's modulus, ρ_t is the dry tendon mass per length, a_t is the transverse added mass per unit length (approximated as $a_t \approx \rho\pi(d_t/2)^2$) and I_t is the area moment of inertia, calculated for a hollow circular section as:

$$I_t = \frac{\pi}{4}\left(r_e^4 - r_i^4\right) \tag{3.31}$$

where $r_e = d_t/2$ and $r_i = (d_t - 2t_t)/2$. Note that Eq. 3.30 is modified from the formula for a dry tensioned pinned-pinned beam [121] by the addition of the transverse added mass term to the mass per unit length.

If we treat the tendon as an unsupported bar element in axial deformation, the axial natural frequency can be found from Eq. 3.32 as in [113].

$$\omega_{axial} = \pi\sqrt{\frac{E_t A_t}{\rho_t l_0^2}} \tag{3.32}$$

For the axial deflections, the added mass is assumed to be negligible. Additional details about the tendon model applied in the dynamic simulations can be found in Sec. 3.6.4.

3.2 Hydrodynamics of TLPWTs

Waves, tidal variations, and current may cause significant loads on TLPWT structures. This thesis focuses on wave loads in intermediate and deep water and does not consider tidal variations or currents.

Given the range of TLPWT displacement, natural frequencies, and diameters, several different hydrodynamic theories may be relevant [88]. First, the hydrostatic restoring coefficients should be computed based on the mean position of the structure (Sec. 3.2.1). For large volume structures, first-order potential flow theory (Sec. 3.2.2) gives a good representation of the wave excitation (both Froude-Krylov and diffraction effects) and provides solutions for the added mass and radiation damping coefficients. First-order potential flow theory considers excitation at the incoming wave frequency and at the undisturbed position of the structure.

Second-order potential flow theory (Sec. 3.2.3) becomes important for structures with natural frequencies that are either quite low or near twice the wave frequency [88]. For TLPWTs, second-order potential flow theory may be important for both low-frequency surge motions and high-frequency pitch or heave springing responses. Forces due to approximations of third-order potential flow theory (Sec. 3.2.4) are relevant for the computation of ringing responses in large, relatively steep waves [100].

Finally, slender structures may be analyzed using the Morison Equation, a semi-empirical formulation developed for circular cylindrical sections [88]. Inertia and viscous drag load components are included in the Morison Equation, which is described in Sec. 3.2.5.

3.2.1 Hydrostatic Analysis

Hydrostatics generally refers to the pressure distribution of a fluid at rest. There are no shearing stresses present, and the pressure (p) depends only on z [122]. For an incompressible fluid with density ρ,

$$\frac{dp}{dz} = -\rho g, \tag{3.33}$$

where the acceleration due to gravity is denoted g.

The distribution of hydrostatic pressure is responsible for the mean loading on the shell structure of the hull, which is an important load component for detailed design. Furthermore, hydrostatic pressure dictates the stability of freely floating structures according to current criteria for offshore structures [88, 123, 124].

Considering the platform as a rigid body, the hydrostatic stiffness depends only on the waterline geometry, overall center of buoyancy (z_B) and overall center of gravity (z_G). Eqns. 3.34-3.37 can be used to determine the nonzero terms in the hydrostatic stiffness matrix for a body with x-z symmetry. Note that these equations are modified from [88] because the calculation of the pitch and roll stiffness must be modified to account for the

inequality between the structural weight and displacement for a TLPWT.

$$C_{33} = \rho g A_{wp} \tag{3.34}$$

$$C_{35} = C_{53} = -\rho g \iint\limits_{A_{wp}} x dx dy \tag{3.35}$$

$$C_{44} = \rho g \nabla z_B - M g z_G + \rho g \iint\limits_{A_{wp}} y^2 dx dy \tag{3.36}$$

$$C_{55} = \rho g \nabla z_B - M g z_G + \rho g \iint\limits_{A_{wp}} x^2 dx dy \tag{3.37}$$

In Eqns. 3.34-3.37, A_{wp} is the waterplane area and ∇ is the displaced volume. The waterplane moment of inertia (I_{wp}) is the same about all axes. For a TLPWT with circular waterplane and diameter D:

$$C_{35} = C_{53} = 0 \tag{3.38}$$

$$A_{wp} = \pi D^2/4 \tag{3.39}$$

$$I_{wp} = \iint\limits_{A_{wp}} y^2 dx dy = \iint\limits_{A_{wp}} x^2 dx dy = \pi D^4/64 \tag{3.40}$$

$$C_{44} = C_{55} = \rho g I_{wp} + \rho g \nabla z_B - M g z_G. \tag{3.41}$$

These coefficients are strictly valid for infinitesimally small motions, but are found to be reasonable approximations for the studied motions. In the operational condition, the mooring system stiffness is much larger than the hydrostatic stiffness; during installation, the hydrostatic stiffness determines the stability of the freely floating platform.

3.2.2 First-Order Potential Flow Theory

First-order potential flow, or linear wave theory, is sufficient to describe the dominant wave loading on many offshore structures [88]. The first-order velocity potential $\Phi^{(1)}$ is a solution of Laplace's equation subjected to appropriate boundary conditions. The details of the boundary value problem are given in several textbooks [88, 125] and will not be repeated here. Incompressible, inviscid, irrotational flow is assumed, and the problem is solved for small-amplitude harmonic waves on a stationary rigid body, or for small rigid body motions in still water. By the Haskind relations, only one of these two problems must be solved.

Using, for example, a source distribution technique, $\Phi^{(1)}$ can be obtained for a general three-dimensional hull in the absence of current. As shown in Eq. 3.42, the time dependence of the first-order results is the same as the incoming wave frequency, ω_j.

$$\Phi^{(1)}(x,t) = \mathrm{Re} \sum_j \phi_j^{(1)}(x) e^{i\omega_j t} \tag{3.42}$$

The solution for the velocity potential gives the frequency-dependent added mass ($A_{ij}(\omega)$), linear damping ($B_{ij}(\omega)$), and wave excitation ($\tilde{X}_j(\omega)$), which are required for setting up the rigid body structural dynamics problem described in Section 3.1.1 [88].

3.2.3 Second-Order Potential Flow Theory

For structures with natural frequencies outside of the wave excitation range, second-order loads due to incompressible, inviscid, irrotational flow may also be important. The interaction between two waves can result in excitation at frequencies outside the wave excitation range. For plane waves with frequency ω_j and ω_l, the full second-order potential ($\Phi^{(2)}$) includes both sum frequency (ϕ^{+}_{jl}) and difference frequency (ϕ^{-}_{jl}) components, as in Eq. 3.43 [95].

$$\Phi^{(2)}(x,t) = \mathrm{Re}\sum_{j}\sum_{l}\left[\phi^{+}_{jl}(x)e^{i(\omega_j+\omega_l)t} + \phi^{-}_{jl}(x)e^{i(\omega_j-\omega_l)t}\right] \tag{3.43}$$

These two components are typically solved separately. Slowly-varying forces are evaluated by integrating pressure from the difference-frequency potential. For a seastate with N wave components of frequency ω_i, amplitude A_i, and phase ϵ_i, the slowly-varying forces and moments F_i^{SV} can be written in the form [88]:

$$F_i^{SV} = \sum_{j=1}^{N}\sum_{l=1}^{N} A_j A_l \Big[T^{ic}_{jl}\cos\{(\omega_l-\omega_j)t + (\epsilon_l-\epsilon_j)\} + T^{is}_{jl}\sin\{(\omega_l-\omega_j)t + (\epsilon_l-\epsilon_j)\}\Big], \tag{3.44}$$

where $i = 1, ..., 6$. The coefficients T^{ic}_{jl} and T^{is}_{jl} are transfer functions for the difference-frequency forces [88]. The well-known Newman's approximation for the slowly-varying force components is then:

$$T^{ic}_{jl} = T^{ic}_{lj} = 0.5\left(T^{ic}_{jj} + T^{ic}_{ll}\right) \tag{3.45}$$

$$T^{is}_{jl} = T^{is}_{lj} = 0. \tag{3.46}$$

The advantage of using Newman's approximation is that the terms T^{ic}_{jj} and T^{ic}_{ll} can be computed directly from the first-order results. This is a reasonable approximation when the natural frequency is very low and the forcing does not change too suddenly as one moves away from the diagonal [88].

For a TLPWT, the sum-frequency forces are particularly important for accurate prediction of vertical plane motions and tendon tension. The sum-frequency pressure variation decays very slowly with depth, particularly for small differences in frequency [88]. Although the contribution from the quadratic term in Bernoulli's equation can be computed from the first-order results, it has been shown that it is nonconservative to consider only this effect; that is, it is necessary to compute the second-order potential to obtain accurate forcing estimates [94, 126].

The boundary value problem that must be solved to find the sum-frequency second-order diffraction potential presents a particular computational challenge: the free-surface forcing term. This term decreases slowly with distance away from the body and includes products of highly oscillatory terms [95]. Careful discretization of the free surface is required to compute the sum-frequency integral. A more detailed mesh study for the structures considered here is presented in Appendix C.

The combined results for the contribution of the quadratic term in Bernoulli's equation due to the first-order potential and the solution of the second-order boundary value problem provide the sum-frequency quadratic transfer function (QTF) for the second-order wave force. The QTF is a function of frequency-pairs. In the time domain, these forces are generated by the double sum of harmonic components [112].

3.2.4 3rd Order Long-Wave Forces (Ringing)

As described in Section 2.5.2, "ringing" loads and responses associated with the third-order potential have been observed in both experiments and full-scale TLPs. Following the approach of Krokstad et al. [104], the second-order forces are considered based on the second-order QTF, and only the third-order components of FNV are considered. Note that the FNV expansion assumes $ka << 1$, $kA << 1$, and $A/a = O(1)$, where A is the wave elevation and a is the radius of a stationary cylinder in infinitely deep water.

The third-order horizontal force component of FNV (applied at $z = 0$) in irregular waves can be obtained by two methods: a direct implementation of FNV or a bandwidth-limited, sum-frequency implementation, as described in Sec. 3.2.4.1 and 3.2.4.2, respectively. The present thesis does not consider the third-order pitch moment about the waterline.

3.2.4.1 Direct Computation of Irregular Wave FNV

The regular wave FNV formula was extended to irregular waves by Newman [102]. Two components ($F_3^{(1)}$ and $F_3^{(2)}$) of the third-order force are included.

The horizontal force due to the first-order potential is given by [102]:

$$F_3^{(1)} = \pi\rho a^2 \left[\zeta_1 \left(u_{tz}\zeta_1 + 2ww_x + uu_x - \frac{2}{g}u_t w_t\right) - \left(\frac{u_t}{g}\right)\left(u^2 + w^2\right)\right] \tag{3.47}$$

where ρ is the water density, g is the acceleration due to gravity, ζ_1 is the first-order wave elevation, and u and w are the horizontal and vertical wave particle velocity, respectively. Differentiation is indicated by subscripts. The third-order force due to the nonlinear potential is given as [102]:

$$F_3^{(2)} = \frac{\pi\rho a^2}{g} u^2 u_t \beta \tag{3.48}$$

where

$$\beta = \int_0^{(h+\zeta_1)/a} \Big(3\Psi_1(Z) + 4\Psi_2(Z)\Big) dZ, \tag{3.49}$$

h is the cylinder draft, and $\beta = 4$ for an infinitely long cylinder. The definitions of Ψ_1 and Ψ_2 can be found in [102]. Then, the third-order force may be implemented directly as in Eq. 3.50.

$$F_x^{FNV(3)} = F_3^{(1)} + F_3^{(2)} \tag{3.50}$$

3.2.4.2 Bandwidth-limited, Sum-frequency Implementation of Irregular Wave FNV

An alternative formulation for the third-order FNV force in irregular waves is given by [107]:

$$F_x^{FNV(3)} = \rho\pi a^2 \left(2\zeta_2\Phi_{xt}^{(1)} + \zeta_1^2\Phi_{xtz}^{(1)} + \zeta_1\Phi_z^{(1)}\Phi_{xz}^{(1)} + \frac{\beta}{g}{\Phi_x^{(1)}}^2\Phi_{xt}^{(1)}\right) \tag{3.51}$$

(where $\beta = 4$ in [107]), using a different perturbation for ζ_2. Rewriting Johannessen's formulation in terms of particle velocities gives:

$$F_x^{FNV(3)} = \rho\pi a^2 \left(2\zeta_2 u_t + \zeta_1^2 u_{tz} + \zeta_1 w w_x + \frac{\beta}{g}u^2 u_t\right) \tag{3.52}$$

which is equivalent to Eq. 3.50, except for certain difference-frequency components. By writing the wave potential as a sum of N linear wave components:

$$\Phi^{(1)} = \sum_{n=1}^{N} a_n \frac{\omega_n}{k_n} \sin(\phi_n) e^{k_n z} \tag{3.53}$$

where $\phi_n = k_n x - w_n t + \epsilon_n$ and deep water is assumed, Johannessen writes the third-order FNV force as in Eqs. 3.54-3.56 [107]. These equations, which do not include any difference-frequency terms, are reproduced here in an effort to clarify the misprinted subscripts in the original paper.

$$
\begin{aligned}
2\zeta_2\Phi^{(1)}_{xt} + \zeta_1^2\Phi^{(1)}_{xtz} =& \frac{g}{4}\sum_{n=1}^{N}\Bigg(3a_n^3k_n^2\sin(3\phi_n) \\
&+ \sum_{m=1}^{n-1}\Bigg(a_na_m(a_n(2k_n+k_m)^2\sin(2\phi_n+\phi_m) \\
&+ a_m(k_n+2k_m)^2\sin(\phi_n+2\phi_m)) \\
&+ \sum_{j=1}^{m-1}2a_na_ma_j((k_n+k_m+k_j)^2 \\
&\qquad \sin(\phi_n+\phi_m+\phi_j))\Bigg)\Bigg)
\end{aligned}
\tag{3.54}
$$

$$
\begin{aligned}
\zeta_1\Phi^{(1)}_{z}\Phi^{(1)}_{xz} =& \frac{1}{4}\sum_{n=1}^{N}\Bigg(a_n^3\omega_n^2k_n\sin(3\phi_n) \\
&+ \sum_{m=1}^{n-1}\Bigg(a_na_m(a_n\omega_n(k_n\omega_n+k_m\omega_m+k_n\omega_m)\sin(2\phi_n+\phi_m) \\
&+ a_m\omega_m(k_n\omega_n+k_m\omega_m+k_m\omega_n)\sin(\phi_n+2\phi_m)) \\
&+ \sum_{j=1}^{m-1}a_na_ma_j(((k_n\omega_n+k_m\omega_m)\omega_j+(k_n\omega_n+k_j\omega_j)\omega_m \\
&+ (k_j\omega_j+k_m\omega_m)\omega_n)\sin(\phi_n+\phi_m+\phi_j))\Bigg)\Bigg)
\end{aligned}
\tag{3.55}
$$

$$\begin{aligned}\frac{\beta}{g}{\Phi_x^{(1)}}^2\Phi_{xt}^{(1)} =& \frac{\beta}{2}\sum_{n=1}^{N}\Bigg(\frac{1}{2}a_n^3\omega_n^2k_n\sin\left(3\phi_n\right)\\ &+\sum_{m=1}^{n-1}\Bigg(a_na_m\big(a_nk_n\omega_m\big(\omega_n+\frac{\omega_m}{2}\big)\sin\left(2\phi_n+\phi_m\right)\\ &+a_mk_m\omega_n\big(\omega_m+\frac{\omega_n}{2}\big)\sin\left(\phi_n+2\phi_m\right)\big)\\ &+\sum_{j=1}^{m-1}a_na_ma_j((k_n\omega_m\omega_j+k_m\omega_n\omega_j+k_j\omega_m\omega_n)\\ &\sin\left(\phi_n+\phi_m+\phi_j\right))\Bigg)\Bigg)\end{aligned} \tag{3.56}$$

In practice, this formulation is computationally expensive for large values of N. To avoid this problem, a window function over 20 periods (with a taper over two wave periods) is used when extracting the wave components, and a bandwidth limitation is applied in the calculation of the forces [107]. This bandwidth limitation prevents interaction among waves of very different frequencies. Fig. 3.4 shows the ringing load calculated for different values of the bandwidth $d\omega$. As shown, there is little change in the force for $d\omega \geq 1.4\omega_p$, where $\omega_p = 2\pi/T_p$, and T_p is the peak period.

The maximum allowable $d\omega$ is chosen to be $1.4\omega_p$. This is a larger bandwidth than Johannessen recommends based on his work at model scale. Although Fig. 3.4 shows differences between Johannessen's formulation with $d\omega = 1.4\omega_p$ and a direct implementation of Eq. 3.50, it gives good agreement with the bandwidth-filtered force time series computed using Eq. 3.50 (not shown).

3.2.5 Morison's Equation

As an alternative to potential flow theories, Morison's equation is often used for slender structures where the diameter D is small compared to the wavelength λ (roughly, $D < \lambda/5$) [88]. The transverse force per length (f) on a cylindrical section is given by Eq. 3.57, where $C_a = C_m - 1$ is the added mass coefficient, C_D is the drag coefficient, u is the transverse wave particle velocity, and v is the local transverse body velocity.

$$f = \rho\pi\frac{D^2}{4}\dot{u} + \rho C_a\pi\frac{D^2}{4}(\dot{u}-\dot{v}) + \frac{1}{2}\rho C_D D\left(u-v\right)\left|u-v\right| \tag{3.57}$$

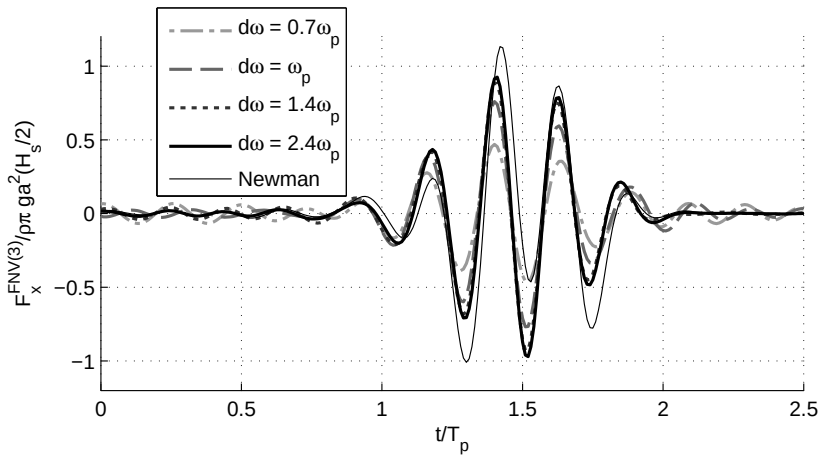

Figure 3.4: Example ringing loads according to Eqs. 3.54-3.56 for variable bandwidth $d\omega$. $\omega_p = 0.63$ rad/s, and $H_s = 8.71$ m. The direct implementation of Newman's formula (Eq. 3.50) is shown for comparison.

The first term in Eq. 3.57 represents the Froude-Krylov force; the second term contains the added mass contributions; and the final term represents the viscous drag forces. According to the deep water limit of linear wave theory, at a location (x, y, z) with z vertically upward from the still water level, the water particle acceleration is given by Eq. 3.58, where ω is the wave angular frequency, ζ is the wave amplitude, and $k = 2\pi/\lambda$ is the wave number.

$$\dot{u} = \omega^2 \zeta e^{kz} \cos(\omega t - kx) \tag{3.58}$$

Assuming deep water ($\omega^2 = gk$) and neglecting $\dot{v}$, a transfer function (H_{Mor}) for the Froude-Krylov and added mass forces on a section of length dl centered at a vertical location z is given by Eq. 3.59.

$$H_{Mor} = \frac{f}{\zeta} \approx \rho V (1 + C_a) \omega^2 e^{(\omega^2 z/g)} \tag{3.59}$$

Noting that the z-coordinate will always be negative, the dependence on ω is $H_{Mor} \propto \omega^2 / e^{\alpha\omega^2}$, where α is a positive constant value for a given depth. Since this function may not decay at the same rate as the excitation force obtained from potential flow theory for high frequencies in the range of the TLPWT pitch natural frequency, the model may predict significantly different responses (see also Sec. 5.2.1).

In a time-domain dynamic analysis, a combination of Morison's equation and potential theory formulation may be used. The full Morison's equation

is applied for slender elements in addition to the potential flow solution for large volume bodies. Viscous damping based on Morison's equation may also be applied to the large volume structure with appropriate coefficients. In the present work, Morison's equation was applied with first-order linear waves, with forces integrated up to the instantaneous free surface. The wave kinematics from the mean wave level were applied above the mean water level (no Wheeler stretching).

MacCamy and Fuchs developed a solution for the wave forces on vertical piles including diffraction effects which may be considered as an alternative to the simple formulation here [127]. Their analytical solution for a vertical pile extending from the bottom through the sea surface is applicable for larger D/λ ratios. This approach has not been applied in the present work.

3.3 Wind Turbine Aerodynamics

Aerodynamic models for wind turbines range from one-dimensional (1-D) momentum balance models to full 3-D Navier-Stokes solutions. In practice, blade element momentum (BEM) and generalized dynamic wake (GDW) models represent computationally efficient options. Despite the limitations of these methods, such as their inability to account for large rotor cone or large blade deflections, such methods have been found to give fairly accurate results for many operational conditions [128, 129].

The development of SIMO-RIFLEX-AeroDyn, which was used for the present thesis work, was performed in parallel with the implementation of a BEM code within RIFLEX. As this BEM implementation differs somewhat from AeroDyn's BEM code, it is of interest to include some comparison between the available methods. A summary of the theories that are implemented in SIMO-RIFLEX-AeroDyn and in SIMO-RIFLEX is presented in Table 3.4.

3.3.1 Blade Element Momentum

A basic implementation of the BEM method iteratively determines the local induction factors to balance the axial thrust on the turbine with the change of momentum of the air passing through the swept annulus, and the turbine torque with the change of angular momentum in the air [130]. The basic theory, the Glauert correction for large induced velocities, and the Prandtl corrections for hub and tip loss are described in greater detail in numerous textbooks [1, 130]. In addition to these universal corrections, additional consideration is given to the effects of dynamic wake, dynamic stall, and

Table 3.4: Implemented aerodynamic theories in SIMO-RIFLEX (SR-BEM), SIMO-RIFLEX-AeroDyn with BEM (SRA-BEM), and SIMO-RIFLEX-AeroDyn with GDW (SRA-GDW).

	SR-BEM	SRA-BEM	SRA-GDW
Tip loss	Prandtl	Prandtl	Prandtl
Hub loss	Prandtl	Prandtl	Prandtl
Dynamic stall	Øye	Beddoes-Leishman	Beddoes-Leishman
Dynamic wake	Øye	not implemented	inherent
Tower shadow	Potential flow	Potential flow	Potential flow
Skewed inflow correction	Glauert	Pitt and Peters	inherent

skewed and sheared inflow.

The dynamic wake effect is the time lag in induced velocities due to the shedding and downstream convection of vorticity [128]. Dynamic wake effects are most pronounced for heavily loaded rotors, corresponding to high induction factors (low wind speeds) [131]. This effect can be modeled by the Stig Øye model, which acts as a filter for induced velocities. The Stig Øye model is applied in Riflex BEM, but the AeroDyn BEM code does not include dynamic wake effects.

3.3.2 Generalized Dynamic Wake

As an alternative to BEM, the GDW method can be used to determine the induced velocities in the rotor plane. The method is based on a potential flow solution to Laplace's equation [129]. The Euler equation (conservation of momentum for inviscid flow, assuming induced velocities are small compared to the incident wind velocity) and conservation of mass lead to Laplace's equation for the pressure distribution. The boundary conditions for the solution are taken from the aerodynamic loading on the rotor blades, the requirement that pressure returns to the ambient pressure far from the rotor, and the requirement that the pressure discontinuity across the rotor plane is equal to the thrust.

The pressure and induced velocity are solved as infinite series of Legendre

functions and trigonometric functions. By including many flow states, a more general pressure distribution on the rotor plane can be achieved than with the BEM method. The GDW method inherently includes the tip losses, skewed wake dynamics, and dynamic wake effects, but can only be used for lightly loaded rotors.

3.3.3 Dynamic Stall and Skewed Inflow

Dynamic stall refers to time-dependent variations in the lift and drag coefficients of an airfoil due to changes in the angle of attack. Two slightly different semi-empirical models are described in the literature. The Stig Øye model gives unsteady lift by filtering the trailing edge separation point with an empirical time constant [128]. The Beddoes-Leishmann model gives unsteady lift and drag based on the indicial response of the normal force coefficient (the response to a step change in angle of attack based on linearized differential equations for unsteady, compressible, inviscid flow) [129]. Both models require tuning based on experimental results, which are not available for the simulated turbine. Using the available input data, the two models give similar results for the variation in lift. The blades are not expected to encounter stall past the quarter radius for constant winds up to 25 m/s, but the dynamic stall model may be more important for turbulent conditions, skewed inflow, and pitch control action.

Skewed inflow may occur due to rotor tilt or a yaw angle between the rotor and the oncoming wind. Glauert developed the basic formulation for correcting the induction factor due to skewed inflow:

$$a_{skew} = a\left[1 + \kappa\frac{r}{R}\cos(\Phi)\right] \tag{3.60}$$

where r is the local radius, R is the maximum radius, Φ is the azimuth angle that is zero at the most downwind position on the rotor, and κ is a factor which depends on the wake skew angle (χ) [130]. The AeroDyn-BEM code uses $\kappa = \frac{15}{32}\tan\chi$ [129].

The flow approaching the turbine may be sheared due to the effect of surface friction or due to the wake of other wind turbines. Local implementation of BEM in both azimuthal and radial directions, as in both Riflex-BEM and AeroDyn-BEM, gives the best agreement with advanced models [132].

3.3.4 Upwind Tower Influence

Since the incoming wind has to travel around the tower, the tower has an effect on the local inflow, even for an upwind turbine. The tower influence is

an important effect for dynamic analysis of TLPWTs: as each blade passes through a region of modified inflow, the resulting thrust variations at f_{3p} can lead to tower and tendon fatigue.

A common method to calculate the velocity deficit due to the tower is based on the 2-D potential solution for constant flow around a circle. Based on the coordinate system shown in Fig. 3.5, the non-dimensional influence at a location (x, y, z) is evaluated as in Eqs. 3.61-3.64, where D_{tow} is the local tower diameter for the given z level, and B_k is the Bak modification factor (0.1 for the Bak model, 0 for potential flow).

$$x_w = \frac{2x}{D_{tow}} + B_k \tag{3.61}$$

$$y_w = \frac{2y}{D_{tow}} \tag{3.62}$$

$$x_{infl} = \left[1 - \frac{x_w^2 - y_w^2}{x_w^2 + y_w^2}\right] \tag{3.63}$$

$$y_{infl} = 2\left[\frac{x_w y_w}{x_w^2 + y_w^2}\right] \tag{3.64}$$

In practice, the horizontal wind direction and speed are computed at the location (x, y, z). This speed is multiplied by the factors x_{infl} and y_{infl}, and the modified speed is then transposed back to the initial wind direction. (See also [129]).

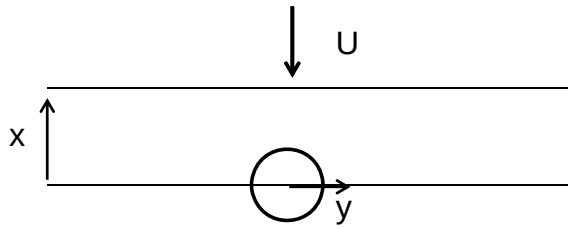

Figure 3.5: Tower upwind influence coordinate system.

Note that the x-coordinate here is upwind and the velocity is set to zero for any point inside the tower. The difference between the Bak and plain potential flow models is illustrated in Fig. 3.6, which shows the resulting x-direction velocity at different locations upstream of the tower.

Note that an additional correction based on the tower drag coefficient is possible but is neither documented nor included here (see [129]).

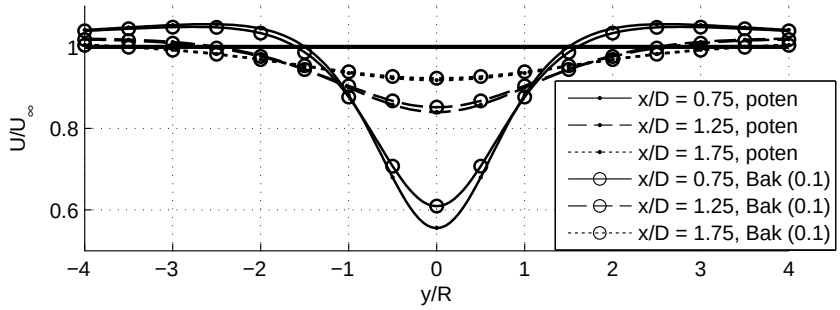

Figure 3.6: Upwind tower influence: x-direction velocity for constant free-stream velocity.

3.3.5 Tower Drag

In addition to the tower's influence on the air flow, the forces on the tower due to the air flow should be considered. The aerodynamic drag force on the tower may be particularly important in extreme wind conditions, where the wind forces on the parked (or idling) rotor are small. By considering a single value for the drag coefficient (C_{D_j}) in each of the local x, y, and z directions, a simple quadratic drag model for the local force can be developed. Then, the drag force in each local direction j is a function of the air density (ρ_{air}), the local diameter D, the local segment length L, the drag coefficient C_{D_j} in direction j, and the relative wind velocity at the center of the element V_{local_j} in direction j, as in Eq. 3.65.

$$F_{local_j} = \frac{1}{2}\rho_{air} D L C_{D_j} V_{local_j} |V_{local_j}| \tag{3.65}$$

The implementation of this model in the SIMO-RIFLEX-AeroDyn code is described in greater detail in Sec. 3.6.2.

3.4 Wind Turbine Control Systems

The purpose of control systems at the wind farm, turbine, and component levels is "to manage the safe, automatic operation of the turbine" [1, Ch. 8, p. 360]. A controller at the wind farm level serves to coordinate the activities of several turbines, while the turbine-level controller regulates the start-up, shut-down, fault monitoring, and operational condition of a single turbine. In order to respond to environmental changes or changes in the operational condition, the turbine-level controller provides some input to dynamic controllers, such as generator torque or blade pitch controllers.

Descriptions of stall-regulated and constant speed control strategies can be found in [1, Ch. 8.3] [130, Ch. 8.2]. The present work is primarily concerned with large horizontal axis wind turbines, which overwhelmingly use pitch-regulated variable speed control to regulate the power output and structural loads.

3.4.1 Pitch-Regulated Variable Speed Control

Pitch-regulated variable speed (PRVS) wind turbines, which are decoupled from the grid frequency by a power converter, can vary both the rotor speed and the blade pitch [130, Ch. 8.4][1, Ch. 8.3]. In between the cut-in wind speed (below which there is effectively too little wind to generate a worthwhile quantity of power) and cut-out wind speed (where the turbine is shut down for structural reasons), PRVS wind turbines have two primary operational regions: below-rated and above-rated wind speeds.

In the below-rated wind region, the blade pitch is kept constant and the generator torque varies such that the WT operates as close as possible to the optimal tip speed ratio. A simple quadratic algorithm for setting the generator torque to track the optimal tip speed ratio is given by Burton et al. [130, Ch. 8.3.2]. In this region, the thrust and torque increase quadratically with wind speed.

At the rated wind speed, the wind turbine reaches the rated torque, rated rotational speed, and rated thrust. In the above-rated wind speed region, the blade pitch is varied in order to minimize the structural loads and the generator torque is chosen to give the rated power output. For a typical land-based turbine, the generator torque is chosen to track the rated power. A simplified WT control system for academic use is included in the definition of the NREL 5 MW wind turbine [72]. For this academic controller, proportional-integral (PI) control is used for the collective blade pitch angle. The gain scheduling for the NREL 5 MW blade pitch controller is based on the nearly linear relationship between aerodynamic power sensitivity to pitch angle and the collective pitch angle.

Namik and Stol studied individual blade pitch control (IBPC) as an alternative to collective pitch control for FWTs [133]. For a TLPWT, they claim that IBPC can reduce rotor speed error, reduce tower side-side loading, and decrease the roll rate. Furthermore, disturbance accommodating control reduces the platform yaw and pitch rates. In order to achieve such improvements, however, the blade pitch actuation may increase by over 400% [133].

3.4.2 Control Challenges for Floating Wind Turbines

The nacelle motions of FWTs present an additional challenge for the control system. For systems with low-frequency surge or pitch motions, there may be a negative feedback mechanism between the nacelle velocity and the blade pitch controller [134, 23]. In above-rated wind speeds, when the blade pitch controller responds to an increase (decrease) in the relative velocity by pitching the blades to feather (stall), the thrust force decreases (increases). The decreased (increased) thrust results in amplified motion into (against) the wind.

Several methods exist to address this negative feedback: an active damping control system can be applied by including measurement of the tower motions or accelerations [23], or the blade pitch control system gains can be modified in order to place the control system frequencies lower than the structural natural frequencies [26, 134].

For a TLPWT, the platform pitch natural frequency is generally higher than the controller frequency, thus eliminating the need for control system modifications in most operating conditions. On the other hand, the surge natural frequency is lower than the control frequency and could theoretically lead to an instability. Matha observed that it was possible to induce such an instability in a contrived condition [12], but the surge damping is generally large enough to avoid unstable response. Still, platform motions at the wave frequency may result in negative feedback. Although wave-induced motions tend to be small, such motions may become a concern in certain operational conditions, particularly when large waves are present.

In most of the simulations, the land-based controller was applied to all TLPWTs. For certain studies, particularly related to ringing, a modified control system was used, as in Table 3.5. This modification is noted where applicable.

Table 3.5: Control system parameters (as in [72])

	Original (land-based)	Modified
K_I at min. pitch	0.008068634	0.00358605
K_P at min. pitch	0.01882681 s	0.0125512 s
$\omega_{\psi n}$	0.6 rad/s	0.4 rad/s
above-rated strategy	constant power	constant torque

3.4.3 Control and Electrical System Faults

In the IEC61400-1 design standard for wind turbines, design load case (DLC) 2.1 requires the consideration of "control system fault or loss of electrical network" [5]. The exact nature of the faults to be analyzed is, however, not specified.

A Failure Mode and Effect Analysis (FMEA) may be used to evaluate failure risks and make a rational decision about the faults one ought to consider. Three metrics may be considered: severity, occurrence, and detection [135]. That is, for any particular scenario, the severity (consequences of failure), occurrence (likelihood of the scenario taking place), and detection (ability of the monitoring system to detect and respond to the failure) should be evaluated. The rotor and blades assembly, generator, and electrical controls have high risk priority numbers according to such an analysis for a 2 MW variable pitch turbine [135]. Although a more detailed FMEA is required for TLPWTs, a first step is to examine the response to certain high-risk faults. Here, blade pitch controller faults and grid faults are considered.

3.4.3.1 Blade Pitch Control System Faults

For pitch-regulated wind turbines, the blade pitch control system contributes significantly to the failure rate [18]. As shown in Fig. 3.7, the blade pitch control system consists of mechanical components, sensors, and software - all of which can be susceptible to failure.

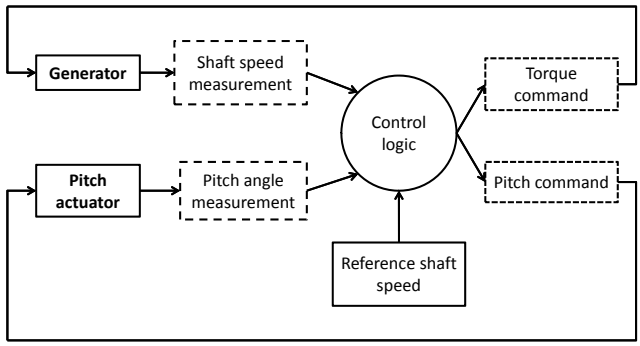

Figure 3.7: Blade pitch and generator torque control overview

Many potential faults related to the pitch actuator and pitch angle sensor are possible: the pitch actuator could get stuck on a particular value, the pitch actuator could run away to a fixed value, the pitch sensor could report

a value with constant offset or multiplicative error from the true value, or the pitch sensor could report a fixed value to the controller [75]. The control system must then recognize the fault and react in some way, typically by shutting down the turbine (by quickly pitching the remaining functional blades to full feather) [74]. The present thesis does not consider pitch sensor faults, but considers the case where the pitch actuator becomes stuck.

3.4.3.2 Grid Faults

In order to serve the power grid, wind turbine farms are required to meet standards regarding voltage and reactive power control, frequency control, and fault ride-through [136]. Fault ride-through refers to the case when a short circuit occurs somewhere in the grid, leading to a loss of voltage at the wind farm.

Specific connection requirements are outside the scope of the current work, but the case where grid fault leads to a complete loss of generator torque has been investigated here as a worst case scenario for the mechanical system. In this case, it is assumed that the blade pitch control mechanism is still able to function, such that all three blades are pitched to feather shortly after the generator torque is lost [74, 76].

3.5 Stochastic Methods for Offshore Structures

TLPWTs are subjected to random load processes. In order to evaluate their performance, it is necessary to consider the loading and response from a probabilistic perspective. The following subsections provide some background about stochastic processes (Sec. 3.5.1) and present models for the environmental input for simulations of TLPWTs (Sec. 3.5.2). Relevant concepts for treatment of the response to stochastic inputs are introduced in Sec. 3.5.3.

3.5.1 Definition of a Stochastic Process

A process x is called *stochastic* if $x(t)$ is a random value for all t on some interval (which may be infinite) [119, Ch. 5.4]. Ocean waves can be taken as an example of a random variable.

For a *stationary* process, the expected values $E[x(t)]$ and $E[x(t)x(t+\tau)]$ are both independent of t. This implies that the mean value of the random variable is constant in time and that the autocorrelation (R_{xx}) is only a function of τ. This further implies that the standard deviation is constant

over time. For ocean waves, stationarity is often a good assumption over time periods of several hours.

If the process is *ergodic*, every ensemble mean can be replaced by a time average over a single representation. If we imagine our knowledge of the ocean wave elevation to consist of reports from a large number of buoys at many points in space, this can be compared to saying that the signal from one wave buoy is representative of the signal of any buoy.

The assumption of stationarity and ergodicity of environmental processes is a key step in the process of estimating structural responses to such processes. A finite number of realizations can be used to study processes that exist in nature over wide ranges of time and space. Furthermore, these assumptions allow us to define the spectral density function. The autocorrelation function R_{xx} in continuous form for a stationary, ergodic process (Eq. 3.66) can be used as the starting point for deriving the spectral density function, which is defined in Eq. 3.67. This is called the Wiener-Khintchine Theorem [137, Ch. 10.1].

$$R_{xx}(\tau) = \lim_{T\to\infty} \frac{1}{2T} \int_{-T}^{T} x(t)x(t+\tau)dt \tag{3.66}$$

$$S_{xx}(\omega) = \lim_{T\to\infty} \frac{1}{2\pi T} |X(\omega)|^2 \tag{3.67}$$

Taking the Fourier transform of Eq. 3.66 gives:

$$\begin{aligned}\int_{-\infty}^{\infty} R_{xx}(\tau)e^{(-i\omega\tau)}d\tau &= \lim_{T\to\infty} \frac{1}{2T} \int_{-\infty}^{\infty}\int_{-\infty}^{\infty} x(t)x(t+\tau)e^{(-i\omega\tau)}dtd\tau \\ &= \lim_{T\to\infty} \frac{1}{2T} \int_{-\infty}^{\infty}\int_{-\infty}^{\infty} x(t)x(t+\tau)e^{(-i\omega(t+\tau))}e^{(i\omega t)}dtd\tau.\end{aligned} \tag{3.68}$$

By noting that:

$$X(\omega) = \int_{-\infty}^{\infty} x(t)e^{(-i\omega t)}dt \tag{3.69}$$

$$X^*(\omega) = \int_{-\infty}^{\infty} x(t)e^{(i\omega t)}dt, \tag{3.70}$$

one can see that R_{xx} and S_{xx} are related:

$$\begin{aligned}\int_{-\infty}^{\infty} R_{xx}(\tau)e^{(-i\omega\tau)}d\tau &= \lim_{T\to\infty} \frac{1}{2T} X(\omega)X^*(\omega) \\ &= \lim_{T\to\infty} \frac{1}{2T} |X(\omega)|^2 \\ &= \pi S_{xx}(\omega).\end{aligned} \tag{3.71}$$

It is also useful to define the moments m_j of the spectrum S_{xx} as in Eq. 3.72.

$$m_j = \int_0^\infty \omega^j S_{xx}(\omega) d\omega, \qquad j = 0, 1, 2... \tag{3.72}$$

3.5.2 Random Environmental Processes

When studying TLPWTs, two random environmental processes are of particular interest: wave elevation and wind speed.

3.5.2.1 Ocean Waves

In reality, ocean waves are generally composed of many nonlinear components traveling in different directions, driven by wind over variable distances. Viscosity is present, and the waves interact with currents, tides, the sea floor and coast lines, as well as natural and man-made obstacles. Fortunately, reasonable approximations of this complicated situation can be obtained by assuming incompressible, irrotational, inviscid fluid flow, and using linear potential wave theory [88].

Linear theory can be used to simulate irregular seas as a sum of a large number of wave components with different frequencies. According to linear wave theory, the free surface elevation for long-crested waves traveling in the positive x-direction is given by Eq. 3.73 [88].

$$\zeta(t) = \sum_{j=1}^{N} A_j \sin\left(\omega_j t - k_j x + \epsilon_j\right) \tag{3.73}$$

In Eq. 3.73, A_j is the amplitude, ω_j is the frequency, k_j is the wave number, and ϵ_j is the phase angle of component j. Note that ω_j and k_j are related by the dispersion relation, which depends on the water depth.

The frequency content of the wave components is described by the wave spectrum, S_w (only positive frequencies are considered here). If the wave spectrum is discretized into j components with constant spacing $\Delta\omega$, and ϵ_j is a uniformly distributed variable over the interval $[0, 2\pi]$, the amplitude A_j is given by:

$$\frac{1}{2} A_j^2 = S_w(\omega_j)\Delta\omega. \tag{3.74}$$

This approach has been used in the present thesis. The wave elevation obtained by Eq. 3.73 is approximately Gaussian-distributed for sufficiently large N. An efficient scheme for generating the wave time series takes

advantage of Fast Fourier Transform (FFT) techniques. In SIMO, a Cooley-Tukey FFT algorithm is used [112]. The number of time steps must then be $N_t = 2^r$, where r is a positive integer. In order to simulate a time series of total length T_{sim}, the time step Δt is related to $\Delta\omega$ by Eq. 3.75.

$$T_{sim} = N_t \Delta t = \frac{2\pi}{\Delta\omega} \tag{3.75}$$

Several numerical approximations of wave spectra based on measured wave data exist: the Pierson-Moskowitz, ISSC, and JONSWAP spectra are single peak spectra which can describe waves generated by local wind conditions, while the Torsethaugen two-peaked spectrum may be applicable in areas where there is an important swell component [88, 119]. The JONSWAP spectrum (Eq. 3.76), which is most relevant for North Sea conditions, has been used for the calculations in the present work [112].

$$S_w(\omega) = \frac{\alpha g^2}{\omega^5} \exp\left(-\beta \left(\frac{\omega_p}{\omega}\right)^4\right) \gamma^{a(\omega)} \tag{3.76}$$

where

$$a(\omega) = \exp\left(\frac{(\omega/\omega_p - 1)^2}{2\tilde{\sigma}^2}\right) \tag{3.77}$$

and

$$\tilde{\sigma} = \begin{cases} 0.07, & \omega \leq \omega_p \\ 0.09, & \omega > \omega_p. \end{cases} \tag{3.78}$$

In Eq. 3.76, α is a spectral parameter, γ is the peakedness parameter, and β is the form parameter [88, 112]. The variance (σ_ζ^2) of the wave elevation can be computed from the spectrum $\sigma_\zeta^2 = m_2$, where m_2 is the moment of S_w as in Eq. 3.72 [119, Ch. 8.2].

The wave crest height can be shown to be Rayleigh-distributed if the wave elevation is a narrow-banded process [119, Ch. 8.2]. Furthermore, if one assumes that a trough of equal magnitude follows each crest, the trough-to-crest wave height is also Rayleigh distributed. This is known to be a simplification compared to observed waves, which tend to have steeper crests and flatter troughs.

Two parameters are often used to describe the wave environment: the significant wave height, H_s, and the peak period, T_p. By definition, H_s is the mean value of the one-third largest waves and T_p is the period at which the spectrum takes on its largest value. H_s can be related to the spectral parameter α in Eq. 3.76, and $T_p = 2\pi/\omega_p$.

In practice, numerical wave spectra may contain small unrealistic components in the high-frequency range. In order to avoid unphysical high-frequency first-order wave excitation, the spectrum may be set to zero above a given wave cutoff frequency ω_c [138]:

$$\omega_c = \sqrt{2g/H_s}. \tag{3.79}$$

This cutoff was applied to simulations which included second-order forces and to the Morison-only model. The cutoff region ($\omega_c \pm 0.25$ rad/s) was smoothed using a LOWESS method with span 0.1 rad/s.

3.5.2.2 Wind

While a detailed description of the atmospheric processes that drive the wind is outside the scope of the present work, a short description of the spatial and temporal variation of the wind speed is of interest. The wind speed consists of longitudinal, lateral, and vertical components, where the longitudinal component is taken to be along the primary wind direction.

Important temporal variations in wind speed occur across a wide range of time scales: inter-annual, annual, diurnal, and short-term [1, Ch. 2.2]. The mean wind speed is typically reported for periods of 10 minutes or 1 hour. Then, the longitudinal wind speed U at a particular point in space is generally described as the sum of mean and fluctuating parts:

$$U = \bar{U} + u' \tag{3.80}$$

where $\bar{U}$ is the short-term mean wind speed and u' is a fluctuating component. Similarly, the lateral and vertical wind speeds consist of mean and fluctuating components. For the present thesis, the mean lateral and vertical wind speeds are assumed to be zero.

Turbulence intensity (I) is defined as the ratio between the mean wind speed at a reference height ($\bar{U}_{ref}$ at z_{ref}) and the standard deviation of the wind speed (Eq. 3.81). I generally varies from approximately 0.1 to 0.4 and tends to be largest for low wind speeds [1, Ch. 2.3].

$$I = \sigma_u / \bar{U}_{ref} \tag{3.81}$$

In the absence of detailed wind observations for a particular location, the turbulence intensity can be obtained from design standards. The IEC standard proposes a normal turbulence model (NTM) and an extreme turbulence model (ETM) [5]. In the present thesis, the NTM and ETM models were applied for IEC Class B and C.

In order to simulate the TLPWT response to turbulent wind, the three-dimensional wind speed across the rotor must be generated. Several methods for constructing a "turbulence box" with the wind components are possible: a one-dimensional FFT may be used to generate time histories of the wind in each direction based on spectra (Kaimal or von Karman, for example); or a three-dimensional FFT can be used to generate correlated components (Mann model) [130, Ch. 2.6].

In the present work, the TurbSim program from NREL was used to generate the turbulence box according to the Kaimal spectrum, including spatial coherence and cross-component correlation [139]. Unless otherwise noted, the grid was taken to be 150 m wide and 150 m tall, with 32x32 points in the y and z directions. The resulting grid spacing is close to the chord length of the NREL 5 MW wind turbine. In TurbSim, the time step for the wind generation was 0.05 seconds. The resulting turbulence box advances through space at the mean wind speed during the dynamic simulations (following Taylor's frozen wake hypothesis). As shown in Fig. 3.8, the FWT moves in space through the planar sections where the turbulent wind is defined. The wind turbine's wake is assumed to move downstream faster than the turbine, such that the turbine does not encounter its own wake as it moves. Based on the surge velocity, this assumption appears to be reasonable [140]. Larger pitch-induced velocities may become important for the aerodynamic calculations.

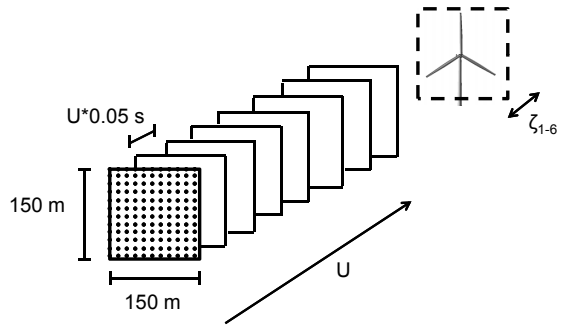

Figure 3.8: Turbulent wind box schematic

In addition to the temporal variation of the wind speed, there is significant variation of the mean wind speed with height above the ground. This variation, called wind shear, is due to viscous boundary layer effects, and it leads to wind turbine load variations at f_{3p}. Two formulations are commonly used: logarithmic and power law [130, Ch. 2.6]. In this study,

the power law formulation of the wind shear is applied to the mean longitudinal wind speed, as in Eq. 3.82, where α is the power law exponent. Here, $\alpha = 0.14$, as is recommended for offshore locations [6].

$$\bar{U}(z) = \bar{U}_{ref} \left(\frac{z}{z_{ref}} \right)^{\alpha} \tag{3.82}$$

3.5.2.3 Joint North Sea Wind-Wave Distributions

The wind and wave conditions are generally correlated. In order to examine the lifetime loads on a TLPWT, a consideration of the joint wind and wave distribution is required. Ideally, one would have access to a very large number of observations of the significant wave height, peak wave period, wave direction, wave spreading, mean wind speed, turbulence intensity, and wind direction. Based on these measurements, fitted joint distributions of the parameters would be used to establish appropriate bins for computing the lifetime fatigue, or for constructing contour surfaces to identify conditions with a certain level of probability.

Johannessen et al. proposed a joint distribution function for the Northern North Sea based on wind and wave measurements from 1973-1999 [141]. The distribution, $f_{UH_sT_p}(u, h, t)$, is based on the 1-hour mean wind speed at 10 m (U_{10}), the significant wave height (H_s), and the peak period (T_p), without regard to the wind and wave directions. As shown in Eq. 3.83, the joint distribution is assumed to be the product of the marginal wind distribution ($f_{U_{10}}(w)$), the conditional distribution of H_s given U_{10}, and the conditional distribution of T_p given H_s and U_{10}.

$$f_{U_{10}H_sT_p}(u, h, t) = f_{U_{10}}(w) f_{H_s|U_{10}}(h|u) f_{T_p|H_sU_{10}}(t|h, u) \tag{3.83}$$

As described in detail by Johannessen et al., 2-parameter Weibull distributions were employed for $f_{U_{10}}(w)$ and $f_{H_s|U_{10}}(h|u)$, while a log-normal distribution was fitted for $f_{T_p|H_sU_{10}}(t|h, u)$ [141].

In addition to the correlation between U, H_s, and T_p, the direction of the wind and waves is of interest. This data was not reported in [141], but observations from the Dutch North Sea have been presented by other researchers [19, 142, 20]. In general, there are misalignments between the wind and waves at all wind speeds: small misalignments at large wind speeds and large misalignments at lower wind speeds [20]. The largest misalignments are associated with stable atmospheric conditions [19]. Observations from the North Sea suggest that misalignment of up to 30° is common, while misalignment larger than 60° occurs less than 5% of the time [142].

Similarly, wave buoy data from Cabo Silleiro (Spain) suggests that misalignment is more common than alignment [143]. The probability of misalignment based on the buoy data is shown in Fig. 3.9. As exemplified by the Cabo Silleiro data, misalignment of up to 90 degrees occurs fairly often.

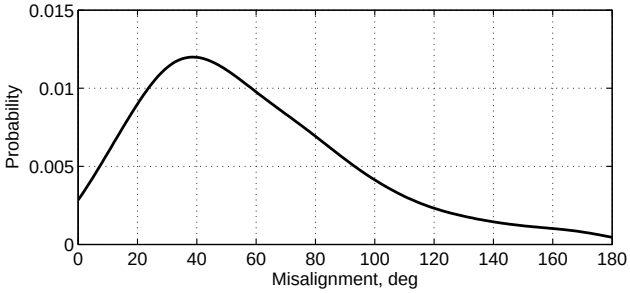

Figure 3.9: Wind-wave misalignment probability distribution function at the Cabo Silleiro buoy.

3.5.2.4 Selected Environmental Conditions

The joint wind-wave distribution for the Northern North Sea [141] was used to choose relevant environmental conditions for simulating TLPWT response. In addition to the North Sea data, Li et al. generated 10-year statistics for several locations in the North Sea, Atlantic Ocean, and Mediterranean Sea for the Marina Platform project based on a numerical hindcast model from the National and Kapodistrian University of Athens (NKUA) [143]. Over the course of the PhD work, several different sets of environmental conditions (ECs) were employed, as summarized here.

First, four baseline ECs were chosen to represent both operational (ECs 1-3) and idling/parked (EC 4) conditions. As shown in Table 3.6, the operational conditions include below-rated, rated, and above-rated wind speeds. As the wind speed increases, there are corresponding increases in H_s and T_p. EC 4 was chosen from a 50-year contour based on the extreme 50-year wind speed. Note that this condition does not necessarily represent the most severe 50-year environment: larger H_s or T_p values are possible with different wind speeds. Furthermore, the 50-year response does not necessarily follow the 50-year environmental contour; EC 4 was chosen to be merely representative, and no 50-year responses were extrapolated.

The baseline conditions from Table 3.6 were used in order to compare linear and nonlinear analyses and in order to evaluate the effects of Morison and second-order potential flow models. For the parametric study, two ad-

Table 3.6: Baseline environmental conditions. The wind and waves travel in the positive x-direction, and the wind speed is reported for the hub height. The NTM model for Class B is used.

	EC1	EC2	EC3	EC4
H_s (m)	2.5	3.1	4.4	12.7
T_p (s)	9.8	10.1	10.6	14.1
$\bar{U}$ (m/s)	8.0	11.4	18.0	50.0
I	0.20	0.17	0.15	0.11

ditional conditions were added to the baseline conditions: a condition with severe waves and operational wind speed (EC5) and a condition near the rated speed with extreme turbulence (EC6). These added conditions, shown in Table 3.7, are useful for examining the design sensitivity to potentially severe conditions.

Table 3.7: Extended baseline environmental conditions. The wind and waves travel in the positive x-direction, and the wind speed is reported for the hub height. The NTM and ETM models are applied for Class B.

	EC5	EC6
H_s (m)	12.7	3.1
T_p (s)	14.1	10.1
$\bar{U}$ (m/s)	18.0	12.0
I	0.15 (NTM)	0.26 (ETM)

In order to examine the effects of second-order and third-order hydrodynamic force models on the simulation results, a different set of environmental conditions was identified, as in Table 3.8. These conditions (R1-R10) fall along the 50-year U, H_s, T_p contour surface based on Johannessen et al.'s data [141]. As shown in Fig. 3.10, combinations with relatively large H_s and small T_p were chosen for wind speeds where the turbine would be operating and for wind speeds where the turbine would be idling. The modified control system was applied for all simulations of the R1-R9. Furthermore, for mean wind speeds of 16 and 24 m/s, the wind turbine was assumed to remain in an operational condition regardless of gusts above the cut-out wind speed (25 m/s).

Table 3.8 includes the characteristic wave steepness, s_0, computed as in Eq. 3.84. These conditions are not breaking wave conditions, but have characteristic wave steepness approximately 4 times larger than that of the operational conditions EC1-3 from Table 3.6.

$$s_0 = \frac{2\pi H_s}{g T_p^2} \tag{3.84}$$

Table 3.8: Ringing environmental conditions. The wind and waves travel in the positive x-direction, and the wind speed is reported for the hub height. The NTM model for Class B is applied.

	R1	R2	R3	R4	R5	R6	R7	R8	R9
H_s (m)	5.68	6.12	7.96	8.22	8.71	9.36	9.87	12.57	14.0
T_p (s)	7.0	7.0	9.0	9.0	10.0	11.0	11.0	13.0	15.0
$\bar{U}$ (m/s)	16.0	24.0	24.0	28.0	24.0	24.0	28.0	44.0	44.0
I	0.15	0.14	0.14	0.13	0.14	0.14	0.13	0.12	0.12
$s_0/100$	7.42	8.00	6.29	6.50	5.58	4.95	5.22	4.76	4.04

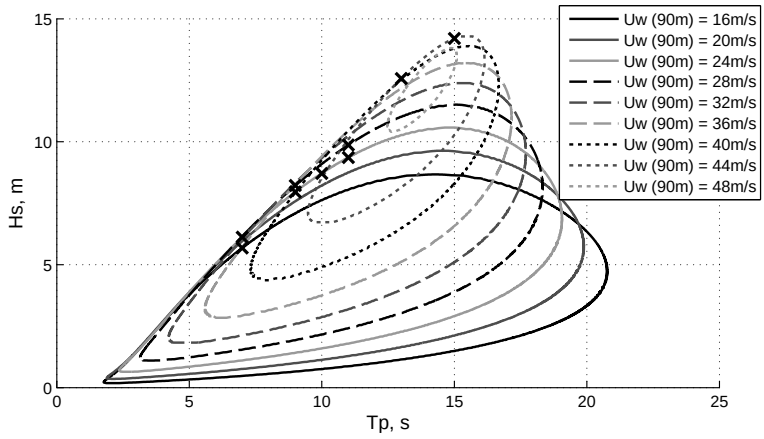

Figure 3.10: 50-year contours of H_s and T_p for different wind speeds, based on [141]. Markers indicate values in Table 3.8.

Environmental conditions for studying the fault conditions were chosen based on Jiang's previous work on the same topic [74]. These conditions (Table 3.9) consider correlated, directionally aligned wind and waves for

the North Sea, where the correlation of wind and waves follows Johannessen's work [141]. ECs F1-F5 represent a range of typical operational conditions. Different faults were considered for these conditions, as described in Sec. 6.1.1. EC F6 is a storm condition, where the turbine idles, and EC F7 is an extreme turbulence condition close to the maximum thrust condition. Faults were not studied in ECs F6 and F7, but the responses in those conditions were used for comparison.

The number and length of simulations were chosen in order to provide a reasonable statistical basis for comparison. In extreme cases, where the load maxima were expected to be driven by waves or lower-frequency wind variations, six three-hour simulations were considered. For fault cases, where the deterministic fault event was expected to dominate, 30 shorter simulations were carried out. Current offshore wind turbine standards suggest that 12 10-minute simulations be carried out for power production plus fault cases [6], but 30 simulations were employed in order to capture some of the significant stochastic and azimuthal variation that have been noticed in previous work [74]. For fault types B (blade pitch fault), C (blade pitch fault with shutdown), and D (grid loss and shutdown), the fault occurred after 400 s of normal operation (see Sec. 6.1.1). Type A simulations have no fault. An additional 600 s (10 minutes) after fault were simulated: this is in keeping with the standards and allows for several cycles of low-frequency responses.

Because this study included semi-submersible and spar platforms with larger wave-induced motions than TLPWTs, the wind was simulated over a slightly larger box than that described in Sec. 3.5.2.2: 160 m wide and 160 m high, with 32x32 points in the y and z directions.

Finally, a set of environmental conditions for examining the effects of wind-wave misalignment is shown in Table 3.10. In this case, the joint distribution was taken from hindcast data obtained by the National and Kapodistrian University of Athens (NKUA) based on the conditions near the Cabo Silleiro buoy off the coast of Portugal [143]. Six environmental conditions (ECs) were selected. These ECs, M1-M6, include lower wind speeds in order to examine relevant fatigue effects. The modified control system was applied in all simulations for M1-M6.

3.5.3 Response Statistics

Time-domain simulations of TLPWTs provide realizations of the motions and certain structural loads. These realizations are of limited duration and comprise limited environmental conditions. A brief overview of some of the theory behind the analysis of the responses is provided in this section.

Table 3.9: Fault environmental conditions. The wind and waves travel in the positive x-direction, and the wind speed is reported for the hub height. The NTM and ETM models are applied for Class C. The simulation lengths given here include 400 s before fault. Fault conditions A-D are defined in Section 6.1.1.

	F1	F2	F3	F4	F5	F6	F7
H_s (m)	2.5	3.1	3.6	4.2	4.8	14.1	3.1
T_p (s)	9.8	10.1	10.3	10.5	10.8	13.3	10.1
$\bar{U}$ (m/s)	8.0	11.2	14.0	17.0	20.0	49.0	11.2
I	0.17	0.15	0.14	0.13	0.12	0.10	0.24
Faults	A-D	A-D	A-D	A-D	A-D	A	A
Num. Seeds	30	30	30	30	30	6	6
Sim. Length (s)	1000	1000	1000	1000	1000	10800	10800

Table 3.10: Wind-wave misalignment environmental conditions. The wind speed is reported for the hub height. The NTM model is applied for Class C. Wave directions $\beta = 0°, 30°, 60°, 90°$ are considered.

	M1	M2	M3	M4	M5	M6
H_s (m)	2.0	4.5	5.0	5.0	4.0	5.5
T_p (s)	8.0	12.0	14.0	12.0	10.0	14.0
$\bar{U}$ (m/s)	4.0	7.0	10.0	12.0	14.0	20.0
I	0.26	0.19	0.16	0.15	0.14	0.12

3.5.3.1 Calculation of Mean and Standard Deviation

The simulations presented in these studies include many realizations of similar conditions. Different wind and wave seeds were employed in order to capture some of the random variation.

One particular difficulty was encountered in the simulation of the response to combined wind and wave conditions: the data files for long wind series were prohibitively large. The original 32-bit version of SIMO-RIFLEX-AeroDyn could not support 32x32 turbulent wind files longer than approximately 40 minutes. In order to obtain 3-hour response statistics, sets of 6 simulations were carried out for 30 minutes (not including the transient effects which were removed from the response) and the mean and standard

deviation were computed based on the 6 simulations taken together. Results are then presented as the expected value of the mean and standard deviation based on many "3-hour" simulations.

In later work, a 64-bit version of SIMO-RIFLEX-AeroDyn was available. This version does not suffer from the same restrictions on wind file size. Response statistics are therefore presented as expected values of the mean (or standard deviation) based on a given number of simulations of the desired length. The response statistics computed from many short simulations were found to agree well with longer simulations.

3.5.3.2 Response Spectra

For a linear, time-invariant system, the response to a stationary input is also stationary. For a single degree of freedom mass-spring-dashpot (m-k-c) system, it is simple to show that the response spectrum (S_x) is related to the forcing spectrum (S_F) by the transfer function H_{FX} [119]:

$$S_x(\omega) = |H_{FX}(\omega)|^2 \, S_F(\omega) \tag{3.85}$$

where

$$H_{FX}(\omega) = \frac{1}{\sqrt{\left(1 - \frac{\omega^2 m}{k}\right)^2 + \left(\frac{c\omega}{k}\right)^2}} \tag{3.86}$$

is a complex function. The phase information is lost in Eq. 3.85.

Linear wave theory suggests that the wave force is proportional to the wave amplitude. Therefore, for offshore structures, it is typical to define the response amplitude operator (RAO) as the transfer function between a particular response and the wave elevation. Then, for a variable with RAO $R(\omega)$, the spectral response S_{resp} to the wave input S_w is given by Eq. 3.87.

$$S_{resp} = |R|^2 \, S_w(\omega) \tag{3.87}$$

For linear systems, the frequency of the response is equal to the input frequency, making the RAO a very useful concept. Due to nonlinearities in both the forcing (such as quadratic drag or nonlinear wave forces) and structure (such as geometrical nonlinearity in the stiffness), the response spectra of offshore structures generally extend beyond the frequencies included in the input wave spectrum. For wind turbines, the wind input and controller further complicate the use of RAOs.

Nonetheless, even without computing RAOs, computation of the spectral response based on the time history of response is a useful method for

identifying the frequencies which are present in the response. Using a FFT, the variance spectrum can be computed directly from the realization by assuming that the response takes on a value of zero outside the simulation time [119, Ch. 6.5].

3.5.3.3 Extreme Value Statistics

Estimates of the largest load effects encountered during a structure's lifetime are important quantities for design. Engineering estimates of the maxima can be obtained based on the concept of level crossings: how often the response exceeds a given value ξ. Assuming that the joint probability density function (PDF) ($f_{X\dot{X}}$) of $x(t)$ and $\dot{x}(t)$ is independent of time, the upcrossing rate ($v^+(\xi)$) in general is given by Eq. 3.88 (Rice formula) [119, Ch. 10.3].

$$v^+(\xi) = \int_{\dot{\xi}}^{\infty} (\dot{x} - \dot{\xi}) f_{X\dot{X}}(\xi, \dot{x}) d\dot{x} \tag{3.88}$$

For a zero-mean Gaussian process, the upcrossing rate is then given by Eq. 3.89.

$$v^+(\xi) = \frac{1}{2\pi} \frac{\sigma_{\dot{x}}}{\sigma_x} \exp\left(-\frac{\xi^2}{2\sigma_x^2}\right) \tag{3.89}$$

Based on the upcrossing rate, the statistical distribution of peaks (f_{X_p}) can be obtained for narrow-banded processes as in Eq. 3.90 [119, Ch. 10.3].

$$f_{X_p} = -\frac{1}{v^+(0)} \frac{dv^+(\xi)}{d\xi}, \quad \xi \geq 0 \tag{3.90}$$

Eq. 3.90 simplifies to a Rayleigh distribution for a narrow-banded Gaussian process.

In the offshore O&G industry, several methods for estimating lifetime extremes have been introduced. The design wave approach is most appropriate for quasi-static load situations, while the design sea state approach and full long-term approach are better suited to dynamic loading [119, Ch. 12]. The design sea state and full long-term approach are appropriate for FWTs.

In the design sea state approach, the short-term extremes are estimated for a given set of ECs [119, Ch. 12.3]. The contour line method is an option for selecting the ECs: the most unfavorable sea states along a surface of equal probability (for example, a return period of 100 years) are investigated. Caution in identifying extreme values is required: the variation in

the three-hour maximum value must be accounted for. Furthermore, the contour method has not been validated for wind turbines.

A full long-term approach requires response calculation for a wide range of environmental conditions. The choice of environmental conditions depends on the region: for the North Sea, the wave conditions can be assumed to change relatively slowly. The long-term situation is then regarded as a sequence of many stationary short-term conditions. The characteristic long-term extremes can be estimated based on all of the peak values, or based on all short-term extremes, or by examining the long-term extreme value [119, Ch. 12].

This thesis does not directly examine the long-term extreme design values. As described in Sec. 3.5.2.4, representative extreme conditions were chosen based on joint probability distributions. These conditions were used to examine both the TLPWT response and the dependence of that response on the analysis methods. For a novel design concept, a full long-term response analysis is required in order to verify a simplified contour line method. Such a response analysis is outside the scope of the present work.

3.6 SIMO-RIFLEX-AeroDyn + Java Control

The majority of the computations presented in this thesis have been performed using the coupled code SIMO-RIFLEX-AeroDyn with an external controller (written in Java). Benchmark results and comparisons with a different BEM implementation are presented in [60]. The SIMO-RIFLEX-AeroDyn User's Manual provides more detailed information about using the code [144].

In order to make use of the open source AeroDyn (v13.00.00) [145, 129, 146] code, a Dynamic Link Library (DLL) was written to communicate with RIFLEX, which models the structural dynamics of the wind turbine and supporting structure [60]. The author's contribution was in writing the interface DLL between RIFLEX and AeroDyn which passes information from Riflex (positions, velocities, orientations) to AeroDyn, and from AeroDyn (element forces) to RIFLEX. The force calculation is done once for each time step (on the first iteration for the structural code). Small modifications to AeroDyn were implemented (such as updating the tower shadow for floating platforms) and additional features (tower drag, constant wind start-up) were added. Verification of the code against FAST and HAWC2 was performed. Additionally, the author wrote the Java code for the NREL baseline controller as well as implementations of fault conditions in the controller. Drs. Harald Ormberg and Elizabeth Passano aided in the interface

development at MARINTEK and Marit Kvittem contributed to the code concept and verification.

The following subsections introduce the basic model components that are considered to be a "wind turbine" structure in RIFLEX (Sec. 3.6.1), provide details about modifications to AeroDyn (Sec. 3.6.2), summarize the control system implementation (Sec. 3.6.3), and describe the resulting coupled model (Sec. 3.6.4).

3.6.1 RIFLEX Model Components

The Riflex model, consisting of lines which compose the blades, eccentricities from the hub center to the blade roots, shaft, and tower, is described in the Riflex 4.0.0 User's Manual [147] and illustrated in Fig. 3.11. The blade pitch control is achieved at the constrained joints between the eccentricities and blades, while the generator torque is applied at the flex joint.

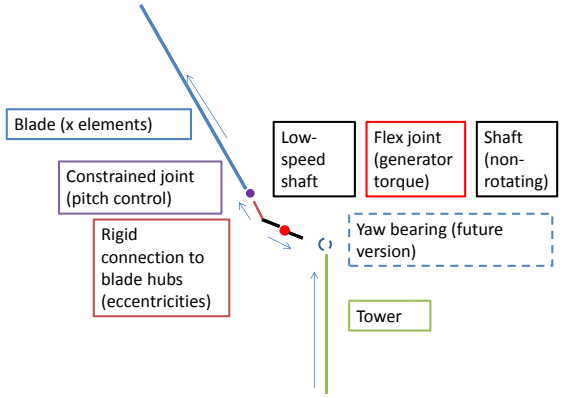

Figure 3.11: RIFLEX components. Arrows indicate direction from first element to last element in each line.

Transformations between the RIFLEX components and the AeroDyn model concepts are described in detail in [144]. Choosing the correct transformation matrices was a significant challenge in developing the DLL.

3.6.2 Modifications to AeroDyn

The AeroDyn v13.00.00 source code (including InflowWind module v1.02.00a-mlb) was implemented in the DLL [145, 129, 146, 148]. Two significant changes were made to the original AeroDyn code used in the DLL: the tower influence model was modified (see also Sec. 3.3.4) and tower drag

forces (see also Sec. 3.3.5) were added. An additional modification was to allow for a period of constant wind at the start of a simulation.

1. *Upwind tower influence*: In AeroDyn v13.00.00, the tower influence model is stationary: the tower influences the flow around the initial position of the tower, making it somewhat irrelevant for platforms with large surge or sway motions. In the DLL, the tower potential flow model was updated to account for tower displacement based on the locations of the top and bottom nodes, without accounting for the velocity of the tower. The tower is assumed to remain approximately vertical and the cross-sections are assumed to remain approximately circular in the horizontal plane. The tower shadow does not affect the vertical wind component.

2. *Tower drag model*: AeroDyn v13.00.00 does not include any forces on the tower. In the DLL, a quadratic drag force was added, as in Eq. 3.65.

   When calculating the drag force, the relative wind velocity is first transformed into the local coordinates:

   $$\vec{V}_{local} = \left[T_{riflex}\right] \left(\vec{V}_{wind_{global}} - \dot{\vec{x}}_{global}\right). \tag{3.91}$$

   Then, after computing the local force as in Eq. 3.65, the force vector is converted back to the global coordinates:

   $$\vec{F} = \left[T_{riflex}\right]^T \vec{F}_{local}. \tag{3.92}$$

   The implemented drag force considers only the undisturbed wind velocity ($\vec{V}_{wind_{global}}$): that is, the effect of the blades on the wind forces on the tower is not included. There are no commonly used models for this influence.

   Furthermore, since the turbulent wind may not be defined below the lowest blade position for the initial turbine configuration, the constant wind velocity given as input to the DLL is applied to the tower elements that fall below that point. For the tower, $C_D = 1.0$ was used in the transverse directions in all simulations.

3. *Initial constant wind period*: In SIMO-RIFLEX-AeroDyn, the wind turbine always starts from a standstill. Constant wind inflow at the start of the simulation can be used to efficiently bring the rotor up to speed and allow the platform to reach the correct mean position. The constant wind speed and duration are specified as input to the DLL.

3.6.3 Control System

An external control code was developed for SIMO-RIFLEX-AeroDyn. The controller follows the logic described in [72] and the DISCON.f90 source code available from NREL, with the additional possibility of running the simulation with a given fixed blade pitch. The fixed blade pitch option makes it possible to run parked or idling turbine simulations. The input and output from the controller are described in detail in [144].

A separate controller with fault condition options was also developed. The fault conditions are described in more detail in Section 6.1.1.

The original contributions to the controller were the implementation and testing of the operational control logic in the Java language and the development of control logic for fault conditions.

3.6.4 Floating Wind Turbine Model

The previously described structural, hydrodynamic, aerodynamic, and control system theories were applied to models such as the one illustrated in Fig. 3.12.

The hull (red), hub, and nacelle were always considered as rigid bodies. The hull location acted as the master node for the fairleads and the tower bottom. No external forcing was applied to the hub or nacelle, but hydrodynamic forces on the hull were applied. The hydrodynamic forces were always applied at the initial position of the TLPWT such that the relative phasing between first-order wave forces, second-order forces, Morison loads, and ringing loads would be correct. Load correction due to yaw motions was not considered, but the Morison drag forces were calculated up to the instantaneous free surface (using wave kinematics at the initial body position). Above the mean water level, wave kinematics from the mean water level were applied. Morison loads on the hull were computed using strip lengths of approximately 1 m for the main column and 2 m for the pontoons.

The tendons, tower, shaft, blade eccentricities, and blades were modeled by lines composed of flexible beam elements. The shaft and blade eccentricities were modeled by relatively stiff elements, while the tendons, tower, and blades were modeled with more physical stiffness properties. Some weight from the hub was moved to the shaft and blade eccentricities, while the total rotational inertia and weight of the hub, shaft, and eccentricities were based on Jonkman's description [72].

The tendons were composed of approximately 60 beam elements per tendon, with cross-sectional properties computed for hollow, air-filled tubu-

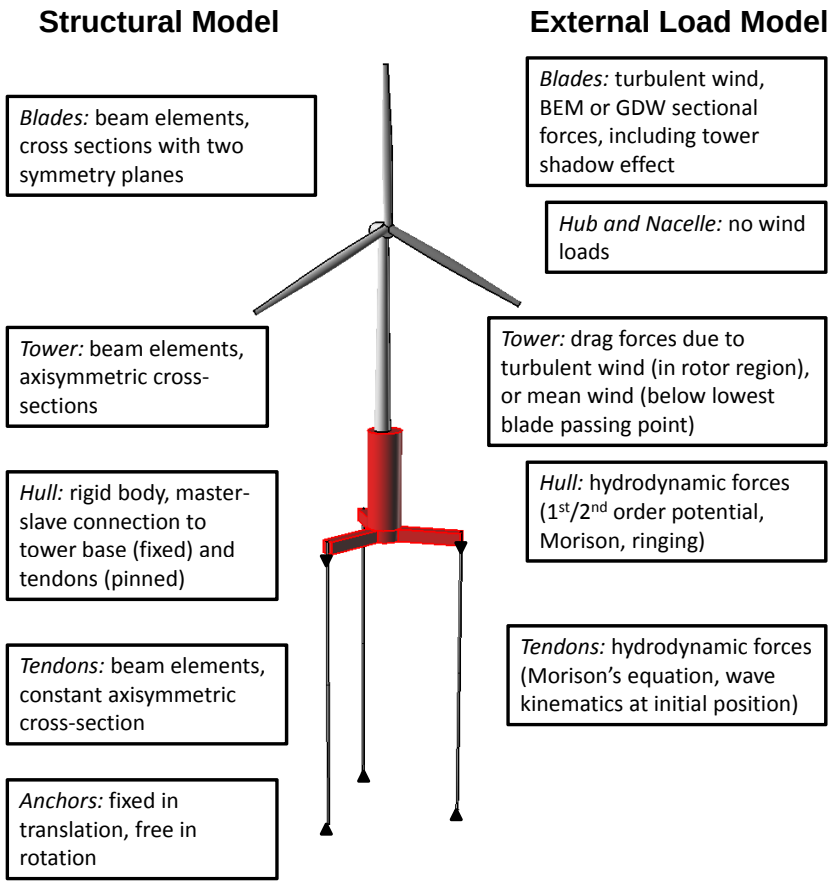

Figure 3.12: SIMO-RIFLEX-AeroDyn floating wind turbine model overview.

lar steel sections. The line length was specified such that the stretched line length would give zero heave for the hull. The anchors were modeled by nodes that were fixed in translation and free in rotation, such that the tendons were pinned to the rigid seabed. Pinned connections to the hull were applied at the fairleads. Hydrodynamic forces were calculated based on strips of length 10 m.

Ten beam elements were used to model the tower. The element diameters and properties were selected based on interpolation of the tower data given by Jonkman for the land-based turbine [72] and for floating wind turbines [26] . The interpolation was based on the midpoint of each element.

The blade model consisted of 17 elements, with a direct correspondence between the structural elements and the aerodynamic elements. A comparison of models with 17, 34, and 51 elements indicated that the difference in the blade deflections was less than 5%. The beam element cross section was specified with two stiffness axes, which were then rotated according to the pre-twist of the airfoil about the pitch axis. The stiffness properties were interpolated based on the data given in [72].

In wind conditions beyond the cut-out wind speed (25 m/s), the model was modified such that the blades were fully feathered. The blade pitch controller was set to keep the blades at the feathered position and no generator torque was applied. As a result, the rotor was simulated in an idling mode.

Chapter 4

TLPWT Design

4.1 Spreadsheet-based Parametric TLPWT Design

4.1.1 Parametric TLPWT Definition

The design space considered here includes single-column TLPWTs with three or four "spokes" or pontoons, intended to support the NREL 5 MW wind turbine with the OC3 Hywind tower design [72, 26]. The hull, made of steel, consists of a main cylindrical column (diameter D_1, length h_1) continued into a base node (diameter D_2, length h_2), with overall draft T. Protruding from one of these cylinders at a vertical location z_s are n_p rectangular or circular pontoons that support the tension legs, as shown in Figure 4.1. For example, a TLPWT that resembles the SeaStar TLPs [149] - with rectangular pontoons (height h_p, width w_p, and total radius from the main column center r_p) and n_t tendons - is depicted in Fig. 4.1b. These pontoons are located at the base of the TLPWT and may provide substantial buoyancy. In contrast, Fig. 4.1c shows another alternative using thin cylindrical pontoons (diameter d_p and total radius from the main column center r_p) and n_t tendons. In order to transfer the tendon forces to the hull, additional support wires may be required, but the structural details of these attachments are not considered in the initial global design.

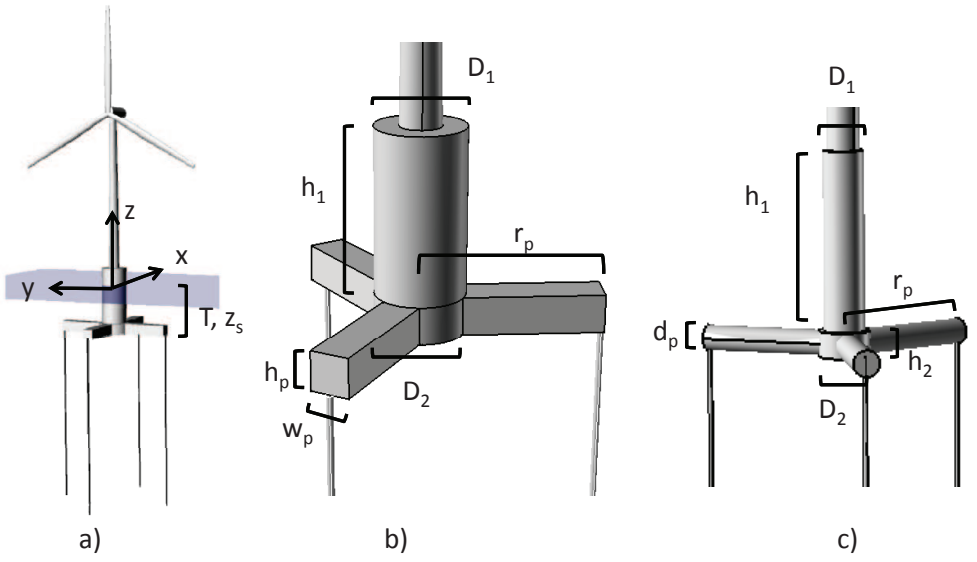

Figure 4.1: Parametric design definitions

The tendons are assumed to be hollow circular pipes, characterized by

their Young's modulus E_t, cross-sectional area A_t, unstretched length l_0, dry mass per length ρ_t, and outer diameter d_t. In general, it is desirable for the tendons to have near zero weight in water (for easier tow-out and installation), which for typical steel density implies a thickness $t_t \approx 0.033 d_t$. In the initial design process, the Young's modulus is taken to be 2.11×10^{11} Pa and only one tendon per pontoon is considered ($n_p = n_t$). The restriction on the number of tendons per pontoon is not a critical simplification: the pretension could easily be divided among several tendons, and the global stiffness would remain the same.

In order to reduce the number of design parameters, the freeboard to the tower base ($b_t = h_1 + h_2 - T$) is constant for all designs (10 m). Some permanent concrete ballast may be added to the base node and center column in order to improve the performance or allow greater stability during installation. The parameter BF is defined as the ballast mass divided by the displaced water mass of the center columns. No ballast is considered in the pontoons.

The coordinate system originates at the center of the main column at the still water level, with z vertically upward and x in the downwind direction, which is also the zero degree wave propagation direction. The first pontoon or strut is oriented in the x direction.

4.1.2 Spreadsheet Design Calculations

Based on the previously described parameters, first predictions of TLPWT behavior can be obtained through simple spreadsheet computations, following engineering assumptions and physical principles.

The displacement was easily found from the geometry, while approximate values for the steel weight in the hull were obtained from assumed steel weights per volume (Table 4.1) [150]. By distributing the computed steel weight into cylinders and boxes of uniform thickness, the 6x6 mass and inertia matrix $\boldsymbol{M}$ was filled.

Table 4.1: Weight approximations for structural steel [150]

Column 1 (upper)	157 kg/m^3
Column 2 (lower)	224 kg/m^3
Pontoons	202 kg/m^3

Simple linear approximations were then used to find the added mass

matrix $\boldsymbol{A}$, hydrostatic stiffness matrix $\boldsymbol{C}$, and mooring system stiffness matrix $\boldsymbol{K}$ based on the geometry and pretension, following for example [151, 152, 88]. The added mass was estimated by summing the 2-D cross-sectional properties of the main columns and pontoons, without considering any interaction. The hydrostatic stiffness in heave is a function of the waterplane area, while the pitch/roll hydrostatic stiffness depends on the waterplane moment of inertia, center of buoyancy, and center of gravity (see Sec. 3.2.1). The mooring system stiffness can be approximated by assuming that the tendons remain straight and disregarding changes in buoyancy. The added mass estimation is described in greater detail in Sec. 4.1.2.1, while the mooring system stiffness was computed as in Sec. 4.1.2.2.

Then, the spreadsheet calculations were used to identify candidate designs that met the criteria described in Section 4.1.3. The resulting designs are described in greater detail in Sec. 4.1.4.

4.1.2.1 Added Mass Estimation

Neglecting both the interaction between the components and any end effects, 2-D added mass coefficients [87, Ch. 4] can be applied for each of the components. For a cylinder with diameter D, the transverse added mass per unit length (a_t) is then given by Eq. 4.1.

$$a_t[D] = \rho\pi D^2/4 \tag{4.1}$$

Eq. 4.2 can be employed for a square section with side length h.

$$a_t[h] = 4.754\rho\left(\frac{h}{2}\right)^2 \tag{4.2}$$

Eq. 4.3 shows the summation of the contributions to the surge added mass from the main column and pontoons. The contribution of the pontoons is summed based on the angle θ about the z-axis. Note that the length of the pontoons (l_p) is measured from r_p to the outer diameter of the hull at the vertical level of the pontoons.

$$A_{11} \approx a_t[D_1]\,(h_1 - b_t) + a_t[D_2]h_2 + \sum_{i=1}^{n_p} l_p a_t[h_p \text{ or } d_p]\cos^2\theta_i \tag{4.3}$$

The heave added mass (Eq. 4.4) includes a contribution from the main column, which is approximated as the added mass of a sphere with diameter equal to D_2 (which is equal to the displaced mass of half of a sphere with

diameter D_2), and contributions due to the pontoons [87, 151].

$$A_{33} \approx \rho\pi\frac{1}{12}D_2^3 + \sum_{i=1}^{n_p} l_p a_t[w_p \text{ or } d_p] \tag{4.4}$$

The added mass in pitch and coupled surge-pitch is computed by integrating the sectional added masses as in Eqs. 4.5 and 4.6.

$$\begin{aligned} A_{55} \approx & a_t[D_1](h_1 - b_t)\left(\frac{1}{12}(h_1 - b_t)^2 + \left(\frac{1}{2}(h_1 - b_t)\right)^2\right) \\ & + a_t[D_2]h_2\left(\frac{1}{12}h_2^2 + \left(\frac{1}{2}\left(-2T + h_2\right)\right)^2\right) \\ & + \sum_{i=1}^{n_p}\cos^2\theta_i\left(\frac{1}{3}\left(r_p^3 - D_2^3\right)a_t[w_p \text{ or } d_p]\right) \\ & + \sum_{i=1}^{n_p}\sin^2\theta_i\left(z_s^2\left(r_p - \frac{D_2}{2}\right)a_t[h_p \text{ or } d_p]\right) \end{aligned} \tag{4.5}$$

$$\begin{aligned} A_{51} \approx & -\frac{1}{2}\left(h_1 - b_t\right)^2 a_t[D_1] - \frac{1}{2}\left(T^2 - \left(-T + h_2\right)^2\right)a_t[D_2] \\ & + \sum_{i=1}^{n_p}\sin^2\theta_i z_s\left(r_p - \frac{D_2}{2}\right)a_t[h_p \text{ or } d_p] \end{aligned} \tag{4.6}$$

Similarly, the yaw added mass is computed by summing the integrated effects of the pontoons (Eq. 4.7). The central column does not contribute to the yaw added mass.

$$A_{66} \approx \sum_{i=1}^{n_p} a_t[w_p \text{ or } d_p]\frac{1}{3}(l_p^3 - \frac{D_2}{2}^3) \tag{4.7}$$

4.1.2.2 Mooring System Stiffness Estimation

The mooring system stiffness matrix due to n_t lines at positions θ_j is approximated for small motions by assuming that the lines remain straight.

Following for example [88, 152]:

$$k_{11} = \frac{F_t}{l_0}, \quad k_{33} = \frac{E_t A_t}{l_0} \tag{4.8}$$

$$K_{11} \approx \sum_{j=1}^{n_t} k_{11} \tag{4.9}$$

$$K_{33} \approx \sum_{j=1}^{n_t} k_{33} \tag{4.10}$$

$$K_{51} = K_{15} \approx \sum_{j=1}^{n_l} k_{11} z_s \tag{4.11}$$

$$K_{55} \approx \sum_{j=1}^{n_l} \left[k_{11} z_s^2 + k_{33} r_p^2\right] \cos^2(\theta_j) \tag{4.12}$$

$$K_{66} \approx \sum_{j=1}^{n_l} k_{11} r_p^2. \tag{4.13}$$

For symmetric mooring systems:

$$K_{22} = K_{11} \tag{4.14}$$

$$K_{24} = K_{42} = -K_{51} \tag{4.15}$$

$$K_{44} = K_{55}. \tag{4.16}$$

4.1.3 Design Criteria

In order to choose somewhat realistic designs for study based on these spreadsheet calculations, some criteria must be defined. When selecting design criteria, one can first consider the overall goal of TLPWT hull design: to minimize the cost of electricity. That is, one would like to maximize power production and minimize construction, installation, and operational costs. A complete calculation of the cost of electricity is not realistic, but one can consider several design and performance characteristics that may affect cost. In order to minimize the construction and material cost, the steel mass, tendon pretension, and displacement should be minimized; to limit the operational costs, the tendon, tower, blade, and nacelle loads and load variations should be minimized. The installation costs, which depend heavily on vessel rent and seabed analysis, are assumed to be similar for all designs, and are neither estimated nor compared here.

With these goals in mind, the following criteria were applied at the spreadsheet design stage:

1. The surge and sway natural periods should be longer than 25 s in order to avoid first-order wave excitation. The decoupled undamped surge natural period T_{n1} may be estimated as in Eq 4.17.

$$T_{n1} = 2\pi\sqrt{\frac{M_{11} + A_{11}}{K_{11}}} \tag{4.17}$$

2. The heave, roll/bending, and pitch/bending natural periods should be shorter than 3.5 s in order to avoid first-order wave excitation. The rigid body natural periods may be approximated by, for example, Eq. 4.18, including the hydrostatic stiffness terms. The effect of tower bending was not included in the spreadsheet design stage, but was checked in the finite element model used in the time-domain analysis.

$$T_{n3} = 2\pi\sqrt{\frac{M_{33} + A_{33}}{C_{33} + K_{33}}} \tag{4.18}$$

3. As in a typical TLP design process, in order to limit the angle at the tendon connectors, the mean offset should not exceed 5% of the water depth [14, Ch. 7.6.3]. The mean offset is a function of the mooring system stiffness and the mean load due to wind, waves, and current. In the preliminary design, the wind effect is taken to be the maximum steady turbine thrust, the mean surge force due to waves ($\bar{F}_1$) is estimated from the pressure integration and viscous forces [88] as in Eq. 4.19 for regular waves with the significant amplitude ζ_a, and current is neglected. The mean offset is estimated for significant wave height 4 m and period 10 s, which corresponds approximately to the wind speed that generates the maximum thrust, using drag coefficient $C_D = 1$.

$$\bar{F}_1 = \frac{2}{3}\rho g \zeta_a^2 \frac{D_1}{2} + \frac{2}{3\pi}\rho C_D D_1 \omega^2 \zeta_a^3 \tag{4.19}$$

4. The tendon area must be sufficient to prevent reaching the yield stress (σ_y), within a given safety factor (SF), for tensions up to twice the initial tension (F_t), as in Eq. 4.20. For the purposes of establishing designs, $SF = 2$ was assumed. This leads to a conservative design, accounting for one tendon being very near slack, and with a high safety factor compared to, for example, the API Recommended Practice 2T [78].

$$\frac{2F_t}{A_t} \leq \frac{\sigma_y}{SF} \tag{4.20}$$

5. $\Delta \geq 2000$ m^3, based on preliminary results that indicated that a minimum displacement may be required to survive extreme wind and wave conditions [153]. A minimum displacement increases both the stiffness of the system, due to higher pretension, and its ability to mitigate extreme loads by platform inertia.

Inherent stability during the float-out phase was not a design requirement in this work. Additionally, the important coupled pitch/tower bending and roll/tower bending modes of the TLPWT system could not be predicted by the spreadsheet calculations. Further constraints on the natural periods should consider 1p and 3p excitation. During normal operation, the maximum f_{1p} is approximately 0.2 Hz, while the minimum f_{3p} approximately 0.37 Hz. In order to avoid both first-order wave and 3p excitation, the first coupled pitch/bending mode should then ideally fall between 2.7 s and 3.5 s. Nonetheless, structures with natural periods between 2.7 s and 3.5 s may still be susceptible to second, third, and higher order wave loads.

4.1.4 Resulting TLPWT Designs

Table 4.2 and Fig. 4.2 present the five baseline designs (in order of decreasing displacement) which resulted from the spreadsheet design procedure with the given design criteria. These designs were not optimized, but were were intended to represent a range of possible geometries.

The first design (TLPWT 1) was based on the MIT/NREL design described in Denis Matha's master's thesis [12]. The mass matrix was significantly modified, however, due to the different steel mass estimation method, and the tendon arrangement was simplified such that only one tendon was considered on each pontoon. In order to satisfy design criteria 3 and 4, the tendon stiffness was increased compared to the MIT/NREL design. TLPWT 1, which had the largest displacement by far, depended almost exclusively on the center column for buoyancy. Furthermore, TLPWT 1 was the only design that would be stable in tow-out, including the wind turbine and appropriate water ballast in the pontoons and center column to achieve the design draft.

TLPWT 2 was a 3-legged platform with approximately 60 % of the displacement and 70 % of the initial tendon tension of the first design. Approximately 30 % of TLPWT 2's displacement came from the pontoons, making it unstable for tow-out.

The hull of TLPWT 3 was an approximately half-scale version of the original Sea Star oil platform [149]. Somewhat higher initial tendon tension

Table 4.2: Baseline designs (water depth 150 m)

	TLPWT 1	TLPWT 2	TLPWT 3	TLPWT 4	TLPWT 5
Pontoons	Rect.	Rect.	Rect.	Rect.	Round
D_1 (m)	18.0	14.0	14.0	6.5	6.5
D_2 (m)	18.0	14.0	14.0	10.0	6.5
h_1 (m)	52.6	40.0	26.0	33.0	23.0
h_2 (m)	2.4	5.0	6.0	6.0	5.0
r_p (m)	27.0	32.0	28.0	25.0	32.5
h_p/w_p or d_p (m)	2.4/2.4	5.0/5.0	6.0/6.0	6.0/6.0	5.0
BF	0.55	0.6	0.4	0.4	0.4
n_p	4	3	3	4	3
z_s	-43.8	-32.5	-19.0	-19.0	-15.5
d_t (m)	1.4	1.1	1.3	1.2	0.9
t_t (mm)	46.2	36.3	42.9	39.6	29.7
Steel mass (tonnes)	2 322	1 518	1 293	859	505
∇ (m^3)	11 866	7 263	5 655	4 114	2 320
F_t (kN)	6 868	4 963	8 262	5 556	3 384

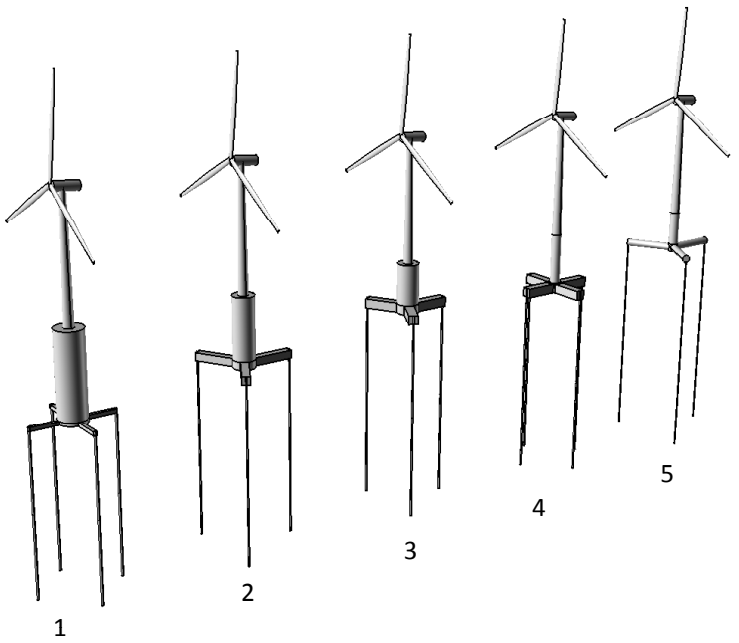

Figure 4.2: Baseline designs (water depth 150 m)

was required to satisfy the third criterion. Approximately 60 % of the displacement came from the center column, with the rest coming from the pontoons. Although TLPWT 3 had approximately half of the displacement of TLPWT 1, the pretension per line was significantly higher.

The fourth and fifth designs were inspired by the GLGH design [34], with some adaptations to support the OC3 wind turbine and satisfy the design criteria. The pontoons provided approximately 70 % of the displacement, and the upper center column diameter was equal to the tower base diameter. The small column diameter was intended to make the structures more transparent to waves, but the low displacement also made TLPWTs 4 and 5 more sensitive to extreme conditions. TLPWT 4 had approximately twice the displacement and total pretension of TLPWT 5, but employed 4 rectangular pontoons instead of 3 round ones. The UMaine TLPWT design falls in between these two designs in terms of displacement and pretension, but has more flexible tendons.

4.1.4.1 Hydrodynamic Coefficients

After establishing the designs based on the spreadsheet analysis, the first-order potential for each baseline TLPWT hull was computed using the 3D panel capability in the Wadam software, which is based on the well-known WAMIT software [154]. In the case of TLPWT 1, the pontoons were not included in the potential flow model, leading to near zero yaw added mass. All other TLPWT potential flow models included the pontoons. The added mass and radiation damping coefficients obtained for each TLPWT hull are shown in Fig. 4.3.

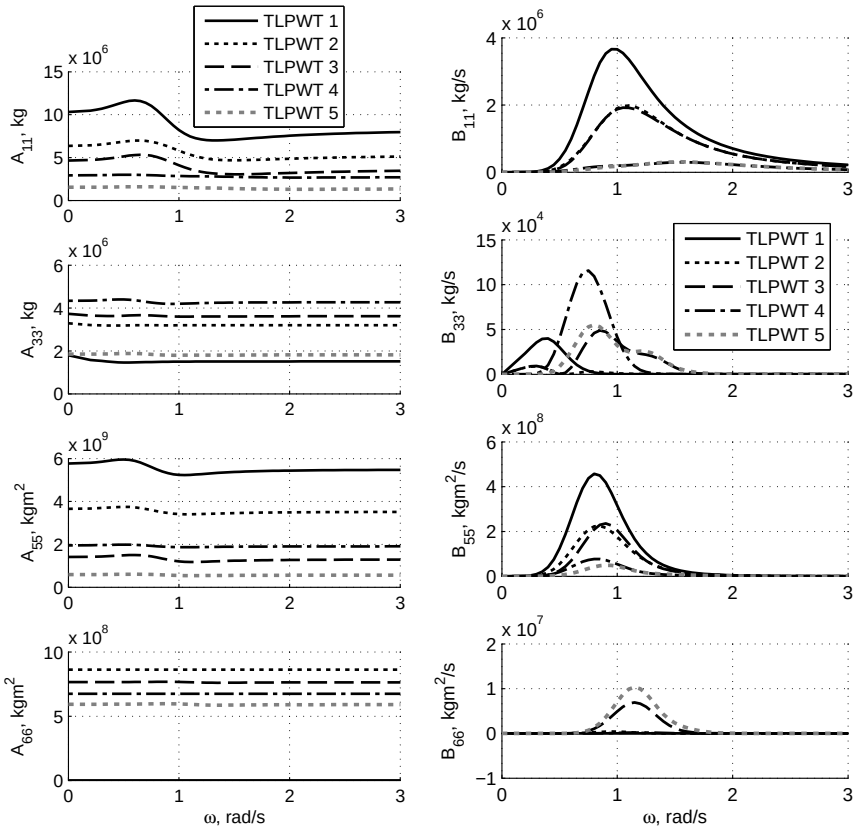

(a) Added mass (b) Damping

Figure 4.3: Added mass and radiation damping coefficients in surge, heave, pitch, and yaw for the baseline designs

As shown, there is some frequency variation in the surge added mass coefficients, and more significant frequency dependence in the damping co-

efficients. The linear radiation damping is small compared to the quadratic viscous damping added to the model using the Morison formulation, and approaches zero for both high and low frequencies.

The first-order wave excitation based on the potential flow solution is shown in Fig. 4.4. The maximum surge force coincides with typical wave frequencies and increases with increasing waterline diameter, while the maximum heave force occurs for very low frequencies. There is very little first-order forcing above 2 rad/s.

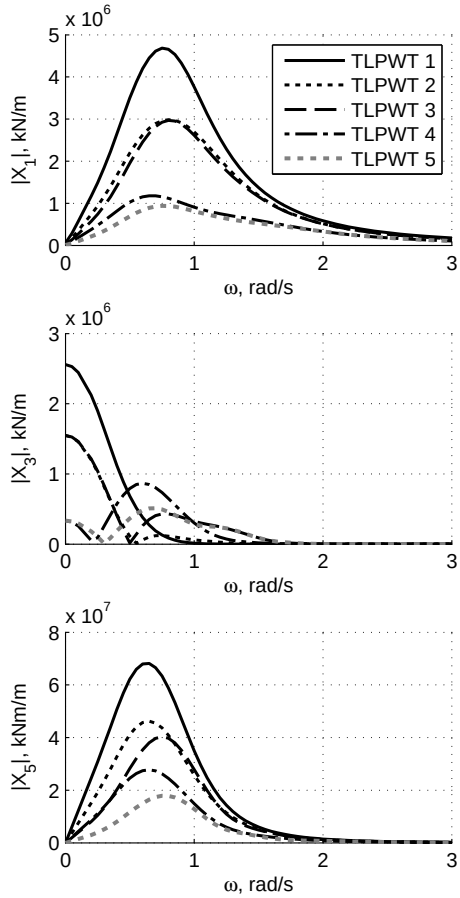

Figure 4.4: First-order wave force excitation amplitude per unit wave amplitude in surge, heave, and pitch for the baseline designs

4.1.4.2 Natural Periods

Next, the natural periods of the floating system were estimated with varying degrees of accuracy, as shown in Table 4.3. In the spreadsheet design process (column 1 in Table 4.3), the entire structure was assumed to be rigid, with 6 decoupled degrees of freedom, and the added mass was estimated based on the component diameters and lengths. A slight improvement to this model (column 2) used the calculated added mass at the estimated natural frequency from panel model results with additional estimates for the added mass of slender hull elements, but neglected off-diagonal terms in the system matrices. A further improvement (column 3) used the NREL BModes program [155] with the calculated added mass terms. Finally, in the FEM model (column 4), the TLPWT was released from an offset position in each rigid body mode of motion and the natural frequency was computed from the decaying motion. The first two coupled platform pitch-tower bending modes are reported for methods which included the tower flexibility (that is, the BModes and FEM models).

The linear estimates gave good approximations of the surge, heave, and yaw natural frequencies. Some discrepancies in the yaw natural period can still be seen: the linear model does not include the tether mass or added mass. In some cases, the "uncorrected" estimated added mass gave a coincidentally good approximation to the FEM model due to overprediction of the pontoon added mass.

The flexibility of the tower had a significant effect on the pitch mode of motion [12]. Two platform pitch/tower bending modes were generally present in the response, as shown for TLPWT 3 in Fig. 4.5. Several frequencies are clearly present in the response, with the high-frequency motions decaying much faster than the first mode. The BModes model tended to overpredict the first pitch frequency compared to the SIMO-RIFLEX-AeroDyn model, but provided a reasonable approximation of the first two pitch-bend mode shapes.

Furthermore, as shown in Table 4.3, the baseline TLPWT designs all had similar pitch-bending natural periods as a consequence of criterion 4 in Section 4.1.3. Due to the large tendon axial stiffness, and the resulting stiffness in platform pitch (rigid modes <1.5 s), the tower-nacelle-rotor modes dominated, giving all of the TLPWTs pitch/bend periods near 2.8 s. Note that this study considered the hull to be a rigid structure, but the flexibility of the hull (particularly the pontoons) may change the natural frequency in heave as well as pitch [34].

In order to examine the effects of the pitch-bending natural period on certain responses, additional "soft" versions of the first four designs were

Table 4.3: Natural periods according to uncoupled and coupled models. RB: rigid body. Est. A: estimated added mass (spreadsheet). Calc. A: panel model added mass with corrections for slender hull elements and tethers. FEM: Simo-Riflex-AeroDyn model with zero wind. The first two coupled platform pitch-tower bending modes are reported for methods which included the tower flexibility.

	TLPWT	Uncoupled (RB + Est. A)	Uncoupled (RB + Calc. A)	Coupled (BModes) (flex tower + Calc. A)	FEM (decay)
Surge (s)	1	57.09	55.38	55.33	55.78
	2	53.18	52.94	52.88	53.13
	3	41.19	41.68	41.60	41.86
	4	33.13	33.06	32.96	34.22
	5	38.56	38.93	38.73	40.13
Heave (s)	1	0.55	0.55	0.55	0.55
	2	0.73	0.74	0.74	0.75
	3	0.58	0.59	0.59	0.60
	4	0.49	0.51	0.51	0.52
	5	0.59	0.59	0.59	0.60
Pitch (s)	1	1.32	1.25	2.16/0.55	2.79/0.51
	2	1.19	1.14	2.19/0.53	2.81/0.48
	3	0.87	0.86	2.15/0.43	2.76/0.39
	4	0.93	0.92	2.14/0.44	2.74/0.39
	5	0.93	0.93	2.10/0.44	2.69/0.39
Yaw (s)	1	11.73	11.72	11.76	13.99
	2	17.28	16.34	16.36	17.97
	3	17.87	16.42	16.44	18.63
	4	19.64	17.43	17.48	19.71
	5	20.61	19.34	19.39	21.76

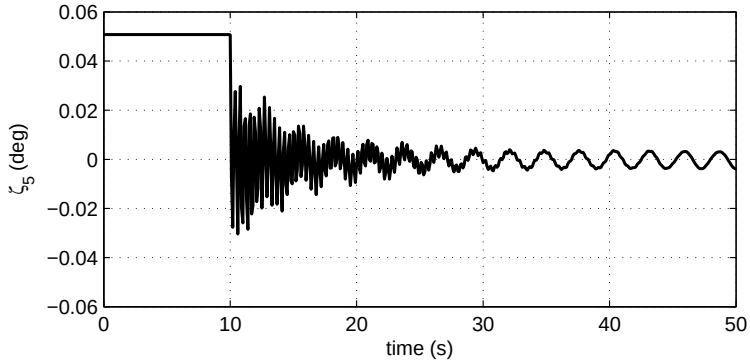

Figure 4.5: TLPWT 3 pitch decay (FEM model).

created by arbitrarily modifying the tendon elasticity: the Young's modulus of the tendons was modified without otherwise changing the design. The natural periods of the soft designs are given in Table 4.4.

Table 4.4: Young's modulus and natural periods of the "soft" TLPWT designs. Natural periods were obtained by decay tests in the FEM model.

TLPWT	E_t (Pa)	Surge (s)	Heave (s)	Pitch (s)	Yaw (s)
1 soft	4.0×10^{10}	55.80	1.26	3.15/1.03	14.05
2 soft	2.3×10^{10}	53.16	2.24	3.79/1.07	18.07
3 soft	1.5×10^{10}	42.00	2.21	4.10/0.96	18.65
4 soft	1.5×10^{10}	34.24	1.94	4.27/0.87	19.83

In addition to the platform natural frequencies, the tendon and blade natural frequencies may be of interest. The transverse and axial tendon natural periods for the baseline and soft TLPWT designs were calculated as in Sec. 3.1.5, treating the tendons as pinned-pinned beams and neglecting the rest of the platform. These analytical tendon periods are shown in Table 4.5.

The axial tendon periods were much shorter than the platform heave periods and were not generally important for the response, although they could be present in the case of snatch loads traveling along the tendon. Some of the transverse tendon modes were close to the combined platform pitch and tower bending modes. These modes interacted with pitch/bending modes, but were unlikely to be excited by motions at the surge natural

Table 4.5: Tendon natural periods for the baseline and "soft" TLPWT designs (analytical results for a pinned-pinned beam in tension with transverse added mass coefficient $C_a = 1$).

TLPWT	T_{axial} (s)	$T_{trans_{(1)}}$ (s)	$T_{trans_{(2)}}$ (s)	$T_{trans_{(3)}}$ (s)	$T_{trans_{(4)}}$ (s)
1	0.042	3.048	0.938	0.438	0.251
2	0.046	3.403	1.254	0.630	0.373
3	0.052	3.873	1.374	0.678	0.390
4	0.049	3.995	1.374	0.668	0.390
5	0.053	4.677	1.837	0.957	0.577
1 soft	0.096	4.082	1.634	0.862	0.523
2 soft	0.140	3.929	1.854	1.136	0.773
3 soft	0.193	4.647	2.214	1.374	0.946
4 soft	0.183	4.935	2.330	1.430	0.973

frequency or at the wave frequency.

Bandpass-filtered time series of displacements from the platform pitch decay tests were used to examine the tower and tendon mode shapes. Results for TLPWT 3 are shown here as an example. First, as shown in Fig. 4.6, the two primary tower modes were obtained by filtering around the main frequencies that are visible in the platform pitch motion. In Fig. 4.6, the motion of the tower base due to the pitch motion of the platform is visible at the lowest point on the tower. The mode shapes are clearly affected by both the platform motion and the rotor and nacelle mass.

The tendon mode shapes can be obtained in a similar manner, as shown in Fig. 4.7. The first, third, fourth, and fifth mode shapes are similar to the pure tendon vibration modes, including good agreement with the predicted frequencies. The second mode, which is not one of the natural modes of a pinned-pinned beam, corresponds to the first pitch-bend natural frequency, and can be seen to have a node at approximately 3/4 of the tendon length.

Looking at the tower and tendon together, and splitting the low- and high-frequency components based on the first two platform modes, the interaction between these modes is more obvious. Fig. 4.8 illustrates the combined modes. As shown, the fifth (four-noded) tendon mode was strongly present in the high-frequency response. The combination of mode shapes depended strongly on the TLPWT design. For the soft TLPWTs, increased tendon bending was observed at the lower modes, but the higher modes were generally less present in the response. Mode shape results for the other

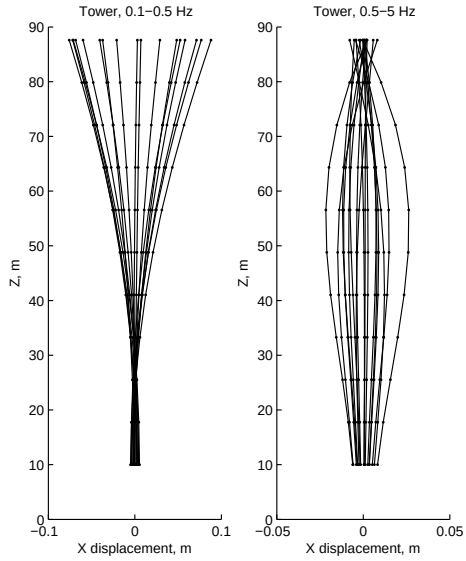

Figure 4.6: Tower bending modes for TLPWT 3 based on bandpassed time series from the pitch decay test

TLPWT designs are provided in Appendix A. The prominent transverse tendon natural periods observed in the decay tests are given in Table 4.6.

The natural periods of the blades are not easily obtained from the decay tests, but can be assumed to be relatively unchanged from the land-based turbine, since the first tower bending natural period is quite similar. Natural periods obtained by an eigenfrequency analysis of the land-based NREL 5 MW wind turbine are given in Table 4.7.

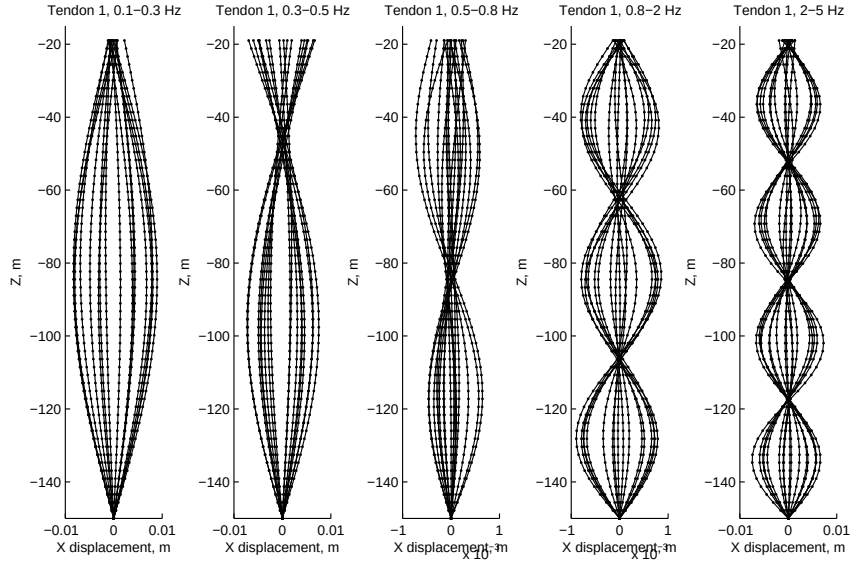

Figure 4.7: Tendon 1 bending modes for TLPWT 3 based on bandpassed time series from the pitch decay test

Table 4.6: Transverse tendon natural periods for the baseline and "soft" TLPWT designs based on platform pitch decay tests. Modes corresponding to the pitch/bending modes are included, and only modes which are clearly present in the decay test are listed.

TLPWT	$T_{trans_{(1)}}$ (s)	$T_{trans_{(2)}}$ (s)	$T_{trans_{(3)}}$ (s)	$T_{trans_{(4)}}$ (s)	$T_{trans_{(5)}}$ (s)
1	3.065	0.931	0.507	0.438	-
2	3.395	2.844	1.249	0.632	0.483
3	3.820	2.761	1.384	0.673	0.397
4	3.910	2.740	1.384	0.664	0.391
5	4.655	2.694	1.828	0.948	0.575
1 soft	4.131	3.152	1.020	0.871	-
2 soft	3.940	3.801	1.896	1.138	0.984
3 soft	4.650	4.101	2.204	1.380	0.948
4 soft	4.953	4.267	2.233	1.422	0.966

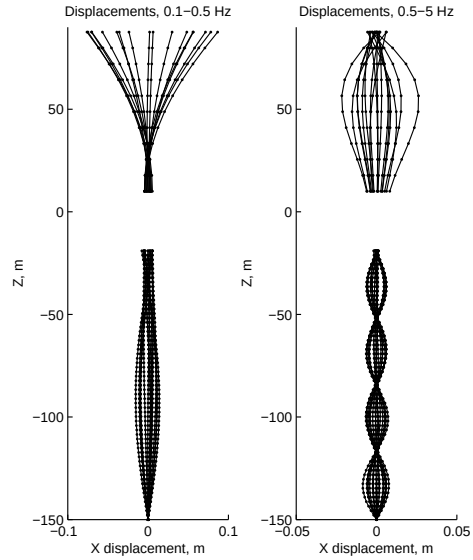

Figure 4.8: Tendon 1 and tower bending modes for TLPWT 3 based on bandpassed time series from the pitch decay test. Note that the x-location of tendon 1 is at +28.0 m.

Table 4.7: Rotor eigenperiods based on the land-based NREL turbine [72]. FAST and ADAMS results are taken from [72]; RIFLEX results were originally published in [60].

	RIFLEX (s)	FAST (s)	ADAMS (s)
1st Drivetrain Torsion	1.638	1.612	1.641
1st Blade Asym. Flapwise Yaw	1.580	1.501	1.588
1st Blade Asym. Flapwise Pitch	1.521	1.498	1.496
1st Blade Collective Flap	1.444	1.430	1.425
1st Blade Asym. Edgewise Pitch	0.935	0.927	0.931
1st Blade Asym. Edgewise Yaw	0.926	0.918	0.919
2nd Blade Asym. Flapwise Yaw	0.594	0.517	0.606
2nd Blade Asym. Flapwise Pitch	0.547	0.520	0.539

4.1.4.3 Linear and Quadratic Damping Ratios

For the baseline and soft designs, the linear and quadratic damping ratios were estimated from the decay tests as described in Sec. 3.1.4.4. The values of the coefficients b_1 and b_2 (linear and quadratic damping in Eq. 3.19, respectively) for surge, heave, and yaw are given in Table 4.8. The damping in surge and yaw is best described as quadratic damping: the viscous forces on the center column and pontoons were much larger than the linear potential damping, particularly for low frequencies. The high-frequency heave motion has a more linear decay. Damping coefficients for the coupled pitch-bending modes are not presented due to the difficulty in accurately fitting coefficients from the filtered data series.

Table 4.8: Linear and quadratic damping coefficients (see Eq. 3.19) based on decay tests for baseline designs (TLPWTs #1-5) and soft designs (TLPWTs #1-4 soft). Decay tests were performed in still water, with no wind, with a parked turbine. The presented coefficients depend on the platform size and natural frequency.

	#	b_1 (rad/s)	b_2 (1/m or 1/deg)	#	b_1 (rad/s)	b_2 (1/m or 1/deg)
Surge	1	2.81×10^{-4}	1.76×10^{-2}	1 soft	2.70×10^{-4}	1.77×10^{-2}
	2	3.79×10^{-4}	2.10×10^{-2}	2 soft	3.83×10^{-4}	2.10×10^{-2}
	3	2.78×10^{-2}	1.62×10^{-2}	3 soft	2.75×10^{-2}	1.78×10^{-2}
	4	2.10×10^{-3}	3.08×10^{-2}	4 soft	2.10×10^{-3}	3.07×10^{-2}
	5	1.81×10^{-4}	2.15×10^{-2}			
Heave	1	1.33×10^{-1}	4.42×10^{-3}	1 soft	3.24×10^{-2}	3.05×10^{-4}
	2	7.47×10^{-2}	8.02×10^{-3}	2 soft	4.18×10^{-2}	1.05×10^{-4}
	3	1.17×10^{-1}	8.81×10^{-3}	3 soft	4.67×10^{-2}	1.01×10^{-4}
	4	1.55×10^{-1}	1.18×10^{-2}	4 soft	7.84×10^{-2}	1.36×10^{-2}
	5	1.18×10^{-1}	7.96×10^{-4}			
Yaw	1	1.62×10^{-3}	2.45×10^{-2}	1 soft	2.02×10^{-3}	2.42×10^{-2}
	2	1.22×10^{-3}	2.74×10^{-2}	2 soft	1.55×10^{-3}	2.66×10^{-2}
	3	1.18×10^{-3}	2.38×10^{-2}	3 soft	1.18×10^{-3}	2.41×10^{-2}
	4	1.04×10^{-3}	2.35×10^{-2}	4 soft	1.03×10^{-3}	2.40×10^{-2}
	5	5.85×10^{-4}	2.03×10^{-2}			

4.1.4.4 Tendon Yield Loads

Table 4.9 shows the axial yield load (P_y, assuming $\sigma_y = 250$ MPa) for the baseline and soft designs. Note that the yield loads for the soft designs depend on the arbitrary reduction of the Young's modulus and do not reflect real physical material characteristics.

Table 4.9: Tendon yield loads

TLPWT	P_y (kN)	TLPWT	P_y (kN)
1	4.745×10^4	1 soft	4.745×10^4
2	2.929×10^4	2 soft	2.929×10^4
3	4.091×10^4	3 soft	4.091×10^4
4	3.485×10^4	4 soft	3.485×10^4
5	1.961×10^4		

4.1.4.5 Cost Estimates

A simplified cost comparison for the baseline TLPWT hulls was performed following Crozier's model, as in Table 4.10 [38]. This simple model considers upper and lower multiplicative factors for the steel mass, concrete ballast mass, and tendon pretension (indicative of anchor system cost). The resulting values are crude estimates for comparing different designs which support the same wind turbine. The cost model results for the baseline designs and several of the published designs are shown in Fig. 4.9. It should be noted that the estimates applied in this model are outdated. While these estimates give generally low estimates of the overall cost, the relative contributions of the different components and the resulting total estimates for different concepts can still be compared.

Table 4.10: Cost estimation model, including lower and upper estimates.

	Lower Estimate	Upper Estimate	
Steel Mass (hull and tendons)	600	800	\$/tonne
Concrete Ballast Mass	50	150	\$/tonne
Tendon pretension	15	25	\$/kN

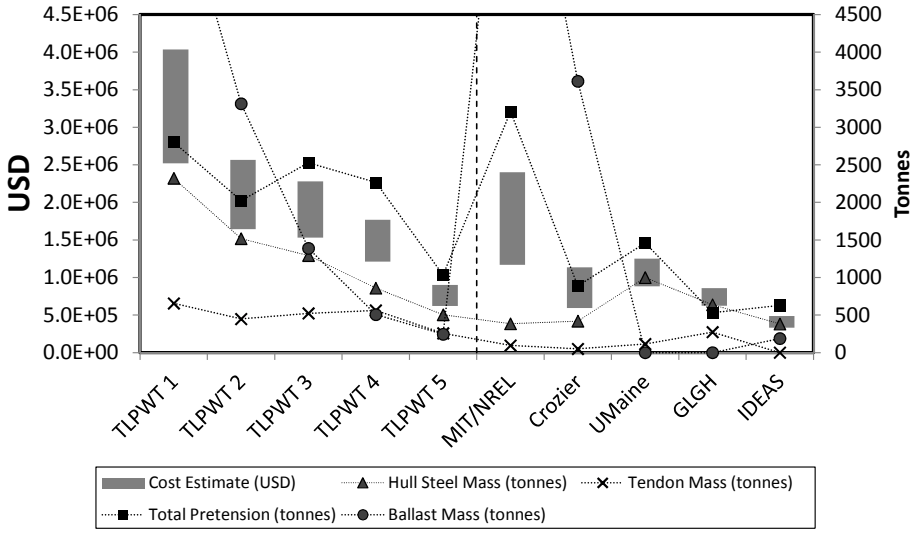

Figure 4.9: Hull and tendon simplified cost estimates, including weight/pretension breakdown, for the baseline designs and selected published designs for TLPWTs supporting a 5 MW turbine. The ballast mass is 6456 tonnes for TLPWT 1 and 8220 tonnes for MIT/NREL.

The construction cost estimates for TLPWTs 1-5 (and parametric variations) were approximately linearly dependent on the displacement. The recomputed costs of the published platform designs also depended on displacement, but were found to be more variable due to differences in assumptions about hull scantlings and tendon weight per length. For example, the MIT/NREL hull design assumes an equivalent hull thickness of only 0.015 m, while the mass model in Table 4.1 gave an average hull thickness of more than twice that. Thus, despite the fact that the geometries and displacements of TLPWT 1 and MIT/NREL are similar, the cost estimates differed significantly due to the large differences in steel mass. Neither installation nor maintenance costs were estimated, but TLPWT 1 was the only self-stable construction among the new TLPWT designs, and can therefore be expected to be somewhat easier to install than TLPWTs 2-5.

4.1.5 Conclusions

Based on the assumed design space (single column TLPWTs supporting the NREL 5 MW wind turbine with the OC3 Hywind tower design [72, 26]),

a simple spreadsheet analysis was used to create designs. The accepted designs met certain criteria for natural periods, estimated mean offset, displacement, and tendon strength.

An important weakness in the spreadsheet design approach was the assumption of a fully rigid structure: the coupled pitch/bending natural frequency could not be estimated. After selecting several baseline designs, a more detailed hydrodynamic and structural analysis was performed. Decay tests of the full structure showed that the flexibility of the tower and tendons created additional important natural frequencies. Simplified cost estimates suggested that the construction cost could be minimized by decreasing the displacement.

Furthermore, the design criteria required very stiff tendons. In order to obtain greater variety in the concepts, "soft" versions of the baseline designs were generated by arbitrarily changing the material properties of the tendons. While these designs are non-physical, their natural periods are representative of other designs in the literature, making them useful for testing the analysis tool.

The performance of the baseline designs, and of parametric variations on these designs, is examined in Sec. 4.2.

4.2 Effects of Parameter Variation on TLPWT Behavior

Comparisons of TLPWT designs are presented in this section and published in [156]. The baseline designs are compared, and parametric variations on these designs are introduced. For the baseline designs, comparisons were made based on 36 x 0.5 hour simulations using SIMO-RIFLEX-AeroDyn, treating the results as 6 x 3 hour simulations for statistical purposes. For the parametric variations on the designs, 6 x 0.5 hour simulations were applied, with the same wind and wave input for all designs. The baseline and extended baseline environmental conditions from Tables 3.6 and 3.7 were applied. The soft TLPWT designs were not included in this study.

First, the performance comparison parameters are described in Sec. 4.2.1. Then, the baseline TLPWT designs from the previous section are studied in Secs. 4.2.2 and 4.2.3. Finally, the effects of parameter variations are examined in Sec. 4.2.4.

Additional figures to complement this section are provided in Appendix B.

4.2.1 Performance Comparison Parameters

Several representative parameters - platform motions (ζ_j, $j = 1-6$), fore-aft tower base bending moment (M_{FA}), side-side tower base bending moment (M_{SS}), and tendon tension in line i (T_i) - were taken as primary performance measures. The tendon tension T_1 refers to the downwind line. As this comparative study considered only aligned wind and wave loads, the surge, heave, and pitch motions and the fore-aft tower base bending moment were expected to be the most important. In turbulent wind conditions, however, both roll and yaw motion may be excited by time-varying torque and asymmetric wind loads. These rotations are coupled via the thrust force and are not subjected to aerodynamic damping. The power production (P) of the different designs was also examined, but the results indicated very little difference among the different designs in that respect. In this chapter, the standard deviation (σ) of these parameters in the different environmental conditions was used as the main comparison measure, rather than predicting extreme values or fatigue cycles.

4.2.2 Comparison of Baseline TLPWT Designs

First, the mean values (μ) of different performance indicators are shown in Fig. 4.10a. The mean values of surge and pitch, $\mu(\zeta_1)$ and $\mu(\zeta_5)$, depended on the mooring system stiffness as well as the wind and wave forcing. The

surge stiffness of TLPWT 5 was less than half that of TLPWTs 2-4 and approximately one-third of TLPWT 1. Because the mean wave force was small compared to the thrust force (or drag force for the parked case), $\mu(\zeta_1)$ was approximately inversely dependent on the stiffness, and varied more with wind speed than wave height. Similarly, $\mu(\zeta_5)$ was primarily dependent on the mooring system pitch stiffness and the moment due to the wind turbine thrust or drag. TLPWT 1 had the largest K_{55}, which was approximately 2.8 times the K_{55} of TLPWT 5, which had the softest mooring system. Because $\mu(\zeta_5)$ was small, $\mu(M_{FA})$ was not strongly affected by gravitational loading. As shown in Fig. 4.10a, $\mu(M_{FA})$ did not vary significantly among the designs.

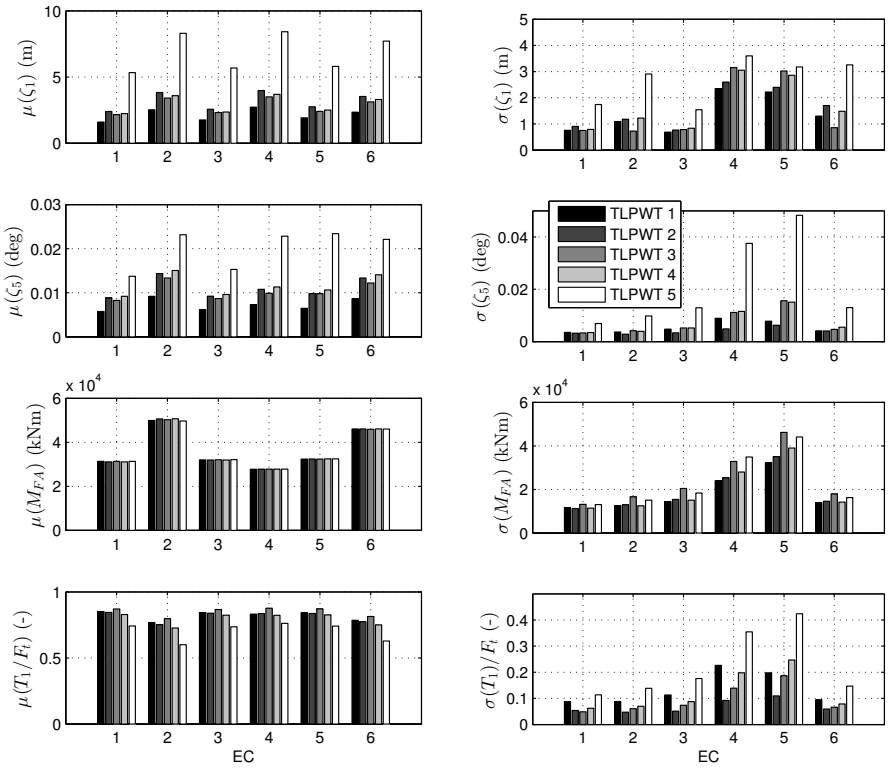

(a) Mean values (b) Standard deviations

Figure 4.10: Comparison of baseline TLPWT means and standard deviations for surge, pitch, tower base bending moment, and line tension

The mean tendon tension ($\mu(T_1)$, Fig. 4.10a) was not necessarily equal to the pretension (F_t), because $\mu(\zeta_1)$ increased the mean tendon tension in all

lines, while $\mu(\zeta_5)$ decreased the tension in the downwind line and increased the tension upwind. For line 1 (downwind), $\mu(T_1)$ can be approximated as:

$$\mu(T_1) \approx \frac{F_t}{\cos\theta_1} + \frac{\rho g D_1^2 \pi l_0 (1-\cos\theta_1)}{4 n_t \cos\theta_1} - \frac{E_t A_t r_p \sin\left(\mu(\zeta_5)\right)}{l_0 \cos\theta_1} \tag{4.21}$$

where $\theta_1 = \arcsin\left(\mu(\zeta_1)/l_0\right)$. The decrease in mean tension due to pitch was generally larger than the increase due to surge motion.

Fig. 4.10b provides an overview of the standard deviation of key performance indicators for the baseline designs in the six environmental conditions. While $\sigma(\zeta_1)$ was very similar for TLPWTs 1-4, it was somewhat higher (particularly around the rated wind speed in ECs 2 and 6, where the thrust force is at a maximum) for TLPWT 5. The low-frequency surge response was primarily excited by the wind, which was identical for all of the designs, and mitigated by platform inertia. While the surge response is not expected to be critical for the wind turbine performance or fatigue, large surge displacements may be critical for the tendon seabed connectors and the power cable due to large induced angles, and can also induce large tension variations due to set-down effects. Assuming that the tendon connectors are similar to those used in the offshore industry, for 150 m water depth, the maximum surge displacement should not exceed 15 m [14, Ch. 7.6.3].

Although $\sigma(\zeta_5)$ was quite small for all of the designs, TLPWT 5 showed significantly larger low-frequency (wind-induced) and wave-frequency response, the latter of which became increasingly important as the wave height increased. Comparing $\sigma(\zeta_5)$ in ECs 4 and 5, the operational turbine caused larger pitch motions than the parked case.

M_{FA} depended on the nacelle motions relative to the platform (gravitational loading), the thrust force, and the load transfer to hull inertia and tendon tension. As shown in Fig 4.10b, the platform pitch motions were not a good predictor of M_{FA}. Significant contributions to $\sigma(M_{FA})$ occurred in three frequency ranges: low-frequency (wind-induced), wave-frequency (wave-induced), and at the first coupled pitch-bending frequency (structural). As an example, the spectrum of M_{FA} for EC 2 is shown in Fig. 4.11. Fig. 4.11 is shown with a log scale on the vertical axis, such that many phenomena can be seen. Wave-frequency loading dominated M_{FA}, suggesting that dynamic inertial loads were important even though the TLPWT motions were small.

The wave-frequency tower bending moment, which varied most among the different designs, was least for TLPWTs 1, 2, and 4, while the loading

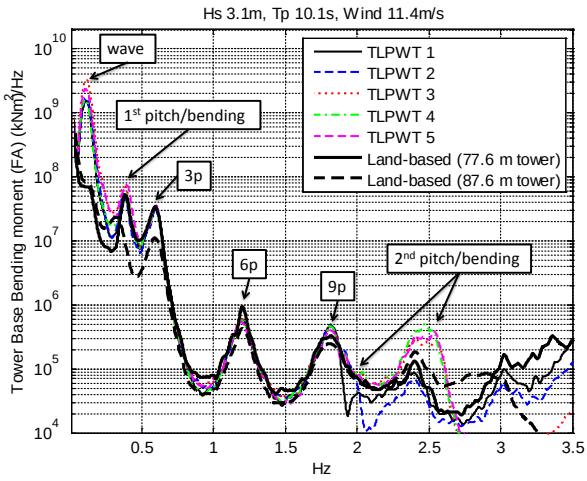

(a)

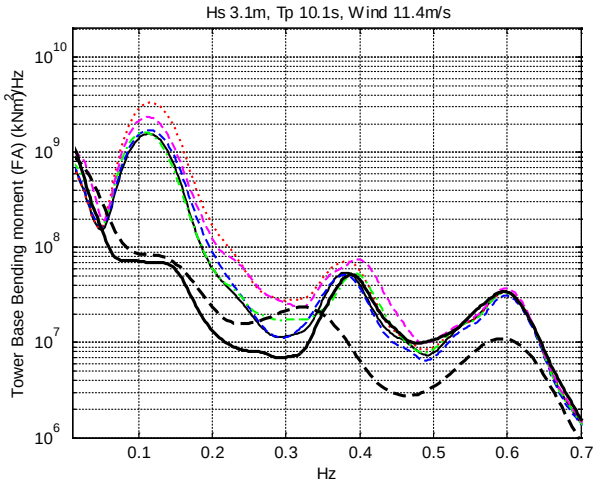

(b)

Figure 4.11: Spectrum of M_{FA} for EC 2 (TLPWTs 1-5 and land-based 5 MW turbine), including zoomed view around the wave frequency (b). Note that M_{FA} is measured 10 m above still water/ground level for all cases. Note log scale on the vertical axis.

near the natural period was more similar. Furthermore, the wave-frequency tower bending moment of TLPWT 3 was larger than expected based on the general trend toward smaller tower loading with increased displacement.

This may be related to the frequency dependence of the wave excitation of platform pitch: the wave forcing transfer function for TLPWT 3 had its peak at a higher frequency. EC 5 was also seen to be a critical load condition for M_{FA}, where the operating turbine increased the loading compared to EC 4.

The standard deviation of line 1 tension, $\sigma(T_1)$, is an important consideration when evaluating the probability of tendon slack and the fatigue life of the tendons. Fig 4.10b shows the standard deviation of the line tension as a fraction of the line pretension. Assuming tendon tension to be a Gaussian process, in order to avoid slack conditions, we require

$$\left([\mu(T_1) - k\sigma(T_1)]\,/F_t\right) > 0, \tag{4.22}$$

where the factor k should be chosen to represent an acceptable probability. Note that the mean tension is also an important factor in slack. The variation in T_1 did not appear to be very sensitive to the wind speed when the turbine was operating, but increased with the wave height in the extreme wave conditions, EC 4 and 5. Assuming a Gaussian distribution for the tendon tension, the probability of slack in EC 5 for TLPWT 5 is approximately 4.25 %, indicating that the design may require further modification.

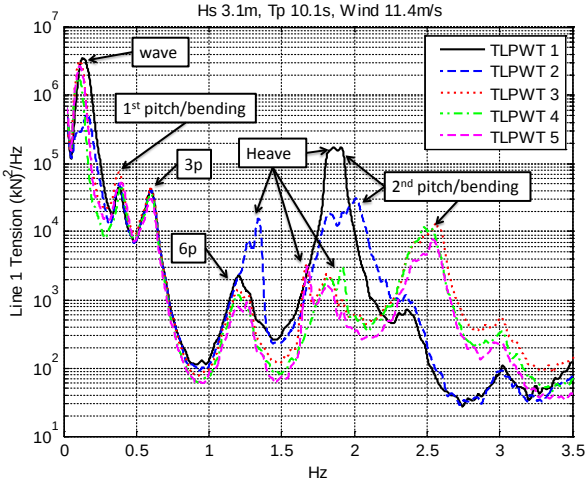

Figure 4.12: Spectrum of T_1 for EC 2.

Fig. 4.12 shows the spectral response of T_1 in EC 2, and highlights the components at the wave, structural, and wind turbine excitation frequencies. The wave-frequency components of T_1 dominated the response. As shown, the heave and second pitch/bending natural frequencies of TLPWT 1 were

very similar, which contributed to a larger peak in the spectrum of T_1. The wave-frequency tension variation for TLPWT 2 was significantly smaller than that of the other designs. As shown, the relative importance of the wind turbine rotation frequencies depended on the design.

In Appendix B, Fig. B.1 shows the coefficient of variation (σ/μ) for the key parameters shown in Fig. 4.10.

4.2.3 Comparison of Baseline Designs with the Land-based Turbine

Fig. 4.13 compares the means and standard deviations of M_{FA}, M_{Oop}, M_{Ip}, and P for the baseline TLPWT designs as a function of the land-based (77.6 m tower) turbine in the same wind conditions. The land-based results are indicated by the subscript f. (Note that the original land-based design is supported by an 87.6 m tower [72], but the OC3 Hywind tower [26] was modeled as though there were a rigid foundation at 10 m height for this comparison.) The results for the land-based turbine are summarized in Table 4.11.

Table 4.11: Fixed turbine with 77.6 m tower: mean and standard deviation of loads and power generation. (EC 5 and EC 3 results are identical).

		M_{FA_f} (kNm)	M_{Oop_f} (kNm)	M_{Ip_f} (kNm)	P_f (kNm)
EC 1	μ	31,299	5183	634	1911
	σ	10,744	1562	2572	800
EC 2	μ	50,910	8719	1265	4714
	σ	6888	1350	2586	487
EC 3	μ	31,970	4517	1316	5000
	σ	6708	1682	2628	33
EC 4	μ	27,741	335	-1339	0
	σ	12,401	424	1157	0
EC 5	μ	31,970	4517	1316	5000
	σ	6708	1682	2628	33
EC 6	μ	45,517	7740	1253	4670
	σ	11,240	2190	2609	698

As shown in Fig. 4.13, the mean bending moments at the tower base and at the blade root were nearly identical to those seen in the land-based turbine. For EC 4, the blade loads are given for the blade that started in a

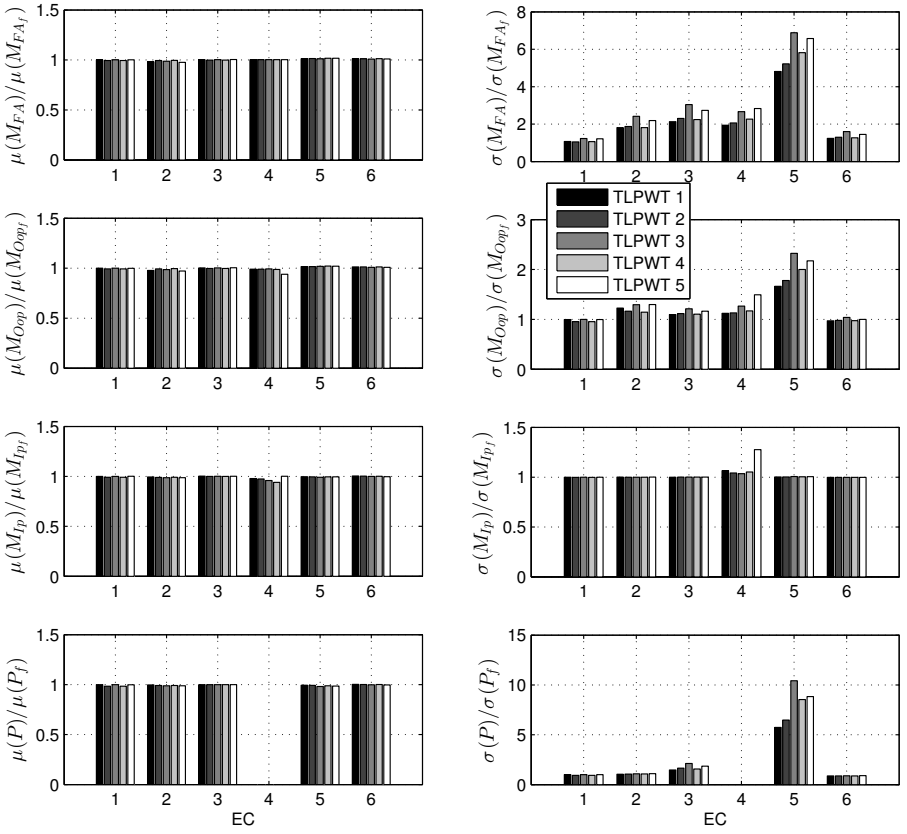

(a) Mean values (b) Standard deviations

Figure 4.13: Comparison of baseline TLPWTs and fixed turbine (77.6 m tower) loads and power generation. The land-based results are indicated by the subscript f.

vertically upward position. The mean power, $\mu(P)$, was also well-regulated by the controller and was not affected by the TLPWT motions.

The structural loading and power production were, however, more variable for the TLPWTs than for the land-based structure. The effect on the blade root moments was relatively small, but $\sigma(M_{FA})$ was significantly higher than in the land-based case, especially as the wind speed increased, and particularly in EC 5 where storm waves were encountered by an operating turbine. The increase in $\sigma(M_{FA})$ occurred at the wave-frequency, which has a lower encounter frequency than the primary bending moment variation for the land-based wind turbine. Other studies of TLPWTs indicate increased design equivalent loading on the order of 1.2 times that of the land-based tower [32]. Furthermore, in Fig. 4.13, the power variation appears to increase significantly in ECs 3 and 5, but it is important to note that $\sigma(P_f)$ is very close to zero (see Table 4.11), making a small increase in the absolute value appear as a large relative change.

4.2.4 Parameter Variations

After comparing the baseline designs, variations in the TLPWT hull diameters (D_1 and D_2 in Fig. 4.1), water depth (H), pontoon radius (r_p in Fig. 4.1), and ballast (BF) were considered. These variations directly affect the natural frequencies and (except for the ballast) the wave loads on the structure, but do not directly affect the wind loading. The range of displacements and total pretension represented by the different design variations is summarized in Fig. 4.14. The resulting natural periods are shown in Appendix B in Table B.1. As shown, the designs considered here are also representative of several published designs.

The trends in behavior observed for the variations are summarized in Table 4.12 and in the sections below. Note that, in Table 4.12, "improved performance" indicates decreased motions and loads. In addition to the results presented in this chapter, more detailed results for the effects of each parameter variation on the standard deviation in surge, pitch, yaw, M_{FA}, and T_1 are presented in Appendix B, Figs. B.2-B.6.

4.2.4.1 Diameter

The first two variations applied to the TLPWT designs were a 10 % increase and a 10 % decrease in the main column diameters, D_1 and D_2. An increase in the diameter by a factor λ increased the column displacement and mass by λ^2. A_{11}, A_{44}, and A_{55} also increased by λ^2, while A_{33} increased by λ^3. The resulting increase in inertia and pretension resulted in little net effect

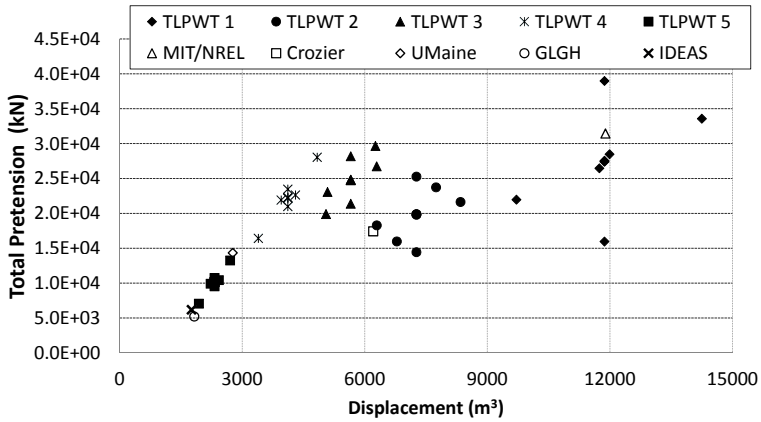

Figure 4.14: Total pretension vs. displacement for all of the TLPWT design variations, including comparisons with published designs [12, 32, 34, 36, 38].

Table 4.12: Effects of increases in D_1 and D_2, H, r_p, and BF on performance parameters. + indicates improved performance, - indicates decreased performance, and 0 indicates no clear trend, with more + or - symbols indicating stronger effects. Where the effect of increasing D_1 and D_2, H, r_p, or BF is dependent on the baseline design displacement (Δ) or wave condition (H_s), symbols are given in order of increasing Δ or H_s.

	D_1 and D_2	H	r_p	BF
$\sigma(M_{FA})$	- -	+ +	0	+ +
$\sigma(T_1/T)$	+	+/- (Δ)	+ + +	- -
$\sigma(M_{Oop})$	-	+ +	0	+ +
$\sigma(\zeta_1)$	0	+/- (Δ)	+/- (H_s)	+/- (H_s)
$\sigma(\zeta_5)$	+/- (Δ)	- - -	+ + +	+/- (Δ)
$\sigma(\zeta_4)$	+ +	- -	+ + +	- - -
$\sigma(\zeta_6)$	+ +	- -	+ + +	- - -

on the surge and yaw natural periods (see also Table B.1 in Appendix B). For the TLPWTs that did not depend heavily on the main column for displacement, changing the diameter by 10% had little effect on the natural periods. On the other hand, for a smaller platform that depended primarily on the column for displacement, the increase in pretension due to an increase in the D_1 and D_2 could be significant, particularly if the unchanging turbine

mass represented a significant component of the overall mass. The increase in volume, and particularly in the cross-sectional area at the waterline, due to an increase in D_1 also caused an increase in wave forces.

The effect of diameter changes on the surge motion depended heavily on the baseline concept and the environmental conditions, and did not show any clear trends (see also Fig. B.2a). For example, $\sigma(\zeta_1)$ increased 10-20 % in EC 1 and EC 3 for TLPWTs 2 and 3 for both a 10 % increase and a 10 % decrease in D_1 and D_2. The increased diameter resulted in longer surge natural periods, which were primarily excited by the wind forces, while the decreased diameter resulted in decreased pretension, and lower stiffness, which gave larger motion responses.

The effect on the pitch motions was also complicated. The increase in D_1 and D_2 resulted in 10-20 % increases in $\sigma(\zeta_5)$ for TLPWTs 1 and 2, and less than 10 % decreases in $\sigma(\zeta_5)$ for the other designs (Fig. B.3a). A corresponding decrease in D_1 and D_2 reduced the pitch motions of TLPWT 1, but slightly increased the pitch motions of the other designs. The effects on the roll and yaw motions were more consistent: an increase in D_1 and D_2 resulted in decreases in both $\sigma(\zeta_4)$ and $\sigma(\zeta_6)$ (Fig. B.4a).

Furthermore, the structural loading also showed varying degrees of sensitivity to D_1 and D_2. Although a 10 % decrease in D_1 and D_2 resulted in a consistent increase in $\sigma(T_1)$ of up to 10 % for TLPWTs 2 and 3, and smaller increases for the others, a corresponding increase in D_1 and D_2 had more mixed impacts on $\sigma(T_1)$ (Fig. B.6a). The increase in diameter decreased $\sigma(T_1)$ by 5-10 % for all of the designs except TLPWT 2, which showed up to 10 % more tendon tension variation, particularly in ECs 3 and 4. The variation in D_1 and D_2 resulted in less than 5 % change in $\sigma(M_{FA})$, with an overall increase (decrease) in $\sigma(M_{FA})$ for increased (decreased) D_1 and D_2 (Fig. B.5a).

Note, however, that these effects only include first-order hydrodynamic loads; second- and third-order wave forces also depend on D_1 and D_2.

4.2.4.2 Water Depth

TLPWT platforms are most likely to be considered for water depths between 80 m (an approximate upper limit for bottom-fixed platforms) and 200 m (where spar platforms are likely to have economic advantages). The performance of the baseline designs was examined for 100 m and 200 m water depths, in addition to the design depth of 150 m. No structural changes were implemented other than shortening or lengthening the tendons. Increasing the water depth did not affect Δ or $\boldsymbol{M}$, and the effect on added mass and wave forcing was negligible. There was, however, a decrease in

tendon stiffness due to the increased line length. Due to the decrease (increase) in k_{11} in Eq. 4.8, the natural periods in surge/sway, heave, and yaw increased (decreased) significantly when the water depth increased from 150 to 200 m (decreased from 150 to 100 m). The coupled pitch/bending natural periods remained relatively unchanged, since K_{55} (Eq. 4.12) was still large compared to the tower bending stiffness. Note that the change in stiffness due to increased water depth is not equivalent to the change in stiffness applied to obtain the "soft" designs. The natural periods of the parametric variations are shown in Table B.1.

In lower sea states (ECs 1, 2, 6), $\sigma(\zeta_1)$ tended to increase with increasing water depth, but this trend was reversed as the wave height increased (Fig. B.2b). Similarly, due to the decreased pitch stiffness, $\sigma(\zeta_5)$ increased with increasing water depth (Fig. B.3b). The pitch motions in 200 m water depth were approximately 50 % greater than in 100m for several designs. The rotations about other axes, $\sigma(\zeta_4)$ and $\sigma(\zeta_6)$, behaved similarly to $\sigma(\zeta_1)$ with respect to water depth. These motions, which can contribute to increased power variability and wind turbine component fatigue, should be carefully examined, particularly for deeper water.

Despite the decrease in $\sigma(\zeta_5)$, $\sigma(M_{FA})$ increased 5-10 % in the 100 m water depth (Fig. B.5b). Inertia forces took up more of the wind and wave forcing in deeper water (200 m), while the structural reactions became more important in shallow water (100 m). The tendon tension was also fairly sensitive to the decrease in water depth: $\sigma(T_1)$ increased by approximately 20 % for TLPWTs 2-5 in 100 m for ECs 3 and 4, while $\sigma(T_1)$ decreased by roughly 10 % for TLPWT 1 (Fig. B.6b). On the other hand, $\sigma(T_1)$ did not change as much when the water depth was increased to 200 m. There was an approximately 3-8 % increase in $\sigma(T_1)$ for TLPWTs 1 and 2, a 2-3 % decrease for TLPWTs 3-4, and a 3-5 % decrease for TLPWT 5.

4.2.4.3 Pontoon Radius

The effects of changing the pontoon radius (r_p, the distance from the main column center to the tendon fairlead) by 20 % depended on the baseline design. For the designs that depended primarily on the main column for displacement, an increase in r_p shortened T_{n6} (due to the increased stiffness) and slightly shortened the coupled pitch-bending periods, with little effect on T_{n1} (Table. B.1). For designs that depended heavily on the pontoons for displacement, the increase in Δ often outpaced the increase in mass (particularly when the turbine and ballast mass were significant compared to the steel mass), resulting in higher pretension and shorter surge and yaw natural periods. T_{n3} was slightly longer due to the increase in mass and

added mass with no change in the tendon axial stiffness.

Variations in r_p had clear effects on the pitch motions, tendon tension, and out-of-plane rotations. Even for the designs that did not depend heavily on the pontoons for buoyancy, a significant reduction (25-40 %) in pitch motion was achieved by increasing r_p by 20 %, while an even more significant (50-100 %) increase in $\sigma(\zeta_5)$ occurred for a corresponding decrease in r_p (Fig. B.3c). The increase in r_p also reduced $\sigma(T_1)$ by up to 20 %, while a 20 % decrease in pontoon radius resulted in up to a (roughly) 50 % increase in $\sigma(T_1)$ (Fig. B.6c). The out-of-plane motions were very sensitive to r_p: the 20 % increase in r_p reduced $\sigma(\zeta_4)$ and $\sigma(\zeta_6)$ by 40-50 %, indicating that this may be an effective method to improve the yaw stability (Fig. B.4c).

The extent of the effects of varying r_p on $\sigma(\zeta_1)$ and $\sigma(M_{FA})$ depended more on the TLPWT design and environmental conditions. The increased surge stiffness due to the buoyancy increase tended to reduce the surge motions in ECs 1, 2 and 6, but the benefit of the added stiffness decreased as the wave height and period increased. An increase in r_p led to larger $\sigma(\zeta_1)$ in ECs 4 and 5 for almost all of the designs (Fig. B.2a). The effects of r_p on $\sigma(M_{FA})$ were small (less than 2 %), even for TLPWTs 4 and 5, which had the largest changes in displacement (Fig. B.5c, and note that the remarks on TLPWT 5 do not consider a decrease in r_p, only an increase).

4.2.4.4 Ballast Fraction

An increase in the ballast fraction (BF) represents a larger quantity of concrete permanent ballast in the main column, without any change in geometry. That is, the mass and inertia increase and the pretension decreases. This results in both an increase in mass and a decrease in stiffness (k_{11} in Eq. 4.8 decreases due to the decreased pretension). An increase in BF does not affect the hydrodynamic added mass, damping, or wave excitation forces. The system natural frequencies decrease as BF increases.

The effects of the changes in BF on the surge, heave, and pitch did not show a clear trend. An increase in ballast resulted in up to 70 % larger $\sigma(\zeta_1)$ - particularly for TLPWTs 1 and 2 - in the lower seastates, but reduced $\sigma(\zeta_1)$ for ECs 4 and 5 (Fig. B.2d). The ballast increase had variable effects on $\sigma(\zeta_5)$: increasing BF increased the pitch motions of TLPWT 1 and 5 the most, slightly increased $\sigma(\zeta_5)$ for TLPWT 2, and reduced $\sigma(\zeta_5)$ for TLPWT 3 and 4 (Fig. B.3d). Overall, the wind- and wave-aligned motions of the designs with the largest ballast fractions (1 and 5) were also most improved by decreasing BF by 0.1.

Clearer trends in $\sigma(\zeta_4)$ and $\sigma(\zeta_6)$ were noted (Fig. B.4d). These rotations increased significantly (up to 70 % for TLPWT 1) when BF increased,

indicating that increased stiffness is more effective than increased inertia in reducing $\sigma(\zeta_4)$ and $\sigma(\zeta_6)$.

Increasing BF resulted in a more distinct increase in $\sigma(T_1)$ and a small but distinct decrease in $\sigma(M_{FA})$ (Figs. B.5d and B.6d). The increase in $\sigma(T_1)$ may be related to the corresponding decrease in F_t: designs with larger pretension tended to have less tension variation. TLPWT 1 was most affected by the increase in BF with almost 80 % increase in $\sigma(T_1)$ in ECs 4 and 5. The up to 8 % decrease in $\sigma(M_{FA})$ associated with increased BF indicated that the increased mass allowed more of the environmental forces to be taken up by inertia. A reduction in BF gave corresponding decreases in $\sigma(T_1)$ and increases in $\sigma(M_{FA})$.

4.2.5 Design Trends

By examining the results for all of the parametric variations, it was possible to identify some design trends that can be used to guide further TLPWT development.

The natural periods of the structure should be chosen carefully to improve the performance. For example, Fig. 4.15 indicates that $\sigma(\zeta_1)$ in operational conditions increased with longer surge natural periods, but decreased in the extreme condition. T_{n1} did not have a large effect on T_1, but the designs with longer surge periods also tended to have decreased $\sigma(M_{FA})$.

Within the range of observed heave periods (0.4 to 0.9 seconds), there was no strong trend relating $\sigma(T_1)$ or $\sigma(M_{FA})$ to T_{n3}. It may be more important to consider the relationship between the T_{n3} and T_{n5} in order to mitigate tendon loading, rather than tuning the T_{n3} independently.

Reducing T_{n6} tended to decrease the yaw and roll motions, as shown in Fig. 4.16 for $\sigma(\zeta_6)$. Because the mean values of yaw and roll were nearly zero, changes in T_{n6} primarily affected the standard deviations. This result agrees with the reduction in yaw motion when r_p was increased. In terms of tower loading, however, T_{n6} did not appear to have a significant influence on M_{SS}.

The range of pitch/bending natural frequencies in this study was very small. A trend toward less pitch motion for longer T_{n5} was observed, but except in the storm conditions EC 4 and 5, $\sigma(M_{FA})$ was not significantly reduced by increasing T_{n5}.

In addition to natural frequencies, overall sizing considerations are a critical aspect of TLPWT design. The results did not show any important trends based on D_1 and D_2 alone, but the choice of displacement and total pretension was important for the variation in T_1. As shown in Fig 4.17, $\sigma(T_1)$ decreased as the total pretension increased, particularly when results

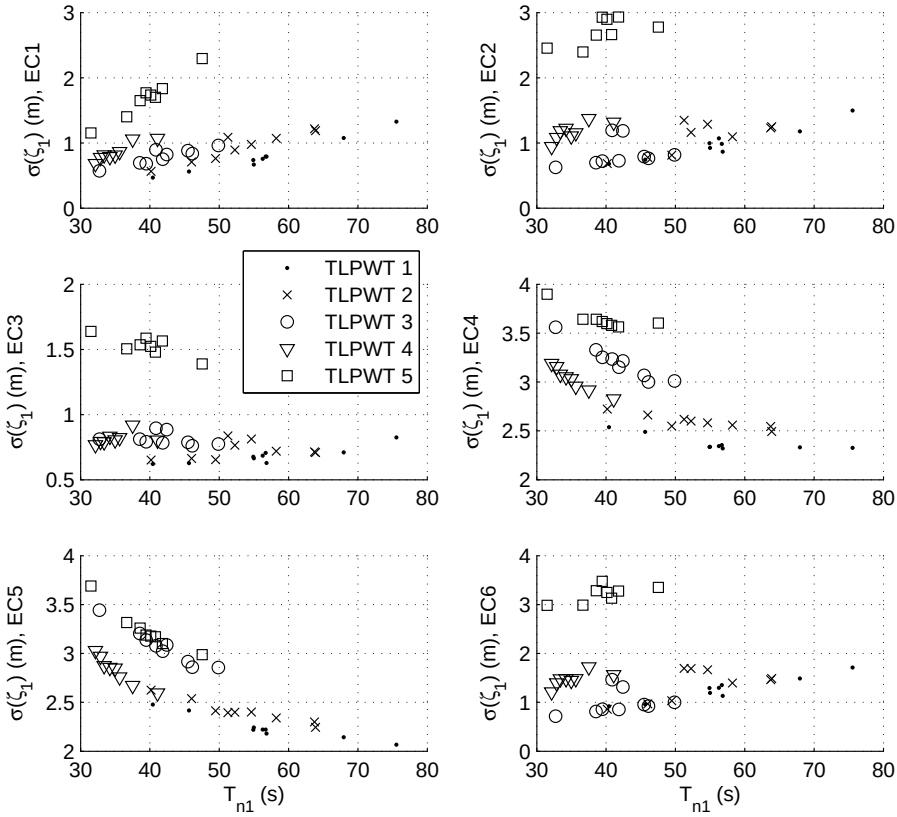

Figure 4.15: Effect of T_{n1} on $\sigma(\zeta_1)$ for all TLPWTs, ECs 1-6

are examined within each TLPWT design and its variations. Note that the results shown in Fig. 4.17 do not include depth variations. Fig. 4.17 does not show the mean values, but an increase in $\mu(T_1)/F_t$ was noted for increasing F_t: there was a lower probability of slack for increased F_t.

When the results were considered in terms of displacement rather than pretension, a reversal in the trend was noted for TLPWT 1, which has the largest displacement. This suggests that a design with less displacement and less permanent ballast may perform equally well in terms of tendon tension variation. On the other hand, the variation in M_{FA} was only weakly dependent on the displacement, and did not show a strong relation to the total pretension.

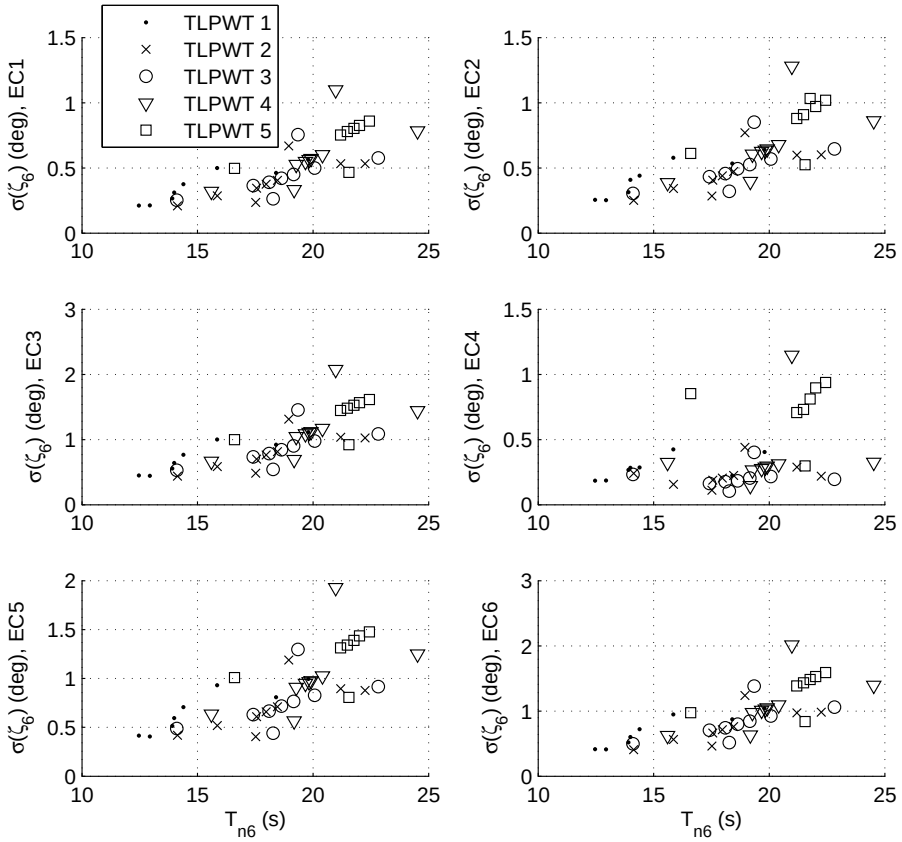

Figure 4.16: Effect of T_{n6} on $\sigma(\zeta_6)$ for all TLPWTs, ECs 1-6

4.2.6 Conclusions

Because construction costs increase roughly linearly with displacement and pretension, the design goal should be to achieve the best performance with the least required displacement and lowest possible pretension. For all of the designs that met some minimum requirements, placing the wind turbine on the TLP platform did not have a large effect on the turbine blade loads or power output, but the bending moment variation at the tower base increased significantly compared to the land-based turbine. In general, the designs with the largest displacement showed the smallest motions and the designs with the highest pretension showed the least relative tension variation (and hence the least fatigue damage). Motions perpendicular to the

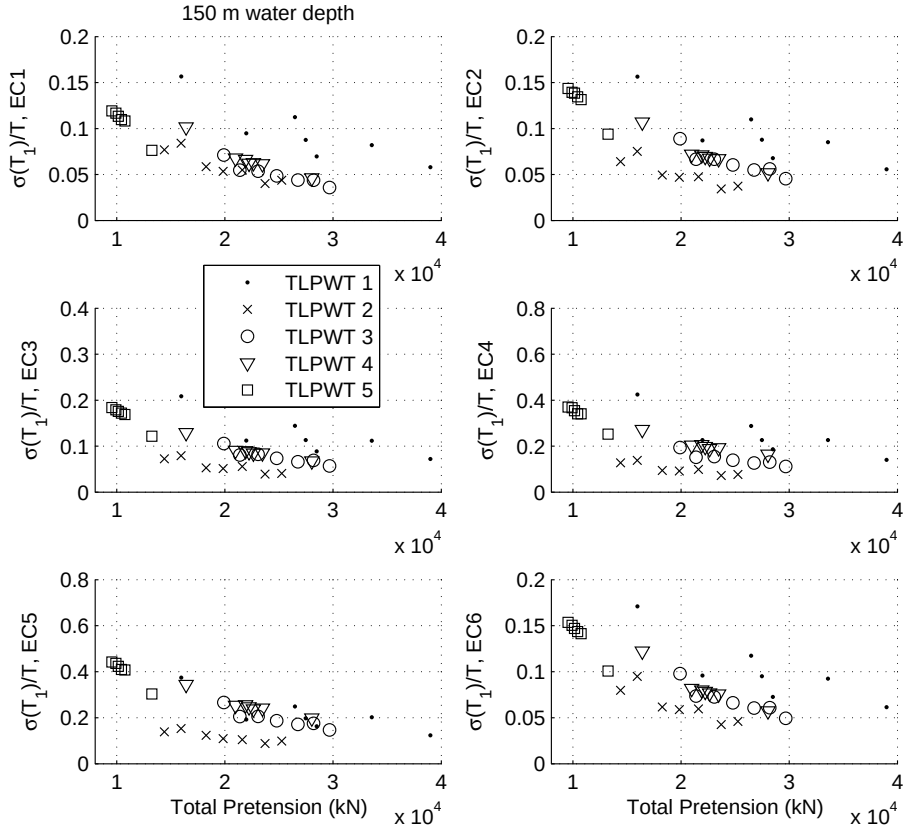

Figure 4.17: Effect of total pretension on $\sigma(T_1)$ for all TLPWTs, ECs 1-6. Variations in water depth are not included.

wind and waves were found to be an important consideration, even in aligned wind-wave conditions. Roll motions, which are very lightly damped, may be excited by the time-dependent wind turbine and generator torque, and yaw motions may be excited both by roll coupling and by the time-varying aerodynamic loading. Due to the low damping, the roll (and yaw) rotations exceeded the pitch motions in some cases, but occurred at lower frequency.

The TLPWT responses were more dependent on changes in mass and stiffness than direct dependence on diameter, water depth, ballast fraction, or pontoon radius. For example, the surge natural period needed to be sufficiently long (>45 s) to reduce surge motions in storm conditions but not too long (<70 s) to see decreased performance in operational conditions.

Decreasing the yaw natural period reduced the platform yaw motions, particularly for yaw periods >20 s. The wind turbine tower base bending moment was only weakly dependent on displacement and pitch/bending natural period. Furthermore, wave-frequency loading dominated M_{FA} even though $\sigma(\zeta_5)$ was not a good predictor of $\sigma(M_{FA})$, suggesting that dynamic inertial loads (also due to surge) were important even though the TLPWT motions were small.

Although the optimal TLPWT design has not been found, TLPWTs 3 and 4 with increased pontoon radius tended to show the best overall behavior considering platform motions, tendon tension, and turbine loads in the considered environmental conditions, and the roughly estimated construction cost. This study was very limited in its consideration of different environmental conditions, and additional simulations are required to more accurately predict fatigue and extreme events. Furthermore, the detailed design and structural integrity of the hull, especially at the pontoon attachment, was not investigated. Nevertheless, the results suggest that a reasonable single column design with displacement between 3500 and 6500 m^3, three pontoons (for easier installation), and pontoon radius (measured from the center of the platform to the tendon fairlead) between 28 and 35 m may be able to support a 5 MW wind turbine and withstand harsh environmental conditions.

Chapter 5

TLPWT Analysis

5.1 Linear vs. Nonlinear Analysis of TLPWTs

There is a need for simplified methods in the analysis of floating wind turbines, since the nonlinear fully-coupled method requires significant computational time. To complement the nonlinear analysis, two frequency-domain linearized analyses were carried out in MATLAB: with and without wind effects. These are described in Sections 5.1.1 and 5.1.2, respectively. The predicted responses are compared to nonlinear analysis results for the baseline TLPWT designs in Section 5.1.3. Selected results from this chapter were presented in [153].

5.1.1 Wave-only Frequency-Domain Analysis

In the wave-only linear analysis, the equations of motion for the rigid body system in three DOFs (Eq. 5.1) were solved across the relevant wave frequencies to obtain response amplitude operators (RAOs). Note that complex values are indicated by tildes in Eq. 5.1. The hydrodynamic added mass, damping, and excitation forces were obtained from a first-order panel model, as in Sec. 3.2.2 and 4.1.4.1. The mooring system stiffness matrix was obtained by linear approximation about the still water, zero wind position of the TLPWT, as in Sec. 4.1.2.2. This simplified analysis neglected aerodynamic damping, wind excitation, tower flexibility effects, set-down effects, additional stiffness due to mean drift, and second-order hydrodynamic effects.

$$\left(-\omega^2 \begin{bmatrix} M_{11}+A_{11} & 0 & M_{15}+A_{15} \\ 0 & M_{33}+A_{33} & 0 \\ M_{51}+A_{51} & 0 & M_{55}+A_{55} \end{bmatrix} + i\omega \begin{bmatrix} B_{11} & 0 & B_{15} \\ 0 & B_{33} & 0 \\ B_{51} & 0 & B_{55} \end{bmatrix} + \begin{bmatrix} K_{11} & 0 & K_{15} \\ 0 & C_{33}+K_{33} & 0 \\ K_{51} & 0 & C_{55}+K_{55} \end{bmatrix} \right) \begin{bmatrix} \widetilde{\zeta}_1 \\ \widetilde{\zeta}_3 \\ \widetilde{\zeta}_5 \end{bmatrix} = \begin{bmatrix} \widetilde{X}_1 \\ \widetilde{X}_3 \\ \widetilde{X}_5 \end{bmatrix} \tag{5.1}$$

All RAOs included amplitude and phase information. Furthermore, the nacelle acceleration RAO ($R_{\ddot{x}_{nac}}$) was computed by linear superposition from the surge and pitch RAOs (Eq. 5.2, where h_{hub} is the hub height above the still water line). The dynamic tendon tension RAO (R_{T_1}) was estimated based on the vertical displacements according to the heave and

pitch RAOs (Eq. 5.3). That is, horizontal motions were neglected in the dynamic tendon tension calculation.

$$R_{\ddot{x}_{nac}} = -\omega^2 \left(R_{\zeta_1} + h_{hub} R_{\zeta_5} \right) \tag{5.2}$$

$$R_{T_1} = \frac{E_t A_t \left(\sqrt{\left| R_{\zeta_3} - R_{\zeta_5} r_p + l_0 \right|^2} - l_0 \right)}{l_0} \tag{5.3}$$

Spectral responses in varying wave conditions were then computed from the RAOs and input wave spectra, as in Eq. 3.87.

5.1.2 Wind-Wave Frequency-Domain Analysis

As an extension of the wave-only model, simple formulations for the effects of wind excitation and aerodynamic damping were estimated. The response spectra for wind-only responses were superimposed on the linear wave-induced response, without considering phase information. That is: the wind-induced RAO was computed for different wind speeds (the aerodynamic damping matrix depends on the mean wind speed), and the resulting platform motion spectra (obtained from the wind-induced RAO and the thrust spectrum) were added to the wave-induced spectra. The effects of wind damping on the wave-induced response were not included here.

First, to obtain the wind-induced platform motion RAO, the aerodynamic damping matrix must be established. Aerodynamic damping can be estimated based on changes in the thrust force due to a change in wind speed without considering the effect of the control system [41, 157, 158]. Simulations in FAST were performed for the isolated NREL 5MW rotor subjected to a range of constant wind speeds, U_i. For each wind speed, two additional simulations were performed for wind speeds $U_i \pm 0.25$m/s, where the blade pitch was held at the value corresponding to steady-state operation at U_i. The resulting values of the thrust force are shown in Fig. 5.1a.

The difference in thrust was used to estimate the critical damping for a bottom-fixed wind turbine, as shown in Fig. 5.1b, where the participating mass and stiffness represent the first fore-aft mode of the NREL 5 MW land-based wind turbine. For comparison, the aerodynamic damping for the 2 MW wind turbines at Blyth was estimated to be near 4% of critical [157].

In the frequency-domain analysis, the aerodynamic damping (B_{aero}) was

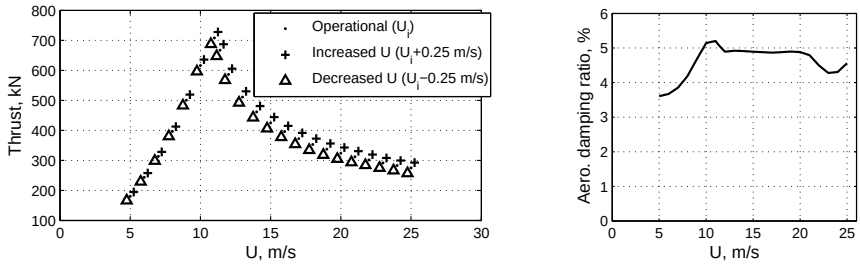

(a) Thrust force (b) Damping ratio

Figure 5.1: Thrust force for aerodynamic damping calculations and aerodynamic damping ratio for the NREL 5 MW land-based turbine [72]

included as:

$$B_{aero} = \begin{bmatrix} \frac{dF_T}{dU} & 0 & \frac{dF_T}{dU} h_{hub} \\ 0 & 0 & 0 \\ \frac{dF_T}{dU} h_{hub} & 0 & \frac{dF_T}{dU} h_{hub}^2 \end{bmatrix} \tag{5.4}$$

where F_T is the thrust force.

In order to obtain reasonable results for the surge motion when the low-frequency thrust force was included, it was also necessary to consider viscous damping. A linearized form of Morison damping on the center column and pontoons was added based on [159]:

$$B_{11visc} \approx C_D \left[D_1 \left(h_1 - b_t \right) + D_2 h_2 + l_p \frac{\sqrt{n_p}}{2} [(h_p \quad \text{or} \quad d_p)] \right] 1.596 \sigma_v \tag{5.5}$$

where σ_v is the standard deviation of the surge velocity. An iterative solution for each environmental condition should be used, but for simplicity the approximation $\sigma_v \approx H_s/2\text{s}$ (where H_s is in m) was employed for all TLPWTs based on the nonlinear analysis results.

These additional damping matrices (aerodynamic and linearized hydrodynamic viscous damping), combined with the mass, added mass, potential damping, and stiffness matrices from Sec. 5.1.1, were used to determine the wind-induced motion RAOs. The wind-induced RAOs were computed separately from the wave-induced motions.

Then, the thrust force spectrum was obtained from turbulent wind simulations of a fixed rotor in FAST. The resulting spectra for different wind speeds are shown in Fig. 5.2. The main force contribution was at low frequencies, although there was some excitation around the 3p and 6p frequencies.

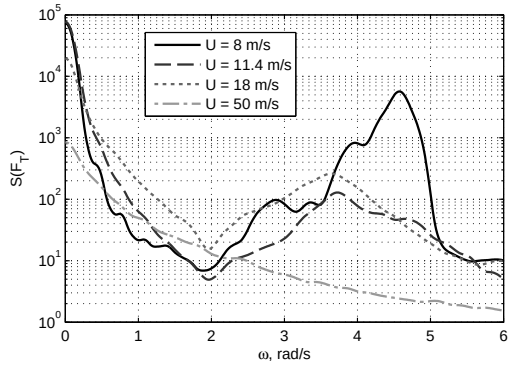

Figure 5.2: Thrust force spectra for linear analysis. Note log scale on the y-axis.

The wind-induced motion spectra (obtained from the wind-induced RAO and the thrust spectrum) were then added to the wave-induced spectra to obtain the total response. This approach neglects phase information from the RAOs and the effects of aerodynamic damping on the wave-induced motions.

5.1.3 Linear and Nonlinear Responses

After computing the natural periods (see Section 4.1.4.2), the linear and nonlinear models were first compared for wave-only excitation. The wave loading in the nonlinear model was limited to the first-order potential and Morison-type viscous forces. The resulting predictions of the surge motions, nacelle acceleration, and dynamic tendon tension standard deviations are compared in Figs. 5.3a-5.5a. The nacelle acceleration was used as a representative measure of the tower loading. Perfect agreement between the linear and non-linear computations would fall along the 1:1 line, with points above the line indicating that the linear prediction is non-conservative. Similarly, combined wind and wave excitation results are shown in Figures 5.3b-5.5b. ECs 1-4 from Table 3.6 are included in these figures.

As shown, the linear simulation tool gave reasonably accurate predictions for the standard deviation of the considered responses in wave-only conditions, but tended to underpredict the nacelle acceleration compared to the nonlinear simulations. The underprediction was worst for TLPWT 2, which was particularly sensitive to excitation in the upper half of the wave frequency range. It is also interesting to note that the linear and nonlinear methods did not necessarily give the same ranking for the different

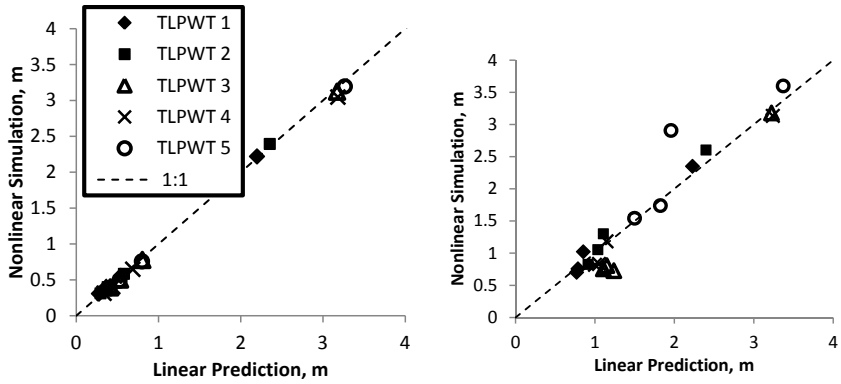

(a) Wave-only (b) Wind and wave

Figure 5.3: Linear and nonlinear predictions of the surge standard deviation, TLPWTs 1-5, ECs 1-4.

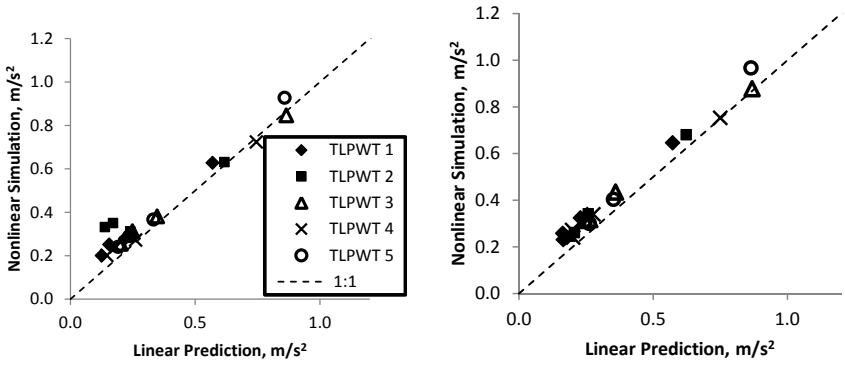

(a) Wave-only (b) Wind and wave

Figure 5.4: Linear and nonlinear predictions of the standard deviation of nacelle acceleration, TLPWTs 1-5, ECs 1-4.

TLPWT designs in wave-only conditions. For example, in the most severe wave condition, the linear analysis predicted that TLPWT 5 would have lower nacelle acceleration than TLPWT 3, while the nonlinear method predicted the opposite trend. This type of difference may lead to poor results for an automatic optimization scheme using linear analysis.

The linear analysis gave somewhat worse agreement with the nonlinear analysis for the combined wind and wave conditions. The surge motion was generally over-predicted in the benign conditions and under-predicted in

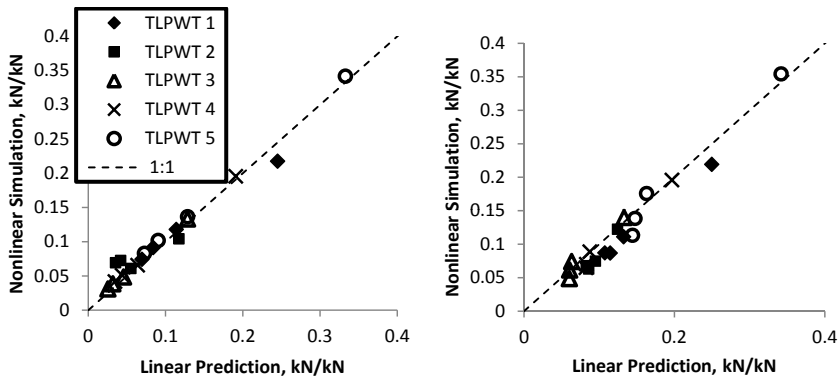

(a) Wave-only (b) Wind and wave

Figure 5.5: Linear and nonlinear predictions of the standard deviation of the tension in tendon 1 (downwind) divided by the pretension, TLPWTs 1-5, ECs 1-4.

the more severe conditions, particularly for TLPWT 5. The standard deviation of the nacelle acceleration was generally under-predicted by the linear analysis, although the error decreased compared to the wave-only condition. There was more spread in the estimates of tendon tension variation in the combined analysis compared to the wave-only analysis. The spectral results may help explain differences in the standard deviation, such as the illustrative examples in Figs. 5.6a-5.7b.

Fig. 5.6a shows the surge spectra for TLPWT 4 for different analyses. In the wave-only case, the response was at the wave frequency, and was captured quite well by the frequency-domain analysis. In the combined wind and wave condition, the wind induced a low-frequency surge response (at the surge natural frequency and across the thrust force frequencies). The low-frequency response in the frequency-domain analysis depended greatly on the Morison and aerodynamic damping and tended to be slightly more narrow-banded than the time domain results.

The nacelle acceleration spectra for TLPWT 1 are shown in Fig. 5.6b. There was no significant low-frequency nacelle acceleration, but there were components near the wave frequency and the first pitch-bend frequency. The high-frequency component is not modeled by the linear analysis. Due to aerodynamic damping, the high-frequency component was reduced during wind turbine operation, which gave improved agreement between the linear and nonlinear analyses.

Figs. 5.7a-5.7b show the downwind tendon tension spectra for TLPWTs

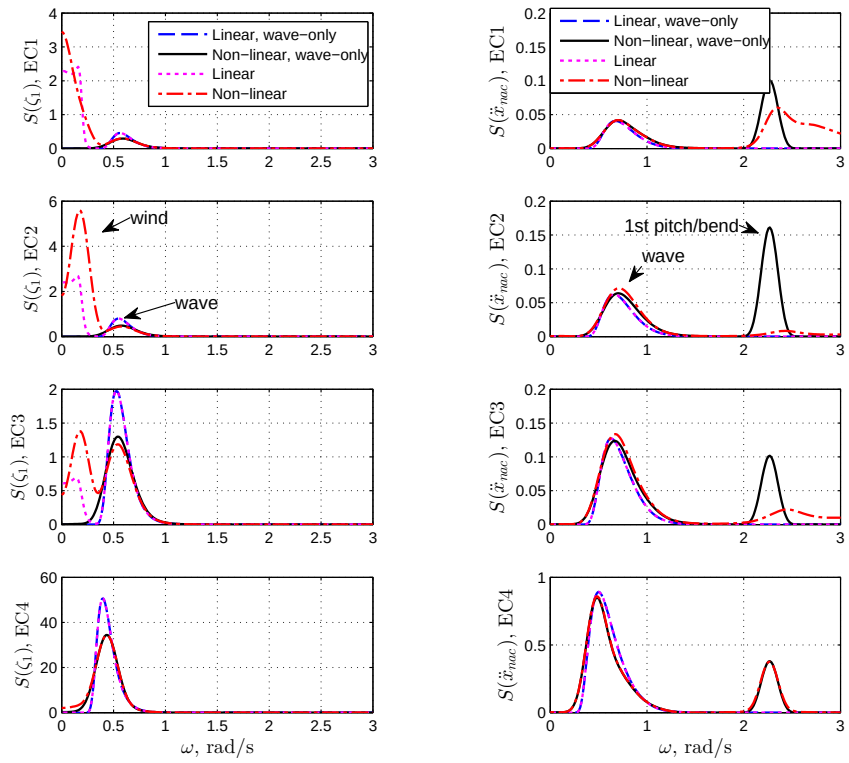

(a) TLPWT 4 surge spectra

(b) TLPWT 1 $\ddot{x}_{nac}$ spectra

Figure 5.6: TLPWT 4 surge spectra and TLPWT 1 nacelle acceleration spectra for linear and nonlinear wave-only and combined wind-wave analyses, ECs 1-4

5 and 2, respectively. There are components in the wind-frequency range; in the wave-frequency range; at the first pitch/bend frequency; and at high wave frequencies, close to twice the peak wave frequency (primarily for TLPWT 2).

As shown in Fig. 5.7a, the linear analysis tended to capture the wave-frequency tendon tension variation of TLPWT 5 fairly well in the wave-only cases, but underpredicted the tendon tension variation for the combined wind and wave condition. The assumed aerodynamic and viscous damping may be too large. The wind-frequency component is reasonably well-approximated, but the pitch/bend frequency component is missing from the linear analysis.

For TLPWT 2 (Fig. 5.7b), the response spectrum is more complicated. There is a significant component of the response at high wave frequencies (close to twice the peak wave frequency), which is present in both the linear and nonlinear analyses. The response at the pitch-bend frequency is, however, still missing from the linear analysis. As with the nacelle acceleration, aerodynamic damping reduced the tendon tension response at the first pitch-bend frequency for the wind-wave nonlinear simulations compared to wave-only nonlinear simulations.

In addition to the surge, heave, and pitch motions, which are included in the linear analysis, the nonlinear analysis showed that the sway, roll, and yaw motions were also excited in long-crested waves and concomitant wind. The aerodynamic torque and the 3p excitation (as the turbine blades pass the tower) transferred energy to other modes, as previously described by Philippe et al. [160].

5.1.4 Conclusions

A linear frequency-domain analysis was investigated as an alternative to the time-consuming nonlinear analyses. The analysis assumed 3 DOF motion of a rigid body, and included the wind-induced loads and damping through approximate methods. While the linear frequency-domain method captured the wave-induced motions, nacelle accelerations, and dynamic tension with reasonable accuracy for low sea states, important wave-induced effects in more severe states were not captured due to the limitations of the rigid-body structural model. Furthermore, the low-frequency wind-induced response in the frequency-domain analysis was damping-dependent and slightly more narrow-banded than that predicted by the nonlinear analysis.

The frequency-domain analysis, in its current form, is insufficient for analyzing floating wind turbine designs, including TLPWTs: it is not accurate enough in modeling the included modes (surge, heave, pitch) and it

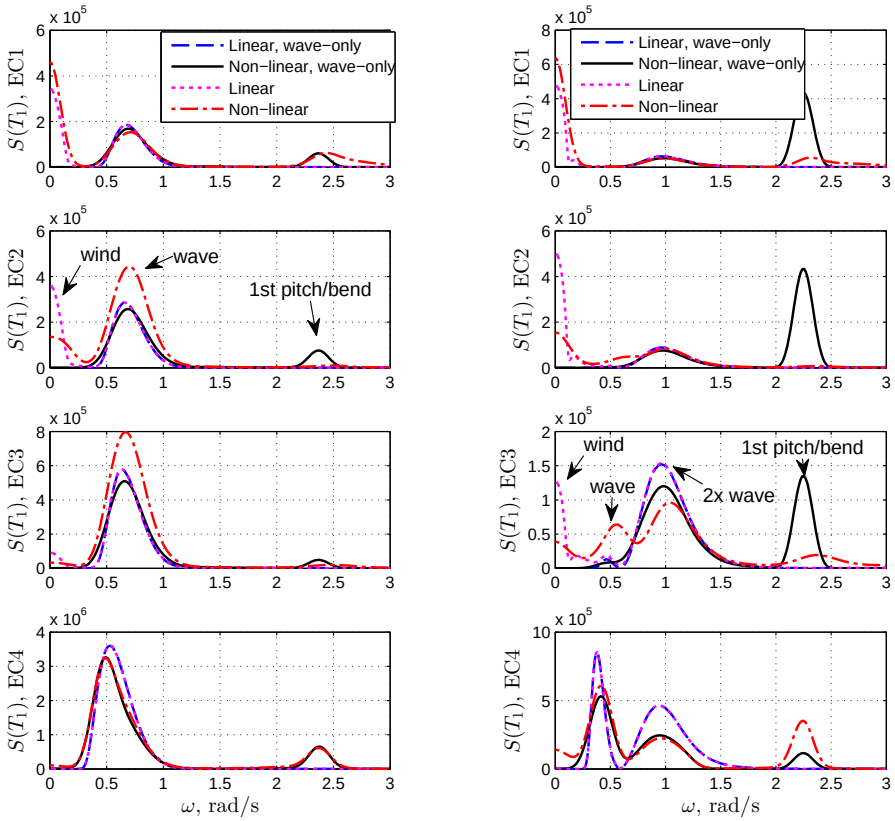

(a) TLPWT 5 (b) TLPWT 2

Figure 5.7: TLPWT 5 and TLPWT 2 spectra of tendon 1 (downwind) tension for linear and nonlinear wave-only and combined wind-wave analyses, ECs 1-4

cannot model enough modes to give a clear picture of the structural loading. The model could be improved by including the tower elasticity in the pitch mode, and attempts to correlate the nacelle acceleration with the tower base bending moment could be pursued.

5.2 Effects of Hydrodynamic Modeling Approaches

In order to develop appropriate numerical tools for initial design of FWTs, the sensitivity of the results to the hydrodynamic modeling must be established.

A comparison of Morison and potential flow models for a semi-submersible wind turbine structure with 10 m characteristic length at the waterline indicated that the Morison formulation, with coefficients chosen based on the potential flow results, could be used to obtain similar structural responses in the turbine and mooring system [161]. For a TLPWT, this approach may not be as successful, as published in [162] and described here. In practice, this means that some wind turbine analysis codes, which were developed for fixed structures and only include Morison wave force models, should not be used for TLPWTs.

Additionally, Roald et al. suggested that second-order sum-frequency forces may be important for TLPWTs [163]. Bae and Kim found that such forces are primarily relevant for severe wave conditions [164], in general agreement with the results presented here and published in [162].

Finally, the importance of ringing loads for TLPs is well-established (see Sec. 2.5.2), but ringing loads have not been included in previous studies of TLPWT concepts. An examination of ringing load effects is presented here and has been submitted for publication [165].

In this section, four hydrodynamic models, given below, are considered:

1. M: Morison formulation (Froude-Krylov excitation, added mass, and viscous drag),
2. P1+V: first-order potential flow and viscous drag,
3. P2+V: first- and second-order potential flow and viscous drag,
4. P2+V+R: first- and second-order potential flow, third-order ringing forces, and viscous drag.

The considerations included in the different models are summarized in Table 5.1, while the background theory is described in Sec. 3.2.

The P1+V formulation is the baseline hydrodynamic model used in Chap. 4. The P1+V, P2+V, and P2+V+R formulations included mean drift forces using the Newman approximation, which depends only on first-order information [88]. Neither the detailed slowly-varying QTF nor the slowly-varying wave-drift damping was modeled. Compared to the wind-induced forces in the low-frequency range, the difference-frequency wave forces are generally small [163].

Table 5.1: Summary of hydrodynamic models

	P1+V	P2+V	P2+V+R	M
Added Mass	freq.-dep.	freq.-dep.	freq.-dep.	constant
Linear Damping	freq.-dep.	freq.-dep.	freq.-dep.	not modeled
Quadratic Damping	Morison	Morison	Morison	Morison
1st Order Wave Excit.	rad. + diff.	rad. + diff.	rad. + diff.	inertia
Sum-Freq. QTF	not modeled	direct method	direct method	not modeled
Diff.-Freq. QTF	not modeled	not modeled	not modeled	not modeled
Mean Wave Drift Forces/-Mom.	Newman approx. + viscous	Newman approx. + viscous	Newman approx. + viscous	viscous
3rd Order Wave Excit.	not modeled	not modeled	FNV [107]	not modeled

Identical transverse viscous damping coefficients were used in all four hydrodynamic models: $C_D = 0.7$ (see Eq. 3.57) for both circular cross sections with diameter D and square cross sections (using the width as the representative length). Although this assumption may underpredict the drag, particularly on the square cross sections, it is taken as a reasonable first approximation based on Reynolds and Keulegan-Carpenter number [88]. In all cases, the viscous damping is applied to all members of the TLPWT hull (in addition to potential forces or Morison inertia forces).

In all cases, the wave forces on the hull and tendons were computed at the static position of the TLPWT. The Morison forces - including the viscous forces in all models - were computed up to the instantaneous water level, based on wave kinematics at the platform's original position. No Wheeler stretching was considered: the wave kinematics at the still water level were used for points above the still water level. A model of the dynamic pressure at the base of the center column was included in the Morison model [166], and the heave added mass of the center column was estimated as the added

mass of a sphere with diameter equal to D_2 (see also Eq. 4.4) [87, 151].

In order to study the effects of different analysis models on a range of platforms, these models were applied to the original and soft versions of TLPWT platforms 1-4 (see Sec. 4.1.4). A comparison of the Morison model and the baseline model is presented in Sec. 5.2.1; the effects of second-order sum-frequency forces are examined in Sec. 5.2.2; ringing loads are investigated in Sec. 5.2.3.

5.2.1 Morison Model vs. First-Order Potential Model

In this section, the Morison (M) model is compared to the first-order potential model (P1+V).

The primary first-order force contribution for a single-column TLP comes from the Froude-Krylov and inertia forces on the main column. The representation of the forcing on the main column (neglecting viscous damping and body acceleration) for the Morison (without diffraction) and potential flow (with diffraction) models can differ significantly in the high-frequency range, as shown in the force transfer functions in Figs. 5.8a and 5.8b for surge and pitch, respectively. Theoretical results were obtained from the potential flow solution and Eq. 3.59, while simulation results in the wave frequency range were obtained from simulations with $H_s = 2.5$m, $T_p = 9.8$s. The difference in surge forcing is not of great importance for the structural response, since the surge natural frequency is lower than the wave frequency, also excited by the turbulent wind, and relatively unimportant for mooring system loads. The pitch/bending natural frequency is close to 2.25 rad/s, where there is a large difference in the forcing and very little hydrodynamic damping. The pitch/bending response is important for the tower bending loads and the variations in tendon tension: despite the relatively small ocean wave energy at this frequency, the large difference in force transfer function may lead to differences in the computed structural response.

Based on the simulations of TLPWTs 1-4 in ECs 1-4, the effects of the Morison model on the mean and standard deviation of the responses, as well as on the short-term fatigue calculations, can be evaluated. The mean and standard deviations of the baseline (P1+V) responses were previously presented in Figs. 4.10a and 4.10b (Sec. 4.2.2).

Changes in the mean and standard deviation of the responses using the Morison model compared to the P1+V model are shown in Figs. 5.9 and 5.10 for the baseline designs. The effect of the Morison model on the mean values is nearly identical for the soft designs and is not shown. Fig. 5.11 shows the change in standard deviations for the soft designs. Positive values

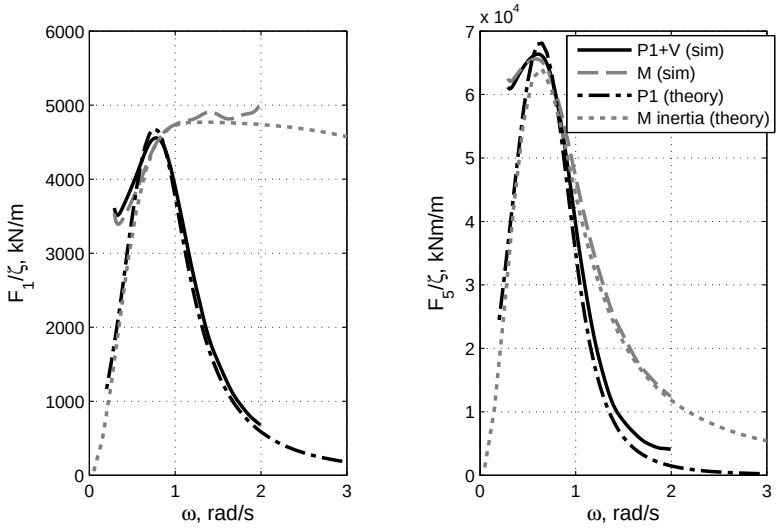

(a) Surge (b) Pitch

Figure 5.8: Potential and Morison (Froude-Krylov and inertia) wave force transfer functions, TLPWT 1

indicate that the Morison model overpredicts the shown quantity compared to the P1+V model.

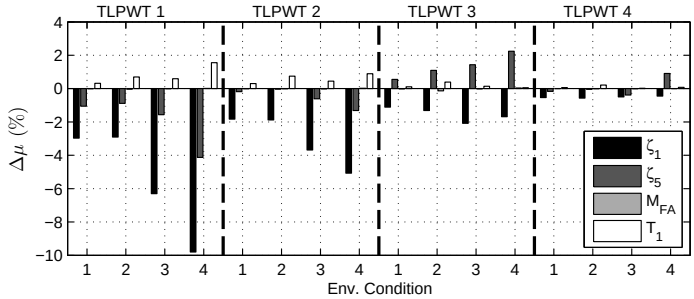

Figure 5.9: Relative changes in the mean of key responses, M vs. P1+V, baseline designs. Positive values indicate that the M model result is larger than the P1+V model result.

First, examining the surge motions, the Morison model predicted smaller $\mu(\zeta_1)$ and larger $\sigma(\zeta_1)$ than the potential flow model, particularly for larger wave heights and large diameters, regardless of the tendon stiffness. The

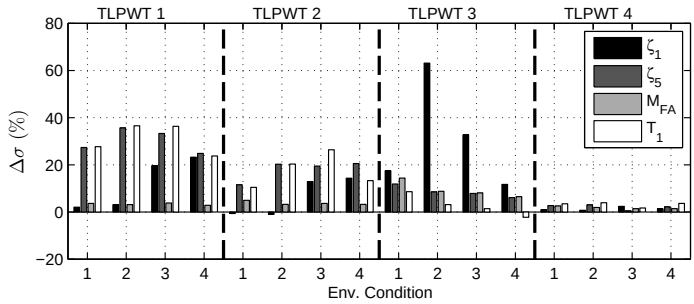

Figure 5.10: Relative changes in the standard deviation of key responses, M vs. P1+V, baseline designs. Positive values indicate that the M model result is larger than the P1+V model result.

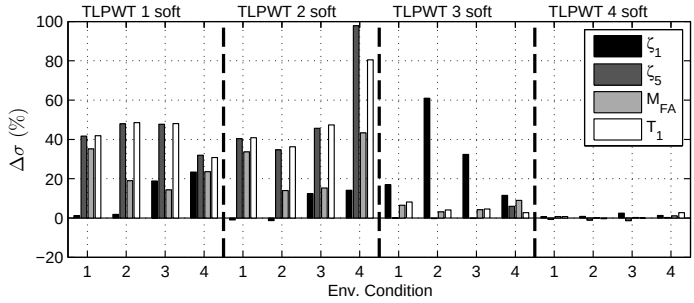

Figure 5.11: Relative changes in the standard deviation of key responses, M vs. P1+V, soft designs. Positive values indicate that the M model result is larger than the P1+V model result.

difference in motions was observed at the surge natural frequency, where there is little damping and small forcing differences become more evident in the response. The large relative difference in $\sigma(\zeta_1)$ in ECs 2 and 3 does not represent a large change in the absolute value.

The agreement between the M and P1+V models was somewhat worse for pitch compared to surge, particularly for TLPWTs with large diameter. While $\mu(\zeta_5)$ depended mainly on the thrust force and was similar for both models, the Morison model predicted significantly larger values of $\sigma(\zeta_5)$. The discrepancy in $\sigma(\zeta_5)$ tended to be largest for TLPWT 1 and smallest for TLPWT 4, regardless of tendon stiffness. The discrepancy for TLPWTs 2 and 3 depended significantly on the tendon stiffness: in both cases, the M model was somewhat worse for TLPWT 2, which had larger displacement, than for TLPWT 3. For the baseline designs of TLPWT 2 and 3, the magnitude of the discrepancy was fairly similar (10-20 %). For the soft designs,

the M model gave over 40 % more pitch response than the P1+V model for TLPWT 2 (soft), but showed relatively good agreement with TLPWT 3 (soft). TLPWT 3 (soft) had a lower pitch/bend natural frequency, such that the wave forcing was more similar between the M and P1+V models in the important frequency range.

Similarly, the mean value of the fore-aft bending moment at the tower base depended primarily on the thrust force and was unaffected by the hydrodynamic model, while $\sigma(M_{FA})$ increased with increasing wave height. For the baseline designs, the M model gave larger load predictions than P1+V (3-14 % for TLPWTs 1-3) in both operational and storm conditions, primarily in the upper half of the wave frequency range and around the pitch natural frequency. Due to the increased importance of gravitational loading as a result of larger pitch motions, the M model gave 15-30% larger tower loads for the soft versions of TLPWTs 1 and 2 in operational conditions. For the baseline and soft versions of TLPWT 4, the M model gave good results for M_{FA}.

Finally, the mean value of the tendon tension in the downwind line was reasonably well predicted by the M model, but $\sigma(T_1)$ differed significantly from the P1+V model. Moreover, while the M model predicted up to 25% larger tendon tension variation for TLPWT 1, it was not necessarily conservative: TLPWT 3 showed less tendon tension variation in the wave-frequency region. The disagreement was even greater for the soft TLPWTs, with up to 85 % overprediction of $\sigma(T_1)$. Even the most slender hull, TLPWT 4, showed increased tendon tension variation using the M model in the extreme wave condition.

As an example of the difference between the M and P1+V models, the spectra of the tendon tension response in all environmental conditions are shown for TLPWT 3 in Fig. 5.12. For the baseline design, the main difference in the response occurred at the platform pitch/tower bending frequency, while an additional important component of the response occurred at the second tendon transverse bending mode for the soft version of TLPWT 3. The response at the second tendon transverse bending mode was apparent in both the M and P1+V models, but much larger for the M model.

5.2.1.1 Conclusions

Morison's equation gave reasonably good agreement for slender structures, but generally led to larger pitch moment predictions for structures with large diameter and in large waves. The Froude-Krylov force as computed by Morison's equation does not decay as quickly as the potential flow wave

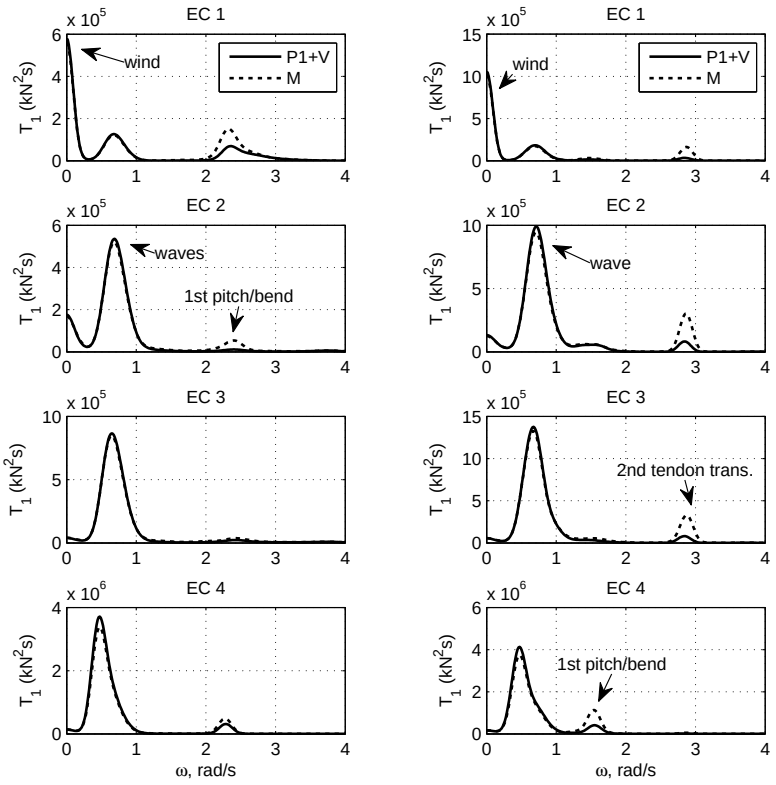

(a) TLPWT 3 baseline (b) TLPWT 3 soft

Figure 5.12: Tendon tension spectra, TLPWT 3, M and P1+V models, ECs 1-4.

excitation, leading to larger (unrealistic) excitation for large wave frequencies and near the pitch/bending natural frequency. It is possible that the agreement between the two models could be slightly improved by varying the Morison coefficients along the length of the cylinder, but the main difference in response is at the pitch natural frequency rather than at the wave frequency. Better agreement between Morison's equation and linear potential theory might also be achieved by implementing a correction based on the MacCamy-Fuchs model, for example (see Sec. 3.2.5). This approach was not considered here.

5.2.2 Effects of Sum-Frequency Second-Order Forces

The first challenge in studying the effects of the sum-frequency second-order wave forces is the generation of the sum-frequency quadratic transfer function (QTF). As described in Section 3.2.3, the free surface-forcing term requires careful discretization of the free surface. The tool used here for computing the second-order potential was WADAM, which has a particular limitation: there may only be 3000 free surface panels in the basic part of the model [154]. After performing a convergence study for the free surface mesh radius and the mesh density at the structure waterline, free surface meshes for each TLPWT were chosen to give the best possible results for both long and short waves within the software limitation. The convergence study is presented in Appendix C.

A partitioning radius $R_2 = 150$ m was found to give acceptable results for long waves, and the diagonal dimension at the structural waterline was always less than 1.0 m. The shortest wave period included in the second-order analysis was 4.5 s. Additionally, non-uniform edge element distributions were used on the hull panel model to obtain finer meshing around corners and the waterline.

Fig. 5.13 shows the sum-frequency pitch moment QTFs for TLPWTs 1 and 3. The first pitch/bend frequency is shown as a dashed line. As shown, the QTF tends to increase for increasing frequencies, and the trough along the diagonal for low frequencies is more pronounced when large pontoons are present.

The effects of the second-order sum-frequency forces were examined for two sets of environmental conditions: ECs 1-4 and ringing conditions R1-R9; selected results are presented here. Note that simulations of ECs 1-4 use the land-based controller, while R1-R9 used the modified controller, which gives additional damping but larger power variation. Not all designs were tested in all ringing conditions: see also Sec. 5.2.3.

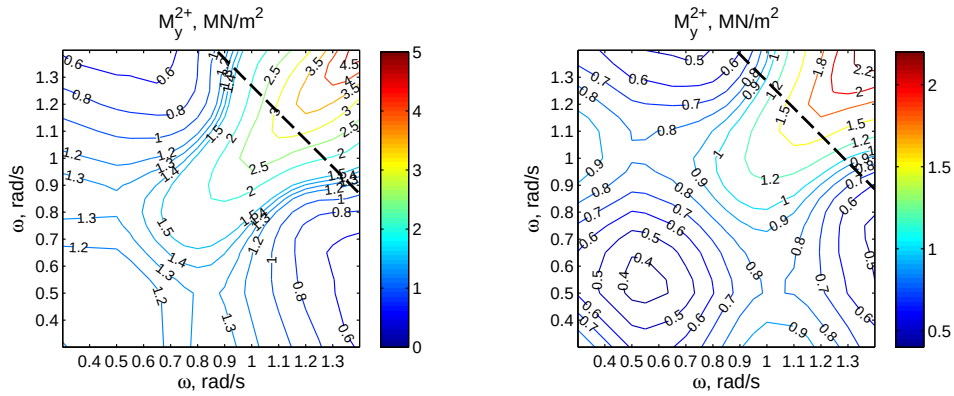

(a) TLPWT 1 (b) TLPWT 3

Figure 5.13: Sum-frequency pitch force QTFs, TLPWTs 1 and 3. The dashed line indicates the first pitch/bending frequency.

The sum-frequency forces had negligible effects on the mean value of the responses, but increases in the standard deviation could be seen, as shown in Fig. 5.14 for the baseline designs in ECs 1-4. (Similar results were seen for R1-R9 and for the soft designs and are not shown here). While the surge motion was not significantly affected, increases in $\sigma(\zeta_5)$, $\sigma(M_{FA})$, and $\sigma(T_1)$ were observed. The increase in standard deviation was largest for large values of H_s, particularly when the turbine was idling, and TLPWT 2 was the most significantly affected. For the baseline designs, the impact was very small (< 1 %) for ECs 1-3, and slightly larger (2-10 %) for EC 4. For the soft designs, the impact of second-order forces on the standard deviation of the key parameters was similarly very small for operational conditions (< 2 %), but somewhat larger for EC 4 (5-30 %).

The effect of sum-frequency forces on the blade root bending moments (not shown) was also small: the observed changes in standard deviation were less than 6 % in all conditions, with less than 0.1 % changes in ECs 1-3. Furthermore, the largest relative increases in the standard deviation were observed for parked conditions, which had lower blade root bending moments than the operational conditions.

Although the observed effect on the standard deviation was small ($< 1\%$ for the baseline designs, $< 2\%$ for the soft designs) in operational conditions, second-order forces may nonetheless be important for fatigue calculations if the number of stress cycles increases significantly. First, the one-hour fatigue damage for the P1+V model is shown in Fig. 5.15. The one-hour

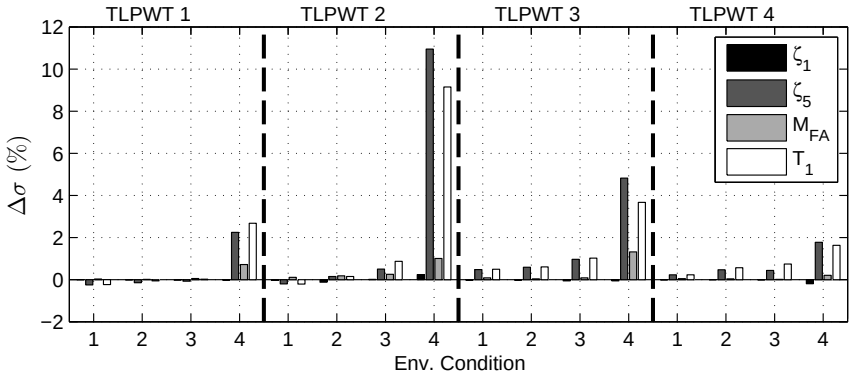

Figure 5.14: Relative changes in the standard deviation of key responses, P2+V vs. P1+V, baseline designs, ECs 1-4. Positive values indicate an increase in the response due to accounting for second-order sum-frequency effects.

fatigue damage for the soft designs followed the same pattern, although the absolute value of the estimated damage was significantly higher.

The effect of the second-order sum-frequency forces on the fatigue damage is shown in Fig. 5.16 for the baseline designs. The relative difference in the fatigue damage was generally more significant than the increase in the standard deviation of the loading. Still, for the baseline designs in operational conditions, the increase in tower base fatigue was less than 5 %. The tendon fatigue damage was sensitive to large waves: in ECs 1-3, there were up to 10 % increases in D_{RFC} for tendon 1, while in R3 and R5-R6, up to 30 % increases were observed for TLPWTs 2 and 3. When the turbine was idling, the second-order forces became even more important, as shown in Fig. 5.16. The effects of second-order forces on the tower top (which is representative of the shaft loading) were also seen to be small in operational conditions. Increased tower top fatigue (up to approximately 50 %) was observed in severe conditions.

The effect of second-order sum-frequency forces on the soft designs showed similar patterns, with generally larger effects. In ECs 1-3, the tower base fatigue damage increased 2-10 % for soft TLPWTs 1 and 4, and up to 30 % for soft TLPWTs 2 and 3; the tendon fatigue damage increased on the order of 60 %. As the wave height increased, and particularly for the parked turbine, 100 % and even 500 % increases in fatigue damage due to sum-frequency loads were observed for the soft designs. So far, these increases in fatigue damage have been investigated for a few environmental

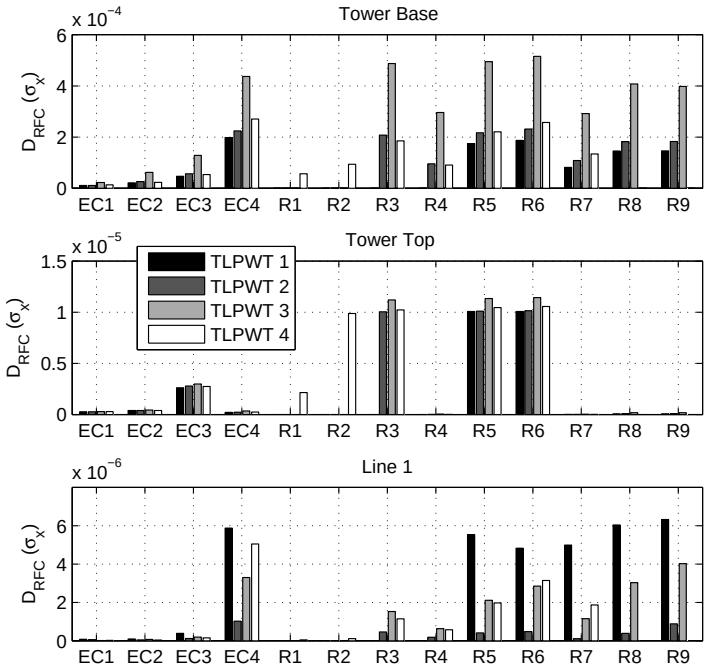

Figure 5.15: One-hour short term fatigue damage due to axial stress in the tower base, tower top, and at the downwind tendon fairlead, P1+V, baseline designs. ECs 1-4 and R1-R9 (note that R1-R9 are extreme conditions, see Table 3.8).

conditions. A full long-term analysis is needed to better understand the effects of second-order sum-frequency forces on the fatigue damage over the structure's lifetime.

5.2.2.1 Conclusions

Second-order sum-frequency wave loads had a significant impact on the response in severe wave conditions, and relatively minor effects on the standard deviation of the loads in typical operational conditions. This finding agrees with Bae and Kim's results [164]. The effect of second-order loads on the short-term tower base and tendon fatigue damage of the soft TLPWTs was, however, quite significant, especially for the parked conditions. For TLPWTs in deeper water, which are likely to have relatively long

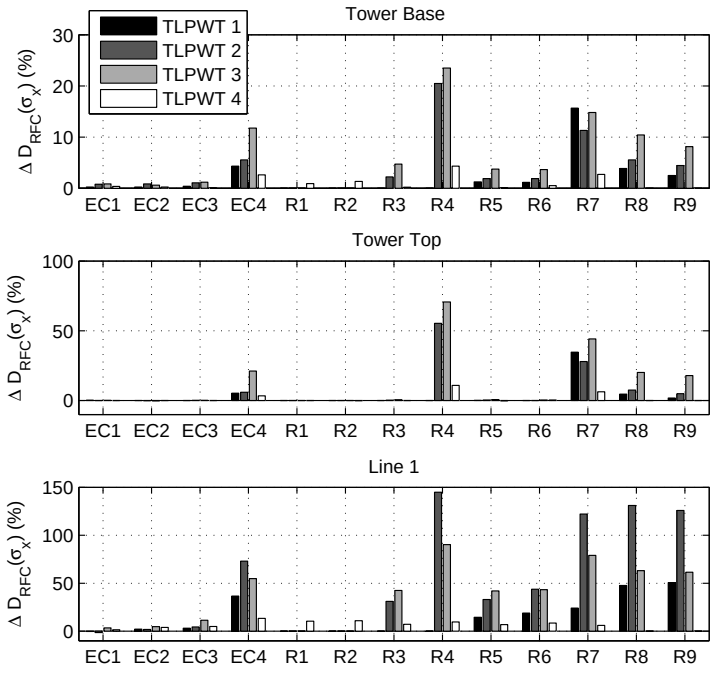

Figure 5.16: Relative changes in the fatigue damage due to axial stress in the tower base, tower top, and at the downwind tendon fairlead, P2+V vs. P1+V, baseline designs, ECs 1-4 and R1-R9.

pitch/bending periods, second-order forces may also have a large impact on fatigue calculations.

5.2.3 Effects of Ringing Forces

Finally, third-order ringing forces were investigated. As described in Sec. 2.5.2 and 3.2.4, ringing loads are expected to occur in large, steep waves, and can lead to large transient responses. The effects of ringing loads on the short-term maxima and on the fatigue loading are examined in Secs. 5.2.3.1 and 5.2.3.2 for the baseline and soft designs, respectively. The effects of wind turbine operation and viscous modeling on the ringing response are discussed in Secs. 5.2.3.3 and 5.2.3.4.

Environmental conditions R1-R9 (Table 3.8), with the modified control parameters, were considered when examining ringing. Not all conditions

were simulated for each TLPWT: an effort was made to select conditions which met the criteria for ringing (Sec. 2.5.2). Thus, the conditions were applied as in Table 5.2. 10x1 hour simulations were considered.

Table 5.2: Range of ringing conditions for each TLPWT. See Table 3.8 for definitions of conditions R1-R9.

TLPWT	ECs	H_s (m)	T_p (s)	ka
1	R5-R9	$8.71 - 14.0$	10.0-15.0	$0.16 - 0.36$
2	R3-R9	$7.96 - 14.0$	9.0-15.0	$0.12 - 0.35$
3	R3-R9	$7.96 - 14.0$	9.0-15.0	$0.12 - 0.35$
4	R1-R7	$5.68 - 9.87$	7.0-11.0	$0.11 - 0.27$

5.2.3.1 Baseline TLPWT Designs

Ringing loads in aligned wind and wave conditions had significant effects on the tendon tension and fore-aft tower base bending moment. In this section, the effect of ringing is first examined for the maximum loads and subsequently for the fatigue loads for the baseline TLPWTs.

Figure 5.17 shows the 1-hour expected maximum tension in the downwind tendon (T_1) divided by the pretension (F_t) and the 1-hour maximum fore-aft tower base bending moment (M_{FA}) for the baseline designs. In this case, the maximum tendon tension in the downwind tension is considered to be representative of the ringing response, as the minimum tension is often negative and is not a reliable measure.

For TLPWT 1, the ringing forces led to negative tension incidents in all of the tested environmental conditions. The resulting tendon loads were quite large, while the tower base loads were less affected.

TLPWTs 2 and 3, which have the same diameter, experienced very similar ringing loads. Ringing led to increased maximum T_1 in all of the considered environmental conditions. The maximum M_{FA} increased for TLPWT 2 in idling conditions, but was almost unchanged in operational conditions compared to the first-order loads. On the other hand, the maximum M_{FA} for TLPWT 3 increased in all conditions, particularly in idling conditions. The reason for the difference in the tower base load response between TLPWTs 2 and 3 is related to the phasing of the responses.

Fig. 5.18 illustrates one instance of the response to a ringing load for TLPWTs 2 and 3 in an operating condition, where there is a mean positive

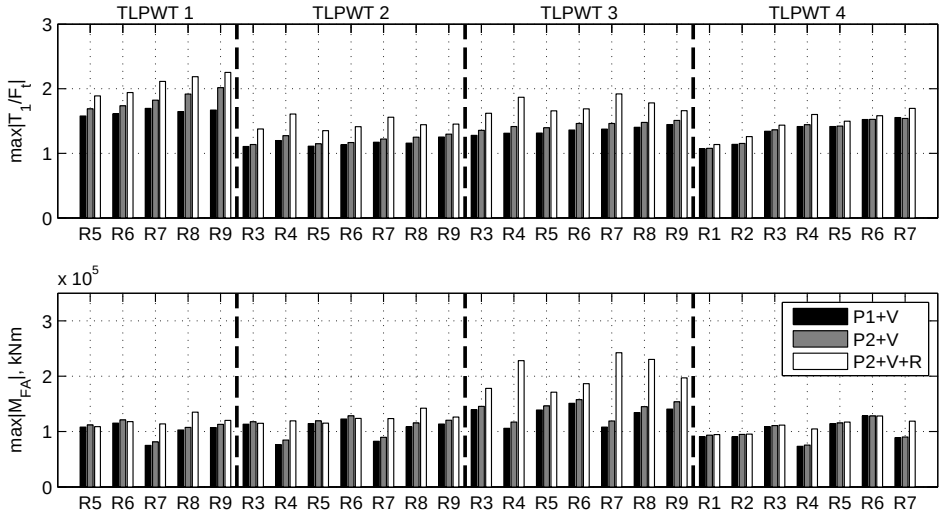

Figure 5.17: Baseline designs: 1-hour expected maximum tension in the downwind tendon (divided by pretension, top) and fore-aft tower base bending moment (bottom)

bending moment at the tower base due to the thrust force. The ringing force decreases M_{FA} at the peak of the first-order response, but adds a peak shortly afterward. This peak is larger for TLPWT 3, which is lighter, has larger pretension, and has a smaller tendon radius. The first-order variation in tension relative to pretension is smaller for TLPWT 2, but the ringing-induced variation is larger, which allows the platform to take up more of the ringing load in the tendons than in the tower base.

Ringing had less impact on the maximum loads for TLPWT 4. An increase in the maximum T_1 (5-10%) was seen in all of the studied environmental conditions, and the maximum M_{FA} increased in idling conditions. For all of the TLPWTs, the maximum M_{FA} in idling conditions (R4, R7, R8, R9) tended to be smaller than the maximum load in operational conditions when ringing was not accounted for, but increased to similar or larger levels when ringing was included in the analysis.

For all of the baseline TLPWTs, ringing loads also caused an increase in the maximum tower top fore-aft bending moment in idling cases, but that moment was much smaller than the moment encountered in operating conditions. The side-side bending moments at the tower top and base, blade root bending moments, and surge and yaw motions were not strongly

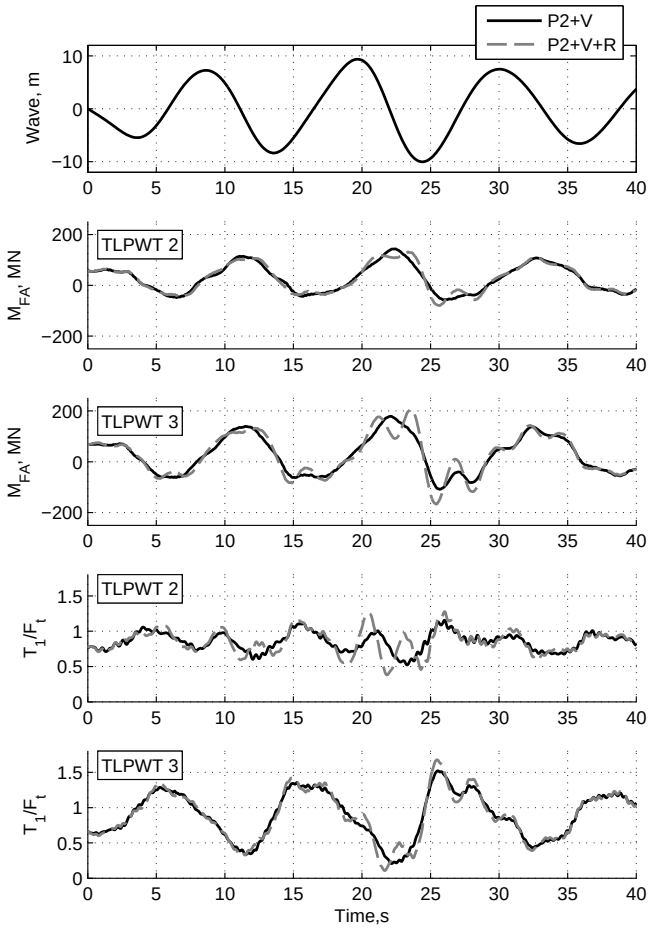

Figure 5.18: TLPWTs 2 and 3: wave, fore-aft tower base bending moment, and tension in the downwind tendon (divided by pretension). R6 (H_s = 9.36 m, $T_p = 11.0$ s)

affected by ringing loads. Ringing-induced increases in the maximum and standard deviation of the edgewise blade root bending moment were observed for idling conditions, but the blade root loads were otherwise largely unchanged.

Fig. 5.19 shows the 1-hour expected short-term fatigue damage in the downwind tendon for the baseline designs. Clearly, the load oscillations after a ringing event also contribute to fatigue. The tendon fatigue damage due

to ringing was particularly large for idling cases. The fatigue damage at the tower base (not shown) followed the maximum M_{FA} patterns quite closely, with TLPWT 3 suffering the greatest increase in damage due to ringing loads. The present calculations indicate that the fatigue damage estimates for these environmental conditions are sensitive to the ringing loads, but do not consider the likelihood of encountering such environmental conditions.

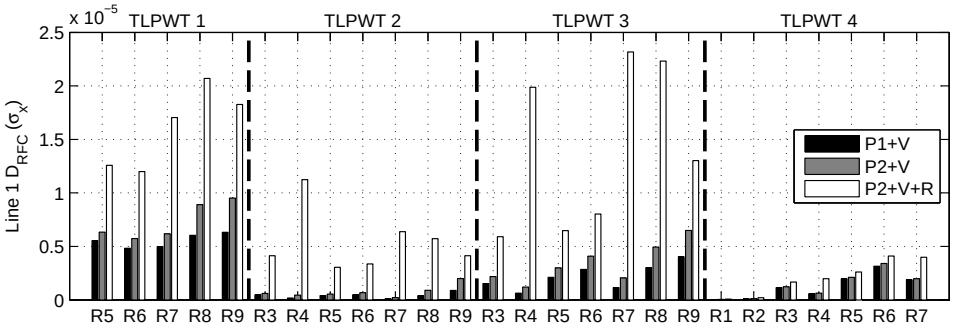

Figure 5.19: Baseline designs: 1-hour expected fatigue damage at the fairlead of the downwind tendon. See Table 3.8 for definitions of conditions R1-R9.

Ringing also affected the short-term fatigue at the tower top in idling conditions, but the fatigue damage there was still much smaller than during the operational cases. In order to understand the effects of ringing on fatigue, a full long-term analysis should be carried out. The conditions which result in ringing do not occur often, but their contribution to fatigue should be considered in light of the full lifetime of the TLPWT.

5.2.3.2 Soft TLPWT Designs

Ringing was found to have severe consequences for the baseline designs. This section presents the effects of ringing loads on the maximum loads and fatigue damage of soft TLPWTs.

Fig. 5.20 shows the 1-hour maximum of T_1 and M_{FA} for the designs with softened tendons. Comparing Figs. 5.17 and 5.20, one can see that the soft designs performed slightly worse than the stiff designs in terms of maximum loads, although TLPWT 4 did not experience very large increases in the loads.

Furthermore, Fig. 5.20 shows that the maximum value of M_{FA} greatly increased for soft TLPWTs 1 and 2 when ringing forces were included in the analysis. The maximum value of T_1 increased for the idling cases. These

TLPWTs have natural pitch bending periods of 3.15 s and 3.79 s, making them particularly sensitive to the third-order loads.

For the soft version of TLPWT 3, second-order forces had a large effect on both T_1 and M_{FA}, but the ringing forces resulted in only a small modification to the second-order results. In many conditions, the maximum response was slightly decreased by including ringing forces due to the phase difference in the forcing. The natural pitch/bending period of soft TLPWT 3 was longer than that of the soft versions of TLPWTs 1 and 2, which may place it slightly further from the third-order forcing.

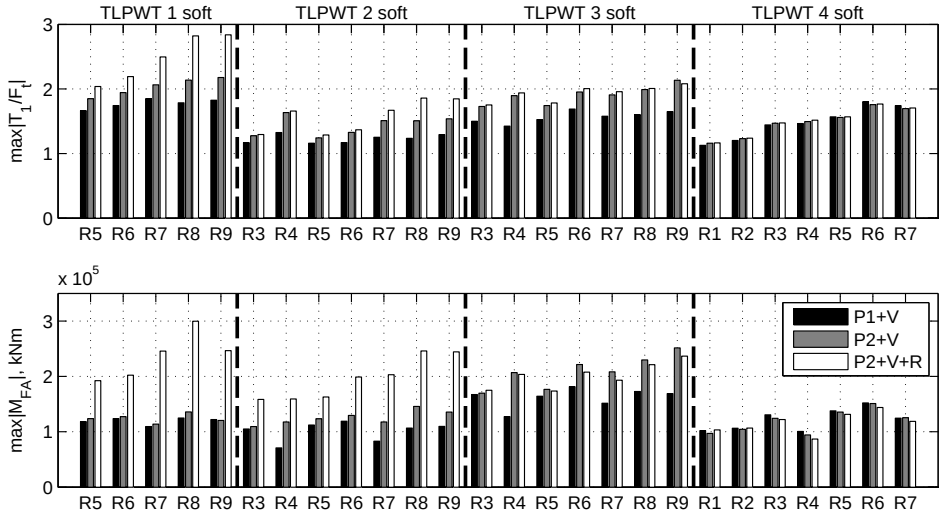

Figure 5.20: Soft designs: 1-hour expected maximum tension in the downwind tendon (divided by pretension, top) and fore-aft tower base bending moment (bottom). See Table 3.8 for definitions of conditions R1-R9.

Similarly, Fig. 5.21, which shows the 1-hour expected fatigue damage in the downwind tendon for the soft designs, suggests that ringing is a particularly important consideration for soft TLPWTs 1 and 2, and that the idling cases are most critical. The tendon fatigue damage for TLPWT 3 depended on the second-order sum-frequency excitation, but was not very sensitive to ringing. The fatigue damage to the downwind tendon of TLPWT 4 did not depend strongly on second-order or third-order forces.

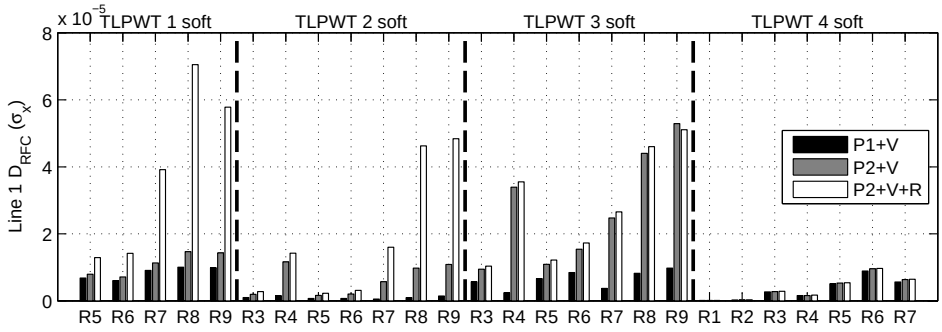

Figure 5.21: Soft designs: 1-hour expected fatigue damage at the fairlead of the downwind tendon. See Table 3.8 for definitions of conditions R1-R9.

5.2.3.3 Operational vs. Parked Turbines

The previously presented results suggested that the tendon tension variation may be quite sensitive to turbine operation. The effect of turbine operation on the response to ringing loads was examined for R5 ($H_s = 8.71$ m, $T_p = 10$ s, $U_w = 24$ m/s) by directly comparing simulations with identical environmental inputs and varying the turbine state. The effect of ringing loads on the expected maxima and on the 1-hour fatigue damage was computed relative to the P2+V simulations. Fig. 5.22 shows the effects of ringing forces on extreme T_1 and M_{FA} and on the fatigue damage in the downwind line and tower base for the operational and idling turbine.

Ringing forces caused an increase in the maximum T_1 regardless of whether or not the turbine was operating. The increase was slightly larger for the idling turbine and for the stiff turbine designs. The effect of ringing on the tendon fatigue damage was, however, more strongly dependent on the turbine operational mode. The simulated 1-hour fatigue damage to the downwind tendon more than doubled for TLPWTs 2 and 3 in the idling condition for R5, suggesting that aerodynamic damping may have an important effect on the ringing-induced short-term fatigue damage in the tendons.

The maximum M_{FA} generally increased more due to ringing when the turbine was idling than when it was operating, but the absolute maximum value was generally larger for an operating turbine (due to the contribution from the thrust force). Ringing caused a very large increase in the tower base damage for the idling turbine, further highlighting the importance of aerodynamic damping in the decay of ringing-induced oscillations.

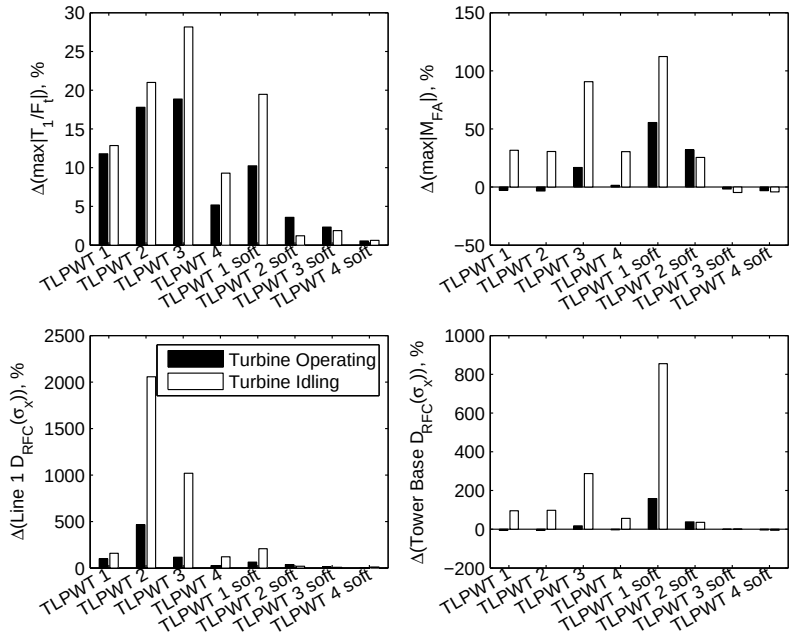

Figure 5.22: Operational and idling turbine: effect of ringing forces on maximum T_1/F_t and M_{FA}, and on the fatigue damage in the downwind line and tower base, environmental condition R5 ($H_s = 8.71$ m, $T_p = 10.$ s)

5.2.3.4 Viscous Damping Effects

In order to examine the effects of viscous damping on the ringing response, simulations for environmental condition R5 ($H_s = 8.71$ m, $T_p = 10$ s, $U_w = 24$ m/s) were carried out for $C_D = 0.4$, 0.7, 1.0, and 1.3. The drag coefficient influences both the wave forcing and damping, but the results were not found to be sensitive to the value of C_D within the given range. As shown in Fig. 5.23, the differences in the maximum T_1 and M_{FA} were less than 3%. The effect on the fatigue damage (not shown) was similarly small.

5.2.3.5 Conclusions

Third-order wave forces on TLPWTs can induce ringing-type responses in a range of environmental conditions which fall along the 50-year probability contour surface for North Sea conditions.

The implementation of the ringing forces is an important consideration. It has been shown that good agreement with experimental results requires

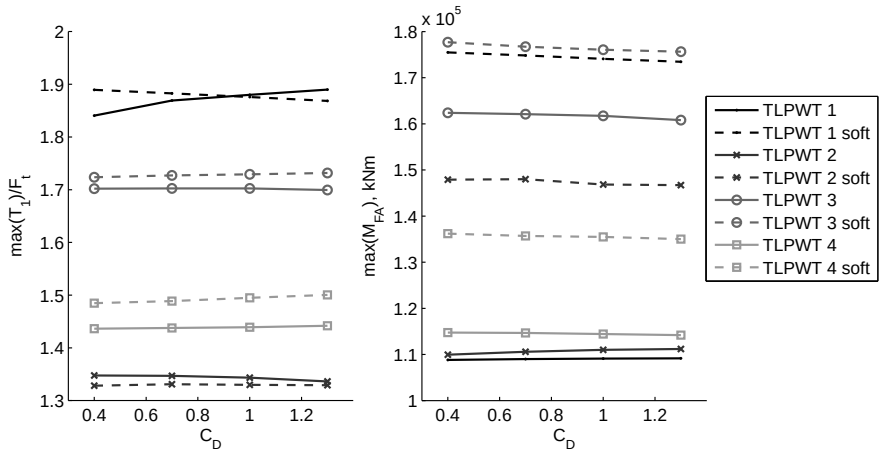

Figure 5.23: The 1-hour expected maximum T_1 and M_{FA} as a function of the viscous damping coefficient, C_D. Results are shown for R5 ($H_s = 8.71$ m, $T_p = 10.$ s), with the turbine operational, second-order forces included, and ringing forces included.

the use of the second-order QTF and the third-order long-wave FNV formulation [104]. A direct implementation of the irregular wave formulation of the FNV equation, however, includes difference-frequency terms which are not desired in the simulation and are over-conservative. In order to give the best possible estimate of the effect of ringing forces, Johannessen's implementation of the ringing force was applied here [107]. Comparisons between Johannessen's implementation and direct implementation of FNV for a single DOF oscillator are included in the work submitted for publication [165].

The effect of ringing forces was seen primarily in the platform pitch motions, which led to increased loads at the base of the tower and in the tendons. Ringing had little effect on surge, roll, and yaw, on the tower top loads, and on the blade loads.

All of the baseline (stiff) designs, with diameter 6.5-18 m and pitch/bending natural period ≈ 2.8 s, showed increased variation in the tendon tension and tower base bending moment when ringing forces were included. Compared to simulations which included only the first and second-order potential flow excitation, the increase in the maximum tendon tension was 12-30 % for TLPWTs 1-3 and 5-10 % for TLPWT 4 (which had the smallest diameter), and did not depend strongly on the turbine operational condition. The increase in the tower base bending moment due to ringing was largest for

idling conditions ($\approx$ 30-40 % increase) and TLPWT 3 was most affected. Within the limited range of studied conditions, ringing also caused increased short-term fatigue damage to the downwind tendon and tower base, particularly in idling conditions.

For the conditions investigated here, the softer TLPWTs showed generally worse performance characteristics with regards to tendon tension variation and the bending moment at the tower base. Ringing forces were found to be most important for the soft versions of TLPWT 1 and 2, which had pitch/bend natural periods of 3.15 and 3.79 s, respectively. Second-order forces were of greater importance for TLPWT 3, which had its pitch/bend natural period at 4.10 s. Both the extreme loads and the fatigue damage increased for the soft versions of the designs compared to the baseline versions.

Viscous damping had very little effect on the extreme loads or on the fatigue, but the aerodynamic damping caused ringing loads to have less relative effect on fatigue in the tendons and tower base for an operating turbine compared to an idling turbine.

The present study considered a limited number of environmental conditions – all of which had aligned wind and long-crested waves. The effects of structural damping on the ringing response were not examined. Although existing load models for the third-order excitation may still be conservative, the present results suggest that ringing may pose a serious problem for TLPWTs in certain environmental conditions. Negative tension was encountered due to ringing loads in at least one simulation of each TLPWT studied here. TLPWT 1 showed a significant number of negative tension incidents, with somewhat more frequent occurrence for the soft version than the baseline version. In order to better understand the effect of ringing forces on extreme loads and on fatigue damage, long-term analysis needs to be performed.

Chapter 6

Severe Operational Conditions

6.1 Effects of Wind Turbine Controller Faults on TLPWTs

Control system faults are the first of two types of severe operational conditions that were examined for TLPWTs. This section examines the dynamic response of TLPWTs during selected control system faults. For pitch-regulated wind turbines, the blade pitch control system contributes significantly to the failure rate [18]. Two types of faults were chosen for study: blade pitch actuator faults and grid loss (see also Sec. 3.4.3.1). In the case of blade pitch actuator faults, the response was studied with and without emergency shutdown of the turbine. For grid loss, emergency shutdown was always considered (to avoid severe overspeed).

This study was initially performed in collaboration with several PhD students at CeSOS: key results and concept comparisons were published in [76]. Additional results for the soft version of TLPWT 3 are included here for comparison with the results for TLPWT 3 and the OC3 Hywind spar wind turbine. Semi-submersible wind turbines, which were studied by M. Kvittem and C. Luan, are not included in this thesis.

First, the fault conditions are defined in Sec. 6.1.1. Then, the responses to shutdown in constant wind - including the dependence of the responses on the azimuth angle at the time of fault and the effects of varying the blade pitch rate - are examined in Sec. 6.1.2. The dynamic responses to controller fault in irregular waves and turbulent wind are studied in Sec. 6.1.3.

6.1.1 Fault Conditions

Four conditions are examined when considering controller fault:

A) Fault-free: normal power generation in ECs F1-F5 and F7, idling in EC F6 (see Table 3.9).

B) Blade seize: the pitch actuator of one blade is blocked at time t_f and the turbine continues to operate for 10 minutes, with the controller trying to maintain the desired rotational speed by pitching the other two blades.

C) Blade seize followed by shutdown: the pitch actuator of one blade is blocked at time t_f, and the controller reacts by shutting down after detection time t_d.

D) Grid loss followed by shutdown: the grid is disconnected at time t_f, and the controller reacts by shutting down after detection time t_d.

When shutdown occurs, the grid is disconnected and all blades with working actuators are pitched to feather (90°) at the pitch rate PR. In the current work, the pitch rate during shutdown is chosen to be $PR = 8$ deg/s, the maximum pitch rate suggested in [72]. The pitch rate can have a significant impact on the loads and motions, as discussed in Sec. 6.1.2.2 and studied by Jiang et al. [74].

For fault types B, C, and D, the fault occurred after 400 seconds of normal operation. An additional 600 seconds after fault were simulated in order to capture several subsequent cycles of low-frequency events. For fault types C and D, $t_d = 0.1$ seconds, which is approximately 10 times the sampling frequency of the controller, as in benchmark studies of fault tolerant control [167].

The wind turbine behavior during fault type C is illustrated in Fig. 6.1 for the land-based NREL 5 MW wind turbine. As shown, the non-faulted blades reached full feather within approximately 10 seconds, and the turbine slowed down within 20 seconds. Fig. 6.1 also shows the characteristic negative thrust and torque during shutdown: the fast pitching action pulled the rotor back into the wind. During shutdown without blade pitch fault, the turbine stopped within 12 seconds, and the peaks in thrust and torque were even more pronounced.

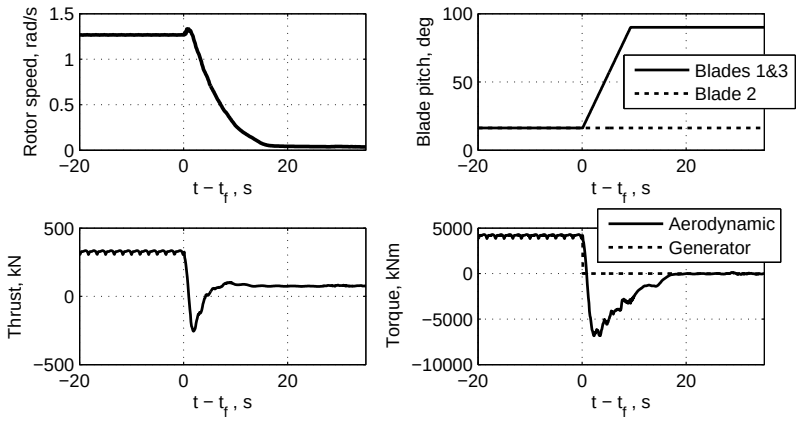

Figure 6.1: Fixed wind turbine: blade 2 seize followed by shutdown (fault type C). Constant wind, 20 m/s.

6.1.2 Constant Wind

Before considering the full response of floating platforms to fault conditions in turbulent wind and irregular waves, an investigation into the deterministic component of the response to controller fault was needed. Constant wind simulations were therefore carried out for the land-based turbine and for TLPWT 3.

Type B faults are, of course, meaningless in constant wind, since an ideal blade pitch controller maintains a constant pitch angle in constant wind. For fault types C and D, however, it is interesting to investigate the importance of the azimuth angle on the blade and tower response during shutdown (Sec. 6.1.2.1) and the impact of blade pitch rate on the response (Sec. 6.1.2.2).

6.1.2.1 Azimuth Angle Dependence

The j-th blade azimuth angle (φ_j) is defined as zero when the blade is oriented directly upward, and increases in the same direction as the turbine rotates (Fig. 6.2). In this section, constant wind results are presented with reference to the φ_2 at the time of fault (t_f), since blade 2 is typically assigned as the "faulty" blade for types B and C controller faults.

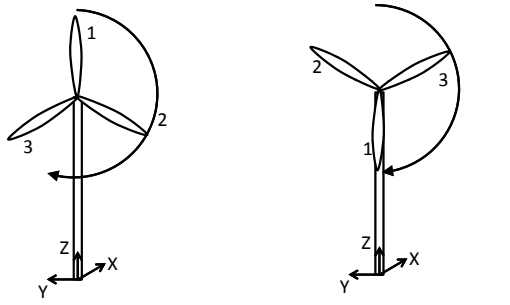

(a) $\varphi_1 = 0$ degrees (b) $\varphi_1 = 180$ degrees

Figure 6.2: Azimuth angle definition for blade 1, including the global coordinate system

As one would expect, given the rotor symmetry, the tower loads did not depend on $\varphi(t_f)$ in response to grid fault followed by shutdown with all three blades pitching properly (fault type D), as shown in Fig. 6.3. For the land-based turbine, a clear dependence on the wind speed can be seen, with wind speeds near rated causing the largest load excursions. For TLPWT 3,

irregular waves were applied together with the constant wind. The wave conditions follow Table 3.10 in Sec. 3.5.2.4. In the case of TLPWT 3 (Fig. 6.3b), the irregular waves added more variation to the results, but there was no dependence on $\varphi(t_f)$. Because the wave height increased with the wind speed, the pattern with respect to wind speed was more difficult to discern when irregular waves were included.

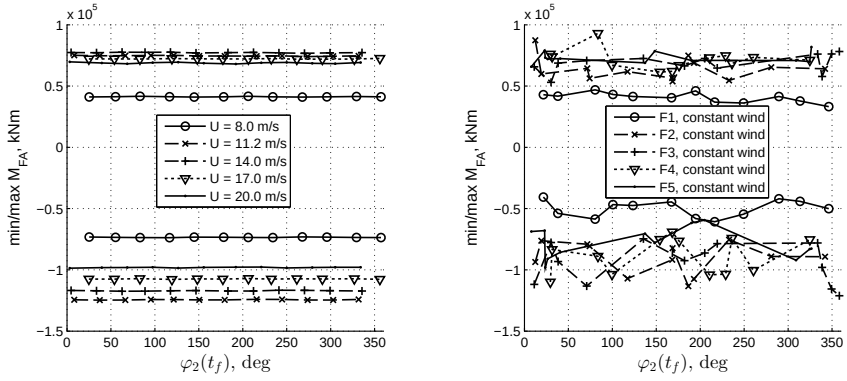

(a) Land-based (b) TLPWT 3

Figure 6.3: Azimuthal dependence of the extreme tower base fore-aft load due to grid loss and shutdown (fault type D). Constant wind speeds 8-20 m/s. Irregular waves are included in the simulations of TLPWT 3.

Moreover, for fault type D, the blade loads depended on $\varphi(t_f)$ due to gravitational loading. Fig. 6.4 shows the maximum flapwise and edgewise blade loads after fault as a function of $\varphi_2(t_f)$. The time to detection was constant ($t_d = 0.1$ seconds), so the azimuth at the start of shutdown ($t = t_f + t_d$) depended on the rotor speed. For 8 m/s wind speed, shutdown began at an azimuth angle approximately 5.5 degrees larger than that at t_f; for wind speeds above rated, $\varphi(t_f + t_d)$ is approximately 7.2 degrees larger than $\varphi(t_f)$.

As shown in Fig. 6.4, for case D, the maximum flapwise loads occurred if the blade was approximately 90 degrees past the upward vertical position at the time of fault (on the way down). Note that, as a blade pitches to feather, the gravitational loads act increasingly in the flapwise direction, and the flapwise aerodynamic loading eventually decreases. The flapwise loads during shutdown were similar or smaller than the operational loads. The maximum edgewise loads after fault occurred on blades that were approximately 90 degrees past the downward vertical position (on the way up), and could be larger than the operational edgewise loads.

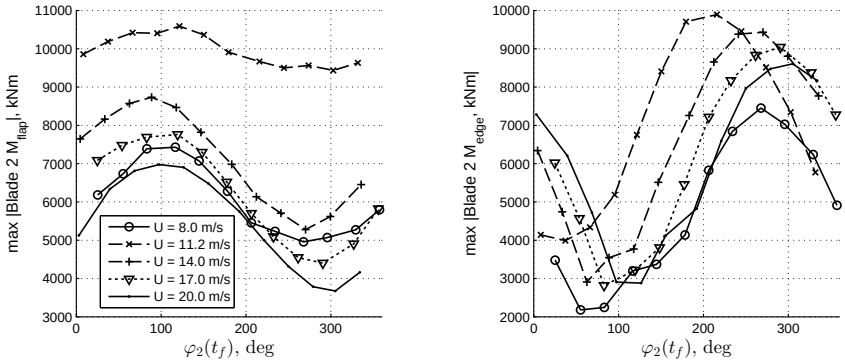

(a) Flapwise (b) Edgewise

Figure 6.4: Azimuthal dependence of the maximum blade root loads due to grid loss and shutdown, land-based wind turbine, constant wind speeds 8-20 m/s.

When blade 2 was not able to pitch to feather (fault type C), $\varphi_2(t_f)$ affected both the tower and blade loads.

The range of the tower base fore-aft bending moment after fault type C is shown in Fig. 6.5 for the land-based turbine and TLPWT 3. The largest load was applied to the tower base when the faulted blade - which continued to provide a thrust force during shutdown - was approaching the vertical upward position at t_f. For the fixed turbine (Fig. 6.5a), $\varphi(t_f)$ can account for a 60 % variation in the fore-aft bending moment range. The same trend was present for TLPWT 3 (Fig. 6.5b), although the wave effects contributed additional load variations.

The land-based wind turbine blade loading in steady wind for fault case C is examined in Fig. 6.6 for the faulted blade (blade 2) and in Fig. 6.7 for a non-faulted blade (blade 1).

The flapwise loads on the faulted blade (Fig. 6.6a) were similar to operational wind loads, while the non-faulted blades encountered both gravitational and aerodynamic loading in the flapwise direction. Furthermore, the flapwise loads on the non-faulted blades in case C (Fig. 6.7a, where only two blades were pitching to feather) were somewhat higher than the loads in case D (Fig. 6.4a), but the same general azimuthal pattern was observed.

The edgewise loads on the faulted blade were smaller than the edgewise loads on the pitching blades (Figs. 6.6b and 6.7b). The edgewise loads on the faulted blade were only slightly larger than the operational loads, while transient edgewise loading affected the pitching blades during the shutdown

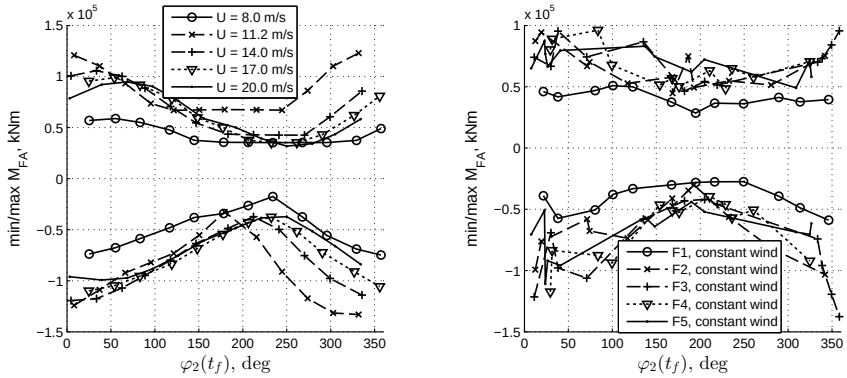

(a) Land-based (b) TLPWT 3

Figure 6.5: Azimuthal dependence of the extreme tower base fore-aft load due to grid loss and shutdown (fault type C), constant wind speeds 8-20 m/s. Irregular waves are included in the simulations of TLPWT 3.

process. The magnitude of the dynamic loading depended partly on gravitational loads, such that the extreme edgewise load depended strongly on φ. The edgewise loads on the non-faulted blades were similar in magnitude to those encountered for type D fault.

For the TLPWTs and spar, similar results were obtained for the azimuthal dependence of the tower and blade loads as for the land-based turbine. Furthermore, the maximum yaw angle in fault case C was found to depend on $\varphi(t_f)$. For TLPWT 3, approximately one degree of the yaw angle variation could be explained by azimuthal variation, with the maximum yaw amplitudes occurring when the faulted blade was near 90 or 270 degrees at the start of the shutdown process.

6.1.2.2 Pitch Rate Dependence

All of the irregular wave and turbulent conditions were studied with a constant value of the blade pitch rate for emergency shutdown ($PR = 8$ deg/s). Jiang et al. showed that the pitch rate affects the loads and motions of land-based and spar wind turbines [74]. Larger turbine loads and decreased platform motions were seen as PR increased. An example of the fixed turbine response for a type C fault with different pitch rates is shown in Fig. 6.8. As expected, the turbine came to a stop sooner when a higher blade pitch rate was used, but the peaks in the negative thrust and torque loads were larger. For a slower pitch rate, the maximum load was smaller,

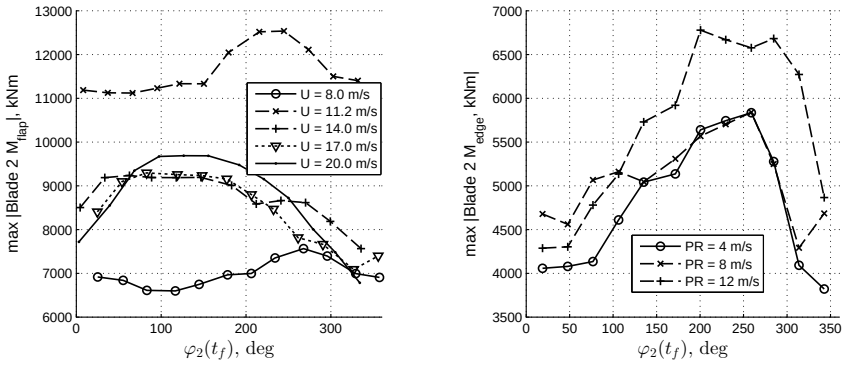

(a) Flapwise (b) Edgewise

Figure 6.6: Azimuthal dependence of the maximum blade root loads on the faulted blade due to blade pitch actuator fault and shutdown, land-based wind turbine, constant wind speeds 8-20 m/s

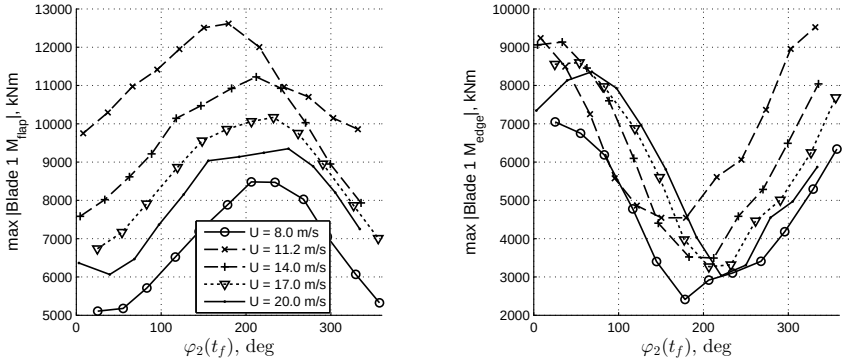

(a) Flapwise (b) Edgewise

Figure 6.7: Azimuthal dependence of the maximum blade root loads on a non-faulted blade due to blade pitch actuator fault and shutdown, land-based wind turbine

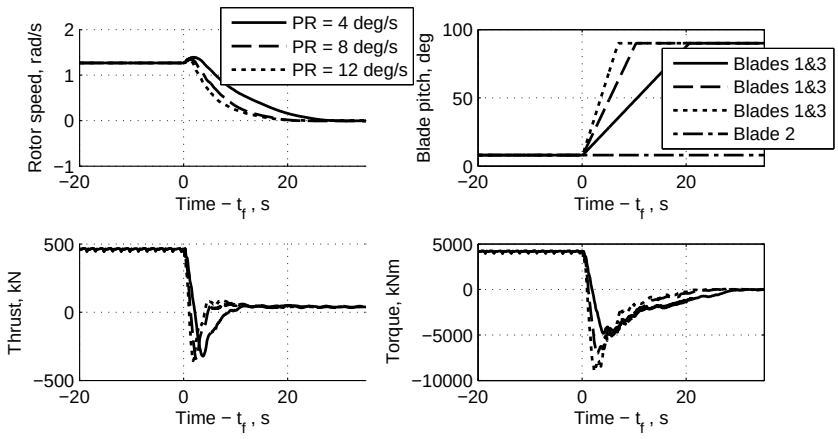

Figure 6.8: Fixed wind turbine: blade 2 seize followed by shutdown (fault type C). Constant wind, 14 m/s.

but the large negative thrust and torque persisted for a longer time period.

For comparison, a brief investigation of the effects of varying PR was performed for TLPWT 3 in constant wind (14 m/s) without waves. The minimum/maximum tower base M_{FA} and the maximum yaw motion amplitude (ζ_6) for type C fault with $PR = 4, 8, 12$ deg/s are shown in Fig. 6.9. As shown, increasing the pitch rate caused increased loads and motions, and decreasing the pitch rate caused decreased response. Surge and pitch motions also increased (decreased) with increasing (decreasing) pitch rate, in contrast to the softer spar platform. The blade loads also tended to increase (decrease) with increasing (decreasing) blade pitch rate, as illustrated for type D fault in Fig. 6.10.

These results suggest that slower blade pitch rate during emergency stop could be considered in order to reduce loads on TLPWTs, without increasing the platform motions. Such a decision would, of course, require operators to accept the increased time required for complete stop.

6.1.3 Turbulent Wind and Irregular Waves

After the constant wind study, fault types A-D were implemented in 5 different environmental conditions (F1-F5), and two additional conditions were examined without fault (F6-F7). As described in Table 3.10 in Sec. 3.5.2.4, ECs F1-F5 represented a range of typical operational conditions. EC F6 was a storm condition, where the turbine idled, and EC F7 was an extreme turbulence condition close to the rated wind speed, which is associated with

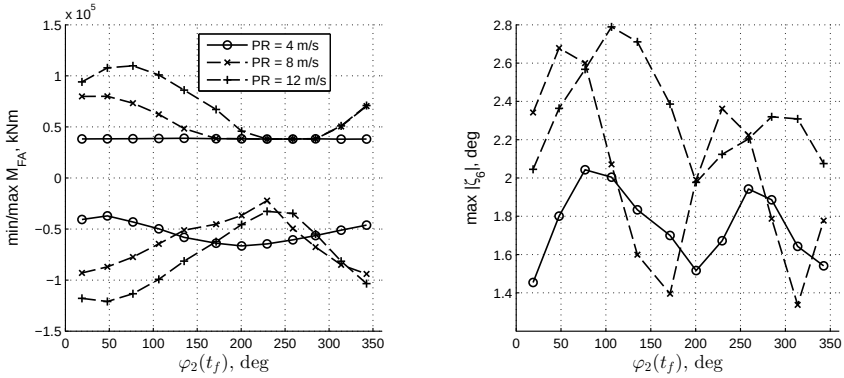

(a) Tower base M_{FA} (b) Yaw motion

Figure 6.9: Pitch rate dependence of tower base fore-aft bending load and yaw motion, fault C, TLPWT 3, 14 m/s constant wind, no waves

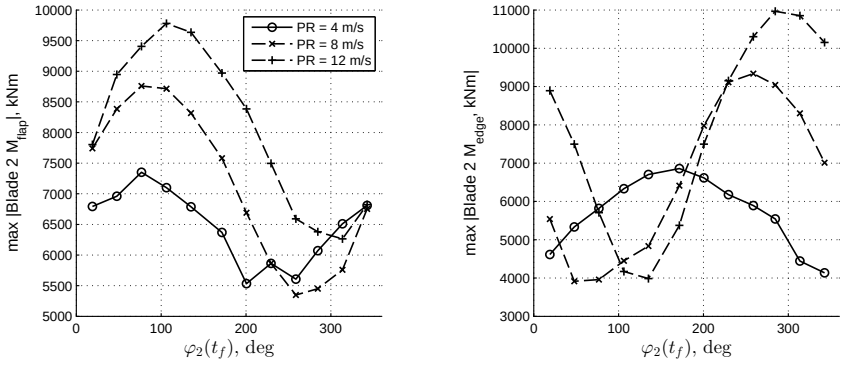

(a) Flapwise (b) Edgewise

Figure 6.10: Pitch rate dependence of blade root bending loads, fault D, TLPWT 3, 14 m/s constant wind, no waves

the maximum thrust. ECs F6 and F7 were included in order to provide a "severe load" with which the fault-induced loads could be compared.

The number and length of simulations were chosen in order to provide a reasonable statistical basis for comparison. In conditions F6 and F7, where the load maxima were expected to be driven by waves or lower-frequency wind variations, six three hour simulations were considered. For fault cases, where the deterministic fault event is expected to dominate, 30 shorter simulations were carried out. Current offshore wind turbine standards suggest that 12 10-minute simulations be carried out for power production plus fault cases [6], but 30 simulations were employed here in order to capture some of the significant stochastic and azimuthal variation [74].

6.1.3.1 Response Maxima

Choosing a consistent method to define maxima is particularly challenging when comparing the fault-induced response, which is a short-term response and often dominated by the transients in the shut-down procedure, and the response in an extreme sea state, which is considered to last for three hours at a time. Adding to the complexity is the azimuth dependence of some fault-induced responses (particularly fault case C). Two different methods were considered:

1. Absolute maximum: largest absolute value encountered in all 30 1000-second simulations (ECs F1-F5), or all 6 3-hour simulations (ECs F6-F7)

2. Expected maximum: average of the largest absolute value encountered in each of the 30 1000-second simulations (ECs F1-F5) or 6 3-hour simulations (ECs F6-F7).

Table 6.1 shows the combined environmental and fault condition leading to the largest responses using both definitions. The studied responses include the global motions, the moments at the tower top and base in the fore-aft (FA) and side-side (SS) directions, blade root bending moments in the local coordinate system, and the mooring system loads. The most severe mooring system loads were evaluated in different ways for different concepts. For the spar, the tension in the delta lines was measured, while the minimum tendon tension was considered as the representative mooring system response for the TLPWTs.

Table 6.1: Load cases resulting in the absolute maxima (1)/ largest expected maxima (2). Note: blade 2 is the faulted blade for type B and C faults and numbers refer to environmental conditions F1-F7.

Response	Land-based	OC3-Hywind	TLPWT 3	TLPWT 3 soft
Surge (ζ_1)	-	6A/6A	6A/6A	6A/6A
Sway (ζ_2)	-	6A/6A	6A/6A	6A/6A
Heave (ζ_3)	-	6A/6A	6A/6A	6A/6A
Roll (ζ_4)	-	6A/6A	6A/6A	6A/6A
Pitch (ζ_5)	-	6A/6A	6A/6A	6A/6A
Yaw (ζ_6)	-	6A/6A	5C/5C	5C/5C
Tower base M_{FA}	2C/2D	6A/6A	6A/6A	6A/6A
Tower base M_{SS}	5C/5C	6A/6A	5C/4C	5C/5C
Tower top M_{FA}	2C/2C	2C/2C	3C/2C	3C/2C
Tower top M_{SS}	5B/5B	4B/5B	5B/5B	5B/5B
Blade 1 M_{flap}	4B/7A	4B/7A	5B/7A	5B/7A
Blade 1 M_{edge}	2C/2D	2C/2C	3C/3D	2D/2D
Blade 3 M_{flap}	4B/7A	4B/7A	5B/7A	5B/7A
Blade 3 M_{edge}	2D/2D	3D/5D	2D/4D	2D/2D
Blade 2 M_{flap}	3B/7A	3B/7A	5B/7A	3B/7A
Blade 2 M_{edge}	3D/3D	5D/3D	2D/3D	5D/2D
Mooring system	-	6A/6A	6A/6A	6A/6A

Table 6.1 highlights several important results:

- The global motions and (consequently) the mooring loads were dominated by the extreme wave condition (F6A), while blade and tower top bending moments were more affected by fault conditions.

- The absolute extreme blade bending loads tended to occur in fault conditions. Flapwise loads were particularly sensitive to imbalance (fault type B), while edgewise loads were most sensitive to shutdown (fault types C and D).

- The extreme blade bending moments depended on the extreme value computation method. While fault conditions may yield the absolute extreme value, the expected maximum value for flapwise loads tended to occur in the extreme turbulence condition (F7A). It is important

to note that the expected maxima for conditions F6 and F7 effectively represent 3.6 times longer time series than the fault conditions. The expected extreme value of a distribution increases when a longer time period is considered [119, Ch. 10.7]. Furthermore, averaging over the randomly distributed azimuth angles for different fault conditions does not necessarily give a good estimate of the condition which will lead to the absolute extreme value (see also Sec. 6.1.2.1 and [74]).

- The tower top bending moments, which are representative of the shaft loading, were sensitive to imbalance loads. The fore-aft tower top loads were largest for blade imbalance followed by shutdown in near-rated conditions, while side-side tower top loads were dominated by blade imbalance at higher wind speeds.

It is important to note, however, that Table 6.1 does not give any indication of the relative severity of different loads, nor does it show the statistical variation present in the extreme values. An illustration of the statistical variation in the maximum value for different simulations is shown in Fig. 6.11. For each environmental and fault condition, the range of the single-simulation maximum absolute value of the fore-aft tower bending moments is shown. The responses in Fig. 6.11 are normalized by the expected absolute value for each condition.

There was significant stochastic variation in the maxima computed for individual simulations – particularly for fault types B and C, where rotor imbalance was present. In some cases, the absolute maximum was up to 50 % larger than the average of the maxima. The relative variation in the maxima tended to be larger at the tower top than at the base for cases A and B, but large variations were seen at both locations. The variation in the response was fairly consistent for different substructures. The baseline and soft versions of TLPWT 3 showed similar trends compared to the land-based turbine.

The following subsections (6.1.3.2-6.1.3.5) discuss the interesting consequences of pitch actuator fault, grid loss, and shutdown on the motions, mooring system loads, tower loads, and blade loads.

6.1.3.2 Platform Motions and Mooring System Loads

With a few exceptions, the platform motions - and the related mooring system loads - were not very sensitive to fault. The heave motions were wave-driven and unaffected by fault, while the decreased thrust due to shutdown resulted in decreased surge and pitch motion.

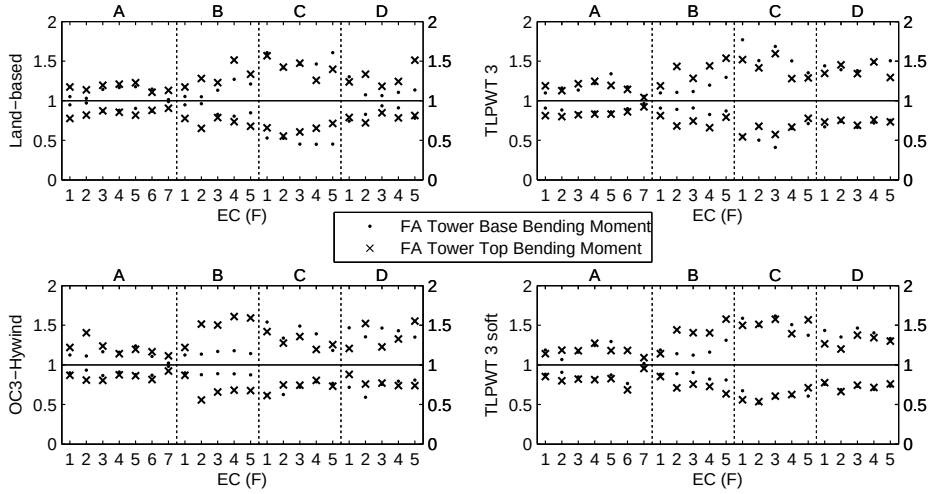

Figure 6.11: Range of absolute maximum response values for different seeds. Land-based, OC3-Hywind spar, and TLPWT 3 (baseline and soft). Response values are normalized by the expected value of the maximum for each fault type (A-D) and EC (1-7).

The sway, roll, and yaw motions, which are generally smaller than the surge and pitch motions, were more affected by controller fault, particularly by imbalance loads. The roll and yaw motions are related: during normal operation, variations in the rotor torque can induce roll motion, which can then induce yaw motion through both wave forces and thrust forces. Additionally, uneven wind across the rotor can induce yaw moments. During blade seize, the yaw motions increased slightly for both the original and soft versions of TLPWT 3 (5-15%) and even more for the spar (up to 50%).

Blade seize followed by shutdown (type C) caused even larger yaw motions: the spar and TLPWT platforms have relatively small inertia and high stiffness, making them responsive to the aerodynamic impulse load. Compared to their normal operation, yaw motions increased by approximately 25% for TLPWT 3, with maximum expected fault-induced yaw of up to 2.9 degrees (2.5 degrees for the soft version), and by almost 400% for the spar (7.3 degrees). The spar experienced only slightly larger yaw motion in the extreme condition (expected maximum 8.3 degrees in F6).

The mooring loads on the original and soft versions of TLPWT 3 generally decreased following fault, because the tendons were most sensitive to platform pitch motion. On the other hand, spar mooring loads were affected

by both yaw and surge motions. The yaw motions due to blade seize caused a 12.5% increase in delta line tension for the spar, while blade seize followed by shutdown led to a 50% increase compared to operational loads. The largest fault-induced mooring loads occurred near the rated condition. The storm-induced loads were, however, still larger (60% larger than operational loads for the spar).

6.1.3.3 Tower Base Bending Moments

The fore-aft tower base bending moment (M_{FA}) is driven by the thrust force, inertial loads, and by the weight of the rotor, which can cause a large bending moment due to platform pitch or tower bending. For the spar and (soft and original) TLPWT 3, shutdown resulted in decreased fore-aft loading due to the decreased thrust, while blade seize had little effect. Shutdown, however, caused relatively large fore-aft tower base bending loads for the land-based wind turbine: the sudden change in the thrust caused relatively large loading at the tower base and lightly-damped vibrations in the first bending mode. Furthermore, the soft version of TLPWT 3 experienced smaller fore-aft loading at the tower base due to shutdown, but larger loading in the extreme environmental condition.

The side-side tower base bending moment (M_{SS}) depends on the torque moment at the top of the tower and the rotor weight (due to sway and roll motions or side-side bending). During normal operation, this moment is much smaller than the fore-aft moment. Fault type D did not result in large tower base side-side loads, but both fault types B and C caused relatively large loads (100 % increase compared to operational conditions). The shutdown process with a faulted blade caused only slightly larger loads than the imbalance condition. Despite the increase, the side-side loads were smaller than the fore-aft moment ($M_{SS} < M_{FA}$).

6.1.3.4 Tower Top Bending Moments

The tower top bending moments, which reflect both aerodynamic loads and loads due to rotor inertia, may be seen as a measure of the drivetrain loads, particularly the shaft bending moments. These loads are known to be larger for floating systems compared to land-based or fixed bottom turbines [168]. As shown in [76], type D faults are unlikely to be design-driving for the tower top, but blade seize - with or without shutdown - could lead to critical load conditions for some platforms.

Figs. 6.12 and 6.13 compare the expected maximum fore-aft and side-side tower top bending moments, respectively. In Figs 6.12 and 6.13, ECs F1-F5

are shown with bars (A), diamonds (B), open circles (C), and triangles (D), and the expected maxima for ECs F6 and F7 for each concept are shown as horizontal lines for comparison. As shown, blade seize increased both the fore-aft and side-side tower top bending moments, particularly in higher wind speeds.

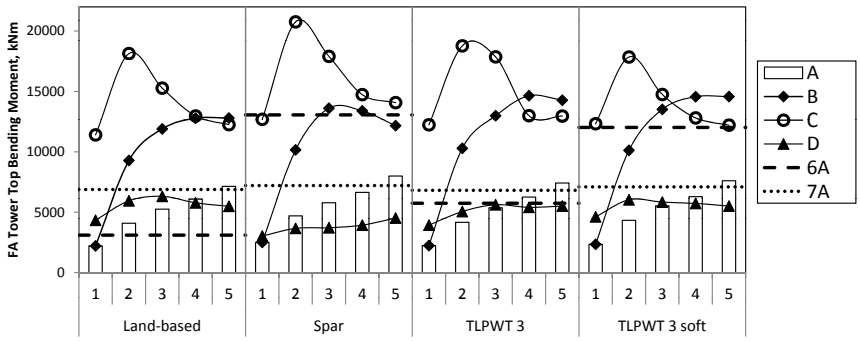

Figure 6.12: Expected maximum tower top fore-aft bending moment for all platforms and conditions.

Fig. 6.12 shows that shutting down the turbine after blade seize error (C) tended to reduce the expected maximum fore-aft moment in high wind speeds for the land-based and TLPWT wind turbines, but tended to greatly increase the maximum load in lower wind speeds. Shutting down the turbine in high wind speeds was less effective for the spar platform: the maximum load due to type C faults was always greater than that due to type B faults. Additionally, Fig. 6.12 shows that the original design of TLPWT 3 was slightly more sensitive to controller fault with respect to the tower top fore-aft loading, while the soft version of TLPWT 3 experienced larger loads in the extreme wind and wave condition (F6).

The side-side bending moment at the tower top was fairly consistent across all platforms. Shutting down the platform gave a clear load reduction of the side-side bending moment for all platforms compared to continued operation with a seized blade (Fig. 6.13).

The nature of the maximum fore-aft tower top load in fault cases B and C is illustrated in Fig. 6.14. When shutdown occurred, the maximum load occurred for a short period immediately after the onset of shutdown, followed by a reduction in the load. The maximum load in case B, on the other hand, took more time to develop. If the blade pitch error were to persist even longer, larger loads than those seen here might occur.

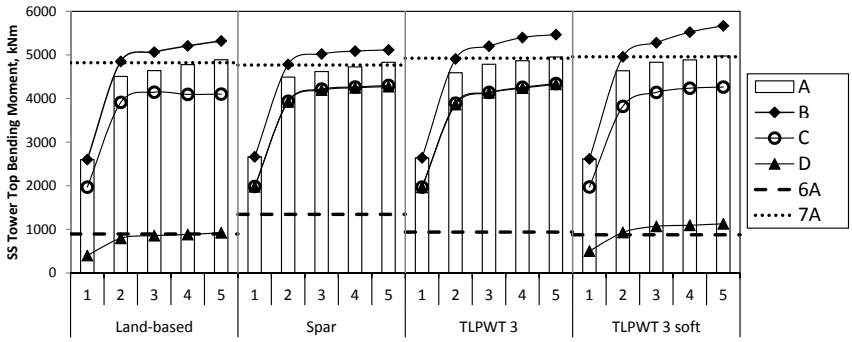

Figure 6.13: Expected maximum tower top side-side bending moment for all platforms and conditions. ECs 1-5 are shown with bars (A), diamonds (B), open circles (C), and triangles (D). The expected maxima for ECs 6 and 7 for each concept are shown as horizontal lines for comparison.

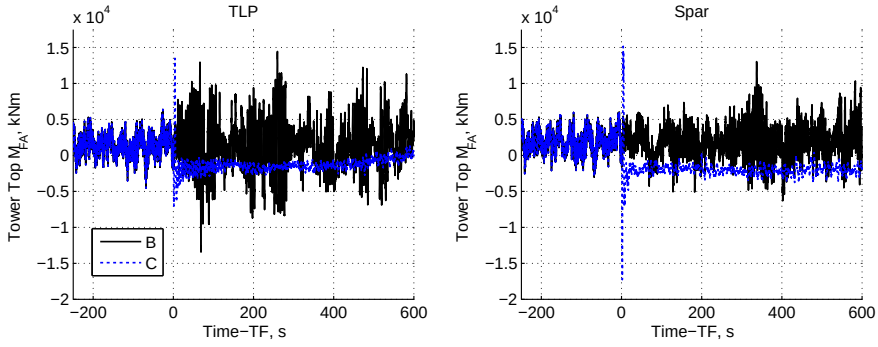

Figure 6.14: Spar and TLP fore-aft tower top bending moment for one realization of EC 5 (cases B and C).

6.1.3.5 Blade Root Bending Moments

In general, the effects of faults and shutdown on the blade loads were similar for all of the platforms (and for the land-based turbine). This is consistent with the steady wind study results (Sec. 6.1.2).

The flapwise bending moment was susceptible to blade seize faults, while shutdown decreased the flapwise loading. Compared to normal operation conditions, blade seize faults (type B) caused small (5-10%) increases in the expected maximum flapwise loads on the faulted blade and somewhat larger (up to 25%) increases for the other two blades. Since the controller continued to try to maintain the rotation speed, the chosen pitch angles for the non-faulted blades often resulted in larger loads. It is expected

that longer simulations with fault case B would result in even larger load increases.

The edgewise bending moment was not affected by blade seize faults, but was sensitive to shutdown. The shutdown process yielded up to 40% increases in the maximum edgewise bending moment compared to normal operational conditions. This increase was observed for all platforms and tended to be maximum near the rated wind speed.

6.1.4 Conclusions

Although extreme weather conditions were found to generally result in more severe motions, mooring loads, and tower base loads, fault conditions were critical in some cases for tower top and blade loads. Furthermore, fault and shutdown induced large yaw motions for the OC3 Hywind spar and both the baseline and soft versions of TLPWT 3.

No unstable behavior was encountered in the simulation of the floating platforms under fault conditions. The nonlinear simulation tool did not reproduce the instability identified by Jonkman and Matha [44, 169] for a TLPWT idling with a blade pitch fault in fault case C after shutdown.

A limited number of realizations of each fault were carried out, and only aligned wind and wave conditions were considered in this section. There are large stochastic variations - and uncertainties - related to the maximum loads induced by fault events. Some of the variation is related to azimuthal variations, while additional uncertainties are related to the stochastic wind and waves (and the phase angle between the platform response and the incoming wind and waves at the time of fault).

6.2 Effects of Wind-Wave Misalignment on TLPWTs

The second severe operational condition that was considered was misalignment between the incoming wind and waves. A selected number of wind-wave misalignment conditions were considered, as illustrated in Fig. 6.15. In all cases, the wind came from the -x direction, and the turbine was aligned with the wind. The wave propagation direction (β_{wave}) varied. The absolute value of the misalignment was limited to 90°, in increments of 30°, as shown in Fig. 6.15.

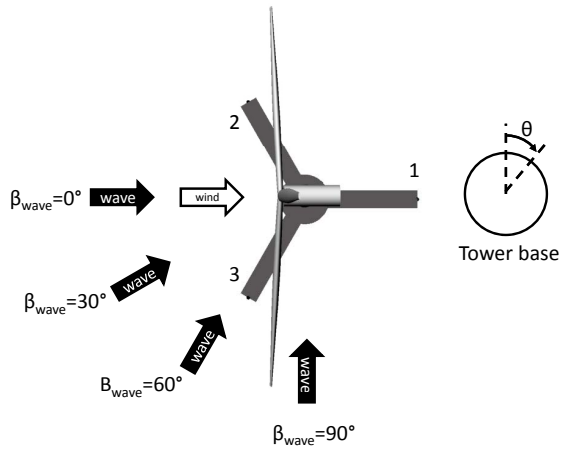

Figure 6.15: Wind-wave misalignment and tower base cross section coordinate system.

These misalignment conditions were applied in a range of operational environmental conditions, M1-M6, as shown in Table 3.10. The effects of misalignment, and the effects of second-order sum-frequency wave forces, on fatigue loads and maximum loads are examined in the following subsections. These results have been submitted for publication [170].

First, the distribution of fatigue damage around the tower base and tower top cross section is examined in Sec. 6.2.1. The tower and tendon fatigue damage in misaligned conditions is examined in Secs. 6.2.2 (first-order wave loads) and 6.2.3 (second-order wave loads). The effects of misalignment on blade root bending moments are briefly examined in Sec. 6.2.4. Finally, the effects of misalignment on the maximum stress in the tower and tendons are presented in Sec. 6.2.5.

6.2.1 Cross-Sectional Fatigue Damage Calculation

There was significant variation in the damage at different points in the tower cross section, as illustrated for the tower base and top in Fig. 6.16. Note that the definition of θ is shown in Fig. 6.15.

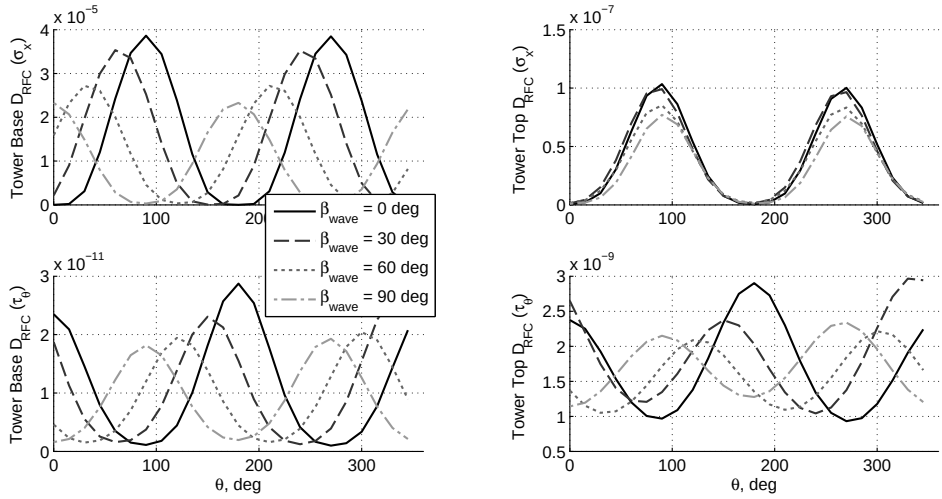

(a) Tower base (b) Tower top

Figure 6.16: Tower base and top damage distribution around the cross section, EC M3.

As shown in Fig. 6.16, $D_{RFC}(\sigma_x)$ at the tower base had two nearly equal maxima, and these were aligned with the wave propagation direction. The damage due to shear stress, which was much smaller in magnitude, also had two maxima, one of which tended to be slightly larger that the other. The location of the maximum $D_{RFC}(\tau_\theta)$ at the tower base was separated from the wave direction by 90 degrees.

At the tower top, $D_{RFC}(\sigma_x)$ depended primarily on the thrust force and did not vary significantly with wave direction. The thrust force creates a bending moment about the tower top due to the offset between the rotor and tower top [72]. The two nearly equal peaks in $D_{RFC}(\sigma_x)$ at the tower top were aligned with the wind. The distribution of $D_{RFC}(\tau_\theta)$ at the tower top was sensitive to the wave direction and followed the same pattern as $D_{RFC}(\tau_\theta)$ at the tower base. While $D_{RFC}(\sigma_x)$ at the tower top was several orders of magnitude smaller than $D_{RFC}(\sigma_x)$ at the tower base due to the difference in moment arm, $D_{RFC}(\tau_\theta)$ was larger at the tower top than at

the base due to the differences in dimensions (6.0 m diameter at the tower base, 3.87 m at the tower top).

The tendon damage was primarily due to tension variations and did not vary significantly around the cross section.

6.2.2 Fatigue Damage from First-Order Wave Loads

Fig. 6.17 shows the computed damage due to axial and shear stresses for both the original and soft designs, as a function of wave direction for different environmental conditions, considering only first-order wave loads. The expected maximum damage is shown: first, the maximum damage among 24 points around the cross section was computed for each simulation, then these values were averaged over 10 seeds for each environmental condition and wave direction. Note that Fig. 6.17 shows the damage multiplied by a scaling factor in ECs M1-M3 in order to make the results more legible.

The top two subplots in Fig. 6.17 show the fatigue damage at the tower base. In general, both $D_{RFC}(\sigma_x)$ and $D_{RFC}(\tau_\theta)$ decreased for increasing misalignment, and the soft design accumulated more fatigue damage than the baseline design. There were some exceptions to these trends: $D_{RFC}(\tau_\theta)$ was slightly greater for waves from 30° than 0° in EC M6, the damage increased with increasing misalignment for the soft design in ECs M1 and M2, and the baseline design had greater $D_{RFC}(\sigma_x)$ in EC M1 due to the interaction between the 3p turbine excitation and the first platform pitch/bending mode.

The third and fourth subplots in Fig. 6.17 show the fatigue damage at the tower top, which exhibited less dependence on the wind-wave misalignment. Except for EC M1, the soft platform encountered slightly more fatigue than the baseline design. In EC M6, $D_{RFC}(\tau_\theta)$ at the tower top was greater for waves from 30° than 0°, but otherwise the damage decreased with increasing misalignment.

The fifth subplot in Fig. 6.17 shows the expected fatigue damage in tendon 1 (downwind). Here, the damage decreased quite clearly for increasing misalignment up to 60°. For the soft TLPWT, the absolute value of the computed fatigue damage is not realistic, since the Young's modulus of the tendons was arbitrarily changed, but the trends are of interest. Furthermore, the other two tendons suffered increased damage when the waves were aligned with their radial position (compared to $\beta_{wave} = 0°$), but tendon 1 in the aligned wind-wave condition was by far the most susceptible to fatigue loading.

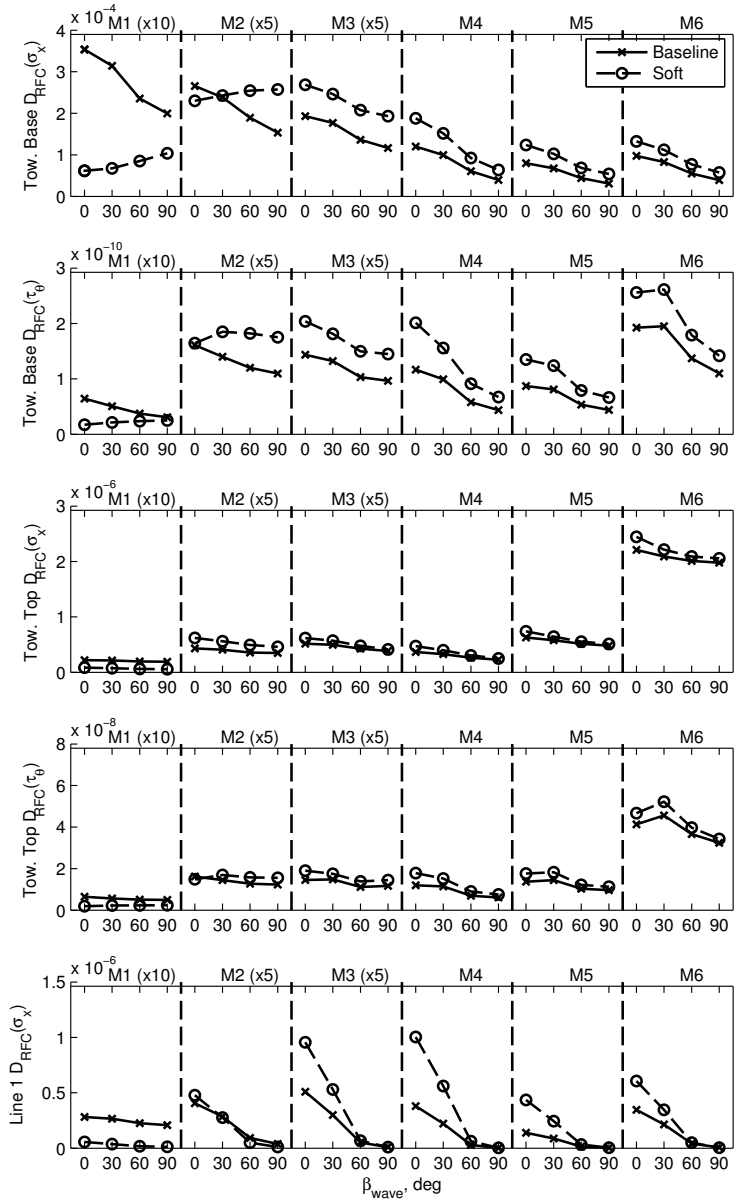

Figure 6.17: One-hour fatigue damage for different load conditions as a function of misalignment. Baseline and soft versions of TLPWT 3, first-order potential flow model.

6.2.3 Second-Order Sum-Frequency Wave Load Effects

Fig. 6.18 shows the computed damage due to axial and shear stresses for both the original and soft designs, as a function of wave direction for differ-

ent environmental conditions, considering both first and second-order wave loads. Fig. 6.19 shows the relative change in the quantities presented in Fig. 6.17 when second-order sum-frequency wave forces are included. A positive ΔD_{RFC} indicates an increase in the computed fatigue damage for the selected condition due to the inclusion of second-order forces.

The second-order forces had a fairly significant impact on the fatigue damage at the tower base in misaligned cases, as shown in the first two subplots in Fig. 6.17. In aligned wind and wave conditions, $D_{RFC}(\sigma_x)$ increased by 1-3 % for the baseline designs, while the soft designs saw 3-13 % increases. In misaligned wind and waves, the differences could be as large as 80 %. Even accounting for the second-order forces, the fatigue damage in the misaligned cases was still significantly lower than that of the aligned cases.

The second-order forces had less effect on the damage at the tower top. The third subplot of Fig. 6.19 shows that $D_{RFC}(\sigma_x)$ at the tower top changed less than 6 %, with the largest changes occurring for the soft design. As shown in the fourth subplot, $D_{RFC}(\tau_\theta)$ increased by up to 40 % at the tower top for severe misalignments, but the changes were small in the aligned conditions (1-2 % for the baseline design, up to 10 % for the soft design). As with the tower base results, the fatigue damage in the aligned condition remained larger than the misaligned conditions (except in EC M6, where 30° misalignment could be more severe for $D_{RFC}(\tau_\theta)$).

The fatigue damage of the tendons was sensitive to second-order forces across all misalignment cases (Fig. 6.19, fifth subplot). For the baseline TLPWT, the effects were on the order of 3-10 %, and did not depend strongly on the wave direction. For the soft TLPWT, the effects were consistently larger, and could account for a 35 % increase in the estimated damage in the aligned wind and wave case. Although the absolute value of the fatigue damage in the soft tendons is not realistic due to the assumed value of the Young's modulus, the effect of the second-order forces is less dependent on such assumptions. Assuming that the chosen slope for the S-N curve is reasonable, the observed increase in the short-term fatigue damage in relatively benign operating conditions suggests that second-order forces should be included in any long-term studies of TLPWT tendon fatigue.

It is also interesting to examine the spectra of the stress when examining the effect of second-order forces on fatigue. As an example, Figs. 6.20a and 6.20b show the axial stress at the tower base for ECs M1 and M4, respectively. For each wave direction, the stress spectrum is shown for a point which corresponds to the maximum damage $D_{RFC}(\sigma_x)$.

As shown in Fig. 6.20a, the f_{3p} excitation in EC M1 led to a large

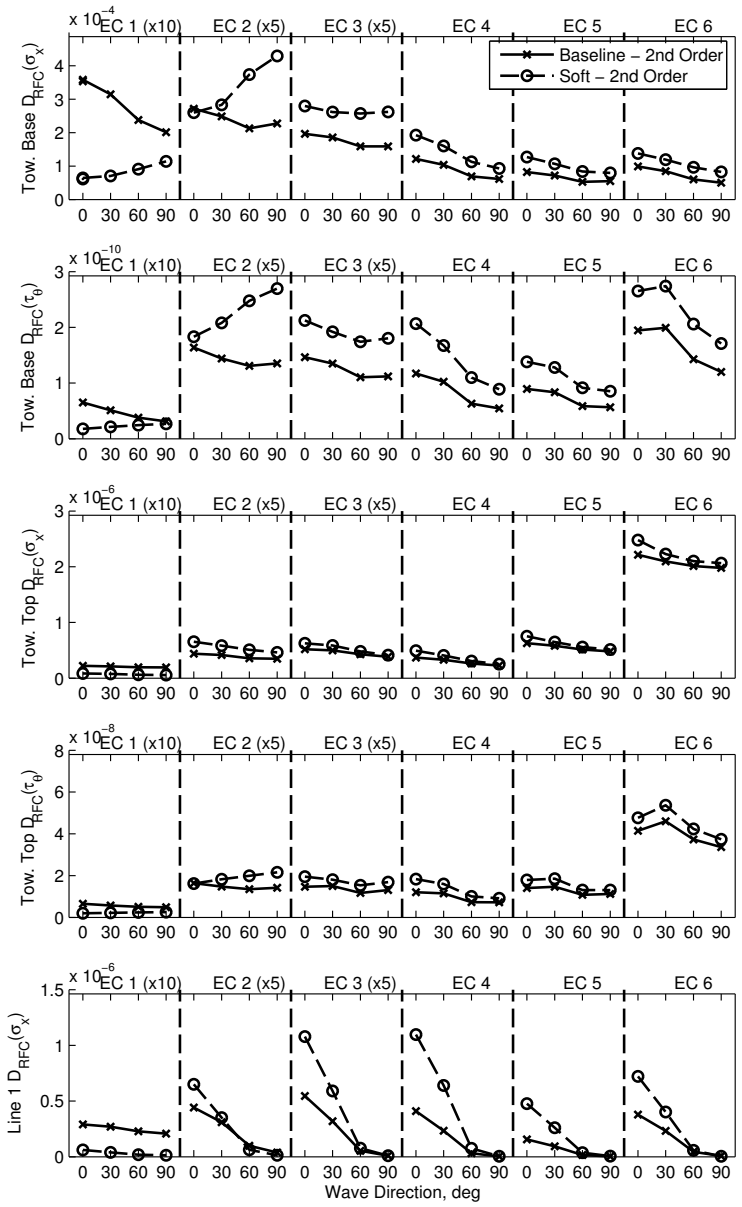

Figure 6.18: One-hour fatigue damage for different load conditions as a function of misalignment. Baseline and soft versions of TLPWT 3, second-order potential flow model.

response at the first pitch/bend natural period. Second-order forces also

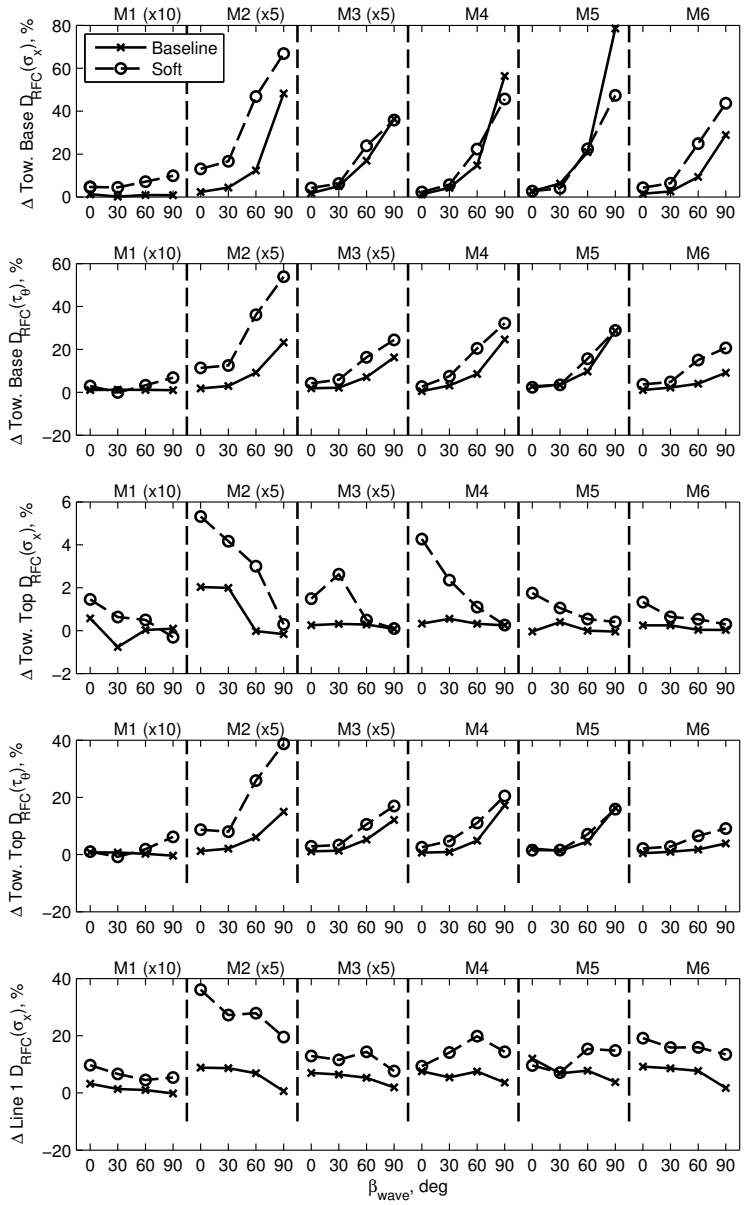

Figure 6.19: Relative change in one-hour fatigue damage for different load conditions as a function of misalignment. Baseline and soft versions of TLPWT 3, P2+V (first- and second-order potential with viscous damping) vs P1+V (1st order potential with viscous damping) models.

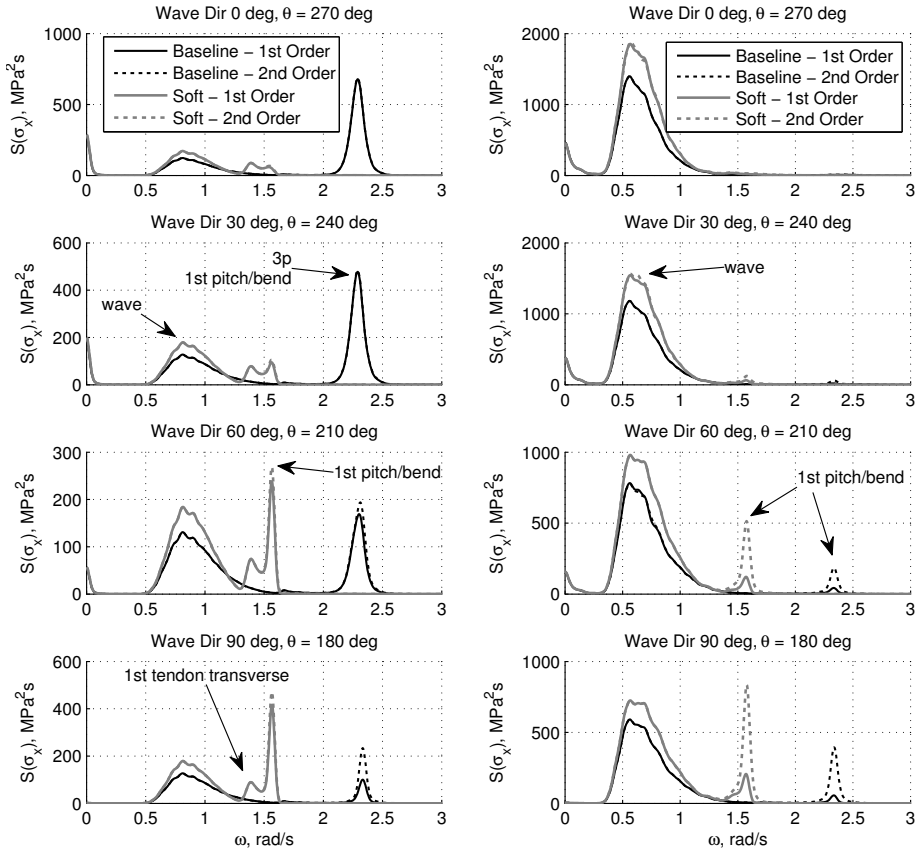

(a) EC M1 (b) EC M4

Figure 6.20: Spectra of axial stress at the tower base, ECs M1 and M4, for varying misalignment. The stress spectra are shown for the point with maximum fatigue damage.

contributed to excitation at such high frequencies. As the misalignment increased, the aerodynamic damping became less effective against the wave-induced response, and the second-order effects become more apparent.

For EC M4 (Fig. 6.20b), the response at the first pitch/bend frequency was much smaller in aligned wind and waves. In misaligned wind and wave conditions, the lack of aerodynamic damping for the second-order excitation nonetheless caused increased response at the first pitch/bend frequency. The contribution from second-order waves was more significant for the soft

design, which encountered more excitation at its (lower) pitch/bend natural frequency.

In the tendon response, the second-order force effects were primarily observed at the pitch/bend natural frequency and, in the case of the soft TLPWT, at the heave natural frequency (which coincided with the second tendon transverse natural frequency). As expected, the second-order forces increased the number of high-frequency, low-amplitude stress cycles.

6.2.4 Blade Root Bending Moments

The effect of misalignment on second-order wave forces on the turbine components can be examined by considering the tower top fatigue damage (which is representative of shaft loads) and by examining blade root bending moments. Fig. 6.21 shows the blade root bending moments for different load conditions as a function of misalignment. As shown, the standard deviation of the flapwise blade root bending moment tended to decrease with increasing misalignment, which can be explained by the fact that the platform motions aligned with the wind direction tended to decrease with increasing misalignment. The edgewise blade root bending moment, which is dominated by gravity loading, was not affected by misalignment. Second-order wave forces had little effect on the blade root bending moments.

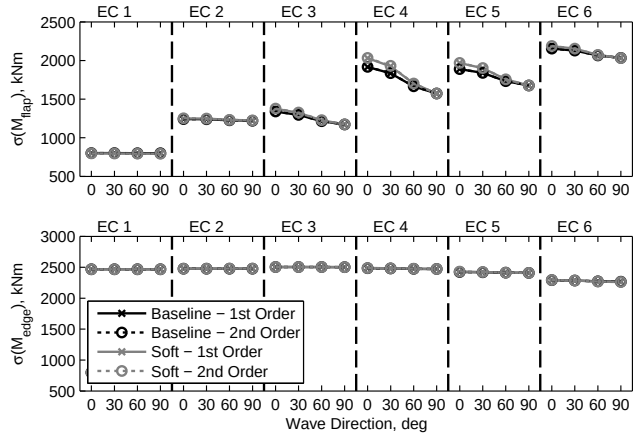

Figure 6.21: Blade root bending moments for different load conditions as a function of misalignment. Baseline and soft versions of TLPWT 3, first- and second-order potential flow models.

6.2.5 Maximum Stress

Second-order wave forces and misalignment may also affect the extreme loads and stresses, not just the fatigue damage. In agreement with the results for a spar wind turbine presented by Barj et al. [21], misalignment caused an increase in the maximum side-side tower base loads and in the maximum tendon loads (depending on the tendon orientation). It is, however, more interesting to examine whether or not this increase in side-side loads corresponds to an increase in stress.

First, the cross section location (θ) of the maximum axial stress (tension or compression) in the tower base for all simulations is plotted in Fig. 6.22. As shown, the maximum stress generally occurred on the downwind side of the tower and followed the wave direction, except for 90° misalignment, where there was more spread in the results. The maximum stress location was also more variable for the soft design than for the baseline design.

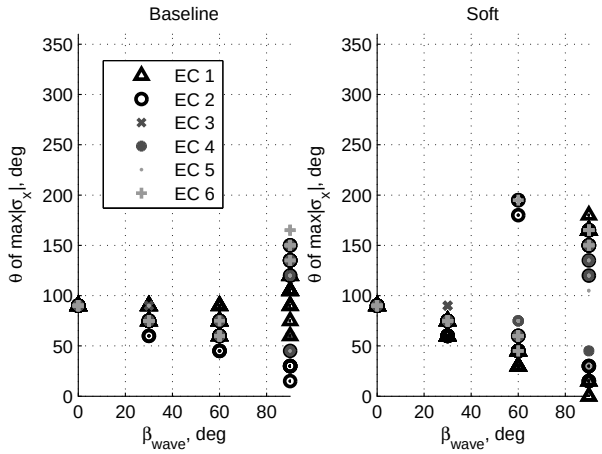

Figure 6.22: Cross-sectional location of maximum stress as a function of misalignment, all seeds, all conditions.

Next, Fig. 6.23 shows the expected maximum stress at the tower top and tower base, as well as the minimum tension in the downwind line, as a function of the wave direction. The results for first-order wave forces are shown with open circle symbols, while results that include the second-order sum-frequency potential are shown with "x" symbols.

The first two rows of subplots of Fig. 6.23 show that the maximum axial and shear stresses at the tower base tend to decrease with increasing misalignment. Sum-frequency forces caused a noticeable increase in the maximum stress for 90° waves, but had relatively little effect on the max-

imum stress in other conditions. In some cases, the expected maximum stress for the soft TLPWT was slightly smaller when second-order effects were included, but the differences were not significant. Furthermore, at the tower top, the maximum stress was not strongly dependent on the wave direction, and second-order forces had almost no effect.

In the last row of Fig. 6.23, the expected minimum tension is shown as a function of wave direction. The expected minimum tension is computed based on 10 1-hour simulations in each condition. As shown, the minimum tension increased for increasing misalignment, that is, the risk of slack decreased for increasing misalignment. The wind force generally determined the mean tension value, but the wave forces largely determined the standard deviation. In the aligned conditions, the second-order forces resulted in a decrease in the expected minimum tension of approximately 3 %. It should be noted that slack is not expected in these operational conditions, and that extreme environmental conditions were not included here.

6.2.6 Conclusions

The dynamic response of the baseline and soft versions of TLPWT 3 in both aligned and misaligned wind and wave conditions, with and without second-order sum-frequency potential forces, was investigated.

The fatigue damage decreased in misaligned wind and wave conditions, but the relative effect of second-order forces increased. In severe misalignment, the inclusion of second-order forces could increase the predicted tower base fatigue by up to 80 %. The short-term fatigue damage computed for the soft TLPWT design was particularly sensitive to sum-frequency forces, especially in the tendons. It is recommended that sum-frequency forces be included in long-term fatigue studies of TLPWTs.

Despite the increase in side-side loading in misaligned conditions, aligned conditions were associated with larger short-term maximum stresses (in operational conditions). These results are limited to conditions which are not, however, expected to lead to lifetime maxima. Further work should investigate the effects of wind and wave misalignment on the response in more severe wave conditions. Additional designs, with differing diameters and geometries, should also be examined.

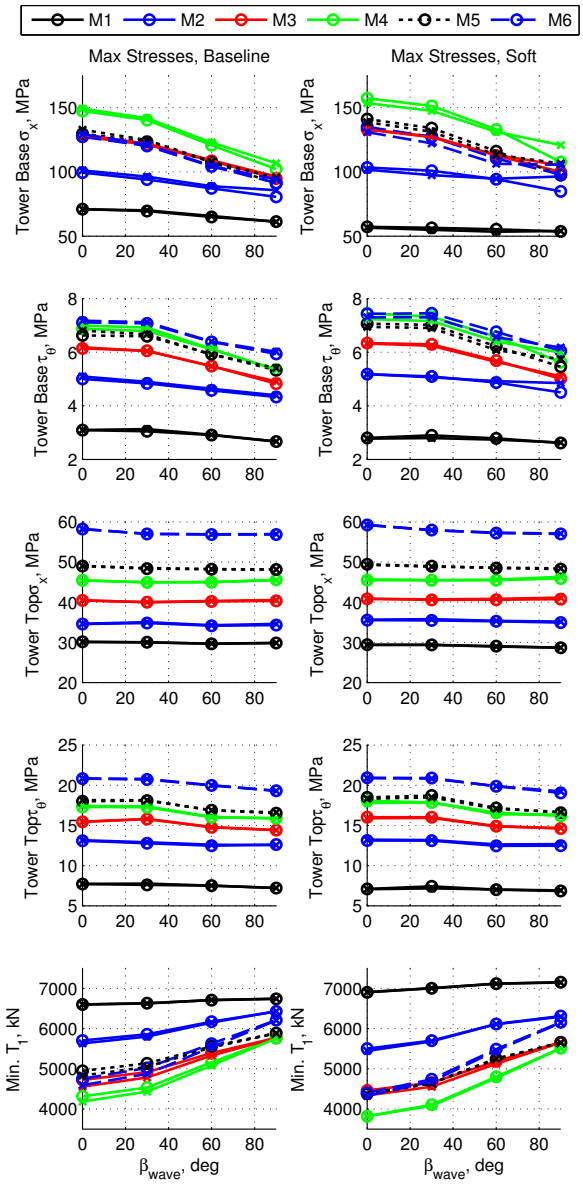

Figure 6.23: Expected maximum stress and minimum tension. Note: "o" indicates P1+V (first-order potential with viscous damping), "x" indicates P2+V (first- and second-order potential with viscous damping).

Chapter 7

Conclusions and Recommendations for Future Work

This thesis examined the design and global analysis of single-column 5 MW TLPWT designs in an effort to inform researchers, designers, and regulatory bodies about the global dynamic response of such concepts. A new computational tool - SIMO-RIFLEX-AeroDyn - was developed and used to examine a range of parametric designs. The effects of higher order hydrodynamic models and atypical operational conditions were also examined. The key results for the design study, analysis sensitivity study, and the simulations of severe operational conditions are summarized in Secs. 7.1-7.3. The original contributions to our understanding of TLPWT design and analysis are summarized in Sec. 7.4. Some of the limitations of the present analysis are noted in Sec. 7.5, while suggestions for future work are listed in Sec. 7.6.

7.1 TLPWT Design

The design space considered here included single-column TLPWTs with three or four "spokes" or pontoons, intended to support the NREL 5MW wind turbine with the OC3 Hywind tower design [72, 26]. A spreadsheet design method was developed based on the definition of the hull and tendon parameters: approximate calculations of hydrodynamic coefficients and mooring system stiffness were used to check if the input parameters resulted in a design that met certain criteria. These design criteria were based on natural periods, the estimated mean offset, the displacement, and the ten-

don yield strength.

An important weakness in the spreadsheet design approach was the assumption of a fully rigid structure: the coupled platform pitch/tower bending natural frequency could not be estimated. After selecting several baseline designs, a more detailed hydrodynamic and structural analysis was performed. Decay tests of the finite element model of the complete structure showed that the flexibility of the tower and tendons created additional important natural frequencies. Simplified cost estimates suggested that the construction cost could be minimized by decreasing the displacement.

In addition to the five baseline designs which were developed from the spreadsheet, forty more designs were obtained by varying the diameter, water depth, ballast fraction, and pontoon radius of the baseline designs. The dynamic response of these 45 designs in a limited set of environmental conditions was then compared by simulations using the nonlinear analysis tool SIMO-RIFLEX-AeroDyn. The TLPWT responses were found to be mostly dependent on changes in natural periods and stiffness, not the exact parameters. Some of the key observations were:

- The designs with the largest displacement showed the smallest motions.
- Designs with the highest pretension showed the least relative tension variation.
- Motions perpendicular to the wind and waves (particularly roll) were found to be an important consideration, even in aligned wind-wave conditions. While there is little excitation of roll, there is also very little damping.
- For best results, the surge natural period needed to be sufficiently long (>45s) to reduce surge motions in storm conditions but not too long (<70s) to see decreased performance in operational conditions.
- For the studied designs, reducing the yaw natural period (T_{n6}) tended to decrease the yaw and roll motions. This can be achieved by increasing r_p.
- The wind turbine tower base bending moment (M_{FA}) was only weakly dependent on displacement and pitch/bending natural period, but the standard deviation of M_{FA} increased significantly compared to the land-based turbine.

7.2 TLPWT Analysis

An understanding of the analysis sensitivity is necessary for comparing the responses of different designs. Considering the SIMO-RIFLEX-AeroDyn with first-order potential wave forces as the baseline analysis tool, both simpler and more advanced methods were considered.

First, a simple, linear, frequency-domain analysis method was developed, including wind turbine effects. While the computationally efficient linear frequency-domain method captured the wave-frequency motions, nacelle accelerations, and dynamic tension with reasonable accuracy for low sea states, important wave-induced effects (particularly tendon tension variation at the wave, tendon, and pitch/bending frequencies) in more severe states were not captured due to the limitations of the structural model. Furthermore, the low-frequency wind-induced response in the frequency-domain analysis was damping-dependent and more narrow-banded than that predicted by the nonlinear analysis. The frequency-domain analysis, in its current form, was found to be insufficient for analyzing TLPWTs: it was not accurate enough in modeling the included modes (surge, heave, pitch) and it could not model enough modes to give a clear picture of the structural loading.

Next, the SIMO-RIFLEX-AeroDyn analysis tool was used with several different hydrodynamic load models:

1. M: Morison formulation (Froude-Krylov excitation, added mass, and viscous drag),
2. P1+V: first-order potential flow and viscous drag,
3. P2+V: first- and second-order potential flow and viscous drag,
4. P2+V+R: first- and second-order potential flow, third-order ringing forces, and viscous drag.

These models were compared with the P1+V model serving as a baseline.

Morison's equation (M, applied with constant C_a) gave reasonable agreement with P1+V for slender structures, but led to larger pitch moment predictions for structures with large diameter and in large waves. The Froude-Krylov force (M) does not decay with increasing frequency as quickly as the potential flow wave excitation (P1+V, including diffraction), leading to larger (unrealistic) excitation for large wave frequencies and near the pitch/bending natural frequency.

Second-order sum-frequency wave loads (P2+V model) had a significant impact on the response in severe wave conditions, and relatively minor

effects on the standard deviation of the loads in typical operational conditions. The effect of second-order loads on the fatigue damage of the soft TLPWTs was, however, significant, especially for the parked conditions. It is recommended that sum-frequency wave loads be included in any fatigue studies of TLPWTs.

For the P2+V+R model, the implementation of the ringing forces was an important consideration. Krokstad et al. showed that good agreement with experimental results requires the use of the second-order QTF and the third-order long-wave FNV formulation [100, 104]. A direct implementation of the irregular wave formulation of the FNV equation includes difference-frequency terms which are not desired in the simulation and are over-conservative. The alternative sum-frequency, bandwidth-limited approach [107] was implemented and used here.

The effect of the ringing forces was seen primarily in the platform pitch motions, which led to increased loads at the base of the tower and in the tendons. The increases in the maximum tendon tension (12-30 % for TLPWTs 1-3 and 5-10 % for TLPWT 4) did not depend strongly on the turbine operational condition, but the increase in the tower base bending moment due to ringing was largest for idling conditions (30-40 % increase). Ringing also caused increased short-term fatigue damage to the downwind tendon and tower base, particularly in idling conditions.

7.3 Severe Operational Conditions

Having established candidate designs and examined the analysis sensitivity, the SIMO-RIFLEX-AeroDyn analysis tool (first and second-order wave forces) was extended to conditions which were seen as potentially interesting or design-driving. Control system faults and wind-wave misalignment during the operational portion of the system's lifetime were considered.

Within the extensive range of possible control system faults, blade pitch actuator and grid faults were chosen for study. For the baseline and soft versions of TLPWT 3, the blade pitch actuator and grid faults were not found to be critical for the mooring system, but could cause large yaw motions (blade pitch actuator fault with shutdown), large tower top loads (blade pitch actuator fault, with and without shutdown), and large edgewise blade loads (shutdown). There was significant deterministic and stochastic variation in the response to blade pitch actuator faults and grid faults, but the baseline and soft versions of TLPWT 3 performed similarly.

Wind-wave misalignment was identified as another potentially interesting condition with respect to both ultimate and fatigue loads. Wind-wave

misalignment is known to occur frequently and to cause increased fatigue loading for monopile bottom-fixed OWTs. In this study, misaligned wind and waves did not generally cause increased fatigue damage for the the baseline and soft versions of TLPWT 3 in operational conditions. Moreover, despite the increase in side-side loading in misaligned conditions, misaligned operational conditions were not associated with large short-term maximum stresses. Second-order sum-frequency forces, however, became more important in misaligned wind and waves. In severe misalignment, the inclusion of second-order forces increased the predicted tower base fatigue damage by up to 80 %.

7.4 Original Contributions

This thesis includes original contributions to the development of design and analysis methods as well as the investigation of several phenomena. First, in order to be able to study TLPWT concepts, the following original software was developed:

- *Coupling between RIFLEX and AeroDyn*: the Fortran DLL for communication between RIFLEX and AeroDyn was written, tested, and documented. In cooperation with MARINTEK, the author wrote the DLL (including modifications to AeroDyn) and documentation and tested the implementation [144, 60]. Marit I. Kvittem also contributed to verification of the implementation [161]. This software is being used by several researchers: continual support and modifications have been provided.

- *WT control system implementation in Java*: the generator torque and blade pitch controller according to [72] was implemented and tested. In addition to the operational control logic, algorithms for controller fault conditions were developed and implemented.

- *Ringing force implementation (Matlab)*: Johannessen's formulation of FNV [107] was implemented in Matlab as an external force for use with SIMO. The implementation was compared with other formulations of FNV and bandwidth effects were investigated.

- *Spreadsheet TLPWT design tool*: an Excel spreadsheet was developed for preliminary analysis of parametric TLPWT designs.

- *Linear TLPWT analysis tool (Matlab)*: a frequency-domain analysis program was developed in Matlab. First-order potential flow results

were read in from existing software (Wadam). Linearized mooring system stiffness, viscous damping, wind spectra, and the frequency-domain response to wind and wave excitation were computed by the Matlab program.

Using the developed tools, the design and analysis of TLPWTs were studied. Several systematic investigations were performed:

- Single column, multiple tendon TLPWT designs were established and compared [153, 156]. The details of five baseline designs are published [156].

- A parametric study was carried out based on the baseline designs [156]. The effects of parameter variations (main column diameter, pontoon radius from the center column, water depth, and ballast) on the global performance in irregular waves and turbulent wind were examined. This provides a consistent study of a range of designs which are representative of those found in the literature.

- Linear, frequency-domain analysis of TLPWTs, including both wind and wave loads, was compared to the coupled analysis with first-order wave loads [153]. Although reasonable agreement could be obtained in the wave-frequency range, the frequency-domain method was found to be insufficient for studying the global responses.

- The effects of different hydrodynamic force models on the global responses of TLPWTs were examined [162, 165]. Morison's equation with constant coefficients was not suitable for modeling the structure. Second-order sum-frequency forces were found to be important for the calculation of short-term fatigue in the tower and tendons. Third-order ringing forces, which have not been previously investigated for TLPWTs, resulted in significantly increased responses in severe wave conditions.

- Selected controller fault conditions were examined: the failure of one blade pitch mechanism, with and without shutdown; and grid loss followed by shutdown. This work was coordinated with other PhD students in order to compare fault effects on several FWT concepts [76]. For TLPWTs, fault conditions may lead to large yaw motions, tower top loads, and blade edgewise bending moments.

- The effects of misalignment between the mean wind direction and the long-crested waves were also investigated, for TLPWTs [170] and, with

contributions from other PhD students, for several types of FWTs [171]. While misaligned wind and wave conditions did not result in increased short-term fatigue damage for the studied platforms, second-order forces became increasingly important for TLPWTs in such conditions.

7.5 Limitations

Certain limits on the design space, model complexity, and simulation time were required in order to approach this topic.

In this thesis, the design space was limited to platforms with a central column, 3-4 pontoons, and one tendon per pontoon, and the NREL 5 MW academic wind turbine as the payload. Within this design space, a limited number of designs, environmental conditions, and operational conditions were investigated. The installation process was not studied, nor was it considered in the design process.

The modeling reductions included assumptions that the hull was relatively stiff compared to the rest of the structure, that the aerodynamic loads could be accurately captured by BEM and GDW theories, that hydrodynamic loads could be calculated at the mean position, that the anchor points were perfectly fixed, that a simple controller would give reasonably accurate results, that the uncertainties in the structural model were acceptable, and that the included load models were sufficient. In particular, current, tides, and wake effects from other turbines were not considered. Furthermore, the focus of the thesis was on global analysis of the system in the installed condition: important couplings were included and investigated, but local loads and structural details were not considered.

Representative loading conditions were chosen in order to demonstrate general trends in behavior, to highlight differences between analysis methods, to suggest nominal loads, and examine fatigue in representative short-term states. No complete long-term fatigue or extreme value analysis was pursued.

7.6 Recommendations for future work

TLPWT (and, more generally, FWT) design and analysis is a young field, with huge potential for innovation and improvement. A few of the many natural extensions of the present work on TLPWT design and analysis are suggested below.

- *Design generation, parametric variation, and optimization:*
  The generation of different designs with consideration of tower flexibility and slightly different acceptance criteria (particularly with regards to the safety factor for tendon yield) could yield better-performing baseline designs. An extension of the parametric study to a wider range of designs, and subsequent hull optimization should be pursued. An optimization study (with an objective function that reflects lifetime costs) would be computationally demanding, as the simulations should include second-order and ringing forces in certain wave conditions, but may be able to identify more efficient and safer designs. Different turbine sizes, such as 10 MW, and types, such as vertical axis turbines, could also be considered.

- *Frequency-domain analysis*:
  The 3 DOF linear frequency-domain analysis attempted here was not sufficient for preliminary design and optimization, but it may be possible to improve the analysis by extending it to more degrees of freedom, such as the first and second pitch/bending (and roll/bending) modes. Better frequency-domain modeling of the wind forces could also be pursued.

- *Long-term fatigue analysis:*
  The present results suggest that second-order sum-frequency forces can have significant effects on the fatigue life of TLPWTs. A long-term study of TLPWT fatigue damage including these effects could help determine whether or not such designs can become practical solutions for electricity generation at a given location.

- *Control system modifications for TLPWTs*:
  The control system applied here - a slightly modified version of the academic NREL 5 MW controller [72] - is not optimized for the given systems. The control system's behavior around rated wind speed could be improved in order to reduce structural loads and power variations.

- *MacCamy-Fuchs correction*:
  The MacCamy-Fuchs correction [127] to Morison's equation should be implemented. This would enable more detailed structural analysis of the hull in the presently available software.

- *Ringing loads and responses*:
  Ringing remains a poorly understood phenomenon. Further experimental analysis of ringing loads - particularly for structures that are

relatively soft in surge - would be very useful for evaluating and improving the currently available simplified models. Furthermore, ringing loads may also be critical for bottom-fixed offshore wind turbines, which are generally located in relatively shallow water, where second-order wave kinematics become more important. A consistent ringing load model should be developed for studying such structures.

- *Modeling of slack incidents*:
  TLPs and TLPWTs are generally designed to avoid loss of tension (slack). Avoiding slack usually implies larger displacement and larger tendons, and consequently higher construction costs. More detailed models are required to examine the structural response during slack conditions, especially in an effort to determine whether or not such conditions are critical.

- *Drivetrain loads*:
  In the global analysis model employed here, the tower top loads and the generator torque are the best available indicators of the input loads to the drivetrain. More refined structural models could use the tower top loads to examine the influence of the platform on the drivetrain extreme loads and fatigue life.

- *Control strategies in response to blade pitch actuator fault*:
  The controller influences the platform response to fault. Different control strategies - such as varying the pitch rate during shutdown or waiting for a particular azimuthal position before starting shutdown - could be investigated as methods to reduce the tower top and blade loads. The optimal strategy may depend on the wind turbine and support structure. The influence of the controller reaction time (t_d) and the details of aerodynmics should also be examined. Furthermore, sensor faults can have significant effects on land-based wind turbines and spar FWTs [75, 71] and should also be considered for TLPWTs.

- *Wind-wave misalignment in extreme conditions and yaw error*:
  The investigation of wind-wave misalignment was limited to operational conditions with the turbine oriented into the wind. Further investigation of both yaw errors and extreme conditions with wind-wave misalignment should be pursued.

References

[1] Manwell, J., McGowan, J. G., and Rogers, A. L., 2009. *Wind Energy Explained*. John Wiley & Sons, Ltd.

[2] Twidell, J., and Gaudiosi, G., eds., 2009. *Offshore Wind Power*. Multi-Science Publishing Co. Ltd.

[3] Butterfield, S., Musial, W., Jonkman, J., Sclavounous, P., and Wayman, L., 2005. "Engineering challenges for floating offshore wind turbines". In 2005 Copenhagen Offshore Wind Conference, no. NREL/CP-500-38776.

[4] Musial, W., Butterfield, S., and Ram, B., 2006. Energy from offshore wind. Tech. Rep. NREL/CP-500-39450, National Renewable Energy Laboratory.

[5] International Electrotechnical Commission (IEC), 2005. Wind turbines: Part 1: Design requirements. IEC61400-1.

[6] International Electrotechnical Commission (IEC), 2009. Wind turbines: Part 3: Design requirements for offshore wind turbines. IEC61400-3.

[7] Det Norske Veritas, 2007. Design of offshore wind turbine structures. DNV-OS-J101.

[8] Germanischer Lloyd, 2012. Guideline for the certification of offshore wind turbines. Edition 2012.

[9] American Bureau of Shipping, 2013. Guide for building and classing floating offshore wind turbine installations.

[10] Det Norske Veritas, 2013. Design of floating wind turbine structures. DNV-OS-J103.

[11] Nihei, Y., Matsuura, M., Fujioka, H., and Suzuki, H., 2011. "An approach for the optimum design of TLP type offshore wind turbines". In 30th International Conference on Ocean, Offshore, and Arctic Engineering, Rotterdam, the Netherlands, no. OMAE2011-50258.

[12] Matha, D., 2009. "Model development and loads analysis of an offshore wind turbine on a tension leg platform, with a comparison to other floating turbine concepts". Master's thesis, University of Colorado-Boulder, April.

[13] Sclavounos, P., Lee, S., DiPietro, J., Potenza, G., Caramuscio, P., and Michele, G. D., 2010. "Floating offshore wind turbines: tension leg platform and taught leg buoy concepts supporting 3-5 MW wind turbines". In European Wind Energy Conference EWEC 2010, Warsaw, Poland.

[14] Chakrabarti, S., ed., 2005. *Handbook of Offshore Engineering*. Elsevier Science.

[15] Cordle, A., and Jonkman, J., 2011. "State of the art in floating wind turbine design tools". In Twenty-first International Offshore and Polar Engineering Conference, Maui, Hawaii, USA. Vol. 1, pp. 367–374.

[16] Jonkman, J. M., and Buhl, Jr., M. L., 2005. FAST user's guide. Tech. Rep. NREL/EL-500-38230, National Renewable Energy Laboratory, August.

[17] Larsen, T. J., 2009. How 2 HAWC2, the user's manual. Tech. Rep. Risø-R-1597(ver. 3-9). http://orbit.dtu.dk/.

[18] Wilkinson, M., Harmann, K., Spinato, F., Hendriks, B., and van Delft, T., 2011. "Measuring wind turbine reliability - results of the reliawind project". In European Wind Energy Conference (EWEA 2011), Brussels, Belgium.

[19] Barth, S., and Eecen, P. J., 2006. Description of the relation of wind, wave and current characteristics at the offshore wind farm Egmond aan Zee (OWEZ) location in 2006. Tech. Rep. ECN-E-07-104, ECN.

[20] Fischer, T., Rainey, P., Bossanyi, E., and Kühn, M., 2011. "Study on control concepts suitable for mitigation of loads from misaligned wind and waves on offshore wind turbines supported on monopiles". *Wind Engineering,* ***35***(5), pp. 561–574.

[21] Barj, L., Stewart, S., Stewart, G., Lackner, M., Jonkman, J., Robertson, A. N., Haid, L., and Matha, D., 2013. "Impact of wind/wave misalignment in the loads analysis of a floating wind turbine". In WINDPOWER 2013. (poster, available in conference proceedings).

[22] Roddier, D., Cermelli, C., and Weinstein, A., 2009. "Windfloat: A floating foundation for offshore wind turbines; Part I: Design basis and qualification process". In 28th International Conference on Ocean, Offshore, and Arctic Engineering, Honolulu, Hawaii, USA, no. OMAE2009-79229.

[23] Skaare, B., Hanson, T. D., Nielsen, F. G., Yttervik, R., Hansen, A. M., Thomsen, K., and Larsen, T. J., 2007. "Integrated dynamic analysis of floating offshore wind turbines". In 2007 European Wind Energy Conference and Exhibition.

[24] Kühn, M., 1997. "Soft or stiff - a fundamental question for designers of offshore wind energy converters". In Proceedings of the European Wind Energy Conference EWEC '97, Dublin, Ireland.

[25] Statoil, 2010. Statoil - a leading energy company in oil and gas production. http://www.statoil.com/.

[26] Jonkman, J., 2010. Definition of the floating system for Phase IV of OC3. Tech. Rep. NREL/TLP-500-47535.

[27] Jonkman, J., and Musial, W., 2010. Offshore code comparison collaboration (OC3) for IEA Wind Task 23 offshore wind technology and deployment. Tech. Rep. NREL/TP-5000-48191, National Renewable Energy Laboratory.

[28] Cermelli, C., Roddier, D., and Aubault, A., 2009. "Windfloat: A floating foundation for offshore wind turbines; Part II: Hydrodynamics analysis". In 28th International Conference on Ocean, Offshore, and Arctic Engineering, Honolulu, Hawaii, USA, no. OMAE2009-79231.

[29] Aubault, A., Cermelli, C., and Roddier, D., 2009. "Windfloat: A floating foundation for offshore wind turbines; Part III: Structural analysis". In 28th International Conference on Ocean, Offshore, and Arctic Engineering, Honolulu, Hawaii, USA, no. OMAE2009-79232.

[30] Principle Power, Inc, 2011. Windfloat. http://www.principlepowerinc.com/products/windfloat.html.

[31] IEA Wind. Task 30 OC4 comparison of dynamic computer codes and models for offshore wind energy. http://www.ieawind.org/task_30/task30_OC4_Semisubmersible.html.

[32] Robertson, A. N., and Jonkman, J. M., 2011. "Loads analysis of several offshore floating wind turbine concepts". In Twenty-First International Society of Offshore and Polar Engineers Conference, Maui, Hawaii, USA, Vol. 1, pp. 443–450, no. NREL/CP-5000-50539.

[33] Moon III, W. L., and Nordstrom, C. J., 2010. "Tension leg platform turbine: A unique integration of mature technologies". In Proceedings of the 16th Offshore Symposium, Texas Section of the Society of Naval Architects and Marine Engineers, pp. A25–A34.

[34] Henderson, A. R., Argyriadis, K., Nichos, J., and Langston, D., 2010. "Offshore wind turbines on TLPs - assessment of floating support structures for offshore wind farms in German waters". In 10th German Wind Energy Conference, Bremen, Germany.

[35] Sclavounos, P., Tracy, C., and Lee, S., 2007. Floating offshore wind turbines: responses in a seastate; Pareto optimal designs and economic assessment. Tech. rep., Department of Mechanical Engineering, Massachusetts Institute of Technology.

[36] Copple, R. W., and Capanoglu, C., 2012. "Tension leg wind turbine conceptual design suitable for a wide range of water depths". In Twenty-Second International Ocean and Polar Engineering Conference, Rhodes, Greece, Vol. 1, pp. 396–403.

[37] Botta, G., Casale, C., Lembo, E., Serri, L., and Viani, S., 2009. "Resource and technology assessment for evaluating Italy's offshore wind energy potential". In 2009 International Conference on Clean Electrical Power, Capri, Italy, pp. 507 –513.

[38] Crozier, A., 2011. "Design and dynamic modeling of the support structure for a 10MW offshore wind turbine". Master's thesis, NTNU (Norwegian University of Science and Technology), June.

[39] Stewart, G., Lackner, M., Robertson, A., Jonkman, J., and Goupee, A., 2012. "Calibration and validation of a FAST floating wind turbine model of the DeepCwind scaled tension-leg platform". In Twenty-Second International Offshore and Polar Engineering Conference, Rhodes, Greece, Vol. 1, pp. 380–387, no. NREL/CP-5000-54822.

[40] Withee, J. E., 2004. "Fully coupled dynamic analysis of a floating wind turbine system". PhD thesis, Massachusetts Institute of Technology, June.

[41] Lee, K. H., 2005. "Responses of floating wind turbines to wind and wave excitation". Master's thesis, Massachusetts Institute of Technology, January.

[42] Wayman, E., Sclavounos, P., Butterfield, S., Jonkman, J., and Musial, W., 2006. Coupled dynamic modeling of floating wind turbine systems. Tech. Rep. NREL/CP-500-39481, National Renewable Energy Laboratory.

[43] Tracy, C., 2007. "Parametric design of floating wind turbines". Master's thesis, Massachusetts Institute of Technology, June.

[44] Jonkman, J., and Matha, D., 2009. "A quantitative comparison of the responses of three floating platforms". In European Offshore Wind 2009 Conference and Exhibition, Stockholm, Sweden.

[45] Matha, D., Fischer, T., Kuhn, M., and Jonkman, J., 2010. "Model development and loads analysis of a wind turbine on a floating offshore tension leg platform". No. NREL/CP-500-46725.

[46] Glosten Associates, 2013. http://www.pelastarwind.com/index.html, March.

[47] Myhr, A., Maus, K. J., and Nygaard, T. A., 2011. "Experimental and computational comparisons of the OC3-HYWIND and tension-leg-buoy (TLB) floating wind turbine conceptual designs". In Twenty-First International Offshore and Polar Engineering Conference, Maui, Hawaii, USA, Vol. 1, pp. 353–361.

[48] Myhr, A., and Nygaard, T. A., 2012. "Load reductions and optimizations on tension-leg-buoy offshore wind turbine platforms". In Twenty-Second International Offshore and Polar Engineering Conference, Rhodes, Greece, Vol. 1, pp. 232–239.

[49] Adam, F., Steinke, C., Dahlhaus, F., and Großmann, J., 2013. "GICON-TLP for wind turbines - validation of calculated results". In Twenty-Third International Offshore and Polar Engineering Conference, Anchorage, Alaska, USA, Vol. 1, pp. 421–427.

[50] Fulton, G., Malcolm, D., Elwany, H., Stuart, W., Moroz, E., and Dempster, H., 2007. Semi-submersible platform and anchor foundation systems for wind turbine support. Tech. Rep. NREL/SR-500-40282, National Renewable Energy Laboratory.

[51] Suzuki, K., Yamaguchi, H., Akase, M., Imakita, A., Ishihara, T., Fukumoto, Y., and Oyama, T., 2010. "Initial design of TLP for offshore wind farm". In Renewable Energy Conference 2010, Yokohama, Japan.

[52] Casale, C., Lembo, E., Serri, L., and Viani, S., 2010. "Preliminary design of a floating wind turbine support structure and relevant system cost assessment". *Wind Engineering,* ***34***(1), pp. 29–50.

[53] Zhao, Y., Yang, J., and He, Y., 2012. "Preliminary design of a multi-column TLP foundation for a 5-MW offshore wind turbine". *energies,* ***5***, pp. 3874–3891.

[54] Jonkman, J., Larsen, T., Hansen, A., Nygaard, T., Maus, K., Karimirad, M., Gao, Z., Moan, T., Fylling, I., Nichols, J., Kohlmeier, M., Vergara, J. P., Merino, D., Shi, W., and Park, H., 2010. Offshore code comparison collaboration within IEA Wind Task 23: Phase IV results regarding floating wind turbine modeling. Tech. Rep. NREL/CP-500-47534, National Renewable Energy Laboratory.

[55] Popko, W., Vorpahl, F., Zuga, A., Kohlmeier, M., Jonkman, J., Robertson, A., Larsen, T. J., and Yde, A., 2012. "Offshore code comparison collaboration continuation (OC4), Phase I results of coupled simulations of an offshore wind turbine with jacket support structure". In Twenty-Second International Society of Offshore and Polar Engineers Conference, Rhodes, Greece, Vol. 1, pp. 337–348, no. NREL/CP-5000-54124.

[56] Robertson, A., Jonkman, J., Musial, W., Vorpahl, F., and Popko, W., 2013. "Offshore code comparison collaboration, continuation: Phase II results of a floating semisubmersible wind system". In EWEA Offshore, Frankfurt, Germany, no. NREL/CP-5000-60600.

[57] Fylling, I., Mo, K., Merz, K., and Luxcey, N., 2009. "Floating wind turbine - response analysis with rigid-body model". In European Offshore Wind, Stockholm, Sweden.

[58] Ormberg, H., Passano, E., and Luxcey, N., 2011. "Global analysis of a floating wind turbine using an aero-hydro-elastic model. Part 1:

Code development and case study". In 30th International Conference on Ocean, Offshore, and Arctic Engineering, Rotterdam, the Netherlands, no. OMAE2011-50114.

[59] Luxcey, N., Ormberg, H., and Passano, E., 2011. "Global analysis of a floating wind turbine using an aero-hydro-elastic numerical model. Part 2: Benchmark study". In 30th International Conference on Ocean, Offshore, and Arctic Engineering, Rotterdam, the Netherlands, no. OMAE2011-50088.

[60] Ormberg, H., and Bachynski, E. E., 2012. "Global analysis of floating wind turbines: Code development, model sensitivity and benchmark study". In Twenty-Second International Ocean and Polar Engineering Conference, Rhodes, Greece, Vol. 1, pp. 366–373.

[61] Hansen, A. D., Cutululis, N. A., Sørensen, P., Iov, F., and Larsen, T. J., 2007. "Simulation of a flexible wind turbine response to a grid fault". In European Wind Energy Conference & Exhibition, Berlin, Germany.

[62] Cutululis, N. A., Hansen, A. D., Iov, F., and Sørensen, P., 2008. "Grid faults impact on the mechanical loads of active stall wind turbine". In Second International Symposium on Electrical and Electronics Engineering (ISEEE-2008), Galati, Romania.

[63] Molin, B., Remy, F., and Facon, G., 2004. "Étude expérimentale du comportement hydro-aéro-élastique d'une éolienne offshore sur ancrages tendus". In Ocean Energy Conference, Brest, France.

[64] Goupee, A. J., Koo, B. J., Lambrakos, K. F., and Kimball, R. W., 2012. "Model tests for three floating wind turbine concepts". In Offshore Technology Conference, Houston, Texas, USA, no. OTC 23470.

[65] Robertson, A. N., Jonkman, J., Goupee, A. J., Coulling, A. J., Prowell, I., Browning, J., Masciola, M. D., and Molta, P., 2013. "Summary of conclusions and recommendations drawn from the DeepCwind scaled floating offshore wind system test campaign". In 32nd International Conference on Ocean, Offshore and Arctic Engineering, Nantes, France, no. OMAE2013-10817.

[66] Coulling, A. J., Goupee, A. J., Robertson, A. N., Jonkman, J. M., and Dagher, H. J., 2013. "Validation of a FAST semi-submersible floating wind turbine numerical model with DeepCwind test data". *Journal of Renewable and Sustainable Energy,* ***5****.*

[67] Fowler, M. J., Kimball, R. W., Thomas, D. A., and Goupee, A. J., 2013. "Design and testing of scale model wind turbines for use in wind/wave basin model tests of floating offshore wind turbines". In 32nd International Conference on Ocean, Offshore and Arctic Engineering, Nantes, France, no. OMAE2013-10122.

[68] Wehmeyer, C., Ferri, F., Skourup, J., and Frigaard, P. B., 2013. "Experimental study of an offshore wind turbine TLP in ULS conditions". In Twenty-Third International Ocean and Polar Engineering Conference, Anchorage, Alaska, USA, Vol. 1, pp. 301–308.

[69] Main(e) International Consulting LLC, 2012. Floating offshore wind foundations: Industry consortia and projects in the United States, Europe and Japan. Tech. rep.

[70] Yu, B., Karr, D. G., Song, H., and Sirinivas, S., 2013. "A surface ice module for wind turbine dynamic response simulation using FAST". In 32nd International Conference on Ocean, Offshore and Arctic Engineering, Nantes, France, no. OMAE2013-11179.

[71] Etemaddar, M., 2013. "Load and response analysis of wind turbines under atmospheric icing and controller system faults with emphasis on spar type floating wind turbine". PhD thesis, Norwegian University of Science and Technology (NTNU).

[72] Jonkman, J., Butterfield, S., Musial, W., and Scott, G., 2009. Definition of a 5-MW reference wind turbine for offshore system development. Tech. Rep. NREL/TP-500-38060, National Renewable Energy Laboratory, February.

[73] Tavner, P., 2012. *Offshore Wind Turbines: Reliability, availability and maintenance*. No. 13 in Renewable Energy Series. The Institution of Engineering and Technology.

[74] Jiang, Z., Karimirad, M., and Moan, T., 2013. "Dynamic response analysis of wind turbines under blade pitch system fault, grid loss and shut down events". *Wind Energy*. (first published online June 13, 2013).

[75] Etemaddar, M., Gao, Z., and Moan, T., 2012. "Structural load analysis of a wind turbine under pitch actuator and controller faults". In The Science of Making Torque from Wind, Oldenburg, Germany.

[76] Bachynski, E. E., Etemaddar, M., Kvittem, M. I., Luan, C., and Moan, T., 2013. "Dynamic analysis of floating wind turbines during pitch actuator fault, grid loss, and shutdown". *Energy Procedia,* ***35***, pp. 210–222.

[77] Demirbilek, Z., 1989. Tension leg platform: A state of the art review. Tech. rep., Task Group on Compliant Offshore Platforms of the Committee on Waves and Wave Forces of the Waterway, Port, Coastal and Ocean Division of the American Society of Civil Engineers.

[78] American Petroleum Institute, 2010. Planning, designing, and constructing tension leg platforms (Edition 3).

[79] Det Norske Veritas, 2008. Structural design of TLPs (LRFD method). DNV-OS-C105.

[80] Marine Division, 2012. Rules for the classification of tension leg platforms (TLP). Tech. rep., Bureau Veritas.

[81] Det Norske Veritas, 1995. Guideline for offshore structural reliability analysis - examples for tension leg platforms. Tech. Rep. 95-3198, Structural Reliability and Marine Technology, September.

[82] Morgan, J. R., and Malaeb, D., 1983. "Dynamic analysis of tension-leg platforms". In Second International Offshore Mechanics and Arctic Engineering Symposium, Houston, Texas, USA.

[83] Low, Y., 2009. "Frequency domain analysis of a tension leg platform with statistical linearization of the tendon restoring forces". *Marine Structures,* ***22***(3), pp. 480 – 503.

[84] Gurley, K. R., and Kareem, A., 1998. "Simulation of ringing in offshore systems under viscous loads". *Journal of Engineering Mechanics,* ***124***, May, pp. 582–586.

[85] Johannessen, T. B., Haver, S., Bunnik, T., and Buchner, B., 2006. "Extreme wave effects on deep water TLPs: Lessons learned from the Snorre A model tests". In Proceedings on Deep Offshore Technology, Houston, TX, USA.

[86] Patel, M. H., and Park, H. I., 1995. "Tensioned buoyant platform tether response to short duration tension loss". *Marine Structures,* ***8***, pp. 543–553.

[87] Newman, J. N., 1977. *Marine Hydrodynamics.* The MIT Press.

[88] Faltinsen, O., 1990. *Sea Loads on Ships and Offshore Structures.* Cambridge University Press.

[89] Journee, J. M. J., and Massie, W. W., 2001. Offshore hydromechanics. Tech. rep., Delft University of Technology.

[90] Lighthill, M. J., 1979. "Waves and hydrodynamic loading". In 2nd International Conference on the Behaviour of Offshore Structures, London, England.

[91] Molin, B., 1979. "Second-order diffraction loads upon three-dimensional bodies". *Applied Ocean Research,* ***4***, pp. 197–202.

[92] Taylor, R. E., and Hung, S. M., 1987. "Second order diffraction forces on a vertical cylinder in regular waves". *Applied Ocean Research,* ***9***(1), pp. 19–30.

[93] Newman, J. N., 1990. "Second-harmonic wave diffraction at large depths". *Journal of Fluid Mechanics,* ***213***, pp. 59–70.

[94] Herfjord, K., and Nielsen, F. G., 1986. "Non-linear wave forces on a fixed vertical cylinder due to the sum frequency of waves in irregular seas". *Applied Ocean Research,* ***8***(1), pp. 8–21.

[95] Kim, M. H., and Yue, D. K. P., 1988. "The nonlinear sum-frequency wave excitation and response of a tension-leg platform". In International Conference on Behaviour of Offshore Structures (BOSS '88), Vol. 2: Hydrodynamics, pp. 687–703.

[96] Kim, M. H., 1991. "Second-order sum-frequency wave loads on large-volume structures". *Applied Ocean Research,* ***13***(6), pp. 287–296.

[97] Liu, Y. H., Kim, M. H., and Kim, C. H., 1995. "The computation of second-order mean and double-frequency wave loads on a compliant TLP by HOBEM". *International Journal of Offshore and Polar Engineering,* ***5***(2), June, pp. 111–119.

[98] Chen, X. B., Molin, B., and Petitjean, F., 1995. "Numerical evaluation of the springing loads on tension leg platforms". *Marine Structures,* ***8***(5), pp. 501 – 524.

[99] Lee, C.-H., 1995. WAMIT theory manual. Tech. Rep. 95-2, Massachusetts Institute of Technology, Department of Ocean Engineering, October.

[100] Faltinsen, O. M., Newman, J. N., and Vinje, T., 1995. "Nonlinear wave loads on a slender vertical cylinder". *Journal of Fluid Mechanics,* ***289***, pp. 179–198.

[101] Tromans, P., Swan, C., and Masterton, S., 2006. Nonlinear potential flow forcing: the ringing of concrete gravity based structures. Research Report 468, Health and Safety Executive.

[102] Newman, J. N., 1996. *Waves and nonlinear processes in hydrodynamics.* Kluwer, ch. Nonlinear scattering of long waves by a vertical cylinder, pp. 91–102.

[103] Rainey, R. C. T., 1995. "Slender-body expressions for the wave load on offshore structures". *Proceedings: Mathematical and Physical Sciences,* ***450***, pp. 391–416.

[104] Krokstad, J., Stansberg, C., Nestegård, A., and Marthinsen, T., 1998. "A new nonslender ringing load approach verified against experiments". *Transactions of the ASME Journal of Offshore Mechanics and Arctic Engineering,* ***120***(1), pp. 20–29.

[105] Marthinsen, T., Stansberg, C. T., and Krokstad, J. R., 1996. "On the ringing excitation of circular cylinders". In Sixth International Offshore and Polar Engineering Conference, Vol. 1, pp. 196–204.

[106] Stansberg, C. T., 1997. "Comparing ringing loads from experiments with cylinders of different diameters - an empirical study". In 8th International Conference on the Behaviour of Off-Shore Structures (BOSS'97).

[107] Johannessen, T. B., 2012. "Nonlinear superposition methods applied to continuous ocean wave spectra". *Journal of Offshore Mechanics and Arctic Engineering,* ***134***, pp. 011302–1–011302–14.

[108] Newman, J. N., 1996. "The second-order wave force on a vertical cylinder". *Journal of Fluid Mechanics,* ***320***, pp. 417–443.

[109] Grue, J., Bjørshol, G., and Strand, Ø., 1993. Higher harmonic wave exciting forces on a vertical cylinder. Tech. rep., Preprint Series, Matematisk Institutt Oslo.

[110] Grue, J., and Huseby, M., 2002. "Higher-harmonic wave forces and ringing of vertical cylinders". *Applied Ocean Research,* ***24***, pp. 203–214.

[111] Taghipour, R., Perez, T., and Moan, T., 2008. "Hybrid frequency-time domain models for dynamic response analysis of marine structures". *Ocean Engineering,* ***35***, pp. 685–705.

[112] MARINTEK, 2012. *SIMO Theory Manual.* (only available with the software).

[113] Cook, R. D., Malkus, D. S., Plesha, M. E., and Witt, R. J., 2002. *Concepts and Applications of Finite Element Analysis, 4th ed.* John Wiley & Sons.

[114] MARINTEK, 2012. *RIFLEX Theory Manual.* (only available with the software).

[115] Hoff, J. R., 2001. Estimation of linear and quadratic roll damping from free-decay tests. Tech. Rep. 601882, NTNU.

[116] Hibbeler, R. C., 2005. *Mechanics of Materials.* Prentice Hall.

[117] Det Norske Veritas, 2010. Fatigue design of offshore steel structures. DNV-RP-C203.

[118] Matsuishi, M., and Endo, T., 1968. "Fatigue of metals subjected to varying stress.". In Proceedings of the Kyushu Branch of Japan Society of Mechanics Engineering, pp. 37–40.

[119] Naess, A., and Moan, T., 2013. *Stochastic Dynamics of Marine Structures.* Cambridge University Press.

[120] Brodtkorb, P., Johannesson, P., Lindgren, G., Rychlik, I., Rydén, J., and Sjö, E., 2000. "WAFO - a MATLAB toolbox for the analysis of random waves and loads". In Tenth International Offshore and Polar Engineering Conference, Seattle, USA, Vol. 3, pp. 343–350.

[121] Shaker, F. J., 1975. Effect of axial load on mode shapes and frequencies of beams. Tech. Rep. NASA TN D-8109.

[122] Munson, B. R., Young, D. F., and Okiishi, T. H., 2006. *Fundamentals of Fluid Mechanics.* Wiley.

[123] Det Norske Veritas, 2012. Stability and watertight integrity. DNV-OS-C301.

[124] American Petroleum Institute, 2001. Recommended practice for planning, designing, and constructing floating production systems. API RP 2FPS

[125] Dean, R. G., and Dalrymple, R. A., 1991. *Water Wave Mechanics for Engineers and Scientists*. World Scientific.

[126] Lee, C.-H., J. N. Newman, M.-H. K., and Yue, D. K. P., 1991. "The computation of second-order wave loads". In Offshore Mechanics and Arctic Engineering Conference, Stavanger, Norway.

[127] MacCamy, R. C., and Fuchs, R. A., 1954. Wave diffraction on piles: A diffraction theory. Tech. Rep. Technical Memorandum 69, Beach Erosion Board; Corps of Engineers.

[128] Hansen, M., Sørensen, J., Voutsinas, S., Sørensen, N., and Madsen, H., 2006. "State of the art in wind turbine aerodynamics and aeroelasticity". *Progress in Aerospace Sciences,* ***42***(4), pp. 285 – 330.

[129] Moriarty, P. J., and Hansen, A. C., 2005. AeroDyn theory manual. Tech. Rep. NREL/TP-500-36881.

[130] Burton, T., Jenkins, N., Sharpe, D., and Bossanyi, E., 2011. *Wind Energy Handbook*. Wiley.

[131] Schepers, J. G., 2007. IEA Annex XX: dynamic inflow effects at fast pitching steps on a wind turbine placed in the NASA-Ames wind tunnel. Tech. Rep. ECN-E–07-085.

[132] Madsen, H. A., Riziotis, V., Zahle, F., Hansen, M. O. L., Snel, H., Grasso, F., Larsen, T. J., Politis, E., and Rasmussen, F., 2012. "Blade element momentum modeling of inflow with shear in comparison with advanced model results". *Wind Energy,* ***15***(1), pp. 63–81.

[133] Namik, H., and Stol, K., 2011. "Performance analysis of individual blade pitch control of offshore wind turbines on two floating platforms". *Mechatronics,* ***21***(4), pp. 691–703.

[134] Larsen, T. J., and Hanson, T. D., 2007. "A method to avoid negative damped low frequent tower vibrations for a floating, pitch controlled wind turbine". *Journal of Physics: Conference Series, The Second Conference on The Science of Making Torque from Wind,* ***75***.

[135] Arabian-Hoseynabadi, H., Oraee, H., and Tavner, P. J., 2010. "Failure modes and effects analysis (FMEA) for wind turbines". *Electrical Power and Energy Systems,* ***32***, pp. 817–824.

[136] de Alegría, I. M., Andreu, J., Martín, J. L., Ibañez, P., Villate, J. L., and Camblong, H., 2007. "Connection requirements for wind farms: A survey on technical requirements and regulation". *Renewable and Sustainable Energy Reviews,* ***11***, pp. 1858–1872.

[137] Ochi, M. K., 1990. *Applied Probability and Stochastic Prcesses In Engineering and Physical Sciences.* Wiley.

[138] Det Norske Veritas, 2010. Environmental conditions and environmental loads. DNV-RP-C205.

[139] Jonkman, B., 2009. TurbSim user's guide: Version 1.50. Tech. Rep. NREL/TP-500-46198, National Renewable Energy Laboratory, September.

[140] de Vaal, J. B., Hansen, M. O. L., and Moan, T., 2014. "Effect of wind turbine surge motion on rotor thrust and induced velocity". *Wind Energy,* ***17***(1), pp. 105–121.

[141] Johannessen, K., Meling, T. S., and Haver, S., 2001. "Joint distribution for wind and waves in the northern North Sea". In Eleventh International Offshore and Polar Engineering Conference & Exhibition, Stavanger, Norway, Vol. 3., pp 19–28.

[142] Kühn, M., 2001. "Dynamics and design optimisation of offshore wind energy conversion systems". PhD thesis, Delft University of Technology.

[143] Li, L., Gao, Z., and Moan, T., 2013. "Joint environmental data at five European offshore sites for design of combined wind and wave energy concepts". In 32nd International Conference on Ocean, Offshore, and Arctic Engineering, Nantes, France, no. OMAE2013-10156.

[144] Bachynski, E. E., 2013. SIMO-RIFLEX-AeroDyn (64-bit) and NREL-Control_fixpitch.jar user manual. Tech. rep., Centre for Ships and Ocean Structures, NTNU. (only available with the software).

[145] Laino, D. J., and Hanson, A. C., 2002. *User's Guide to the Wind Turbine Aerodynamics Computer Software AeroDyn.* Salt Lake City, UT: Windward Engineering, Prepared for the National Renewable Energy Laboratory under Subcontract No. TCX-9-29209-01, 57 pp.

[146] Jonkman, B. J., and Jonkman, J. M., 2010. Documentation of updates to FAST, A2AD, and AeroDyn: Released March 31, 2010, including the revised AeroDyn interface. Tech. rep. NREL.

[147] MARINTEK, 2013. *RIFLEX User's Manual*. only available with the software.

[148] National Renewable Energy Laboratory - National Wind Technology Center, 2011. NWTC design codes. http://wind.nrel.gov/designcodes/.

[149] Kibbee, S. E., Leverette, S. J., Davies, K. B., and Matten, R. B., 1999. "Morpeth SeaStar mini-TLP". In Offshore Technology Conference, no. OTC 10855.

[150] Leverette, S., 2011. personal communication.

[151] Chakrabarti, S. K., and Hanna, S. Y., 1990. "Added mass and damping of a TLP column model". In Offshore Technology Conference, no. OTC 6406, pp. 559–571.

[152] Jain, A. K., 1997. "Nonlinear coupled response of offshore tension leg platforms to regular wave forces". *Ocean Engineering,* ***24***(7), pp. 577–592.

[153] Bachynski, E. E., and Moan, T., 2012. "Linear and nonlinear analysis of tension leg platform wind turbines". In Twenty-Second International Ocean and Polar Engineering Conference, Rhodes, Greece, Vol. 1, pp. 240–247, no. 2012-TPC-0629.

[154] Det Norske Veritas, 2010. *Wadam User Manual*, 8.1 ed., January.

[155] Bir, G. S., 2007. *User's Guide to BModes (Software for Computing Rotating Beam Coupled Modes)*.

[156] Bachynski, E. E., and Moan, T., 2012. "Design considerations for tension leg platform wind turbines". *Marine Structures,* ***29***, pp. 89–114.

[157] van der Tempel, J., 2006. "Design of support structures for offshore wind turbines". PhD thesis, Delft University of Technology, April.

[158] Salzmann, D. J. C., and van der Tempel, J., 2005. "Aerodynamic damping in the design of support structures for offshore wind turbines". In Proceedings of the Offshore Wind Energy Conference, Copenhagen, Denmark.

[159] Wolfram, J., 1999. "On alternative approaches to linearization and Morison's equation for wave forces". *Proceedings of the Royal Society of London A,* ***455***, pp. 2957–2974.

[160] Philippe, M., Babarit, A., and Ferrant, P., 2011. "Comparison of time and frequency domain simulations of an offshore floating wind turbine". In 30th International Conference on Ocean, Offshore, and Arctic Engineering, Rotterdam, the Netherlands, no. OMAE2011-49722.

[161] Kvittem, M. I., Bachynski, E. E., and Moan, T., 2012. "Effects of hydrodynamic modelling in fully coupled simulations of a semi-submersible wind turbine". *Energy Procedia,* ***24***, pp. 351–362.

[162] Bachynski, E. E., and Moan, T., 2013. "Hydrodynamic modeling of tension leg platform wind turbines". In 32nd International Conference on Ocean, Offshore and Arctic Engineering, Nantes, France no. OMAE2013-10120.

[163] Roald, L., Jonkman, J., Robertson, A., and Chokani, N., 2013. "Effect of second-order hydrodynamics on floating offshore wind turbines". *Energy Procedia,* ***35***, January, pp. 253–264.

[164] Bae, Y. H., and Kim, M. H., 2013. "Turbine-floater-tether coupled dynamic analysis including second-order sum-frequency wave loads for a TLP-type FOWT (floating offshore wind turbine)". In 32nd International Conference on Ocean, Offshore and Arctic Engineering, Nantes, France, no. OMAE2013-11261.

[165] Bachynski, E. E., and Moan, T., 2013. "Ringing loads on tension leg platform wind turbines". *Ocean Engineering.* (under review).

[166] Karimirad, M., Meissonnier, Q., Gao, Z., and Moan, T., 2011. "Hydroelastic code-to-code comparison for a tension leg spar-type floating wind turbine". *Marine Structures,* ***24***, pp. 412–435.

[167] Odgaard, P. F., Stoustrup, J., and Kinnaert, M., 2009. "Fault tolerant control of wind turbines - a benchmark model". In 7th IFAC Symposium on Fault Detection, Supervision and Safety of Technical Processes, pp. 155–160.

[168] Xing, Y., Karimirad, M., and Moan, T., 2013. "Modelling and analysis of floating spar-type wind turbine drivetrain". *Wind Energy.* (first published online February 6, 2013).

[169] Jonkman, J. M., and Matha, D., 2011. "Dynamics of offshore floating wind turbines". *Wind Energy,* ***14***, pp. 557–569.

[170] Bachynski, E. E., and Moan, T., 2014. "Second order wave force effects on tension leg platform wind turbines in misaligned wind and waves". In 33rd International Conference on Ocean, Offshore and Arctic Engineering, San Francisco, California, USA, no. OMAE2014-23131. (submitted for review).

[171] Bachynski, E. E., Kvittem, M. I., Luan, C., and Moan, T., 2013. "Wind-wave misalignment effects on floating wind turbines: motions and tower load effects". *Journal of Offshore Mechanics and Arctic Engineering.* (submitted for review).

[172] Det Norske Veritas, 2010. Global performance analysis of deepwater floating structures. DNV-RP-F205.

Appendix A

Tower and Tendon Modes Shapes

Bandpass-filtered time series of displacements from the platform pitch decay tests were used to examine the tower and tendon mode shapes. The results for TLPWT 3 are presented in Sec. 4.1.4.2. For the other designs, two figures are presented in each of the following sections: 1) the tendon bending modes split into five frequency ranges, and 2) the tower and tendon modes split into two frequency ranges. The first plot shows the different tendon modes which are all present in the response, while the second plot is useful for highlighting the most important modes. In the second plot, note that the tendon is plotted as though it were horizontally aligned with the tower, but it is in fact offset by a horizontal distance r_p.

A.1 TLPWT 1 Tower and Tendon Mode Shapes

For TLPWT 1, based on Fig. A.1, four tendon modes are identifiable: the first pinned-pinned mode, the second pinned-pinned mode, a mode associated with the second platform pitch/tower bending mode, and the third pinned-pinned mode. The first platform pitch/tower bending mode is close to the first pinned-pinned mode.

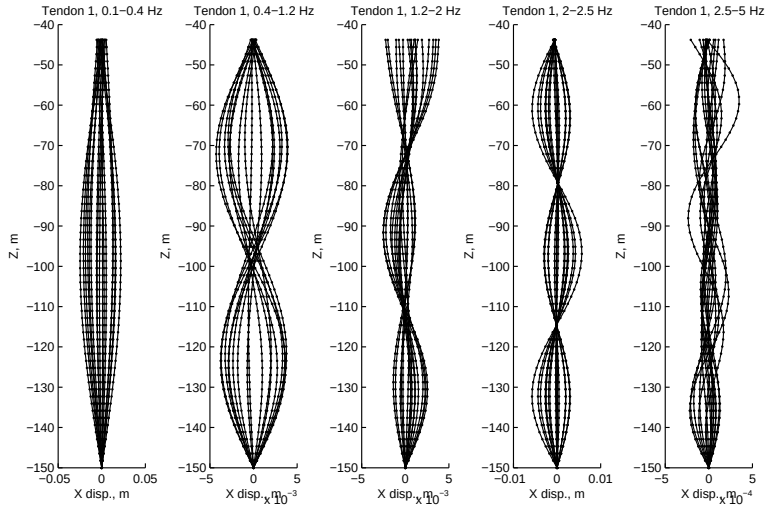

Figure A.1: Tendon 1 bending modes for TLPWT 1 based on bandpassed time series from the pitch decay test.

As shown in Fig. A.2, the first and third tendon modes are perhaps the most important in the response.

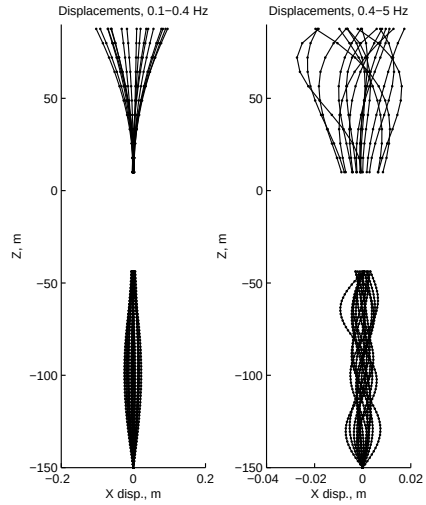

Figure A.2: Tendon 1 and tower bending modes for TLPWT 1 based on bandpassed time series from the pitch decay test.

A.2 TLPWT 2 Tower and Tendon Mode Shapes

For TLPWT 2, based on Fig. A.3, five tendon modes are identifiable: the first pinned-pinned mode, a mode associated with the first platform pitch/-tower bending mode, the second and third pinned-pinned modes, and a mode associated with the second platform pitch/tower bending mode.

In Fig. A.4, the second and fifth modes from Fig. A.3 dominate in the response.

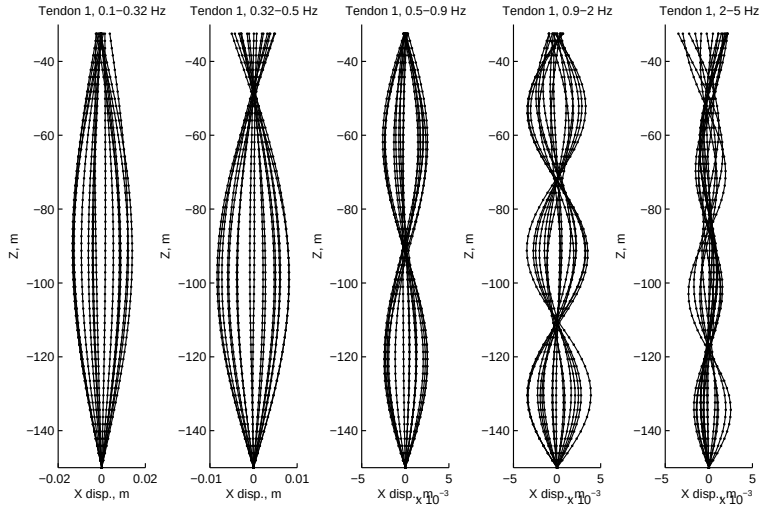

Figure A.3: Tendon 1 bending modes for TLPWT 2 based on bandpassed time series from the pitch decay test.

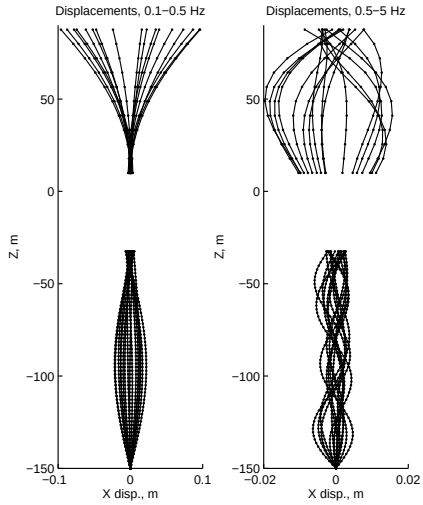

Figure A.4: Tendon 1 and tower bending modes for TLPWT 2 based on bandpassed time series from the pitch decay test.

A.3 TLPWT 4 Tower and Tendon Mode Shapes

Fig. A.5 shows five tendon modes for TLPWT 4: the first pinned-pinned mode, a mode associated with the first platform pitch/tower bending mode,

the second and third pinned-pinned modes, and the fourth pinned-pinned mode, which also corresponds to the second platform pitch/tower bending frequency.

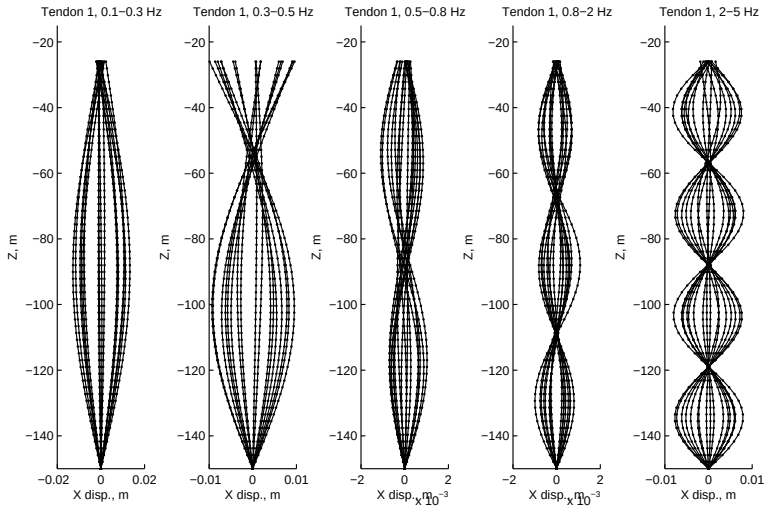

Figure A.5: Tendon 4 bending modes for TLPWT 4 based on bandpassed time series from the pitch decay test.

As shown in Fig. A.6, the first and fifth tendon modes are strongly present in the response. This suggests that the fourth pinned-pinned mode may be significant in the system response to irregular waves and turbulent wind.

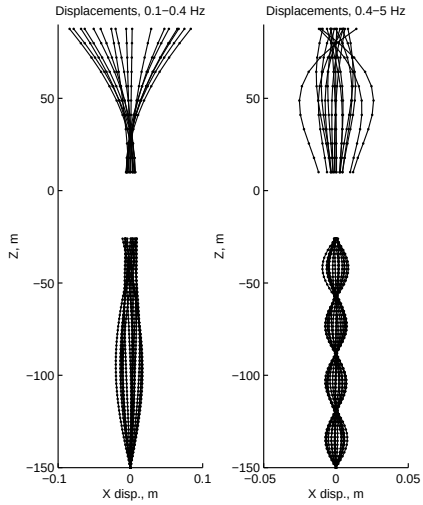

Figure A.6: Tendon 1 and tower bending modes for TLPWT 4 based on bandpassed time series from the pitch decay test.

A.4 TLPWT 5 Tower and Tendon Mode Shapes

Fig. A.7 shows six tendon modes for TLPWT 5: the first pinned-pinned mode, a mode associated with the first platform pitch/tower bending mode, the second, third, and fourth pinned-pinned modes, and the fifth pinned-pinned mode, which also corresponds to the second platform pitch/tower bending frequency. The fifth pinned-pinned mode has a period of 0.383 seconds.

In Fig. A.8, it is easy to see that the fifth pinned-pinned tendon mode is significant.

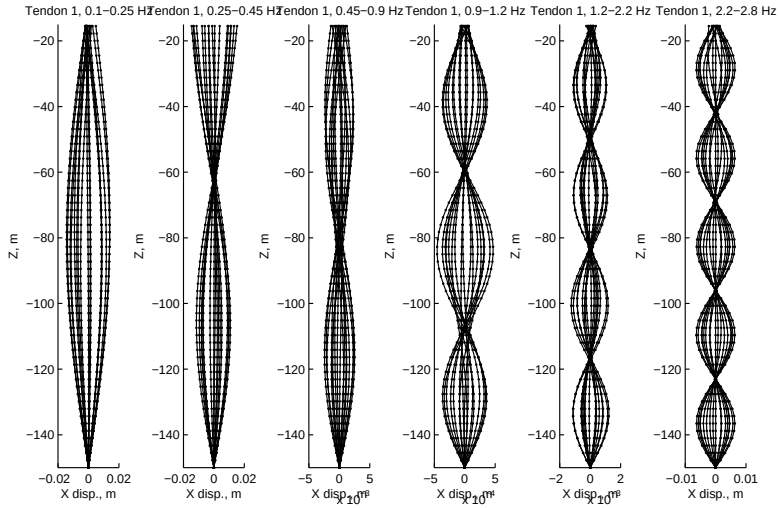

Figure A.7: Tendon 1 bending modes for TLPWT 5 based on bandpassed time series from the pitch decay test.

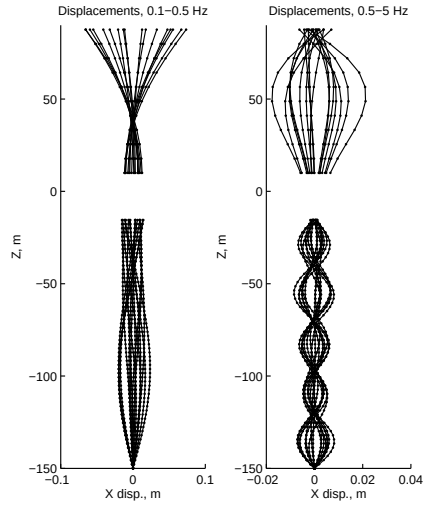

Figure A.8: Tendon 1 and tower bending modes for TLPWT 5 based on bandpassed time series from the pitch decay test.

A.5 Soft TLPWT 1 Tower and Tendon Mode Shapes

For the soft version of TLPWT 1, four tendon modes can be identified (Fig. A.9): the first pinned-pinned mode, a mode associated with the first

platform pitch/tower bending mode, a mode associated with the second platform pitch/tower bending mode, and the third pinned-pinned mode. The second pinned-pinned mode was not observed in the response.

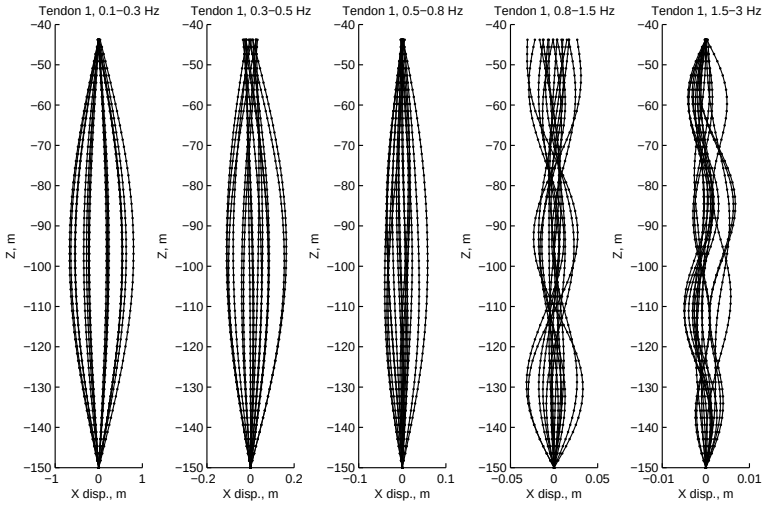

Figure A.9: Tendon 1 bending modes for soft TLPWT 1 based on bandpassed time series from the pitch decay test.

From Fig. A.10, it is clear that the displacement associated with the first transverse mode is significant for the soft tendons. There is no clearly dominant higher frequency mode.

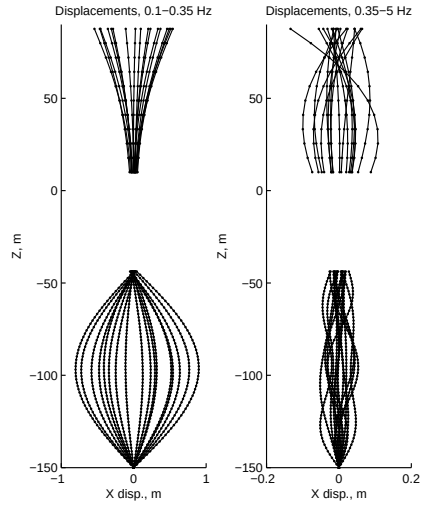

Figure A.10: Tendon 1 and tower bending modes for soft TLPWT 1 based on bandpassed time series from the pitch decay test.

A.6 Soft TLPWT 2 Tower and Tendon Mode Shapes

Fig. A.11 shows five tendon modes for the soft version of TLPWT 2: the first pinned-pinned mode, a mode associated with the first platform pitch/tower bending mode, the second and third pinned-pinned modes, and a mode associated with the second platform pitch/tower bending mode. The first two modes are quite close in frequency, but nonetheless distinct. The second pinned-pinned mode is, however, not strongly present.

For the soft version of TLPWT 2, the mode associated with the first platform pitch/tower bending mode causes significant displacements, and the mode associated with the second platform pitch/tower bending mode is dominant over the other high-frequency modes.

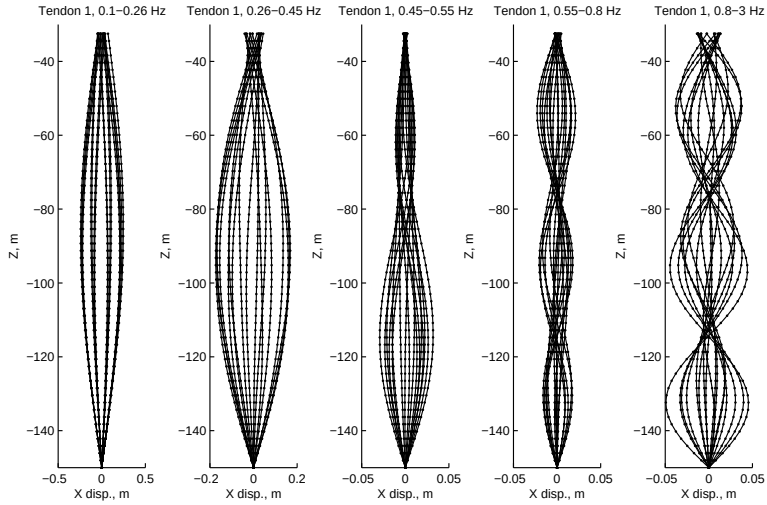

Figure A.11: Tendon 1 bending modes for soft TLPWT 2 based on bandpassed time series from the pitch decay test.

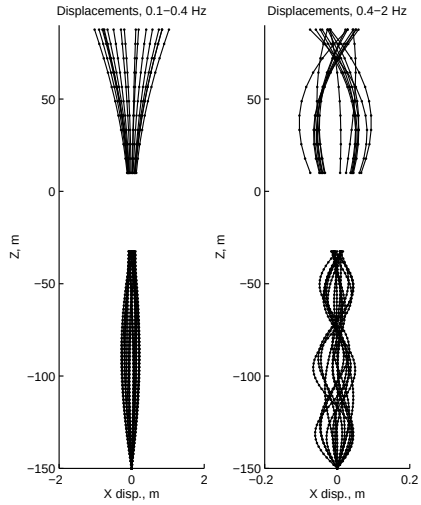

Figure A.12: Tendon 1 and tower bending modes for soft TLPWT 2 based on bandpassed time series from the pitch decay test.

A.7 Soft TLPWT 3 Tower and Tendon Mode Shapes

The tendon modes for the soft TLPWT 3 follow the same pattern as the soft TLPWT 2, except that the mode associated with the second plat-

form pitch/tower bending mode corresponds to the fourth pinned-pinned mode. As with the soft TLPWT 2, the second pinned-pinned mode for soft TLPWT 3 is not strongly present.

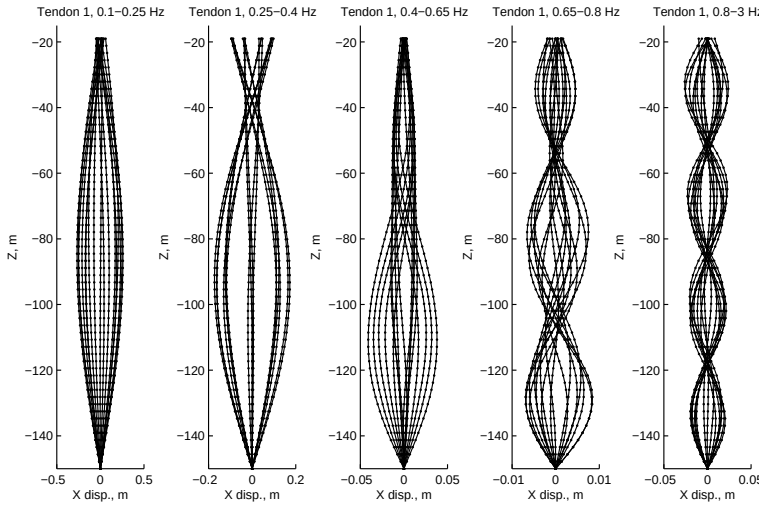

Figure A.13: Tendon 1 bending modes for soft TLPWT 3 based on band-passed time series from the pitch decay test.

As expected, the fourth pinned-pinned mode is strongly present in the high frequencies of Fig. A.14.

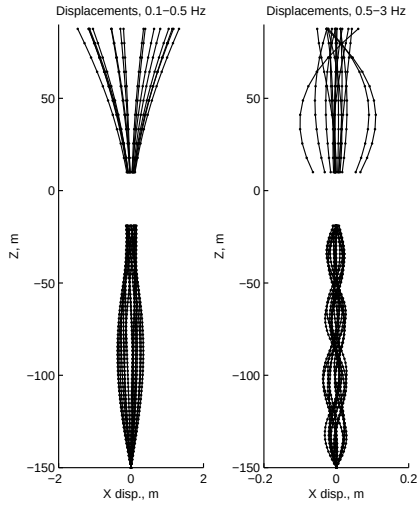

Figure A.14: Tendon 1 and tower bending modes for soft TLPWT 3 based on bandpassed time series from the pitch decay test.

A.8 Soft TLPWT 4 Tower and Tendon Mode Shapes

Six tendon modes for the soft TLPWT 4 are shown in Fig. A.15: the first pinned-pinned mode, a mode associated with the first platform pitch/tower bending mode, the second, third, and fourth pinned-pinned modes, and a mode associated with the second platform pitch/tower bending mode.

There was no clear dominance among the high-frequency modes, but the mode associated with the first platform pitch/tower bending mode was clearly dominant in the lower-frequency range (Fig. A.16).

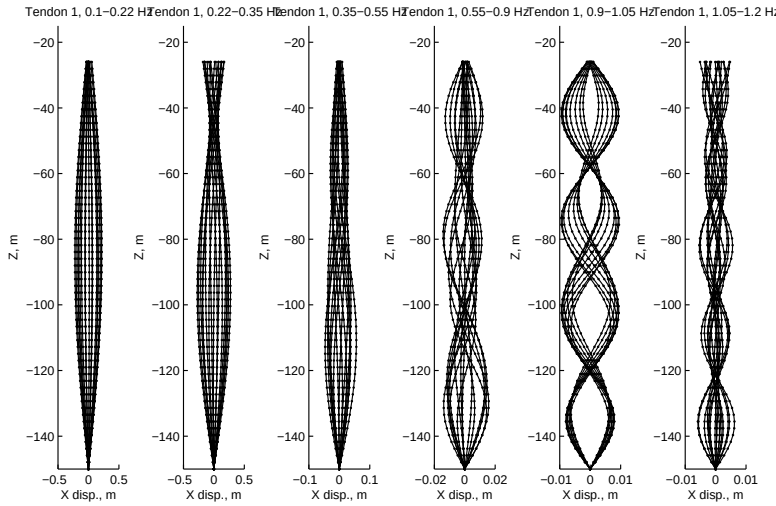

Figure A.15: Tendon 1 bending modes for soft TLPWT 4 based on bandpassed time series from the pitch decay test.

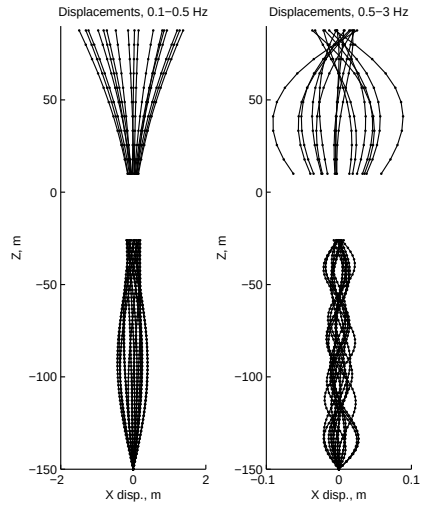

Figure A.16: Tendon 1 and tower bending modes for soft TLPWT 4 based on bandpassed time series from the pitch decay test.

Appendix B

Parameter Variations

This appendix complements Sec. 4.2.

Table B.1 shows the natural periods of the baseline designs and all parametric variations.

Fig. B.1 shows the coefficient of variation (σ/μ) for the key parameters shown in Fig. 4.10. The variation in $\sigma(\zeta_1)$ is related, to some extent, to the variation in$\mu(\zeta_1)$: smaller platforms tended to have both larger mean and larger standard deviations, while the coefficient of variation was more similar among the different platforms for a given EC. On the other hand, the coefficient of variation of the pitch motion was large for both large platforms (which had small mean pitch) and small platforms (which had large pitch standard deviation). Because $\mu(M_{FA})$ varied very little among the concepts, the coefficient of variation of M_{FA} primarily reflects the standard deviation. Finally, the coefficient of variation for the tendon tension is large for both large displacement concepts (with large $\sigma(T_1)$) and small displacement concepts (with low mean tension in the downwind tendon).

The effects of parameter variations on the standard deviation of the surge, pitch, and yaw motions, the tendon tension, and the tower base fore-aft bending moment are shown in Figs. B.2-B.6. In all cases, the change in standard deviation is computed as in Eq. B.1.

$$\Delta\sigma = \frac{\sigma(\text{Variation}) - \sigma(\text{Baseline})}{\sigma(\text{Baseline})} \tag{B.1}$$

These effects are also summarized in Sec. 4.2.4.

Table B.1: Natural periods of TLPWTs 1-5, baseline designs and parametric variations

		baseline	1.1D	0.9D	100 m	200 m	$1.2r_p$	$0.8r_p$	BF+0.1	BF-0.1
TLPWT 1	Surge (s)	55.78	54.99	56.83	40.41	67.94	54.90	56.70	75.54	45.64
	Heave (s)	0.55	0.60	0.50	0.40	0.67	0.55	0.55	0.58	0.53
	Pitch/Bend 1 (s)	2.79	2.79	2.80	2.77	2.84	2.76	2.84	2.80	2.82
	Pitch/Bend 2 (s)	0.51	0.58	0.48	0.39	0.63	0.45	0.64	0.51	0.50
	Yaw (s)	13.99	13.91	14.39	9.27	18.40	12.94	15.85	19.80	12.46
TLPWT 2	Surge (s)	53.13	54.64	51.26	40.16	63.73	49.47	58.23	63.90	46.01
	Heave (s)	0.75	0.79	0.70	0.57	0.89	0.78	0.72	0.77	0.72
	Pitch/Bend 1 (s)	2.81	2.82	2.80	2.76	2.86	2.78	2.88	2.82	2.81
	Pitch/Bend 2 (s)	0.48	0.50	0.47	0.39	0.60	0.46	0.58	0.48	0.48
	Yaw (s)	17.97	17.56	18.46	14.13	22.25	17.52	18.95	21.20	15.86
TLPWT 3	Surge (s)	41.86	42.43	40.87	32.73	49.86	39.47	45.48	46.12	38.54
	Heave (s)	0.60	0.62	0.58	0.47	0.71	0.64	0.56	0.61	0.59
	Pitch/Bend 1 (s)	2.76	2.77	2.75	2.73	2.81	2.74	2.81	2.77	2.75
	Pitch/Bend 2 (s)	0.39	0.40	0.38	0.34	0.44	0.38	0.41	0.39	0.39
	Yaw (s)	18.63	18.10	19.16	14.10	22.82	18.27	19.35	20.07	17.41
TLPWT 4	Surge (s)	34.22	34.98	33.41	26.07	41.09	32.14	37.51	35.63	32.88
	Heave (s)	0.52	0.53	0.52	0.40	0.62	0.57	0.48	0.53	0.52
	Pitch/Bend 1 (s)	2.74	2.75	2.73	2.70	2.80	2.72	2.71	2.74	2.74
	Pitch/Bend 2 (s)	0.39	0.40	0.39	0.34	0.44	0.38	0.41	0.40	0.39
	Yaw (s)	19.71	19.67	19.91	15.60	24.52	19.18	20.98	20.41	19.27
TLPWT 5	Surge (s)	40.13	40.80	39.45	31.49	47.55	36.67	46.15	41.80	38.60
	Heave (s)	0.60	0.61	0.59	0.47	0.70	0.64	0.55	0.60	0.59
	Pitch/Bend 1 (s)	2.69	2.69	2.66	2.68	2.70	2.64	2.72	2.67	2.66
	Pitch/Bend 2 (s)	0.39	0.39	0.39	0.34	0.43	0.39	0.40	0.39	0.39
	Yaw (s)	21.76	21.48	22.01	16.60	26.44	21.55	24.01	22.44	21.19

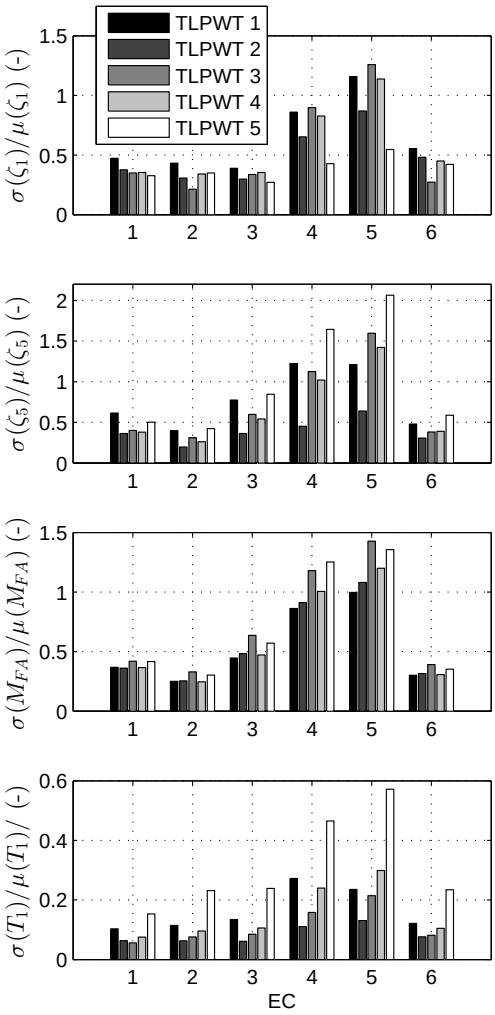

Figure B.1: Baseline TLPWT coefficient of variation for surge, pitch, tower base bending moment, and line tension

Figure B.2: Change in $\sigma(\zeta_1)$ due to parametric variations

(a) Diameter variation

(b) Water depth variation

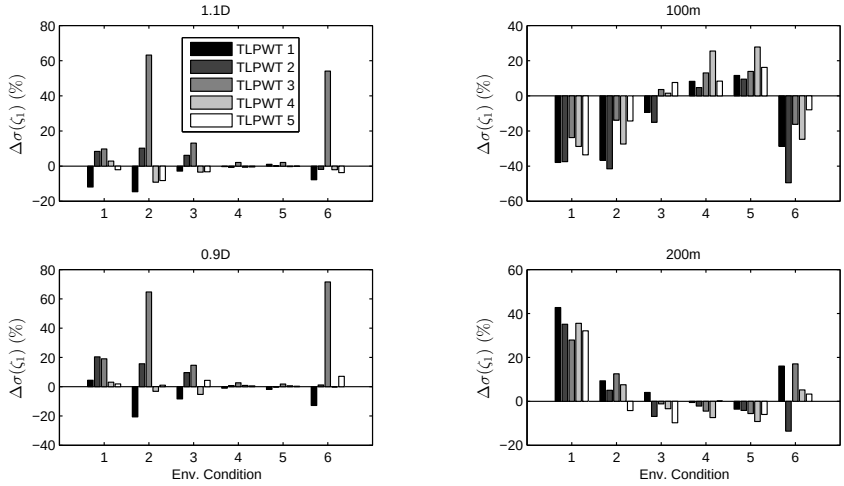

(c) Pontoon radius variation

(d) Ballast fraction variation

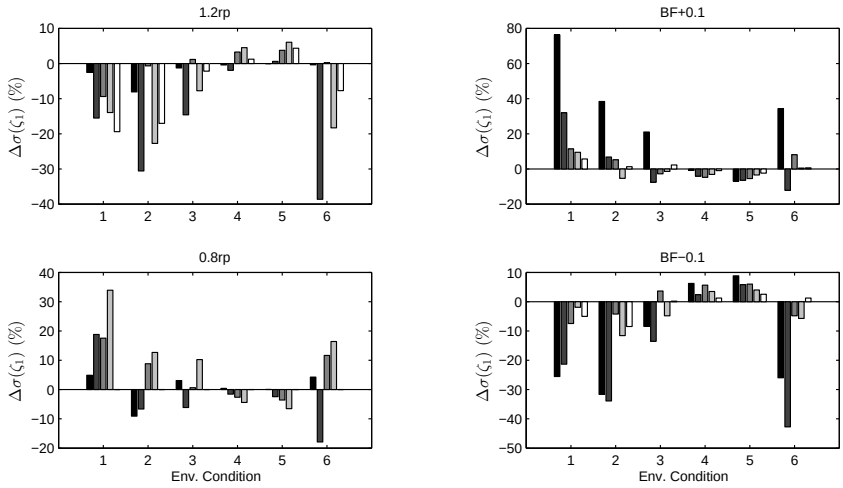

Figure B.3: Change in $\sigma(\zeta_5)$ due to parametric variations

(a) Diameter variation

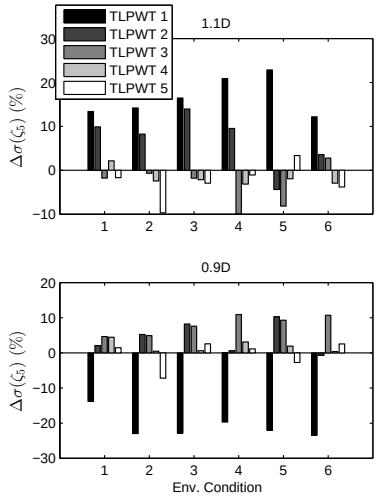

(b) Water depth variation

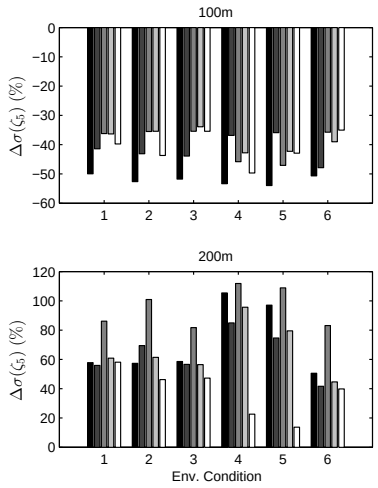

(c) Pontoon radius variation

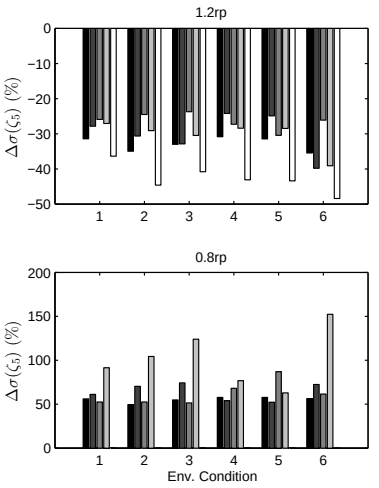

(d) Ballast fraction variation

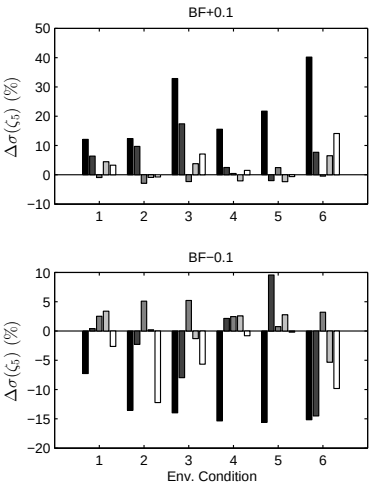

Figure B.4: Change in $\sigma(\zeta_6)$ due to parametric variations

(a) Diameter variation

(b) Water depth variation

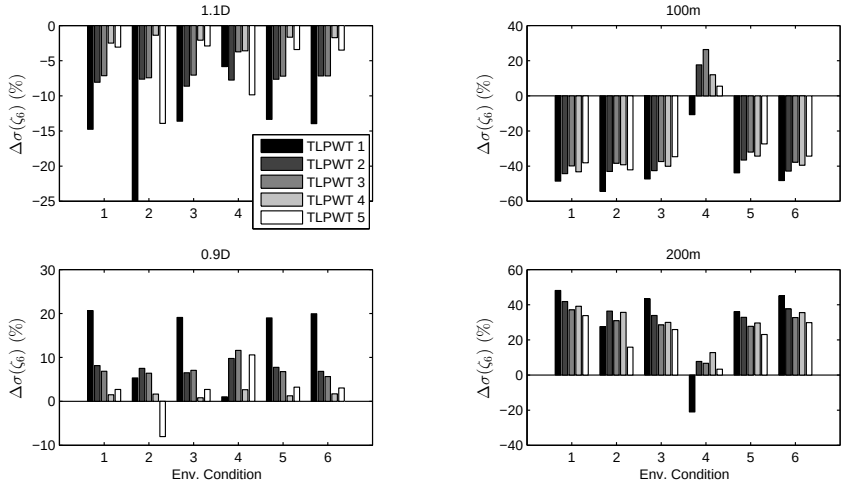

(c) Pontoon radius variation

(d) Ballast fraction variation

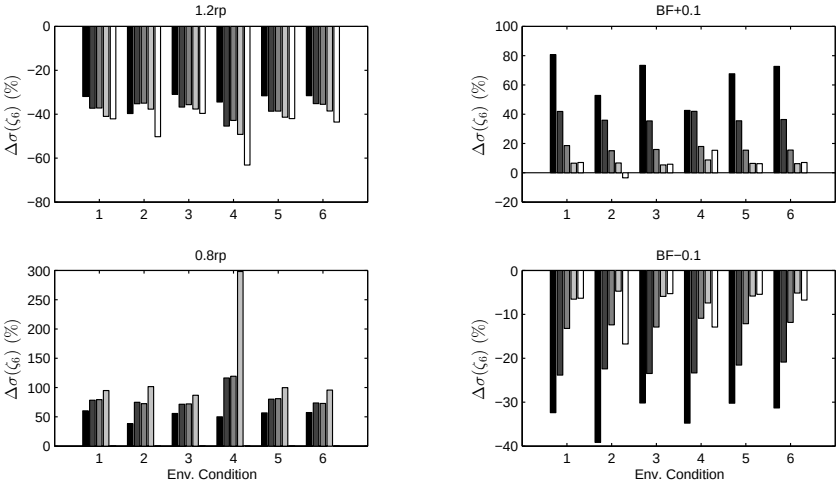

Figure B.5: Change in $\sigma(M_{FA})$ due to parametric variations

(a) Diameter variation

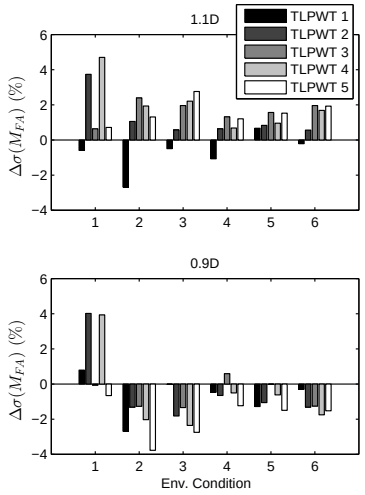

(b) Water depth variation

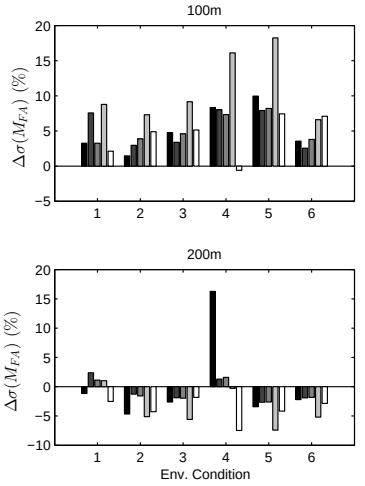

(c) Pontoon radius variation

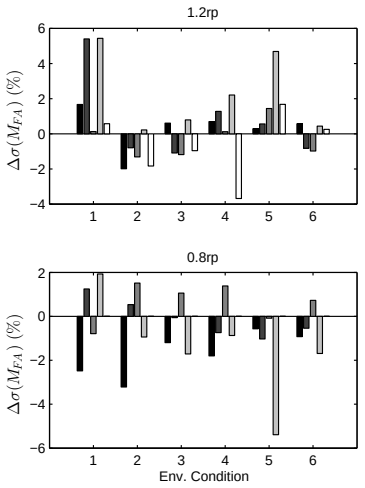

(d) Ballast fraction variation

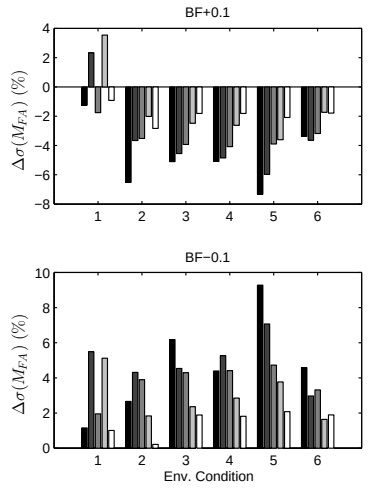

Figure B.6: Change in $\sigma(T_1)$ due to parametric variations

(a) Diameter variation

(b) Water depth variation

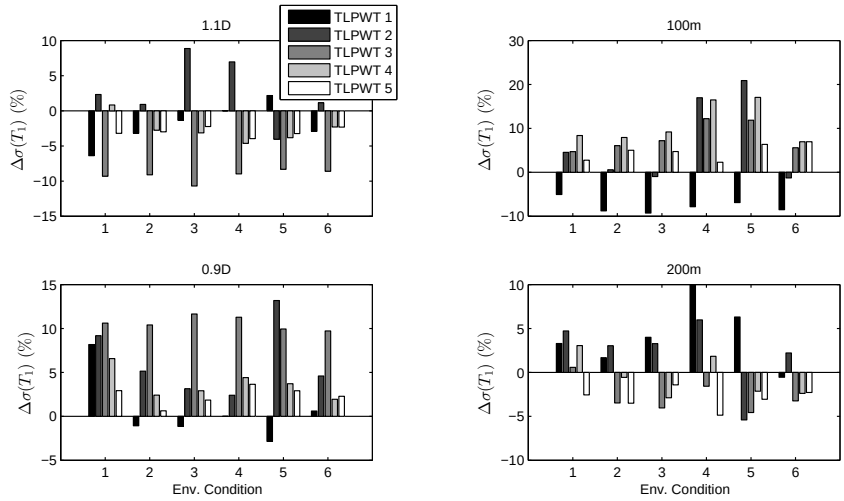

(c) Pontoon radius variation

(d) Ballast fraction variation

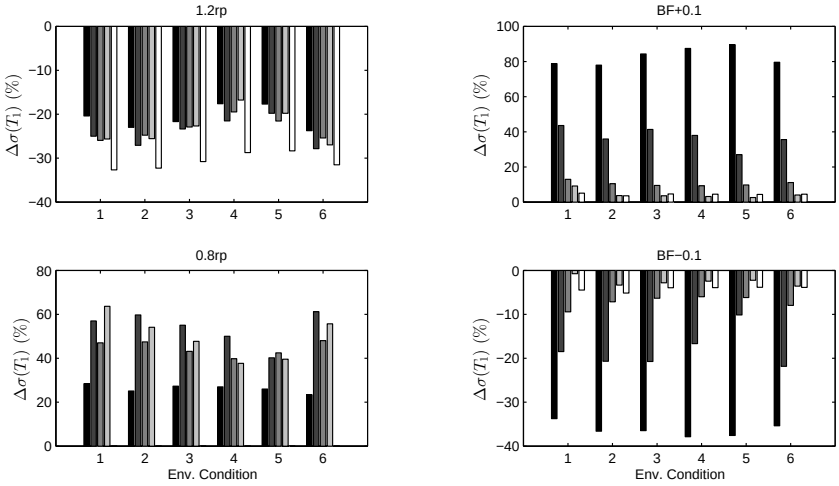

Appendix C

Second-Order Potential Flow Calculations

This appendix examines the second-order force computation for three single-column TLPWT designs (TLPWTs 1-3, see Section 4.1.4). The tool used here for loads prediction is WADAM, which has a particular limitation: there may only be 3000 free surface panels in the basic part of the model (ie, one quadrant for double-symmetric hulls, or two quadrants for hulls with a single plane of symmetry) [154]. It is therefore necessary to carefully examine the free surface and body meshing to optimize the use of the available computational resources, and to examine the effects of different meshes on the results. Due to the difficulty of perfectly predicting the first-order motions including viscous damping, it is also of interest to examine whether results for the stationary hull can give a reasonable estimate of the second-order forcing on the moving hull. The effect of pontoons and use of Newman's approximation are also examined.

C.1 Free Surface Meshing

The free surface mesh was created with the same symmetry settings as the hull panel model. For TLPWT 1, a single quadrant may be modeled, while two quadrants are required for TLPWTs 2 and 3. The mesh geometry is defined as in Fig. C.1, with a finer mesh inside the radius R1, and a coarser mesh out to radius R2. An identical number of elements (NC) were distributed on the curved edges, and two distributions (NX1 elements and NX2 elements) were used on the straight edges. In order to use the maximum number of elements, a mesh with $NC \times (NX1 + NX2) = 3000$ may be chosen.

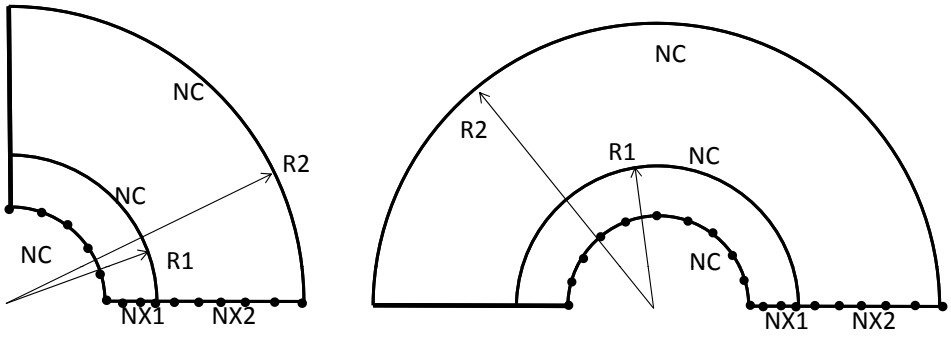

Figure C.1: Free surface meshing

Recommendations for the panels on the TLPWT hull include:

- 6 panels per second-order wavelength [172]: For panels with diagonal

dimension 0.5m, this implies greatest confidence in results for incoming waves with periods of at least 5.5s. The shortest wave periods included in the second-order analysis were 4.5s.

- Finer mesh around corners [172]: This was achieved by non-uniform edge element distributions in the meshing program PatranPre.
- Finer mesh around waterline [172]: This was achieved by non-uniform edge element distributions in the meshing program PatranPre.

Recommendations for the panels on the free surface include:

- The partitioning radius R_2 must enclose the hydro model [154].
- $R_2 \approx O(H)$ for shallow water and $R_2 \approx O(\lambda)$ for deep water [154]: The water depth considered here is $H = 150$m, which can be considered deep water for waves shorter than approximately 14s, or intermediate water depth for longer waves. The partition radius should ideally be larger than 150m to capture the longest waves, but the panel size is also an important consideration, within the limitations of the number of panels available. For the ISSC TLP, the convergence of the heave force was relatively slow with respect to the partition radius, as compared to surge and pitch components [126].

In the following sections, the first and second-order forcing on the different TLPWT hulls are examined in detail, considering the meshing geometry, the forces on the stationary hull, and then adding the first-order motions.

C.2 TLPWT 1

For TLPWT 1, the small pontoons were not included in the panel model, and due to the symmetry, only one quadrant of the hull and free surface was modeled. Three free surface meshes (Sec. C.2.1) were first compared for the stationary platform, to examine the effects of the number of panels and the partition radius on the sum- and difference-frequency force computations (Sec. C.2.2 and C.2.3). The effect of the first-order motions is then examined in Sec. C.2.4 and C.2.5.

C.2.1 Free Surface Meshes

Three meshes were compared for TLPWT 1 as a stationary platform, as shown in Table C.1 and Fig. C.2. Mesh 2 was approximately twice as fine

as Mesh 1, while Mesh 3 was coarser but had a larger partition radius. A comparison between meshes 1 and 2 was used to find out whether or not a mesh density similar to Mesh 1 could be used for the other platforms (which required 2 quadrants in the basic model). Comparing Mesh 3 and Mesh 2 for longer waves served as an indication of the limitations of the 150 m partition radius.

Table C.1: TLPWT 1 free surface meshes

	Mesh 1	Mesh 2	Mesh 3
R1 (m)	27	27	60
R2 (m)	150	150	250
NC	18	36	30
NX1	18	30	30
NX2	50	50	70
Free Surface Elements	1224	2880	3000

C.2.2 Sum-Frequency Forces on Stationary TLPWT 1

The first-order and the double-frequency exciting forces and moments on the stationary structure are shown in Fig. C.3. Note that the frequency given on the x-axis represents the incoming wave frequency and all transfer functions are presented for unit wave amplitudes. The mean excitation is shown in the right-hand plots. As shown, the sum-frequency forces were approximately an order of magnitude smaller than the first-order forces. Good agreement for the double-frequency forces was seen for heave and pitch, which are most sensitive to high-frequency forcing. A slight mesh dependence was seen in the real part of the double-frequency surge forcing.

In addition to the double-frequency forces, it is interesting to examine the shape of the full sum-frequency force quadratic transfer function (QTF) for heave and pitch for the stationary structure. Fig. C.4 shows the QTF obtained from mesh 2, which agreed well with results for the other meshes. As shown, the heave force was maximum along the double-frequency line, and increased with increasing frequency, with a fairly sharp decline outward. The heave natural frequency for TLPWT 1 (11.4 rad/s) was so high that it was very unlikely to be excited.

The pitch moment QTF also had its maximum along the double-frequency line and increased with increasing frequency, but did not decrease as sharply

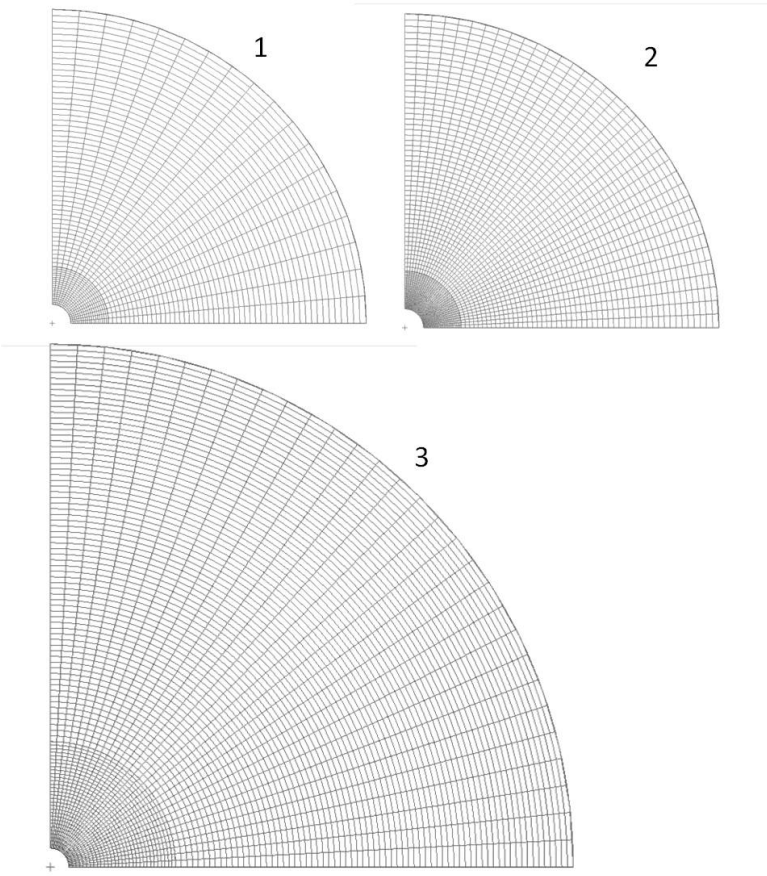

Figure C.2: TLPWT 1 free surface meshes

away from the double-frequency line. The dashed line shows the points where $\omega_i + \omega_j = \omega_5$, where ω_5 is the first coupled pitch/tower bending frequency [156]. As shown, there may be significant excitation around these frequencies.

C.2.3 Difference-Frequency Forces on Stationary TLPWT 1

Since the structure has a low-frequency resonance in surge, the primary low-frequency excitation of interest is in surge. The diagonal terms of the difference-frequency QTF are independent of the free surface mesh, and can be computed from the first-order solution. These terms are known to be sensitive to the number of elements on the waterline [172]. The difference-frequency QTF showed good agreement between meshes 2 and 3, with mesh

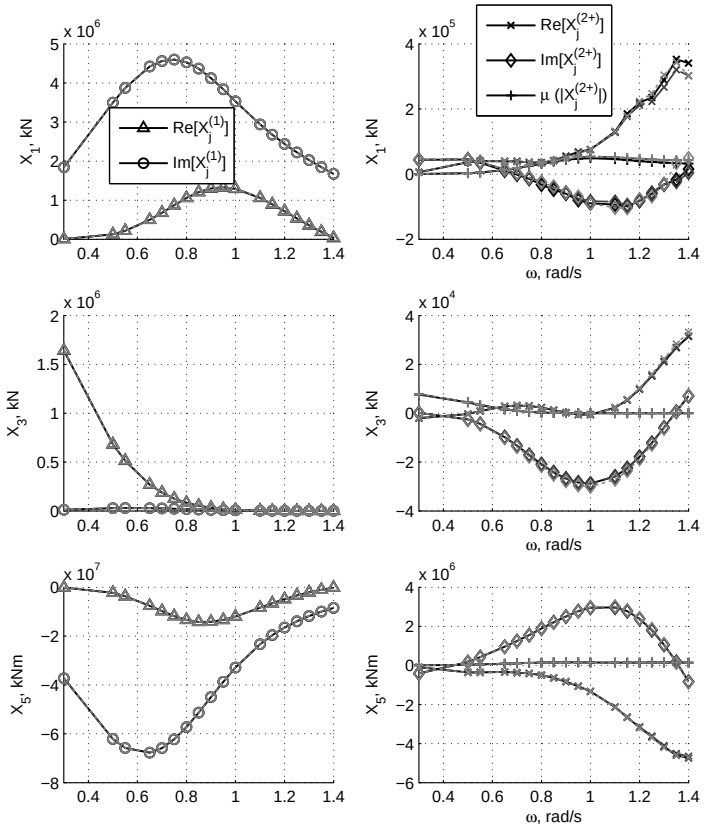

Figure C.3: First-order (left) and double-frequency (right) surge force, heave force, and pitch moment transfer function components, stationary TLPWT 1. Mesh 1: solid black line, mesh 2: dashed gray line, mesh 3: dotted light gray line.

1 giving slightly smaller surge forcing. (Mesh 1 was coarser around the waterline). Fig. C.5a shows the QTF computed using mesh 2, including the surge resonance frequency.

By computing the QTF values along the dashed and dotted lines in Fig. C.5a, we can examine whether or not Newman's approximation is appropriate in this context. For a stationary cylinder, as shown in Fig. C.5b, the Newman approximation worked very well across a wide range of frequencies, as expected. The discrepancy in the lowest frequencies stemmed from interpolation from the rather coarse QTF in the low-frequency range.

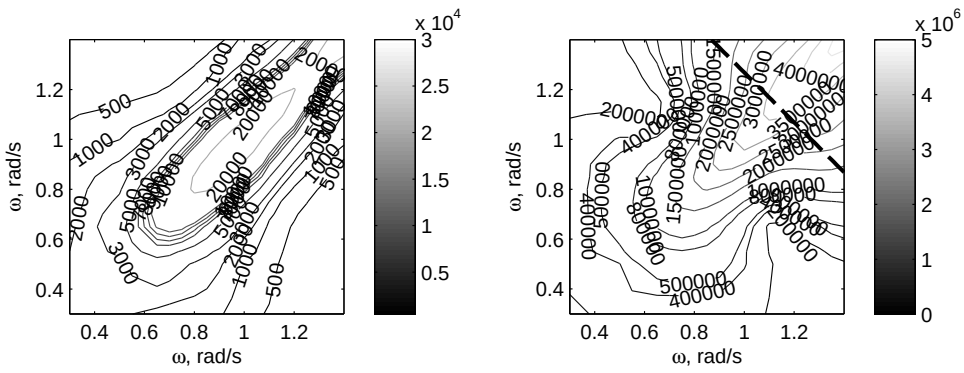

Figure C.4: Sum-frequency heave force (left) and pitch moment (right) QTFs for the stationary TLPWT 1 (mesh 2). The first pitch/bending natural frequency is indicated by the dashed line.

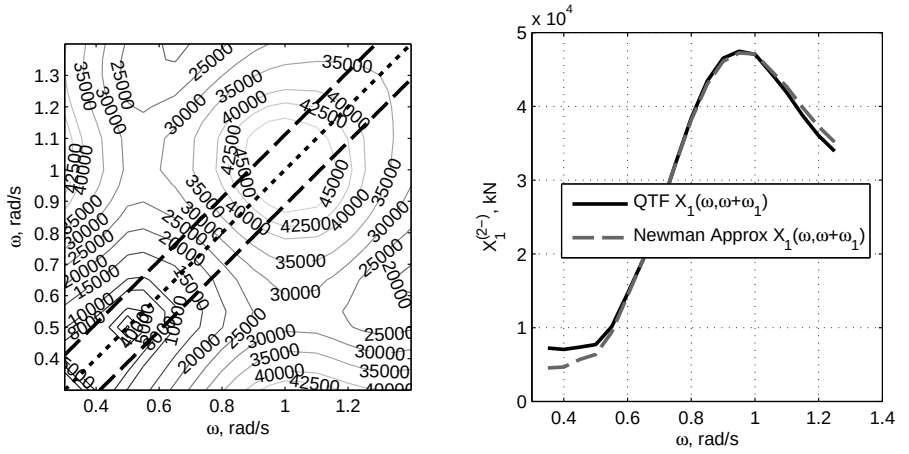

(a) Diff.-freq. surge force QTF (b) QTF and Newman's approx. at T_{n1}

Figure C.5: a) Difference-frequency surge force transfer functions, for stationary TLPWT 1 (mesh 2). Heavy dashed lines indicate the surge resonance difference-frequency ($\omega_i - \omega_j = \pm\omega_1$), dotted line shows $\omega_i = \omega_j$. b) Difference-frequency surge force at the TLPWT 1 surge natural frequency, based on QTF and Newman's approximation for the fixed structure.

C.2.4 Sum-Frequency Forces on Moving TLPWT 1

The previous results were computed for the stationary platform, but the correct solution for the second-order potential should include the first-order

platform motions. Tension leg elements and appropriate Morison damping were included in the WADAM model in order to achieve first-order motion RAOs.

Fig. C.6 compares the first-order RAOs computed by WADAM to time domain simulation results in irregular wave-only conditions using SIMO/RIFLEX. The SIMO/RIFLEX results include structural non-linearities and quadratic damping from the Morison equation, but no second-order potential forces. The results show reasonable agreement, although the WADAM RAO overestimates the pitch response for TLPWT 1.

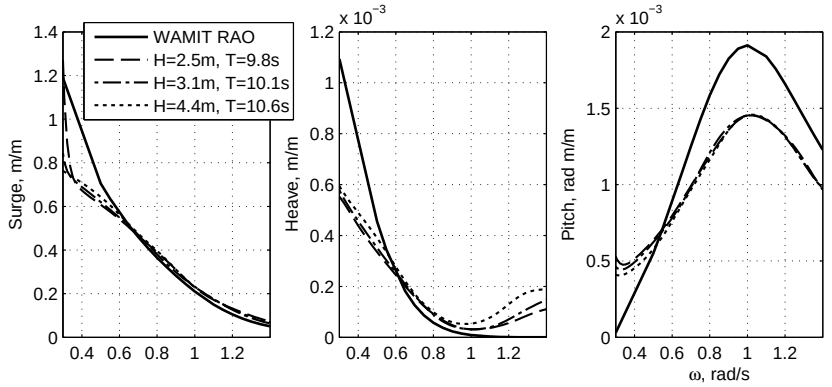

Figure C.6: TLPWT 1: first-order motion RAOs. Note: pitch non-dimensionalized by D/ζ.

The components of the double-frequency forces on TLPWT 1 for the stationary and moving structure are shown in Fig. C.7. All results in this section use mesh 2.

Fig. C.7 suggests that the first-order motions had a particularly large effect on the real component of the double-frequency surge force, while the mean and imaginary components were quite similar. The double-frequency heave force was significantly underestimated when the first-order motions were not included, while the imaginary component of the pitch moment was overestimated.

The effect of the first-order motions on the force QTFs can also be examined by comparing the contour plots shown in Fig. C.4 for the stationary hull and Fig. C.8 for the moving hull. The computed heave QTFs were smaller in the high frequency range, and tended to decrease more sharply, when the first-order motions were included. For the low frequencies, the heave QTF values were slightly larger when first-order motions were included. The pitch moment QTFs similarly had smaller peak values, but

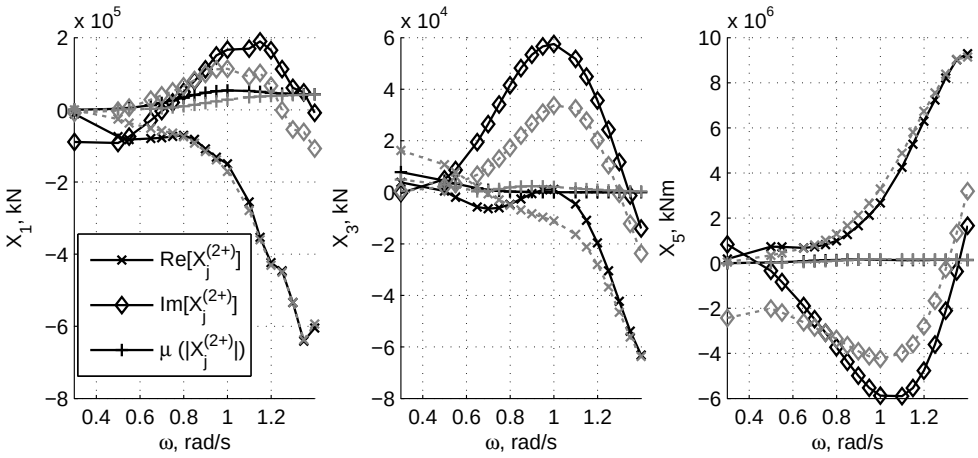

Figure C.7: Double-frequency surge force, heave force, and pitch moment transfer function components, for TLPWT 1 fixed in space (solid, black) and moving (dotted, gray). (mesh 2)

less narrow peaks.

The most important consideration for determining whether or not the QTF for a stationary platform could give a reasonable approximation is the forcing obtained near the natural frequency. Fig. C.9 shows the pitch moment transfer function along the line $\omega_i + \omega_j = \omega_5$ for the stationary and moving models. The stationary model overpredicts the pitch excitation compared to the moving model by approximately 12% at the peak and as much as 30% in the lower frequency range (where there is expected to be more incoming wave excitation).

C.2.5 Difference-Frequency Forces on Moving TLPWT 1

The effect of the first-order motions on the difference-frequency forces may also be important. The shape of the surge force difference-frequency QTF changed significantly when the first-order motions were included (Fig. C.10a). (All results in this section use mesh 2). Forcing along the diagonal ($\omega_i = \omega_j$) tended to decrease, while the off-diagonal forcing increased for large frequency differences. When the first-order motions were included, the QTF was found to change more quickly near the surge frequency, which called into question the validity of Newman's approximation.

Fig. C.10b compares the validity of Newman's approximation with and without the first-order motions. When the first-order motions were included, Newman's approximation underpredicted the forcing for incoming wave fre-

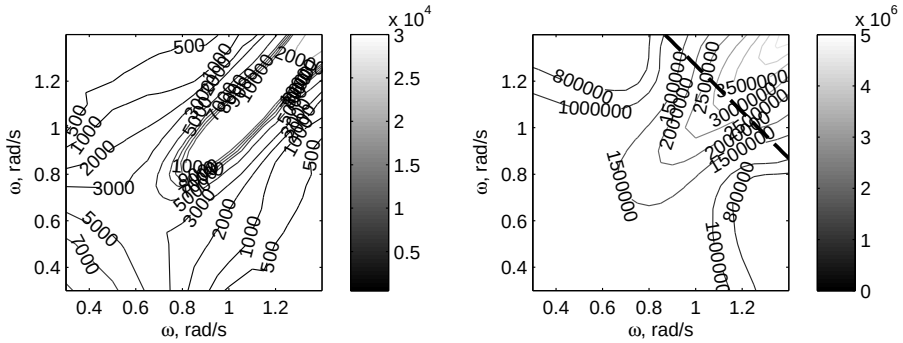

Figure C.8: Sum-frequency heave force (left) and pitch moment (right) QTFs. The first pitch/bending natural frequency is indicated by the dashed line.

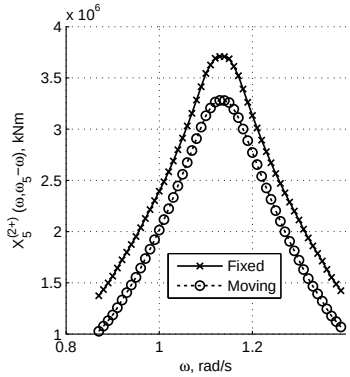

Figure C.9: Sum-frequency pitch moment along the first pitch/bend natural frequency line for the stationary and moving TLPWT 1

quencies 0.3 rad/s - 0.8 rad/s: that is, a significant portion of the typical wave energy spectrum. Furthermore, a comparison between the stationary and moving approximations indicated that the forces given by the stationary hull computation exceeded those for the moving hull.

C.3 TLPWT 2

The three free surface meshes which were compared for TLPWT 2 are summarized in Sec. C.3.1. Sum- and difference-frequency forces on the station-

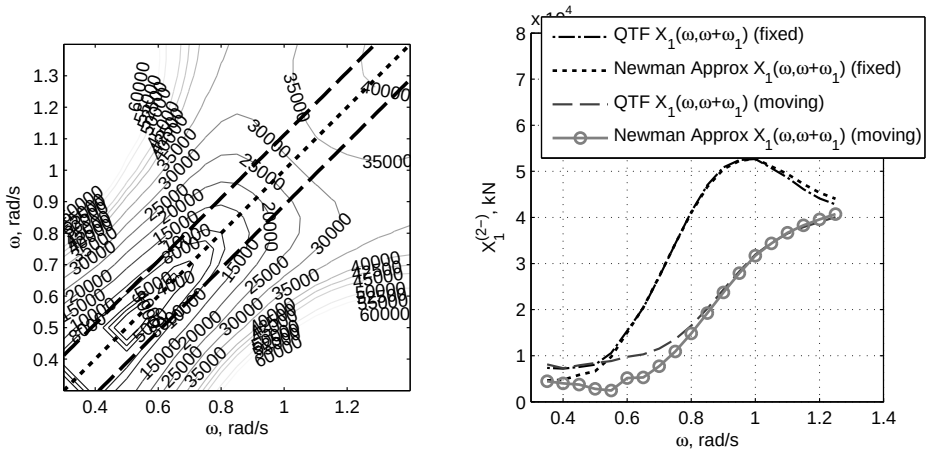

(a) Diff.-freq. surge force QTF (b) QTF and Newman's approx. at T_{n1}

Figure C.10: a) Difference-frequency surge force QTF for TLPWT 1, including first-order motions (mesh 2). Heavy dashed lines indicate the surge resonance difference-frequency, dotted line shows $\omega_i = \omega_j$. b) Difference-frequency surge force at the TLPWT 1 surge natural frequency, based on QTF (mesh 2) and Newman's approximation for the fixed and moving structure.

ary hull are examined in Secs. C.3.2-C.3.3. The effect of first-order motions on the second-order forces is examined in Secs. C.3.4-C.3.5.

C.3.1 Free Surface Meshes

Three free surface meshes were compared for TLPWT 2, as described in Table C.2. Due to the three pontoons, the hull had only one plane of symmetry, so half of the free surface had to be modeled. All of the meshes employed the maximum possible number of elements. The first two meshes were very similar, but the second mesh had smaller spacing close to the waterline and fewer elements outside $R1$. The third mesh had the same concentration of elements along the waterline as mesh 1, but a coarser mesh and larger partition radius.

C.3.2 Sum-Frequency Forces on Stationary TLPWT 2

The three meshes were first compared for the stationary TLPWT. Fig. C.11 shows the first-order and double-frequency surge, heave, and pitch excita-

Table C.2: TLPWT 2 free surface meshes

	Mesh 1	Mesh 2	Mesh 3
R1 (m)	28	28	35
R2 (m)	150	150	250
NC	40	50	40
NX1	20	20	20
NX2	55	40	55
Free Surface Elements	3000	3000	3000

tion. As with TLPWT 1, the second-order forces were typically 1 or 2 orders of magnitude smaller than the first-order forces in the main wave excitation frequencies (<1 rad/s). Good agreement was seen for the double-frequency excitation in heave and pitch, while small discrepancies were noted in the double-frequency surge. The coarse outer mesh of Mesh 2 gave slightly different results for some (lower-frequency) components of the double-frequency heave forcing, indicating that the mesh density over the whole free surface mesh matters.

The QTFs of heave and pitch excitation for the stationary TLPWT 2 are shown in Fig. C.12. The heave excitation was not strictly maximum along $\omega_i = \omega_j$ in this case, but the pitch forcing qualitatively resembled the pitch forcing for the fixed TLPWT 1. Fig. C.12 also indicated that there may be significant pitch excitation due to the second-order potential around the first pitch natural frequency.

C.3.3 Difference-Frequency Forces on Stationary TLPWT 2

Consistent with the results from TLPWT 1, the difference-frequency results for TLPWT 2 were found to depend only slightly on the distribution of elements along the waterline. The surge force QTF for the fixed platform is shown in Fig. C.5a, with the resonance frequency indicated by the dashed lines. As shown in Fig. C.13b, the Newman approximation works quite well for the stationary TLPWT 2. Since the second-order force in surge depended primarily on the elements at the waterline, it also seen that the difference-frequency surge force at the natural frequency is estimated very well by a stationary cylinder without pontoons. This could be used to save computational time if the results were similar to the full model when first-order motions are included (see Section C.3.5).

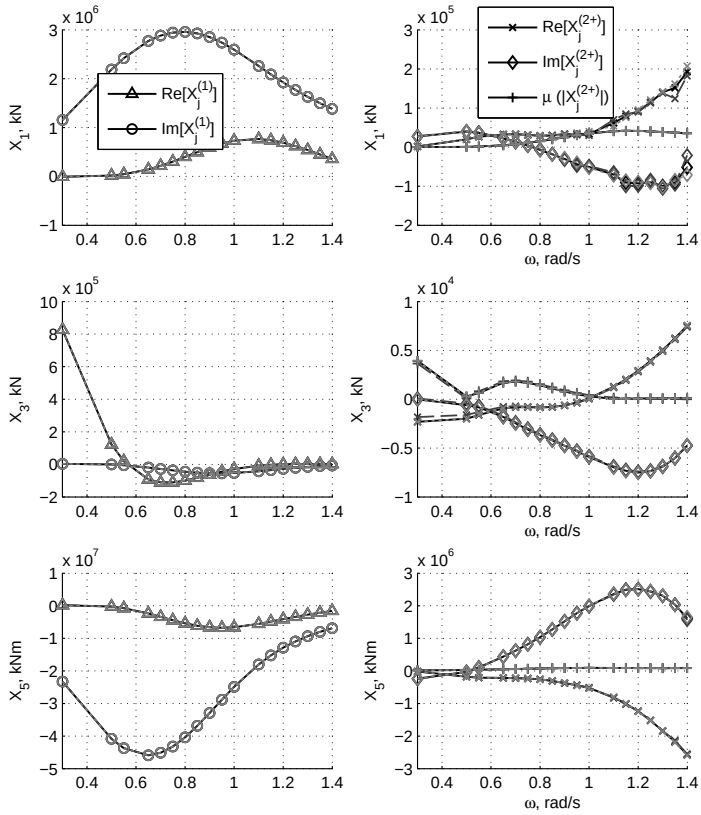

Figure C.11: First-order (left) and double-frequency (right) surge force, heave force, and pitch moment transfer function components, stationary TLPWT 2. Mesh 1: solid black line, mesh 2: dashed gray line, mesh 3: dotted light gray line.

C.3.4 Sum-Frequency Forces on Moving TLPWT 2

The first-order motion RAOs for TLPWT 2 are shown in Fig. C.14. The Wadam model captured the motions quite well.

The inclusion of the first-order motions in the calculation of the second-order potential changed the result significantly for some frequencies. Fig. C.15 shows the double-frequency force transfer function components for the stationary and moving hull. All comparisons are shown for mesh 1. As shown, the imaginary components of the surge, heave, and pitch forcing

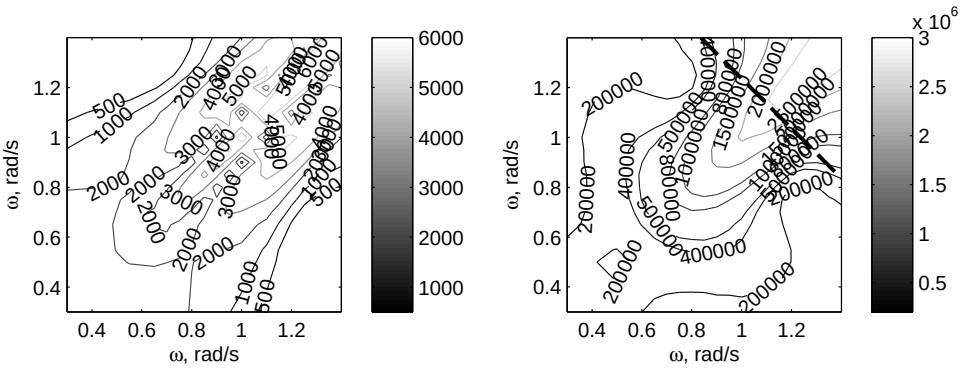

Figure C.12: Sum-frequency heave force (left) and pitch moment (right) QTFs. The first pitch/bending natural frequency is indicated by the dashed line.

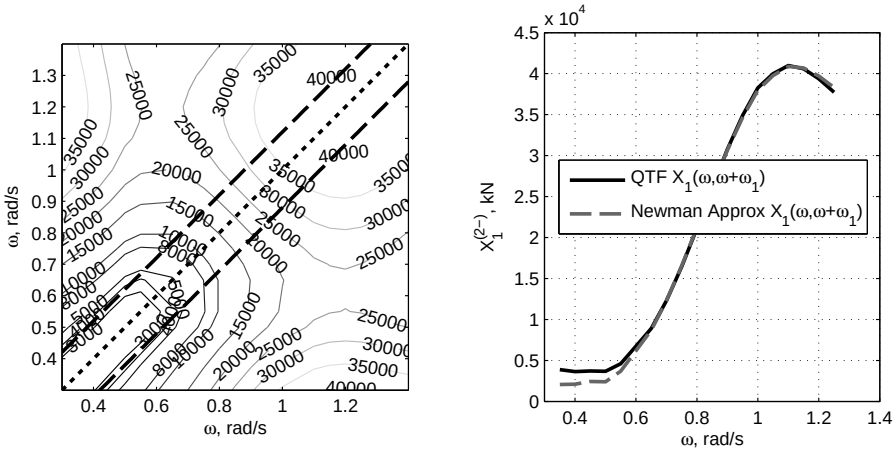

(a) Diff.-freq. surge force QTF (b) QTF and Newman's approx. at T_{n1}

Figure C.13: a) Difference-frequency surge force transfer functions, for stationary TLPWT 2 (mesh 1). Heavy dashed lines indicate the surge resonance difference-frequency ($\omega_i - \omega_j = \pm\omega_1$), dotted line shows $\omega_i = \omega_j$. b) Difference-frequency surge force at the TLPWT 2 surge natural frequency, based on QTF and Newman's approximation for the fixed structure.

were changed more than the real components. The results for the stationary hull were conservative in magnitude for some, but not all, frequencies.

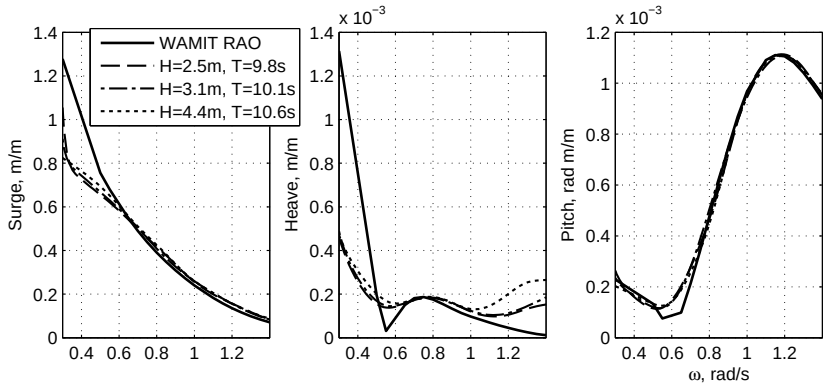

Figure C.14: TLPWT 2: first-order motion RAOs. Note: pitch non-dimensionalized by D/ζ.

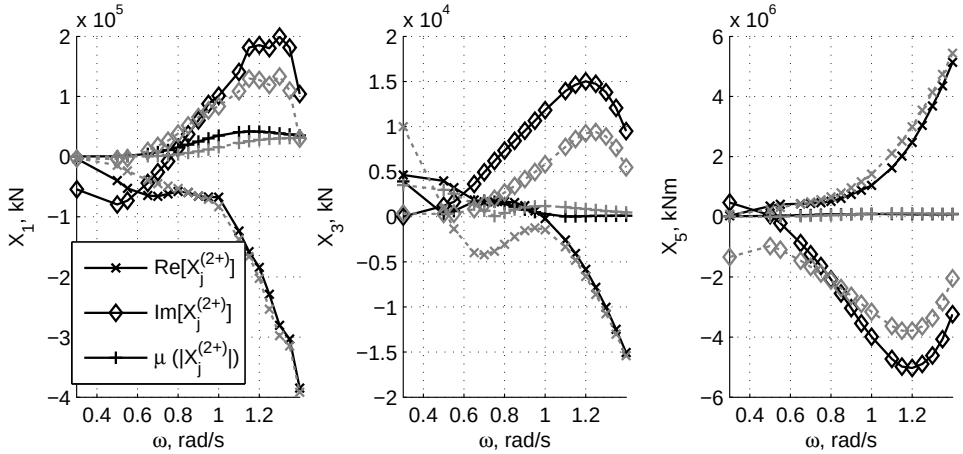

Figure C.15: Double-frequency surge force, heave force, and pitch moment transfer function components, for TLPWT 2 fixed in space (solid, black) and moving (dotted, gray). (mesh 1)

The effect of the motion on the overall shape of the QTF in heave and pitch can be seen by comparing Figs. C.12 and C.16. While the peak values of the force amplitude tended to decrease, the low-frequency components of the QTFs increased. These frequencies represent a large part of the available wave energy.

Examining the pitch moment QTF along the line $\omega_i + \omega_j = \omega_5$ in Fig. C.17, the forcing on the stationary structure matched well around the main wave frequencies but overpredicted the peak by approximately 20 %.

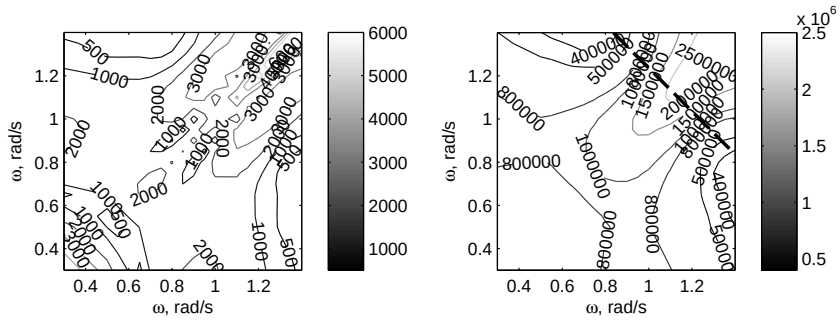

Figure C.16: Sum-frequency heave force (left) and pitch moment (right) QTFs for TLPWT 2 including first-order motions. The first pitch resonance is indicated by the dashed line.

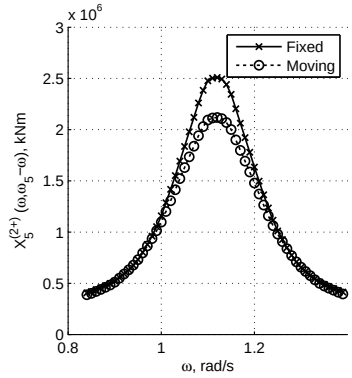

Figure C.17: Sum-frequency pitch moment along the first pitch/bend natural frequency line for the fixed and moving structure.

C.3.5 Difference-Frequency Forces, Moving TLPWT 2

The effect of the first-order motions on the difference-frequency forces was also quite significant. Fig. C.18a shows the surge excitation QTF, which can be compared to Fig. C.13a for the stationary hull. Again, all results are shown for mesh 1. When the first-order motions were considered, the heave forcing decreased along the diagonal, but increased away from the diagonal. The Newman approximation became more tenuous, as illustrated in Fig. C.18b. In the main wave excitation frequencies, the Newman approximation appears to be quite non-conservative.

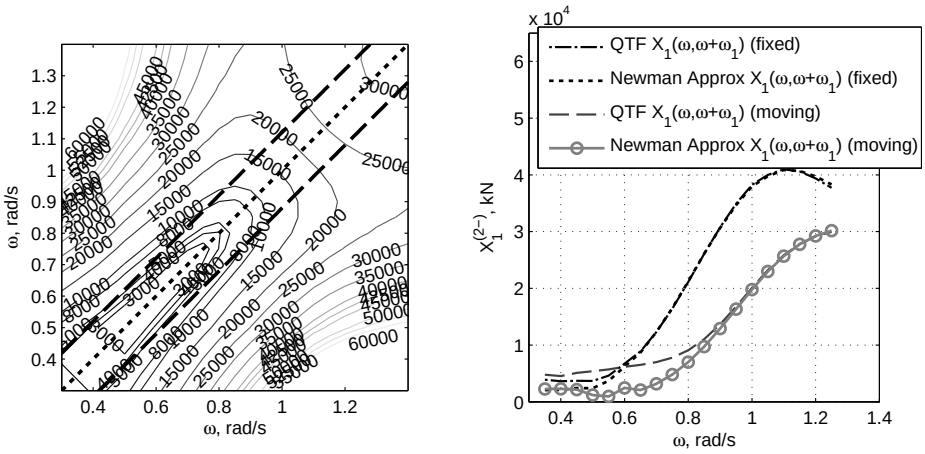

(a) Diff.-freq. surge force QTF (b) QTF and Newman's approx. at T_{n1}

Figure C.18: a) Difference-frequency surge force QTF for TLPWT 2, including first-order motions (mesh 1). Heavy dashed lines indicate the surge resonance difference-frequency, dotted line shows $\omega_i = \omega_j$. b) Difference-frequency surge force at the TLPWT 2 surge natural frequency, based on QTF (mesh 2) and Newman's approximation for the fixed and moving structure.

C.4 TLPWT 3

The free surface mesh used for TLPWT 3 was identical to Mesh 1 for TLPWT 2, as given in Table C.2. No mesh convergence study was performed for TLPWT 3, but the stationary (Secs. C.4.1-C.4.1) and moving (Secs. C.4.3-C.4.3) results were compared, and some consideration was given to the importance of the pontoons in the computation of slow-drift forces.

C.4.1 Sum-Frequency Forces on Stationary TLPWT 3

The first-order and double-frequency forces on TLPWT 3 are shown in Fig. C.19. The surge and pitch forces on TLPWTs 2 and 3 were very similar, as they had the same waterline geometry, though TLPWT 2 had a significantly larger draft. The heave forces on TLPWT 3 were much larger than those on TLPWT 2 due to TLPWT 3's smaller draft and larger pontoons.

The heave and pitch excitation QTFs are shown in Fig. C.20. As shown, both the heave and pitch force generally increased with frequency. The

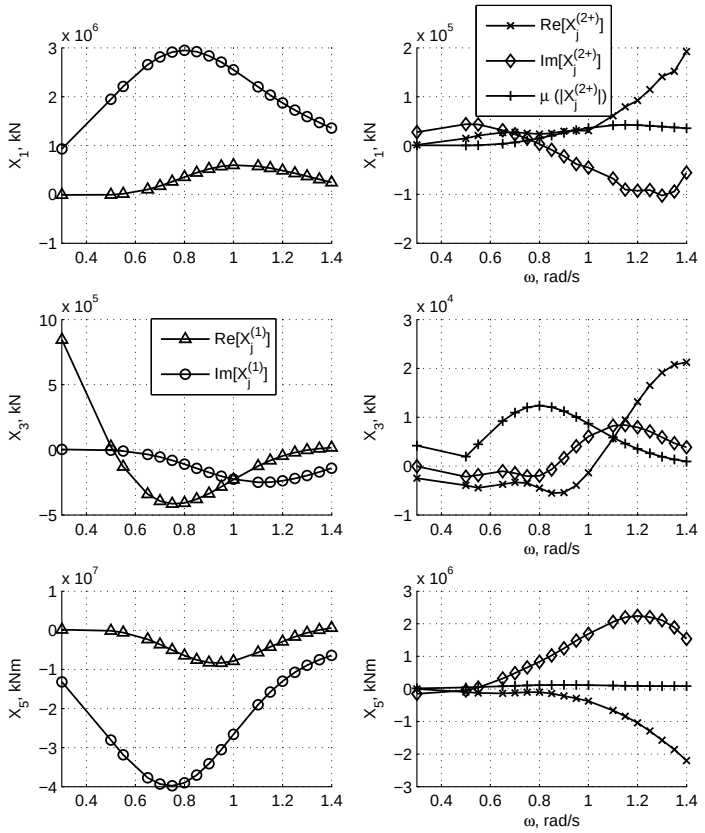

Figure C.19: First-order (left) and double-frequency (right) surge force, heave force, and pitch moment transfer function components, stationary TLPWT 3.

heave force QTF had peak values away from the diagonal. Relatively large values of the pitch QTF intersected the line indicating the first pitch/bending natural frequency.

C.4.2 Difference-Frequency Forces on Stationary TLPWT 3

Fig. C.21a shows the difference-frequency QTF for the stationary TLPWT 3, while Fig. C.21b shows the surge force transfer function at the surge natural frequency. The corresponding surge force transfer function based on Newman's approximation and based on only considering the main column

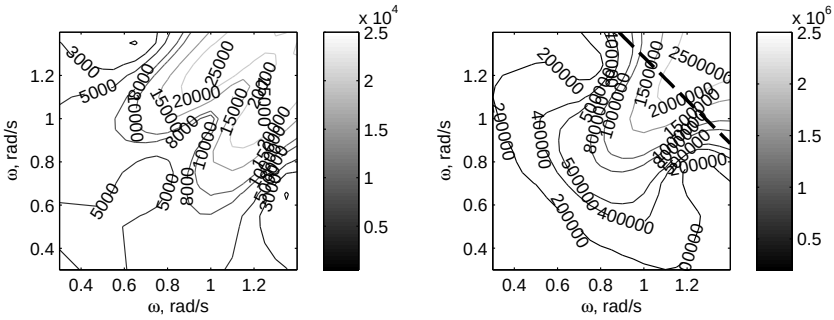

Figure C.20: Sum-frequency heave force (left) and pitch moment (right) QTFs. The first pitch/bending natural frequency is indicated by the dashed line.

(no pontoons) in the model are also shown. For the stationary structure, Newman's approximation worked quite well, and the pontoons did not contribute significantly to the difference-frequency surge force.

C.4.3 Sum-Frequency Forces on Moving TLPWT 3

The first-order motion RAOs for TLPWT 3 are shown in Fig. C.22. The pitch response is somewhat underestimated by Wadam for TLPWT 3.

Fig. C.23 compares the double-frequency transfer function components for the stationary and moving TLPWT. Similarly to TLPWTs 1 and 2, the first-order motions had a considerable impact on the second-order excitation. The imaginary components of the surge force and pitch moments were more affected than the real components, but both components of the heave force (as well as the mean value) were significantly changed.

The changes in the overall shape of the heave and pitch sum-frequency excitation QTFs can be seen by comparing Figs. C.20 and C.24. The inclusion of the first-order motions tended to decrease the high-frequency excitation, but increased the low-frequency and off-diagonal terms. The peak pitch moment along the resonance line (Fig. C.25) decreased by approximately 25% compared to the value for the stationary structure, but changed very little in the lower frequency range.

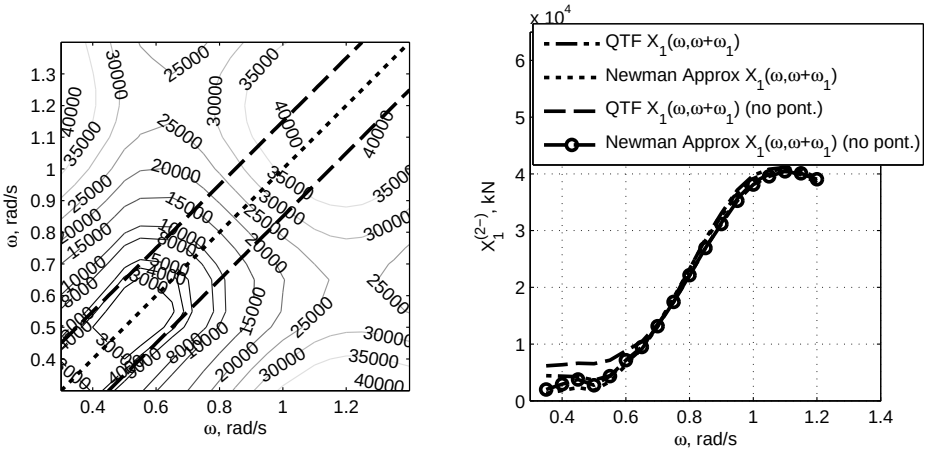

(a) Diff.-freq. surge force QTF (b) QTF and Newman's approx. at T_{n1}

Figure C.21: a) Difference-frequency surge force QTF, for stationary TLPWT 3. Heavy dashed lines indicate the surge resonance difference-frequency, dotted line shows $\omega_i = \omega_j$. b) Difference-frequency surge force at the TLPWT 3 surge natural frequency, based on QTF and Newman's approximation for the stationary structure. Results for the main column only (QTF and Newman approximation) are also shown.

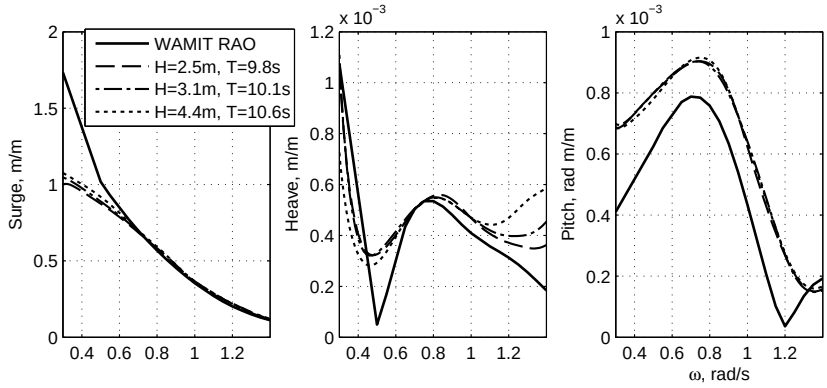

Figure C.22: TLPWT 3: first-order motion RAOs. Note: pitch non-dimensionalized by D/ζ.

C.4.4 Difference-Frequency Forces on Moving TLPWT 3

The first-order motions also had a significant impact on the difference-frequency wave excitation on TLPWT 3. The surge force QTFs in Figs. C.21a

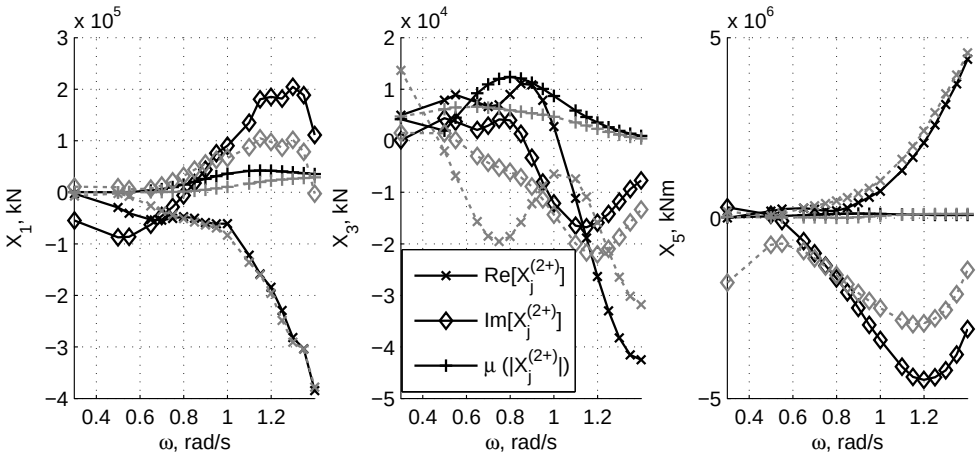

Figure C.23: Double-frequency surge force transfer function components, for TLPWT 3 fixed in space (solid black line) and moving (dotted gray line).

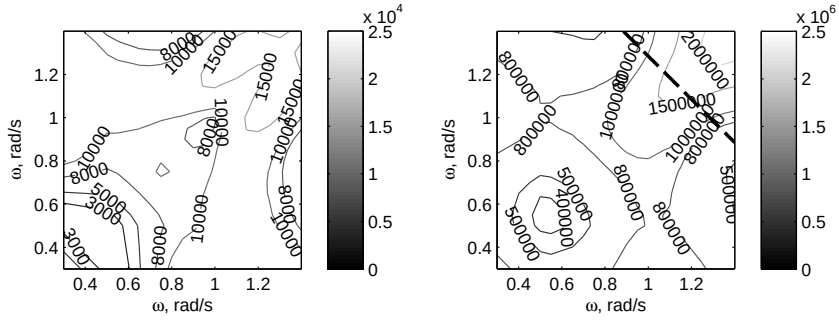

Figure C.24: Sum-frequency heave force (left) and pitch moment (right) QTFs for TLPWT 3 including first-order motions. First pitch/bend natural frequency is indicated by the dashed line.

and C.26a can be compared to see the influence of the TLPWT motions: the forces along the diagonal decreased, especially for combinations of high frequencies, while the off-diagonal terms increased. As with TLPWTs 1 and 2, the Newman approximation became less accurate and non-conservative around the surge natural period, especially for wave frequencies between 0.3 and 1.0 rad/s.

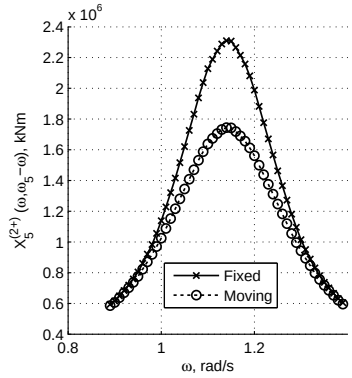

Figure C.25: Sum-frequency pitch moment along the natural frequency line for the stationary and moving structure.

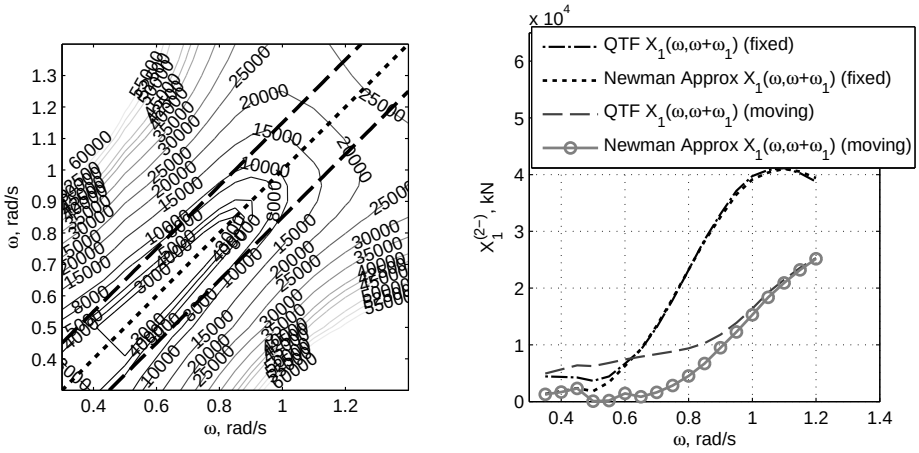

(a) Diff.-freq. surge force QTF (b) QTF and Newman's approx. at T_{n1}

Figure C.26: a) Difference-frequency surge force QTF for TLPWT 3, including first-order motions. Heavy dashed lines indicate the surge resonance difference-frequency, dotted line shows $\omega_i = \omega_j$. b) Difference-frequency surge force at the TLPWT 3 surge natural frequency, based on QTF (mesh 2) and Newman's approximation for the fixed and moving structure.

C.5 Discussion

The main results of the examination of second-order forces are summarized below.

- **Body and free surface meshing:**

  Within the bounds of the computational restrictions, a detailed examination of mesh refinement was not possible. The results from TLPWT 1 indicated that 1.5 m long mesh elements along the waterline did not give sufficiently good resolution for the computation of second-order forces, but that approximately 1 m long elements improved the results. Increasing the resolution from 1.1 m to 0.88 m for TLPWT 2 did not change the results. Elements with length 1.1 m were used for TLPWTs 2 and 3.

  Increasing the partition radius from 150 m to 250 m (with corresponding loss of mesh refinement) did not significantly impact the results for long wave frequencies. Therefore, the 150 m radius was considered to be sufficient.

  If the Newman approximation is to be used, it is recommended to solve the first-order potential with a finer mesh than is used on the the free surface and with a finer frequency resolution, in order to obtain the most accurate possible answers and avoid interpolation errors.

- **Effect of pontoons on QTFs:**

  The effect of the pontoons on the QTFs was only considered for the stationary case of TLPWTs 2 and 3. The sum-frequency surge and pitch results and difference-frequency surge results were largely unaffected by the presence of the pontoons, but the first-order heave and pitch and the sum-frequency heave forcing were significantly changed. Based on the present results, the difference-frequency surge forcing for the stationary structure may be reasonably approximated by ignoring the pontoons, but this is not a useful result due to the effect of first-order motions on the QTFs.

- **Effect of first-order motions on QTFs:**

  In the cases considered here, the 1st order motions had a non-negligible effect on both sum- and difference-frequency QTFs. The peak sum-frequency heave and pitch forcing tended to decrease between 10 and 30 % when first-order motions were included, and the peaks became less pronounced. The surge difference-frequency excitation decreased along the diagonal of the QTF, but increased away from the diagonal.

- **Appropriateness of Newman approximation:**

  The Newman approximation gave a good approximation of the forcing on a stationary TLPWT at the surge natural frequency, but tended to

underpredict the forcing at the surge natural frequency for a moving TLPWT. Since the TLPWT has a shorter surge natural period than a typical TLP construction, Newman's approximation is likely to be less accurate, and is not necessarily conservative, particularly in the frequency range 0.3 - 1.0 rad/s, which corresponds to the majority of the incoming waves in a typical open water seastate.

Previous PhD theses published at the Departement of Marine Technology
(earlier: Faculty of Marine Technology)
NORWEGIAN UNIVERSITY OF SCIENCE AND TECHNOLOGY

Report No.	Author	Title
	Kavlie, Dag	Optimization of Plane Elastic Grillages, 1967
	Hansen, Hans R.	Man-Machine Communication and Data-Storage Methods in Ship Structural Design, 1971
	Gisvold, Kaare M.	A Method for non-linear mixed -integer programming and its Application to Design Problems, 1971
	Lund, Sverre	Tanker Frame Optimalization by means of SUMT-Transformation and Behaviour Models, 1971
	Vinje, Tor	On Vibration of Spherical Shells Interacting with Fluid, 1972
	Lorentz, Jan D.	Tank Arrangement for Crude Oil Carriers in Accordance with the new Anti-Pollution Regulations, 1975
	Carlsen, Carl A.	Computer-Aided Design of Tanker Structures, 1975
	Larsen, Carl M.	Static and Dynamic Analysis of Offshore Pipelines during Installation, 1976
UR-79-01	Brigt Hatlestad, MK	The finite element method used in a fatigue evaluation of fixed offshore platforms. (Dr.Ing. Thesis)
UR-79-02	Erik Pettersen, MK	Analysis and design of cellular structures. (Dr.Ing. Thesis)
UR-79-03	Sverre Valsgård, MK	Finite difference and finite element methods applied to nonlinear analysis of plated structures. (Dr.Ing. Thesis)
UR-79-04	Nils T. Nordsve, MK	Finite element collapse analysis of structural members considering imperfections and stresses due to fabrication. (Dr.Ing. Thesis)
UR-79-05	Ivar J. Fylling, MK	Analysis of towline forces in ocean towing systems. (Dr.Ing. Thesis)
UR-80-06	Nils Sandsmark, MM	Analysis of Stationary and Transient Heat Conduction by the Use of the Finite Element Method. (Dr.Ing. Thesis)
UR-80-09	Sverre Haver, MK	Analysis of uncertainties related to the stochastic modeling of ocean waves. (Dr.Ing. Thesis)
UR-81-15	Odland, Jonas	On the Strength of welded Ring stiffened cylindrical Shells primarily subjected to axial Compression
UR-82-17	Engesvik, Knut	Analysis of Uncertainties in the fatigue Capacity of

		Welded Joints
UR-82-18	Rye, Henrik	Ocean wave groups
UR-83-30	Eide, Oddvar Inge	On Cumulative Fatigue Damage in Steel Welded Joints
UR-83-33	Mo, Olav	Stochastic Time Domain Analysis of Slender Offshore Structures
UR-83-34	Amdahl, Jørgen	Energy absorption in Ship-platform impacts
UR-84-37	Mørch, Morten	Motions and mooring forces of semi submersibles as determined by full-scale measurements and theoretical analysis
UR-84-38	Soares, C. Guedes	Probabilistic models for load effects in ship structures
UR-84-39	Aarsnes, Jan V.	Current forces on ships
UR-84-40	Czujko, Jerzy	Collapse Analysis of Plates subjected to Biaxial Compression and Lateral Load
UR-85-46	Alf G. Engseth, MK	Finite element collapse analysis of tubular steel offshore structures. (Dr.Ing. Thesis)
UR-86-47	Dengody Sheshappa, MP	A Computer Design Model for Optimizing Fishing Vessel Designs Based on Techno-Economic Analysis. (Dr.Ing. Thesis)
UR-86-48	Vidar Aanesland, MH	A Theoretical and Numerical Study of Ship Wave Resistance. (Dr.Ing. Thesis)
UR-86-49	Heinz-Joachim Wessel, MK	Fracture Mechanics Analysis of Crack Growth in Plate Girders. (Dr.Ing. Thesis)
UR-86-50	Jon Taby, MK	Ultimate and Post-ultimate Strength of Dented Tubular Members. (Dr.Ing. Thesis)
UR-86-51	Walter Lian, MH	A Numerical Study of Two-Dimensional Separated Flow Past Bluff Bodies at Moderate KC-Numbers. (Dr.Ing. Thesis)
UR-86-52	Bjørn Sortland, MH	Force Measurements in Oscillating Flow on Ship Sections and Circular Cylinders in a U-Tube Water Tank. (Dr.Ing. Thesis)
UR-86-53	Kurt Strand, MM	A System Dynamic Approach to One-dimensional Fluid Flow. (Dr.Ing. Thesis)
UR-86-54	Arne Edvin Løken, MH	Three Dimensional Second Order Hydrodynamic Effects on Ocean Structures in Waves. (Dr.Ing. Thesis)
UR-86-55	Sigurd Falch, MH	A Numerical Study of Slamming of Two-Dimensional Bodies. (Dr.Ing. Thesis)
UR-87-56	Arne Braathen, MH	Application of a Vortex Tracking Method to the Prediction of Roll Damping of a Two-Dimension Floating Body. (Dr.Ing. Thesis)

UR-87-57	Bernt Leira, MK	Gaussian Vector Processes for Reliability Analysis involving Wave-Induced Load Effects. (Dr.Ing. Thesis)
UR-87-58	Magnus Småvik, MM	Thermal Load and Process Characteristics in a Two-Stroke Diesel Engine with Thermal Barriers (in Norwegian). (Dr.Ing. Thesis)
MTA-88-59	Bernt Arild Bremdal, MP	An Investigation of Marine Installation Processes – A Knowledge - Based Planning Approach. (Dr.Ing. Thesis)
MTA-88-60	Xu Jun, MK	Non-linear Dynamic Analysis of Space-framed Offshore Structures. (Dr.Ing. Thesis)
MTA-89-61	Gang Miao, MH	Hydrodynamic Forces and Dynamic Responses of Circular Cylinders in Wave Zones. (Dr.Ing. Thesis)
MTA-89-62	Martin Greenhow, MH	Linear and Non-Linear Studies of Waves and Floating Bodies. Part I and Part II. (Dr.Techn. Thesis)
MTA-89-63	Chang Li, MH	Force Coefficients of Spheres and Cubes in Oscillatory Flow with and without Current. (Dr.Ing. Thesis
MTA-89-64	Hu Ying, MP	A Study of Marketing and Design in Development of Marine Transport Systems. (Dr.Ing. Thesis)
MTA-89-65	Arild Jæger, MH	Seakeeping, Dynamic Stability and Performance of a Wedge Shaped Planing Hull. (Dr.Ing. Thesis)
MTA-89-66	Chan Siu Hung, MM	The dynamic characteristics of tilting-pad bearings
MTA-89-67	Kim Wikstrøm, MP	Analysis av projekteringen for ett offshore projekt. (Licenciat-avhandling)
MTA-89-68	Jiao Guoyang, MK	Reliability Analysis of Crack Growth under Random Loading, considering Model Updating. (Dr.Ing. Thesis)
MTA-89-69	Arnt Olufsen, MK	Uncertainty and Reliability Analysis of Fixed Offshore Structures. (Dr.Ing. Thesis)
MTA-89-70	Wu Yu-Lin, MR	System Reliability Analyses of Offshore Structures using improved Truss and Beam Models. (Dr.Ing. Thesis)
MTA-90-71	Jan Roger Hoff, MH	Three-dimensional Green function of a vessel with forward speed in waves. (Dr.Ing. Thesis)
MTA-90-72	Rong Zhao, MH	Slow-Drift Motions of a Moored Two-Dimensional Body in Irregular Waves. (Dr.Ing. Thesis)
MTA-90-73	Atle Minsaas, MP	Economical Risk Analysis. (Dr.Ing. Thesis)
MTA-90-74	Knut-Aril Farnes, MK	Long-term Statistics of Response in Non-linear Marine Structures. (Dr.Ing. Thesis)
MTA-90-75	Torbjørn Sotberg, MK	Application of Reliability Methods for Safety Assessment of Submarine Pipelines. (Dr.Ing.

		Thesis)
MTA-90-76	Zeuthen, Steffen, MP	SEAMAID. A computational model of the design process in a constraint-based logic programming environment. An example from the offshore domain. (Dr.Ing. Thesis)
MTA-91-77	Haagensen, Sven, MM	Fuel Dependant Cyclic Variability in a Spark Ignition Engine - An Optical Approach. (Dr.Ing. Thesis)
MTA-91-78	Løland, Geir, MH	Current forces on and flow through fish farms. (Dr.Ing. Thesis)
MTA-91-79	Hoen, Christopher, MK	System Identification of Structures Excited by Stochastic Load Processes. (Dr.Ing. Thesis)
MTA-91-80	Haugen, Stein, MK	Probabilistic Evaluation of Frequency of Collision between Ships and Offshore Platforms. (Dr.Ing. Thesis)
MTA-91-81	Sødahl, Nils, MK	Methods for Design and Analysis of Flexible Risers. (Dr.Ing. Thesis)
MTA-91-82	Ormberg, Harald, MK	Non-linear Response Analysis of Floating Fish Farm Systems. (Dr.Ing. Thesis)
MTA-91-83	Marley, Mark J., MK	Time Variant Reliability under Fatigue Degradation. (Dr.Ing. Thesis)
MTA-91-84	Krokstad, Jørgen R., MH	Second-order Loads in Multidirectional Seas. (Dr.Ing. Thesis)
MTA-91-85	Molteberg, Gunnar A., MM	The Application of System Identification Techniques to Performance Monitoring of Four Stroke Turbocharged Diesel Engines. (Dr.Ing. Thesis)
MTA-92-86	Mørch, Hans Jørgen Bjelke, MH	Aspects of Hydrofoil Design: with Emphasis on Hydrofoil Interaction in Calm Water. (Dr.Ing. Thesis)
MTA-92-87	Chan Siu Hung, MM	Nonlinear Analysis of Rotordynamic Instabilities in Highspeed Turbomachinery. (Dr.Ing. Thesis)
MTA-92-88	Bessason, Bjarni, MK	Assessment of Earthquake Loading and Response of Seismically Isolated Bridges. (Dr.Ing. Thesis)
MTA-92-89	Langli, Geir, MP	Improving Operational Safety through exploitation of Design Knowledge - an investigation of offshore platform safety. (Dr.Ing. Thesis)
MTA-92-90	Sævik, Svein, MK	On Stresses and Fatigue in Flexible Pipes. (Dr.Ing. Thesis)
MTA-92-91	Ask, Tor Ø., MM	Ignition and Flame Growth in Lean Gas-Air Mixtures. An Experimental Study with a Schlieren System. (Dr.Ing. Thesis)
MTA-86-92	Hessen, Gunnar, MK	Fracture Mechanics Analysis of Stiffened Tubular Members. (Dr.Ing. Thesis)

MTA-93-93	Steinebach, Christian, MM	Knowledge Based Systems for Diagnosis of Rotating Machinery. (Dr.Ing. Thesis)
MTA-93-94	Dalane, Jan Inge, MK	System Reliability in Design and Maintenance of Fixed Offshore Structures. (Dr.Ing. Thesis)
MTA-93-95	Steen, Sverre, MH	Cobblestone Effect on SES. (Dr.Ing. Thesis)
MTA-93-96	Karunakaran, Daniel, MK	Nonlinear Dynamic Response and Reliability Analysis of Drag-dominated Offshore Platforms. (Dr.Ing. Thesis)
MTA-93-97	Hagen, Arnulf, MP	The Framework of a Design Process Language. (Dr.Ing. Thesis)
MTA-93-98	Nordrik, Rune, MM	Investigation of Spark Ignition and Autoignition in Methane and Air Using Computational Fluid Dynamics and Chemical Reaction Kinetics. A Numerical Study of Ignition Processes in Internal Combustion Engines. (Dr.Ing. Thesis)
MTA-94-99	Passano, Elizabeth, MK	Efficient Analysis of Nonlinear Slender Marine Structures. (Dr.Ing. Thesis)
MTA-94-100	Kvålsvold, Jan, MH	Hydroelastic Modelling of Wetdeck Slamming on Multihull Vessels. (Dr.Ing. Thesis)
MTA-94-102	Bech, Sidsel M., MK	Experimental and Numerical Determination of Stiffness and Strength of GRP/PVC Sandwich Structures. (Dr.Ing. Thesis)
MTA-95-103	Paulsen, Hallvard, MM	A Study of Transient Jet and Spray using a Schlieren Method and Digital Image Processing. (Dr.Ing. Thesis)
MTA-95-104	Hovde, Geir Olav, MK	Fatigue and Overload Reliability of Offshore Structural Systems, Considering the Effect of Inspection and Repair. (Dr.Ing. Thesis)
MTA-95-105	Wang, Xiaozhi, MK	Reliability Analysis of Production Ships with Emphasis on Load Combination and Ultimate Strength. (Dr.Ing. Thesis)
MTA-95-106	Ulstein, Tore, MH	Nonlinear Effects of a Flexible Stern Seal Bag on Cobblestone Oscillations of an SES. (Dr.Ing. Thesis)
MTA-95-107	Solaas, Frøydis, MH	Analytical and Numerical Studies of Sloshing in Tanks. (Dr.Ing. Thesis)
MTA-95-108	Hellan, Øyvind, MK	Nonlinear Pushover and Cyclic Analyses in Ultimate Limit State Design and Reassessment of Tubular Steel Offshore Structures. (Dr.Ing. Thesis)
MTA-95-109	Hermundstad, Ole A., MK	Theoretical and Experimental Hydroelastic Analysis of High Speed Vessels. (Dr.Ing. Thesis)
MTA-96-110	Bratland, Anne K., MH	Wave-Current Interaction Effects on Large-Volume Bodies in Water of Finite Depth. (Dr.Ing. Thesis)
MTA-96-111	Herfjord, Kjell, MH	A Study of Two-dimensional Separated Flow by a Combination of the Finite Element Method and

		Navier-Stokes Equations. (Dr.Ing. Thesis)
MTA-96-112	Æsøy, Vilmar, MM	Hot Surface Assisted Compression Ignition in a Direct Injection Natural Gas Engine. (Dr.Ing. Thesis)
MTA-96-113	Eknes, Monika L., MK	Escalation Scenarios Initiated by Gas Explosions on Offshore Installations. (Dr.Ing. Thesis)
MTA-96-114	Erikstad, Stein O., MP	A Decision Support Model for Preliminary Ship Design. (Dr.Ing. Thesis)
MTA-96-115	Pedersen, Egil, MH	A Nautical Study of Towed Marine Seismic Streamer Cable Configurations. (Dr.Ing. Thesis)
MTA-97-116	Moksnes, Paul O., MM	Modelling Two-Phase Thermo-Fluid Systems Using Bond Graphs. (Dr.Ing. Thesis)
MTA-97-117	Halse, Karl H., MK	On Vortex Shedding and Prediction of Vortex-Induced Vibrations of Circular Cylinders. (Dr.Ing. Thesis)
MTA-97-118	Igland, Ragnar T., MK	Reliability Analysis of Pipelines during Laying, considering Ultimate Strength under Combined Loads. (Dr.Ing. Thesis)
MTA-97-119	Pedersen, Hans-P., MP	Levendefiskteknologi for fiskefartøy. (Dr.Ing. Thesis)
MTA-98-120	Vikestad, Kyrre, MK	Multi-Frequency Response of a Cylinder Subjected to Vortex Shedding and Support Motions. (Dr.Ing. Thesis)
MTA-98-121	Azadi, Mohammad R. E., MK	Analysis of Static and Dynamic Pile-Soil-Jacket Behaviour. (Dr.Ing. Thesis)
MTA-98-122	Ulltang, Terje, MP	A Communication Model for Product Information. (Dr.Ing. Thesis)
MTA-98-123	Torbergsen, Erik, MM	Impeller/Diffuser Interaction Forces in Centrifugal Pumps. (Dr.Ing. Thesis)
MTA-98-124	Hansen, Edmond, MH	A Discrete Element Model to Study Marginal Ice Zone Dynamics and the Behaviour of Vessels Moored in Broken Ice. (Dr.Ing. Thesis)
MTA-98-125	Videiro, Paulo M., MK	Reliability Based Design of Marine Structures. (Dr.Ing. Thesis)
MTA-99-126	Mainçon, Philippe, MK	Fatigue Reliability of Long Welds Application to Titanium Risers. (Dr.Ing. Thesis)
MTA-99-127	Haugen, Elin M., MH	Hydroelastic Analysis of Slamming on Stiffened Plates with Application to Catamaran Wetdecks. (Dr.Ing. Thesis)
MTA-99-128	Langhelle, Nina K., MK	Experimental Validation and Calibration of Nonlinear Finite Element Models for Use in Design of Aluminium Structures Exposed to Fire. (Dr.Ing. Thesis)
MTA-99-	Berstad, Are J., MK	Calculation of Fatigue Damage in Ship Structures.

129		(Dr.Ing. Thesis)
MTA-99-130	Andersen, Trond M., MM	Short Term Maintenance Planning. (Dr.Ing. Thesis)
MTA-99-131	Tveiten, Bård Wathne, MK	Fatigue Assessment of Welded Aluminium Ship Details. (Dr.Ing. Thesis)
MTA-99-132	Søreide, Fredrik, MP	Applications of underwater technology in deep water archaeology. Principles and practice. (Dr.Ing. Thesis)
MTA-99-133	Tønnessen, Rune, MH	A Finite Element Method Applied to Unsteady Viscous Flow Around 2D Blunt Bodies With Sharp Corners. (Dr.Ing. Thesis)
MTA-99-134	Elvekrok, Dag R., MP	Engineering Integration in Field Development Projects in the Norwegian Oil and Gas Industry. The Supplier Management of Norne. (Dr.Ing. Thesis)
MTA-99-135	Fagerholt, Kjetil, MP	Optimeringsbaserte Metoder for Ruteplanlegging innen skipsfart. (Dr.Ing. Thesis)
MTA-99-136	Bysveen, Marie, MM	Visualization in Two Directions on a Dynamic Combustion Rig for Studies of Fuel Quality. (Dr.Ing. Thesis)
MTA-2000-137	Storteig, Eskild, MM	Dynamic characteristics and leakage performance of liquid annular seals in centrifugal pumps. (Dr.Ing. Thesis)
MTA-2000-138	Sagli, Gro, MK	Model uncertainty and simplified estimates of long term extremes of hull girder loads in ships. (Dr.Ing. Thesis)
MTA-2000-139	Tronstad, Harald, MK	Nonlinear analysis and design of cable net structures like fishing gear based on the finite element method. (Dr.Ing. Thesis)
MTA-2000-140	Kroneberg, André, MP	Innovation in shipping by using scenarios. (Dr.Ing. Thesis)
MTA-2000-141	Haslum, Herbjørn Alf, MH	Simplified methods applied to nonlinear motion of spar platforms. (Dr.Ing. Thesis)
MTA-2001-142	Samdal, Ole Johan, MM	Modelling of Degradation Mechanisms and Stressor Interaction on Static Mechanical Equipment Residual Lifetime. (Dr.Ing. Thesis)
MTA-2001-143	Baarholm, Rolf Jarle, MH	Theoretical and experimental studies of wave impact underneath decks of offshore platforms. (Dr.Ing. Thesis)
MTA-2001-144	Wang, Lihua, MK	Probabilistic Analysis of Nonlinear Wave-induced Loads on Ships. (Dr.Ing. Thesis)
MTA-2001-145	Kristensen, Odd H. Holt, MK	Ultimate Capacity of Aluminium Plates under Multiple Loads, Considering HAZ Properties. (Dr.Ing. Thesis)
MTA-2001-146	Greco, Marilena, MH	A Two-Dimensional Study of Green-Water Loading. (Dr.Ing. Thesis)

MTA-2001-147	Heggelund, Svein E., MK	Calculation of Global Design Loads and Load Effects in Large High Speed Catamarans. (Dr.Ing. Thesis)
MTA-2001-148	Babalola, Olusegun T., MK	Fatigue Strength of Titanium Risers – Defect Sensitivity. (Dr.Ing. Thesis)
MTA-2001-149	Mohammed, Abuu K., MK	Nonlinear Shell Finite Elements for Ultimate Strength and Collapse Analysis of Ship Structures. (Dr.Ing. Thesis)
MTA-2002-150	Holmedal, Lars E., MH	Wave-current interactions in the vicinity of the sea bed. (Dr.Ing. Thesis)
MTA-2002-151	Rognebakke, Olav F., MH	Sloshing in rectangular tanks and interaction with ship motions. (Dr.Ing. Thesis)
MTA-2002-152	Lader, Pål Furset, MH	Geometry and Kinematics of Breaking Waves. (Dr.Ing. Thesis)
MTA-2002-153	Yang, Qinzheng, MH	Wash and wave resistance of ships in finite water depth. (Dr.Ing. Thesis)
MTA-2002-154	Melhus, Øyvin, MM	Utilization of VOC in Diesel Engines. Ignition and combustion of VOC released by crude oil tankers. (Dr.Ing. Thesis)
MTA-2002-155	Ronæss, Marit, MH	Wave Induced Motions of Two Ships Advancing on Parallel Course. (Dr.Ing. Thesis)
MTA-2002-156	Økland, Ole D., MK	Numerical and experimental investigation of whipping in twin hull vessels exposed to severe wet deck slamming. (Dr.Ing. Thesis)
MTA-2002-157	Ge, Chunhua, MK	Global Hydroelastic Response of Catamarans due to Wet Deck Slamming. (Dr.Ing. Thesis)
MTA-2002-158	Byklum, Eirik, MK	Nonlinear Shell Finite Elements for Ultimate Strength and Collapse Analysis of Ship Structures. (Dr.Ing. Thesis)
IMT-2003-1	Chen, Haibo, MK	Probabilistic Evaluation of FPSO-Tanker Collision in Tandem Offloading Operation. (Dr.Ing. Thesis)
IMT-2003-2	Skaugset, Kjetil Bjørn, MK	On the Suppression of Vortex Induced Vibrations of Circular Cylinders by Radial Water Jets. (Dr.Ing. Thesis)
IMT-2003-3	Chezhian, Muthu	Three-Dimensional Analysis of Slamming. (Dr.Ing. Thesis)
IMT-2003-4	Buhaug, Øyvind	Deposit Formation on Cylinder Liner Surfaces in Medium Speed Engines. (Dr.Ing. Thesis)
IMT-2003-5	Tregde, Vidar	Aspects of Ship Design: Optimization of Aft Hull with Inverse Geometry Design. (Dr.Ing. Thesis)
IMT-2003-6	Wist, Hanne Therese	Statistical Properties of Successive Ocean Wave Parameters. (Dr.Ing. Thesis)

IMT-2004-7	Ransau, Samuel	Numerical Methods for Flows with Evolving Interfaces. (Dr.Ing. Thesis)
IMT-2004-8	Soma, Torkel	Blue-Chip or Sub-Standard. A data interrogation approach of identity safety characteristics of shipping organization. (Dr.Ing. Thesis)
IMT-2004-9	Ersdal, Svein	An experimental study of hydrodynamic forces on cylinders and cables in near axial flow. (Dr.Ing. Thesis)
IMT-2005-10	Brodtkorb, Per Andreas	The Probability of Occurrence of Dangerous Wave Situations at Sea. (Dr.Ing. Thesis)
IMT-2005-11	Yttervik, Rune	Ocean current variability in relation to offshore engineering. (Dr.Ing. Thesis)
IMT-2005-12	Fredheim, Arne	Current Forces on Net-Structures. (Dr.Ing. Thesis)
IMT-2005-13	Heggernes, Kjetil	Flow around marine structures. (Dr.Ing. Thesis
IMT-2005-14	Fouques, Sebastien	Lagrangian Modelling of Ocean Surface Waves and Synthetic Aperture Radar Wave Measurements. (Dr.Ing. Thesis)
IMT-2006-15	Holm, Håvard	Numerical calculation of viscous free surface flow around marine structures. (Dr.Ing. Thesis)
IMT-2006-16	Bjørheim, Lars G.	Failure Assessment of Long Through Thickness Fatigue Cracks in Ship Hulls. (Dr.Ing. Thesis)
IMT-2006-17	Hansson, Lisbeth	Safety Management for Prevention of Occupational Accidents. (Dr.Ing. Thesis)
IMT-2006-18	Zhu, Xinying	Application of the CIP Method to Strongly Nonlinear Wave-Body Interaction Problems. (Dr.Ing. Thesis)
IMT-2006-19	Reite, Karl Johan	Modelling and Control of Trawl Systems. (Dr.Ing. Thesis)
IMT-2006-20	Smogeli, Øyvind Notland	Control of Marine Propellers. From Normal to Extreme Conditions. (Dr.Ing. Thesis)
IMT-2007-21	Storhaug, Gaute	Experimental Investigation of Wave Induced Vibrations and Their Effect on the Fatigue Loading of Ships. (Dr.Ing. Thesis)
IMT-2007-22	Sun, Hui	A Boundary Element Method Applied to Strongly Nonlinear Wave-Body Interaction Problems. (PhD Thesis, CeSOS)
IMT-2007-23	Rustad, Anne Marthine	Modelling and Control of Top Tensioned Risers. (PhD Thesis, CeSOS)
IMT-2007-24	Johansen, Vegar	Modelling flexible slender system for real-time simulations and control applications
IMT-2007-25	Wroldsen, Anders Sunde	Modelling and control of tensegrity structures. (PhD Thesis, CeSOS)
IMT-	Aronsen, Kristoffer Høye	An experimental investigation of in-line and

2007-26		combined inline and cross flow vortex induced vibrations. (Dr. avhandling, IMT)
IMT-2007-27	Gao, Zhen	Stochastic Response Analysis of Mooring Systems with Emphasis on Frequency-domain Analysis of Fatigue due to Wide-band Response Processes (PhD Thesis, CeSOS)
IMT-2007-28	Thorstensen, Tom Anders	Lifetime Profit Modelling of Ageing Systems Utilizing Information about Technical Condition. (Dr.ing. thesis, IMT)
IMT-2008-29	Berntsen, Per Ivar B.	Structural Reliability Based Position Mooring. (PhD-Thesis, IMT)
IMT-2008-30	Ye, Naiquan	Fatigue Assessment of Aluminium Welded Box-stiffener Joints in Ships (Dr.ing. thesis, IMT)
IMT-2008-31	Radan, Damir	Integrated Control of Marine Electrical Power Systems. (PhD-Thesis, IMT)
IMT-2008-32	Thomassen, Paul	Methods for Dynamic Response Analysis and Fatigue Life Estimation of Floating Fish Cages. (Dr.ing. thesis, IMT)
IMT-2008-33	Pákozdi, Csaba	A Smoothed Particle Hydrodynamics Study of Two-dimensional Nonlinear Sloshing in Rectangular Tanks. (Dr.ing.thesis, IMT/ CeSOS)
IMT-2007-34	Grytøyr, Guttorm	A Higher-Order Boundary Element Method and Applications to Marine Hydrodynamics. (Dr.ing.thesis, IMT)
IMT-2008-35	Drummen, Ingo	Experimental and Numerical Investigation of Nonlinear Wave-Induced Load Effects in Containerships considering Hydroelasticity. (PhD thesis, CeSOS)
IMT-2008-36	Skejic, Renato	Maneuvering and Seakeeping of a Singel Ship and of Two Ships in Interaction. (PhD-Thesis, CeSOS)
IMT-2008-37	Harlem, Alf	An Age-Based Replacement Model for Repairable Systems with Attention to High-Speed Marine Diesel Engines. (PhD-Thesis, IMT)
IMT-2008-38	Alsos, Hagbart S.	Ship Grounding. Analysis of Ductile Fracture, Bottom Damage and Hull Girder Response. (PhD-thesis, IMT)
IMT-2008-39	Graczyk, Mateusz	Experimental Investigation of Sloshing Loading and Load Effects in Membrane LNG Tanks Subjected to Random Excitation. (PhD-thesis, CeSOS)
IMT-2008-40	Taghipour, Reza	Efficient Prediction of Dynamic Response for Flexible amd Multi-body Marine Structures. (PhD-thesis, CeSOS)
IMT-2008-41	Ruth, Eivind	Propulsion control and thrust allocation on marine vessels. (PhD thesis, CeSOS)
IMT-2008-42	Nystad, Bent Helge	Technical Condition Indexes and Remaining Useful Life of Aggregated Systems. PhD thesis, IMT

IMT-2008-43	Soni, Prashant Kumar	Hydrodynamic Coefficients for Vortex Induced Vibrations of Flexible Beams, PhD thesis, CeSOS
IMT-2009-43	Amlashi, Hadi K.K.	Ultimate Strength and Reliability-based Design of Ship Hulls with Emphasis on Combined Global and Local Loads. PhD Thesis, IMT
IMT-2009-44	Pedersen, Tom Arne	Bond Graph Modelling of Marine Power Systems. PhD Thesis, IMT
IMT-2009-45	Kristiansen, Trygve	Two-Dimensional Numerical and Experimental Studies of Piston-Mode Resonance. PhD-Thesis, CeSOS
IMT-2009-46	Ong, Muk Chen	Applications of a Standard High Reynolds Number Model and a Stochastic Scour Prediction Model for Marine Structures. PhD-thesis, IMT
IMT-2009-47	Hong, Lin	Simplified Analysis and Design of Ships subjected to Collision and Grounding. PhD-thesis, IMT
IMT-2009-48	Koushan, Kamran	Vortex Induced Vibrations of Free Span Pipelines, PhD thesis, IMT
IMT-2009-49	Korsvik, Jarl Eirik	Heuristic Methods for Ship Routing and Scheduling. PhD-thesis, IMT
IMT-2009-50	Lee, Jihoon	Experimental Investigation and Numerical in Analyzing the Ocean Current Displacement of Longlines. Ph.d.-Thesis, IMT.
IMT-2009-51	Vestbøstad, Tone Gran	A Numerical Study of Wave-in-Deck Impact usin a Two-Dimensional Constrained Interpolation Profile Method, Ph.d.thesis, CeSOS.
IMT-2009-52	Bruun, Kristine	Bond Graph Modelling of Fuel Cells for Marine Power Plants. Ph.d.-thesis, IMT
IMT 2009-53	Holstad, Anders	Numerical Investigation of Turbulence in a Sekwed Three-Dimensional Channel Flow, Ph.d.-thesis, IMT.
IMT 2009-54	Ayala-Uraga, Efren	Reliability-Based Assessment of Deteriorating Ship-shaped Offshore Structures, Ph.d.-thesis, IMT
IMT 2009-55	Kong, Xiangjun	A Numerical Study of a Damaged Ship in Beam Sea Waves. Ph.d.-thesis, IMT/CeSOS.
IMT 2010-56	Kristiansen, David	Wave Induced Effects on Floaters of Aquaculture Plants, Ph.d.-thesis, CeSOS.
IMT 2010-57	Ludvigsen, Martin	An ROV-Toolbox for Optical and Acoustic Scientific Seabed Investigation. Ph.d.-thesis IMT.
IMT 2010-58	Hals, Jørgen	Modelling and Phase Control of Wave-Energy Converters. Ph.d.thesis, CeSOS.
IMT 2010- 59	Shu, Zhi	Uncertainty Assessment of Wave Loads and Ultimate Strength of Tankers and Bulk Carriers in a

		Reliability Framework. Ph.d. Thesis, IMT/ CeSOS
IMT 2010-60	Shao, Yanlin	Numerical Potential-Flow Studies on Weakly-Nonlinear Wave-Body Interactions with/without Small Forward Speed, Ph.d.thesis,CeSOS.
IMT 2010-61	Califano, Andrea	Dynamic Loads on Marine Propellers due to Intermittent Ventilation. Ph.d.thesis, IMT.
IMT 2010-62	El Khoury, George	Numerical Simulations of Massively Separated Turbulent Flows, Ph.d.-thesis, IMT
IMT 2010-63	Seim, Knut Sponheim	Mixing Process in Dense Overflows with Emphasis on the Faroe Bank Channel Overflow. Ph.d.thesis, IMT
IMT 2010-64	Jia, Huirong	Structural Analysis of Intect and Damaged Ships in a Collission Risk Analysis Perspective. Ph.d.thesis CeSoS.
IMT 2010-65	Jiao, Linlin	Wave-Induced Effects on a Pontoon-type Very Large Floating Structures (VLFS). Ph.D.-thesis, CeSOS.
IMT 2010-66	Abrahamsen, Bjørn Christian	Sloshing Induced Tank Roof with Entrapped Air Pocket. Ph.d.thesis, CeSOS.
IMT 2011-67	Karimirad, Madjid	Stochastic Dynamic Response Analysis of Spar-Type Wind Turbines with Catenary or Taut Mooring Systems. Ph.d.-thesis, CeSOS.
IMT - 2011-68	Erlend Meland	Condition Monitoring of Safety Critical Valves. Ph.d.-thesis, IMT.
IMT – 2011-69	Yang, Limin	Stochastic Dynamic System Analysis of Wave Energy Converter with Hydraulic Power Take-Off, with Particular Reference to Wear Damage Analysis, Ph.d. Thesis, CeSOS.
IMT – 2011-70	Visscher, Jan	Application of Particla Image Velocimetry on Turbulent Marine Flows, Ph.d.Thesis, IMT.
IMT – 2011-71	Su, Biao	Numerical Predictions of Global and Local Ice Loads on Ships. Ph.d.Thesis, CeSOS.
IMT – 2011-72	Liu, Zhenhui	Analytical and Numerical Analysis of Iceberg Collision with Ship Structures. Ph.d.Thesis, IMT.
IMT – 2011-73	Aarsæther, Karl Gunnar	Modeling and Analysis of Ship Traffic by Observation and Numerical Simulation. Ph.d.Thesis, IMT.
Imt – 2011-74	Wu, Jie	Hydrodynamic Force Identification from Stochastic Vortex Induced Vibration Experiments with Slender Beams. Ph.d.Thesis, IMT.
Imt – 2011-75	Amini, Hamid	Azimuth Propulsors in Off-design Conditions. Ph.d.Thesis, IMT.
IMT – 2011-76	Nguyen, Tan-Hoi	Toward a System of Real-Time Prediction and Monitoring of Bottom Damage Conditions During

		Ship Grounding. Ph.d.thesis, IMT.
IMT-2011-77	Tavakoli, Mohammad T.	Assessment of Oil Spill in Ship Collision and Grounding, Ph.d.thesis, IMT.
IMT-2011-78	Guo, Bingjie	Numerical and Experimental Investigation of Added Resistance in Waves. Ph.d.Thesis, IMT.
IMT-2011-79	Chen, Qiaofeng	Ultimate Strength of Aluminium Panels, considering HAZ Effects, IMT
IMT-2012-80	Kota, Ravikiran S.	Wave Loads on Decks of Offshore Structures in Random Seas, CeSOS.
IMT-2012-81	Sten, Ronny	Dynamic Simulation of Deep Water Drilling Risers with Heave Compensating System, IMT.
IMT-2012-82	Berle, Øyvind	Risk and resilience in global maritime supply chains, IMT.
IMT-2012-83	Fang, Shaoji	Fault Tolerant Position Mooring Control Based on Structural Reliability, CeSOS.
IMT-2012-84	You, Jikun	Numerical studies on wave forces and moored ship motions in intermediate and shallow water, CeSOS.
IMT-2012-85	Xiang ,Xu	Maneuvering of two interacting ships in waves, CeSOS
IMT-2012-86	Dong, Wenbin	Time-domain fatigue response and reliability analysis of offshore wind turbines with emphasis on welded tubular joints and gear components, CeSOS
IMT-2012-87	Zhu, Suji	Investigation of Wave-Induced Nonlinear Load Effects in Open Ships considering Hull Girder Vibrations in Bending and Torsion, CeSOS
IMT-2012-88	Zhou, Li	Numerical and Experimental Investigation of Station-keeping in Level Ice, CeSOS
IMT-2012-90	Ushakov, Sergey	Particulate matter emission characteristics from diesel enignes operating on conventional and alternative marine fuels, IMT
IMT-2013-1	Yin, Decao	Experimental and Numerical Analysis of Combined In-line and Cross-flow Vortex Induced Vibrations, CeSOS
IMT-2013-2	Kurniawan, Adi	Modelling and geometry optimisation of wave energy converters, CeSOS
IMT-2013-3	Al Ryati, Nabil	Technical condition indexes doe auxiliary marine diesel engines, IMT
IMT-2013-4	Firoozkoohi, Reza	Experimental, numerical and analytical investigation of the effect of screens on sloshing, CeSOS
IMT-2013-5	Ommani, Babak	Potential-Flow Predictions of a Semi-Displacement Vessel Including Applications to Calm Water Broaching, CeSOS

IMT-2013-6	Xing, Yihan	Modelling and analysis of the gearbox in a floating spar-type wind turbine, CeSOS
IMT-7-2013	Balland, Océane	Optimization models for reducing air emissions from ships, IMT
IMT-8-2013	Yang, Dan	Transitional wake flow behind an inclined flat plate-----Computation and analysis, IMT
IMT-9-2013	Abdillah, Suyuthi	Prediction of Extreme Loads and Fatigue Damage for a Ship Hull due to Ice Action, IMT
IMT-10-2013	Ramìrez, Pedro Agustìn Pèrez	Ageing management and life extension of technical systems- Concepts and methods applied to oil and gas facilities, IMT
IMT-11-2013	Chuang, Zhenju	Experimental and Numerical Investigation of Speed Loss due to Seakeeping and Maneuvering. IMT
IMT-12-2013	Etemaddar, Mahmoud	Load and Response Analysis of Wind Turbines under Atmospheric Icing and Controller System Faults with Emphasis on Spar Type Floating Wind Turbines, IMT
IMT-13-2013	Lindstad, Haakon	Strategies and measures for reducing maritime CO2 emissons, IMT
IMT-14-2013	Haris, Sabril	Damage interaction analysis of ship collisions, IMT
IMT-15-2013	Shainee, Mohamed	Conceptual Design, Numerical and Experimental Investigation of a SPM Cage Concept for Offshore Mariculture, IMT
IMT-16-2013	Gansel, Lars	Flow past porous cylinders and effects of biofouling and fish behavior on the flow in and around Atlantic salmon net cages, IMT
IMT-17-2013	Gaspar, Henrique	Handling Aspects of Complexity in Conceptual Ship Design, IMT
IMT-18-2013	Thys, Maxime	Theoretical and Experimental Investigation of a Free Running Fishing Vessel at Small Frequency of Encounter, CeSOS
IMT-19-2013	Aglen, Ida	VIV in Free Spanning Pipelines, CeSOS
IMT-1-2014	Song, An	Theoretical and experimental studies of wave diffraction and radiation loads on a horizontally submerged perforated plate, CeSOS
IMT-2-2014	Rogne, Øyvind Ygre	Numerical and Experimental Investigation of a Hinged 5-body Wave Energy Converter, CeSOS
IMT-3-2014	Dai, Lijuan	Safe and efficient operation and maintenance of offshore wind farms ,IMT
IMT-4-2014	Bachynski, Erin Elizabeth	Design and Dynamic Analysis of Tension Leg Platform Wind Turbines, CeSOS